Shape and topology optimization of frame structures considering uncertainty in variables and parameters

Wei Shen

2022

Contents

List of Figures

List of Tables

List of Abbreviations

CDF	Cumulative distribution function
DOF	Degree of freedom
DRM	Dimensional reduction method
FDM	Force density method
FEA	Finite element analysis
GA	Genetic algorithm
GRG	Generalized reduced gradient
i.i.d.	Independent and identically distributed
L-moment	Linear moment
L-statistic	Linear statistic
MCEP	Minimum cross-entropy principle
MCS	Monte Carlo simulation
MEM	Maximum entropy method
MPP	Most probable point
NLP	Nonlinear programming
PDF	Probability distribution function
PWM	Probability-Weighted Moment
RBSO	Reliability-based structural optimization
RSO	Robust structural optimization
SORA	Sequential optimization and reliability assessment
SQP	Sequential quadratic programming
Std. Dev.	Standard deviation
WCO	Worst case optimization

Chapter 1

Introduction

1.1 Research background

Design process of building structures is a collaborative work due to the interdisciplinary requirements from various aspects of architects and engineers, and the final result of a building project could be a compromise or synergy of different even conflict goals of the structure, such as aesthetics in appearance, structural strength and construction cost [1][2]. As a result, a large number of revisions are needed to iteratively balance the decisions made by architects and engineers which is inefficient and complicated. To alleviate this difficulty, one of the alternatives is to introduce structural optimization into the design process for generating design options with specified objectives and constraints [3]. In this way architects and engineers can work more interactively to save design time, and find out the optimal solution from these proposed designs that benefits the both sides [4][5]. Although the early idea of structural optimization can be traced back to the pioneering work of Michell truss [6] [7], it is not widely applied as a powerful tool until 1980s when the high performance computer system is rapidly developed [8]. Among all types of structures, optimization of frame structures is one of the standard research topic in structural optimization because it is commonly used in civil and architectural engineering. Typically, the optimization problem of frame structure is formulated as minimizing the structural cost (e.g., structural volume or weight) subject to constraints on structural response (e.g., deformation or stress), or vice versa, and the design variables are usually the cross-sectional properties and/or nodal locations. Then the problem is solved by either mathematical programming method [9][10], heuristic method [11][12] or the recently developed machine learning method [13][14], and the optimal solution can be considered as a design option or initial guess of the frame to be modified by architects and engineers [15].

Moreover, because uncertainties are unavoidable in the real world structure which could have impact on the result designed by structural optimization, it is more reasonable to incorporate uncertainty during optimization process to ensure that the result is practically useful [16]. Therefore, the research topic of structural optimization under uncertainty has attracted attention from researchers since the early works in 1960s [17], and become increasingly important in today's building industry [18][19]. Among them the robust structural optimization (RSO) [20] and reliability-based structural optimization (RBSO) [21] are two frequently used methods which consider the effects of uncertainties in different ways. On the one hand, RSO usually focuses on

searching for a result which is relatively insensitive to the variation of uncertainties, and several problem formulations are proposed based on different description of uncertainty [22]. Roughly speaking, when uncertainty is described by probabilistic model with available distribution information, the RSO problem is formulated to minimize the expectancy and discrepancy of structural response, including the standard measure of weighted sum of mean value and standard deviation of structural response [23][24]; otherwise, when uncertainty is described by non-probabilistic model, the RSO problem is formulated to minimize the worst structural response with all the possible realizations of uncertainties, which is also called worst case optimization (WCO) [25–27]. On the other hand, RBSO aims at finding a design satisfying the structural safety requirement, which is usually quantified by the probability of failure or reliability index [28][29]. Generally, RBSO consists two main calculation procedures: structural optimization procedure and reliability analysis procedure, and the methods for solving RBSO problem can be classified into different types depending on how reliability analysis is incorporated into structural optimization [21][30].

In addition, since the goal of frame optimization is usually to produce lighter and stronger structure, it often leads to a frame composed of slender members, and thus lacks sufficient stability. Therefore, the need to include stability constraint in frame optimization has been emphasized by many studies [31–33]. Among all the different phenomena covered by stability theory, because the detailed nonlinear stability information about the structure is not available at the early stage of design process, global stability (also called global buckling or linear buckling) is widely used to consider instability problem into structural optimization [34], and the nonlinear buckling load factor can be obtained by scaling the linear buckling load factor [35]. This procedure works well for many real-world structures to account for structural stability. When solving frame optimization problem with global stability constraint, a local buckling mode may appear if some of the members have very small cross-sectional areas, resulting in an artificial or pseudo buckling mode which violates the stability constraint. This is called singularity phenomenon in structural optimization considering global stability [36][37]. One of the alternatives is to penalize the geometrical stiffness matrices of thin members to reduce theirs contributions to the global geometrical stiffness matrix, and thus the artificial buckling mode can be eliminated from global stability analysis [38]. This penalization method has been used by many researchers and currently appears to be a standard approach to alleviate the difficulty caused by singularity phenomenon in global stability [39][40].

1.2 Literature review

1.2.1 Optimization of frame structures

Optimization of frame structures can be classified into three categories, namely, sizing, shape (or geometry) and topology optimization, which are illustrated in Fig. 1-1. Sizing optimization, which aims at finding the optimal cross-sectional properties of members, is usually included in shape and topology optimization, and the change of structural topology can be achieved in the standard framework of sizing optimization [41][42]. Based on the well-established ground structure method [43], the optimal topology of a frame structure is obtained by removing the unnecessary members

from the set of potential connections of nodes with fixed locations and retaining the members with positive cross-sectional properties. Compared to the optimal Michell truss which is composed of an infinite number of members, the ground structure method provides an alternative by using a finite number of members [44]. It has been further refined by Sokol [45] to an easy-to-use implementation for truss topology optimization in structured orthogonal domains, which is also extended to unstructured meshes in initial ground structure [46]. Lewinski *et al*. [47] also used ground structure method to approximate the exact solution of optimization problem with complicated domain. However, since the nodal locations are unable to vary during the optimization process, it is necessary to work with as many nodes and members as possible for shape optimization, resulting in a large number of design variables.

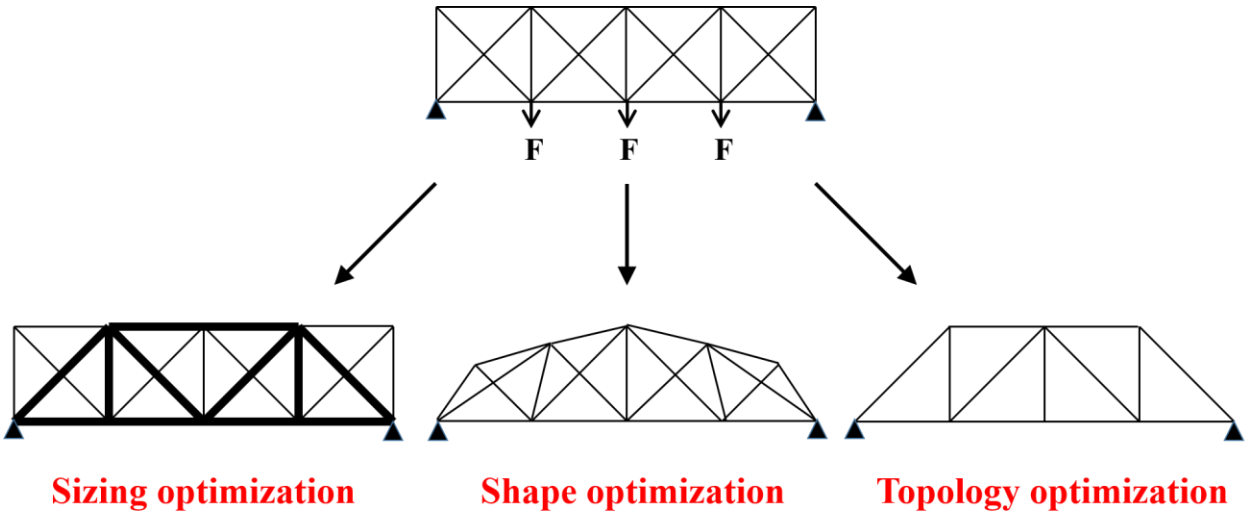

Fig. 1-1 Classification of optimization of frame structure

Unlike the ground structure method, shape and topology optimization of frame structures allows the node to vary in a given range, leading to an effective improvement of objective function value [48–50]. Therefore, it may start from a sparse initial structure with less members. When shape optimization is involved, however, one of the main difficulties is the existence of melting nodes, or coalescent nodes, resulting in extremely short member in the structure and making the stiffness matrix singular [51]. Moreover, the derivative of the objective function with respect to the nodal coordinates becomes discontinuous due to existences of extremely short members. Ohsaki [52] modeled a regular grid truss as a frame with beam elements and adjusted the stiffness of a short member using a Sigmoid function. Wang *et al*. [53][54] proposed a node shift method for truss shape optimization where the intervals of node shift are controlled not to cause a large variation in stiffness matrix.

To widen the moving range of nodes during shape optimization and at the same time to alleviate the difficulty of melting node, Ohsaki and Hayashi [55][56] recently explored the merit of force density method (FDM) to shape and topology optimization of pin-jointed trusses, in which

the objective and constraint functions are expressed explicitly by the force densities only; thus, the problem caused by melting nodes is alleviated. FDM is primarily applied in the form-finding process of cable nets and tensegrity structures, where the nonlinear equilibrium equations with respect to the unknown nodal coordinates is converted to a set of linear equations by prescribing the force density of each member which is defined as the ratio of member force to its length [57][58]. Kimura *et al*. [59][60] optimized the shape of shear wall consisting of latticed blocks, where force densities of members are used as auxiliary parameters for arrangement of lattice members, and the problem is solved by alternatively optimizing the geometry and topology of the lattice. Descamps and Coelho [61] used force density as an intermediate variable in the formulation of compliance minimization problem of truss. However, since the members of a frame are rigidly-jointed, not only axial force but also shear force and bending moment exist in frame structures, to which the FDM for cable nets and trusses cannot be directly applied.

1.2.2 Optimization under uncertainty

In RSO, when probabilistic model is used to describe the uncertainties, the variation of structural response is usually represented by its second-order statistical moment, and it is simultaneously minimized or assigned as constraints with its first-order statistical moment (i.e., mean value) [23][24]. However, substantial effort is needed for calculation of the statistical moments and their derivatives if more than one type of random variables are involved, or uncertainty is assumed in the structural stiffness because the displacement is a function of the inverse of uncertain stiffness matrix [62][63]. To alleviate this difficulty, the stochastic method has been introduced to describe the characteristics of the uncertain parameters, and it attracts more attention from the researchers due to its explicit form of uncertainty propagation [64][65] [66]. However, balancing the accuracy and computational efficiency is still a challenge and such kind of method has not been fully explored yet. In addition, this type of RSO requires accurate distribution information of uncertainties to ensure accuracy of the solution, and a large estimation error will occur when the information about uncertainty is insufficient [67][68].

By contrast, the WCO provides an alternative if the uncertainty is described by a non-probabilistic model [19]. Traditionally, the procedure of WCO consists of a two-level problem: the upper- and lower-level problems are solved for structural optimization and worst value evaluation, respectively [26][69][70]. However, the computational cost for searching the exact worst value is very large even for a simple interval model or a well-defined ellipsoid model to define the region of uncertain parameters [27] [71]. To save computational cost without loss of generality, Kanno and Takewaki [72][73] constructed a minimum confidence ellipsoid of the structural response to solve the WCO problem in a confidence way, and the uncertainty is considered in the cross-sectional areas and the applied load; Guo *et al*. [74] extended this method to a single-level problem formulation with stiffness uncertainty and fixed nodes; Kanno and Guo [75] reduced the discrete WCO of truss structure to a mix-integer programming problem where the uncertain load is predefined in an ellipsoid. Although these WCO approaches with confidence robustness model can be successfully solved, their application to shape optimization requires uncertainty in nodal locations, which is another common source of uncertainty. Fu *et al*. [76] solved the truss topology optimization problem with uncertain nodal locations using proportional

topology optimization method, where the inverse of stiffness matrix is expressed based on Neumann series expansion. However, since its objective function is the expected value of structural response, this method might be insufficient to characterize the uncertain properties of the structure if the deviation of response is moderately large. Recently, Ohsaki *et al*. [77][78] developed an order statistic approach to consider the worst value with certain confidence level, in which the worst value is approximated by the *k*th order statistic and the parameter *k* is regarded as the robustness level according to the theory of distribution-free tolerance interval. This method can be regarded as a special case of scenario optimization where the scenario theory is used to provide a certain robustness for the optimal solution [79], that is, the probability of the solution not to violate the requirements in the unseen future with given sample set and confidence level.

As for RBSO, according to their strategies to incorporate reliability constraints in optimization procedure, the methods for solving RBSO problem can be classified into three categories: double-loop method, single-loop method and decoupling method, and their corresponding schematic presentations are shown in Fig. 1-2. In double-loop method the probability constraints are evaluated at each iteration of the optimization procedure with the current values of design variables. Therefore, there are two nested loops in the double-loop method: the inner loop evaluates the probability constraints at each iteration of the outer loop of optimization procedure. Although the double-loop method is easy to implement, it would become computationally infeasible because it consists of nested loops of design optimization and reliability analysis [80]. Therefore, great effort has been made in the past two decades to improve its computational efficiency by either facilitating the procedure of reliability analysis [81] or modifying the formulation of probability constraints [82]. Lee *et al*. [83] introduced the popular dimensional reduction method (DRM) into the double-loop RBSO with a new inverse reliability analysis to reduce the number of function evaluations in multidimensional probability integration; Rahman and Wei [84] also applied DRM to a double-loop RBSO procedure where the sensitivity coefficients of probability with respect to design variables are derived. However, since the inner loop of reliability analysis is called at each time when the design variables are updated at the outer loop, the number of reliability analyses could be still very large, leading to a high computational cost. On the other hand, the single-loop method provides an alternative to reduce the number of RBSO function calls, where the reliability constraint is converted into approximated deterministic constraint at most probable point (MPP). Chen *et al*. [85] first proposed the single-loop single-vector method where the unit direction vector for searching the MPP is assumed to be constant, and Liang *et al*. [86] further developed the method by adaptively calculating the unit direction vector during the optimization procedure. It is proven that the single-loop method is one of the most efficient approaches for solving RBSO problems [87]; however, its numerical stability is still a challenge when the limit state function is highly nonlinear [30].

The decoupling method improves the efficiency of double-loop method from another perspective, where the inner loop of reliability analysis is decoupled from the outer loop of optimization, and the evaluations of probabilistic constraints are only conducted at the end of each sub-deterministic optimization process. Early works of decoupling method approximate the probability constraints using sensitivity information of the previous iteration [88]. Du and Chen [89] proposed the sequential optimization and reliability assessment (SORA) method which

decouples the reliability analysis from structural optimization using the shifting vector. Since then, SORA has gradually become one of the frequently used methods for solving RBSO problems because of its simplicity and stability [30], and many researches have been conducted to enhance its performance. Du [90] further improved the accuracy of SORA by using saddle point approximation to handle the nonlinearity in probability constraints caused by the transformation between non-normal and normal random variables. Chen *et al*. [91] searched the optimal shifting vector using the limit state functions to accurately adjust the boundaries of probability constraints when they are highly nonlinear. However, as most of the existing SORAs are MPP-based methods, one of the challenges is that the MPP-based SORA may not be able to converge if there are multiple MPPs [92]. To overcome this difficulty, recently Li *et al*. [93] proposed a quantile-based SORA method where the shifting vector is calculated in the probability space without relying on the accurate MPP. The Kriging model is also applied instead of the crude Monte Carlo simulation (MCS) to reduce the computational cost for calculating the quantile. He *et al*. [94] further extended the quantile-based SORA method by calculating the quantile corresponding to the target reliability using fractional moment-based maximum entropy method (MEM), where the two-level optimization problem to obtain the values of Lagrangian multipliers and the orders of fractional moments is reduced to a single-loop optimization problem by using Laplace transform [24]. However, the Laplace transform of unknown probability distribution function (PDF) needs to be carefully chosen otherwise it may spoil the result [95].

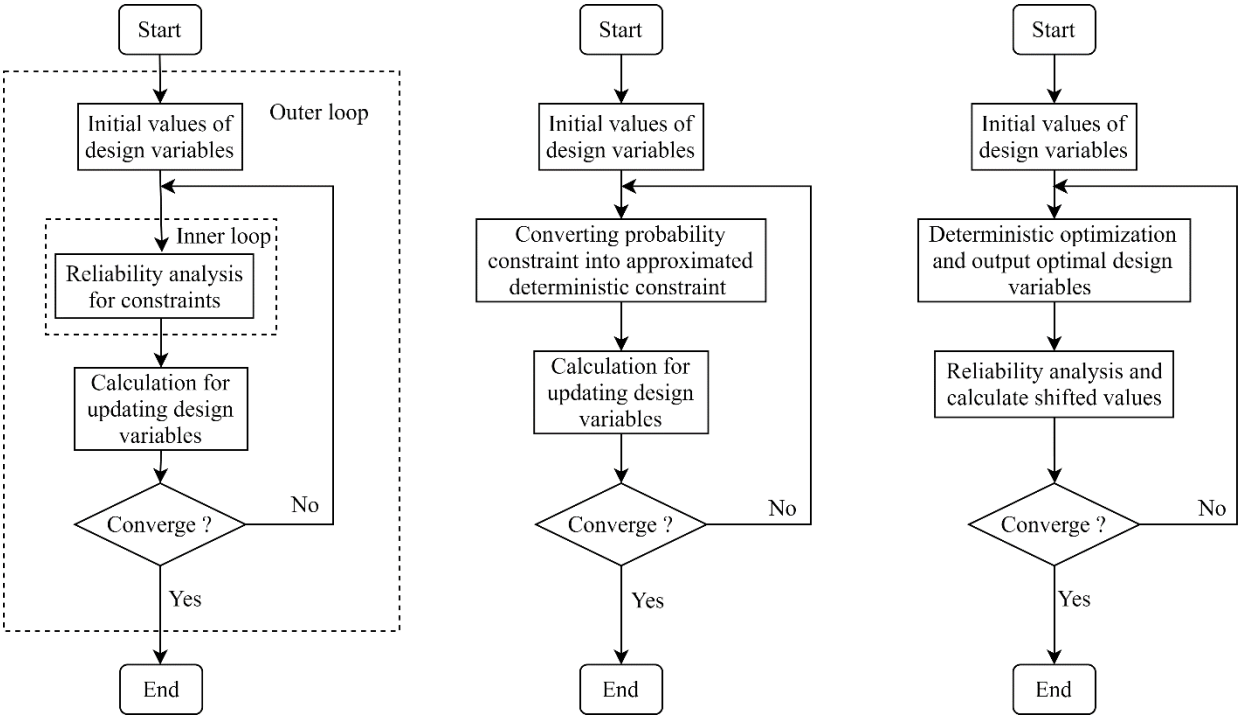

Fig. 1-2 Strategies for solving RBSO problem, from left to right: double-loop method, single-loop method and decouple method

Similar to RSO problem, another challenge in RBSO problem is that in practice the exact probability information of uncertainties may be unavailable beforehand, and one would need to estimate the structural reliability with a given set of random samples of uncertain parameters [96][97]. Moreover, the sample size and sampling variability have great effect on the accuracy of reliability estimation [98–101], and it is recognized that the estimation of higher order central moment from a set of random samples tends to be biased when the sample size is small [99] [102]. To overcome such difficulties, Pandey [102] estimated the quantile function of a random variable with unknown distribution using MEM subject to sample probability-weighted moments (PWMs), and the results showed that this method is more reliable than the method using sample central moments when sample size is small. Deng and Pandey [103] further improved this method with fractional PWMs; however, the Lagrange multipliers and the orders of fractional moments are determined by the computationally expensive two-level nested optimization procedure. Besides, since the single-level method in Ref. [95] is constructed for ordinary fractional moments, it cannot be directly applied to the quantile-based MEM subject to fractional PWM constraints. On the other hand, Pandey [104][105] also presented an approach for quantile estimation using minimum cross-entropy principle (MCEP) subject to PWM constraints, and stated that if the prior distribution in MCEP is uniform, the cross-entropy minimization is equivalent to entropy maximization. However, since MCEP requires a prior distribution for quantile estimation, the MEM is more appropriate than MSEP when any prior information of uncertainties is absent. Hosking [106] found that by using MEM subject to specified linear moments (L-moments), the density-quantile function of an unknown random variable, which is the derivative of the quantile function, has a polynomial form, and the corresponding quantile function can then be obtained by numerical integration. However, the unknown coefficients in density-quantile function are derived by solving a complex system of nonlinear equations.

1.2.3 Optimization with stability constraints

Global stability constraint in frame optimization is typically formulated using linear buckling load factor, and the geometric nonlinearity induced by large deformation under external loading is ignored. Ohsaki *et al*. [107] solved the truss topology optimization problem under frequency constraints by using semidefinite programming, and Kanno and Ohsaki [108] extended the method to optimization of frame structures with global stability constraint, where the optimization problem is transformed into a nonlinear semidefinite programming problem with a matrix inequality constraint . Ben-Tal *et al*. [109] also proposed a semidefinite programming formulation for truss optimization with global stability constraint. Weldeyesus *et al*. [110] introduced shape optimization to an existing truss topology optimization with global stability constraints, whereas the range of node shift is limited. Moreover, in order to take into account both global and local stabilities of the structure, Torii *et al*. [111] modeled the truss structure using frame elements to capture the local buckling without the use of the Euler formula, and formulated the optimization problem with only one global stability constraint to consider both local and global buckling constraints. Madah and Amir [112] simulated each truss member by a sequence of geometrically nonlinear beam elements which release the bending moments at the ends of a bar, and the global

stability is taken into account by applying appropriate imperfections on the structure. Descamps and Coelho [61] used force density as an intermediate variable in the formulation of compliance minimization problem, and avoided the nodal instability by applying the nominal force method to simulate the geometric imperfection. Meanwhile, Evgrafov [37] showed that global stability consideration may face singularity phenomenon when the cross-sectional area approaches the small lower bound. To alleviate this difficulty, Guo *et al*. [113][114] extended the relaxation technique, which is firstly proposed to handle stress constraints, to optimization problem of truss structure under stability and stress constraints. On the other hand, Bendsøe and Sigmund [3] proposed to use a scheme for penalizing the geometric stiffness matrix of thin members. Furthermore, based on the identification scheme of pseudo buckling mode in continuous structural topology optimization [39], Asadpoure *et* al [34] introduced a set of indicator variables of existence for each member in the frame structure to exclude the contributions of geometric matrices of thin elements, which can be also considered as a variant of penalization method [115]. It has been pointed out that the penalization method works well[39][40]; therefore, the method is used by many other researchers to deal with singularity phenomenon [38].

1.3 Research objectives

Objective of this research is to investigate and exploit new methods for shape and topology optimization of plane frame structures, which aims at alleviating some difficulties and challenges in the existing methods. The specific goals relevant to this work are:

1) To develop a new method for simultaneous shape and topology optimization of plane frame structures which is capable of avoiding melting nodes.

2) To define the structural robustness level in RSO problem formulation without any prior assumption on the distributions of uncertainties.

3) To express the reliability constraint in RBSO problem formulation in terms of quantile of structural response without searching MPP.

4) To discuss the influence of stability constraint on the optimal result.

1.4 Thesis outline

The rest of dissertation is organized as follows: in **Chapter 2** the basic concepts of methodologies and techniques which contributes to the main novelties and findings of the dissertation are introduced; in **Chapter 3** the method of simultaneous shape and topology optimization of plane frames is presented with illustrative examples, and the method will also be applied to both robust optimization in **Chapter 4** and reliability-based optimization in **Chapter 5**; finally, **Chapter 6** summaries the results of **Chapters 2-5**, and gives some suggestions to the future study.

Chapter 2

Basic concepts

2.1 Brief introduction

Chapter 2 is to give some basic concepts and definitions of some terminologies and techniques, which will be used for further investigation and discussion of optimization of frame structures in this research. A brief introduction of this chapter is given as follows.

In Section 2.2, the idea of FDM is briefly explained, which will be used for shape optimization of frame structures in Chapters 3–5. Unlike the traditional FDM, in this research the fixed nodes include supporting nodes, loading nodes and the nodes for specific reason, and the locations of free nodes are obtained by solving the equilibrium equations to determine the structural shape.

In Section 2.3, the definition of order statistics is first given, which will be used to define structural robustness level in Chapter 4. Unlike the traditional definition, in this research the order statistics are sorted in a descending order for convenience, and some properties of order statistics are also presented. Moreover, by using order statistics the calculations of linear moments (L-moments) and sample L-moments are derived, which will be used to compute the reliability constraints in Chapter 5.

In Section 2.4, the definitions of uncertainties in nodal locations, cross-sectional areas and Young's modulus are given, which will be used in Chapters 4 and 5. When the global stability constraint is involved in the problem, each frame member is modeled by four Euler-Bernoulli beam elements for application to the linear buckling analysis, and the uncertainty should also be considered at the end nodes of these beam elements, making the frame member no longer straight. Note that in this research no assumption is made on the distribution types of the uncertainties.

In Section 2.5, the singularity phenomenon of global stability is discussed. When the thin elements are not removed from the structure, the linear buckling load factor is much smaller than that after removing the thin elements, which makes the structure easier to violate the stability constraint.

2.2 Force density method

FDM is widely used in the form-finding process of pin-jointed structures, such as cable nets and tensegrity structures, where the force density is defined as the axial force divided by the length of a member. In this study for optimization of frame structures, FDM is used for an auxiliary pin-jointed truss or cable net structure to generate nodal locations. Let m and n represent the numbers of members and nodes of the auxiliary truss, respectively. If member i connects nodes j and k $\left(j \neq k\right)$, then the m-by-n connectivity matrix $\boldsymbol{C}$ is given by defining each entry as [55][58]

$$\boldsymbol{C}_{(i,p)} = \begin{cases} 1 & p = j \\ -1 & p = k \\ 0 & \text{other case} \end{cases} \quad \left(i = 1, 2, \cdots, m;\ j, k = 1, 2, ..., n\right) \tag{2.1}$$

where the subscript (i, p) indicates the entry of $\boldsymbol{C}$ at the ith row and pth column. The force density t_i of the ith member is defined as

$$t_i = \frac{N_i}{L_i} \tag{2.2}$$

where N_i is the axial force and L_i is the length of the ith member. Accordingly, the m-by-1 force density vector is denoted by $\boldsymbol{t} = \left(t_1, t_2, ..., t_m\right)^T$. Let $\boldsymbol{x}_{\text{free}}$, $\boldsymbol{x}_{\text{fix}}$, $\boldsymbol{y}_{\text{free}}$ and $\boldsymbol{y}_{\text{fix}}$ represent the x- and y-coordinates of the free nodes and the fixed nodes, respectively, and arrange the columns of connectivity matrix $\boldsymbol{C}$ such that the columns corresponding to the free nodes precede those corresponding to the fixed nodes, i.e., $\boldsymbol{C} = \left(\boldsymbol{C}_{\text{free}}, \boldsymbol{C}_{\text{fix}}\right)$. Then the equilibrium equations at the free nodes and the fixed nodes of the auxiliary pin-jointed structure are written as

$$\begin{aligned}
&\boldsymbol{C}_{\text{free}}^T \text{diag}\left(\boldsymbol{t}\right)\boldsymbol{C}_{\text{free}}\boldsymbol{x}_{\text{free}} + \boldsymbol{C}_{\text{free}}^T \text{diag}\left(\boldsymbol{t}\right)\boldsymbol{C}_{\text{fix}}\boldsymbol{x}_{\text{fix}} = \boldsymbol{P}_{x,\text{free}} \\
&\boldsymbol{C}_{\text{free}}^T \text{diag}\left(\boldsymbol{t}\right)\boldsymbol{C}_{\text{free}}\boldsymbol{y}_{\text{free}} + \boldsymbol{C}_{\text{free}}^T \text{diag}\left(\boldsymbol{t}\right)\boldsymbol{C}_{\text{fix}}\boldsymbol{y}_{\text{fix}} = \boldsymbol{P}_{y,\text{free}} \\
&\boldsymbol{C}_{\text{fix}}^T \text{diag}\left(\boldsymbol{t}\right)\boldsymbol{C}_{\text{free}}\boldsymbol{x}_{\text{free}} + \boldsymbol{C}_{\text{fix}}^T \text{diag}\left(\boldsymbol{t}\right)\boldsymbol{C}_{\text{fix}}\boldsymbol{x}_{\text{fix}} = \boldsymbol{P}_{x,\text{fix}} \\
&\boldsymbol{C}_{\text{fix}}^T \text{diag}\left(\boldsymbol{t}\right)\boldsymbol{C}_{\text{free}}\boldsymbol{y}_{\text{free}} + \boldsymbol{C}_{\text{fix}}^T \text{diag}\left(\boldsymbol{t}\right)\boldsymbol{C}_{\text{fix}}\boldsymbol{y}_{\text{fix}} = \boldsymbol{P}_{y,\text{fix}}
\end{aligned} \tag{2.3}$$

where diag($\boldsymbol{t}$) is the square diagonal matrix with the elements of vector $\boldsymbol{t}$ on the main diagonal, and $\boldsymbol{P}_{x,\text{free}}$, $\boldsymbol{P}_{x,\text{fix}}$, $\boldsymbol{P}_{y,\text{free}}$ and $\boldsymbol{P}_{y,\text{fix}}$ are the external forces applied at the free nodes and fixed nodes in x- and y-directions, respectively. For the conventional FDM, the free nodes and fixed nodes are determined in accordance with the support conditions. However, in this research, the fixed nodes consist of the supported nodes and loaded nodes, as well as the nodes for specific reason, e.g., requirement of structural shape, that are not allowed to move during the optimization process.

If the force densities are given for all members in the structure and the locations of fixed nodes are assigned, then the locations of free nodes can be obtained from Eq. (2.3), that is

$$\boldsymbol{x}_{\text{free}} = -\left(\boldsymbol{C}_{\text{free}}^T \text{diag}\left(\boldsymbol{t}\right)\boldsymbol{C}_{\text{free}}\right)^{-1}\boldsymbol{C}_{\text{free}}^T \text{diag}\left(\boldsymbol{t}\right)\boldsymbol{C}_{\text{fix}}\boldsymbol{x}_{\text{fix}}$$
$$\boldsymbol{y}_{\text{free}} = -\left(\boldsymbol{C}_{\text{free}}^T \text{diag}\left(\boldsymbol{t}\right)\boldsymbol{C}_{\text{free}}\right)^{-1}\boldsymbol{C}_{\text{free}}^T \text{diag}\left(\boldsymbol{t}\right)\boldsymbol{C}_{\text{fix}}\boldsymbol{y}_{\text{fix}} \tag{2.4}$$

It has been proved by Kanno and Ohsaki [116] that the submatrix corresponding to free nodes in the connectivity matrix, i.e., $\boldsymbol{C}_{\text{free}}$, is non-singular if at least one node is fixed. Therefore, if $\boldsymbol{t}$ is a non-zero vector and at least one node is fixed, then the matrix $\boldsymbol{C}_{\text{free}}^T \text{diag}\left(\boldsymbol{t}\right)\boldsymbol{C}_{\text{fix}}$ is non-singular and Eq. (2.4) has a solution for $\boldsymbol{x}_{\text{free}}$ and $\boldsymbol{y}_{\text{free}}$.

2.3 Order statistics and L-moments

Order statistic is a very useful concept in statistical science and one of the most fundamental tools in non-parametric statistics and inference [117]. Suppose $\boldsymbol{d} = \left(d_1, d_2, \ldots, d_{n_d}\right)$ and $\boldsymbol{\theta} = \left(\theta_1, \theta_2, \ldots, \theta_{n_{\text{u}}}\right)$ are the vectors of n_{d} design variables and n_{u} uncertain parameters, and let $\boldsymbol{\theta}_1$, $\boldsymbol{\theta}_2, \ldots, \boldsymbol{\theta}_{m_{\text{s}}}$ be the m_{s} independent and identically distributed (i.i.d.) vectors of uncertain parameters. The corresponding m_{s} structural responses are denoted as

$$Z_1 = g\left(\boldsymbol{d};\boldsymbol{\theta}_1\right),\ Z_2 = g\left(\boldsymbol{d};\boldsymbol{\theta}_2\right), \ldots,\ Z_{m_{\text{s}}} = g\left(\boldsymbol{d};\boldsymbol{\theta}_{m_{\text{s}}}\right) \tag{2.5}$$

where $g\left(\boldsymbol{d};\boldsymbol{\theta}_i\right),\ i = 1, 2, \ldots, m_{\text{s}}$ is the ith stochastic structural response corresponding to $\boldsymbol{d}$ and $\boldsymbol{\theta}_i$. Because Z_1, Z_2, …, $Z_{m_{\text{s}}}$ are obtained from the same response function with i.i.d. uncertain parameters, it is rational to assume that these responses are samples from the same distribution with unknown cumulative distribution function (CDF) denoted by $F\left(z\right) = \Pr\left\{Z \le z\right\}$. We further define the values $Z_{1:m_{\text{s}}}$, $Z_{2:m_{\text{s}}}$, …, $Z_{m_{\text{s}}:m_{\text{s}}}$ as a permutation of Z_1, Z_2, …, $Z_{m_{\text{s}}}$ such that $Z_{1:m_{\text{s}}} \ge Z_{2:m_{\text{s}}} \ge \ldots \ge Z_{m_{\text{s}}:m_{\text{s}}}$, and the kth $\left(1 \le k \le m_{\text{s}}\right)$ response $Z_{k:m_{\text{s}}}$ is called the kth order statistic. Note that the descending order statistics herein are used for convenience to approximate the maximum structural response, which is different from the conventional definition of order statistics arranged in an ascending order.

Next we introduce some properties of order statistics. Firstly, let U_1, U_2, …, $U_{m_{\text{s}}}$ be the m_{s} random samples from standard uniform distribution, and $U_{1:m_{\text{s}}}$, $U_{2:m_{\text{s}}}$, …, $U_{m_{\text{s}}:m_{\text{s}}}$ be the corresponding order statistics in a descending order as defined above. Then we can have the following relation [117]

$$F\left(Z_{k:m_{\text{s}}}\right) \triangleq U_{k:m_{\text{s}}},\ k = 1, 2, ..., m_{\text{s}} \tag{2.6}$$

for any arbitrary CDF $F\left(z\right)$. Using the inverse CDF $F^{-1}\left(z\right)$ we can also have

$$F^{-1}\left(U_{k:m_s}\right) \triangleq Z_{k:m_s},\ k=1,2,...,m_s \tag{2.7}$$

Another useful property of order statistics $U_{1:m_s}$, $U_{2:m_s}$,…, $U_{m_s:m_s}$ is the distribution of range between two order statistics. Suppose $U_{k_1:m_s}$ and $U_{k_2:m_s}$ are the two order statistics with orders $1 \le k_1 < k_2 < m_s$, and denote $U_{k_2-k_1:m_s}$ as the range between $U_{k_1:m_s}$ and $U_{k_2:m_s}$. According to Ref. [117] we have

$$U_{k_2-k_1:m_s} = U_{k_1:m_s} - U_{k_2:m_s} = U_{m_s-(k_2-k_1)+1:m_s} \tag{2.8}$$

Besides, let $F_{k:m_s}\left(z\right) = \Pr\left\{Z_{k:m_s} \le z\right\}$ be the CDF of $Z_{k:m_s}$ which is computed as [117]

$$F_{k:m_s}\left(z\right) = \Pr\left\{Z_{k:m_s} \le z\right\} = \sum_{r=m_s-k+1}^{m_s} \binom{m_s}{r} \left\{F\left(z\right)\right\}^r \left\{1-F\left(z\right)\right\}^{m_s-r} \tag{2.9}$$

By using the identity equation [117]

$$\sum_{r=m_s-k+1}^{m_s} \binom{m_s}{r} \left\{F\left(z\right)\right\}^r \left\{1-F\left(z\right)\right\}^{m_s-r} = \int_0^{F(z)} \frac{m_s!}{\left(m_s-k\right)!\left(k-1\right)!} u^{m_s-k}\left(1-u\right)^{k-1} du \tag{2.10}$$

Eq. (2.9) can then be rewritten with respect to incomplete beta function $I_{F(z)}\left(m_s-k+1,k\right)$ as

$$\begin{aligned} F_{k:m_s}\left(z\right) &= \Pr\left\{Z_{k:m_s} \le z\right\} = \sum_{r=m_s-k+1}^{m_s} \binom{m_s}{r} \left\{F\left(z\right)\right\}^r \left\{1-F\left(z\right)\right\}^{m_s-r} \\ &= \int_0^{F(z)} \frac{m_s!}{\left(m_s-k\right)!\left(k-1\right)!} u^{m_s-k}\left(1-u\right)^{k-1} du = I_{F(z)}\left(m_s-k+1,k\right) \end{aligned} \tag{2.11}$$

Clearly, if $F\left(z\right)$ is a CDF of standard uniform distribution, then we can have $I_{F(z)}\left(m_s-k+1,k\right) = I_z\left(m_s-k+1,k\right)$, $0<z<1$.

Furthermore, let $Z_{k_1:m_s}$ and $Z_{k_2:m_s}$ be the two order statistics with orders $1 \le k_1 < k_2 < m_s$. Based on Eqs. (2.6) and (2.11), the probability $\beta_{k_1,k_2:m_s}$ of a random sample falling into the interval between $Z_{k_1:m_s}$ and $Z_{k_2:m_s}$ is calculated as follows:

$$\beta_{k_1,k_2:m_s} = F\left(Z_{k_1:m_s}\right) - F\left(Z_{k_2:m_s}\right) = U_{k_1:m_s} - U_{k_2:m_s} = U_{m_s-(k_2-k_1)+1:m_s} \tag{2.12}$$

Then based on Eqs. (2.9) and (2.12), the probability of $\beta_{k_1,k_2:m_s}$ no less than a specific value $\beta\left(0<\beta<1\right)$ is calculated as

$$\Pr\left\{\beta_{k_1,k_2:m_s} \ge \beta\right\} = \Pr\left\{U_{m_s-(k_2-k_1)+1:m_s} \ge \beta\right\} = \sum_{r=0}^{m_s-(k_2-k_1)} \binom{m_s}{r} \beta^r \left(1-\beta\right)^{m_s-r} = \alpha_{k_1,k_2:m_s} \tag{2.13}$$

It can be observed in Eq. (2.13) that $\alpha_{k_1,k_2:m_s}$ only depends on the orders k_1, k_2 and sample size m_s, and is free of distribution F. In other words, the interval between $Z_{k_1:m_s}$ and $Z_{k_2:m_s}$ forms a distribution free 100β% tolerance interval for the population at confidence level $\alpha_{k_1,k_2:m_s}$. Therefore, Eq. (2.13) is called distribution-free tolerance interval at the confidence level $\alpha_{k_1,k_2:m_s}$ [117].

As for L-moments, they are defined as linear combinations of order statistics analogously to conventional moments. Taking the aforementioned stochastic structural response Z as example, the rth (r≥1) order L-moment of Z, denoted as LM_r, is given as follows [118]:

$$LM_r = r^{-1}\sum_{k=0}^{r-1}(-1)^k \binom{r-1}{k} \mathrm{E}\left(Z_{k+1:r}\right) \tag{2.14}$$

where $\mathrm{E}\left(Z_{k+1:r}\right)$ is the expectation (i.e., mean value) of the order statistic $Z_{k+1:r}$. Since the distribution information of $Z_{k+1:r}$ is unknown, in practice it is usually estimated by the sample L-moments from the m_s samples $Z_{1:m_s}$, $Z_{2:m_s}$,…, $Z_{m_s:m_s}$. Denoting the rth order sample L-moment of Z as lm_r, it can be obtained by

$$lm_r = \sum_{s=0}^{r-1}(-1)^{r-1-s} \binom{r-1}{s} \binom{r-1+s}{s} b_s \tag{2.15}$$

where b_s is one kind of the sample probability weighted moments (PWMs) of Z calculated as follows [118]:

$$b_s = m_s^{-1}\sum_{i=1}^{m_s} \frac{(m-i)(m-i-1)\cdots(m-i-s+1)}{(n-1)(n-2)\cdots(n-s)} Z_{i:m_s} \tag{2.16}$$

2.4 Uncertainty in structural stiffness

Since in practical engineering the joint locations and cross-sectional areas of members in the frame structure may deviate from their corresponding nominal values due to manufacturing or on-site construction error, and uncertainty in the material property should also be considered. Therefore, in this research the uncertainties in structural stiffness is assumed to possibly exist in the x- and y-coordinates of nodes, cross-sectional areas and Young's modulus, and they are modeled as random variables with unknown distribution information. For simplicity, the fixed nodes, such as loading and supporting nodes, are assumed to be precisely located, and uncertainties are only considered in x- and y-coordinates of free nodes, respectively, although it is also possible to add uncertainties to the x- and y-coordinates of fixed nodes to simulate the variations such as installation error at the

support in practical engineering. It should be noted in the problem formulations of Chapters 4 and 5 that no assumption is made on the distribution information of uncertainty. However, in the numerical examples of Chapters 4 and 5, we choose uniform distribution as the sample-generating mechanism for conveniently constructing the random sample set for order statistics [79].

The details of modeling uncertainties will be illustrated below. Suppose the *i*th member is connected by two nodes *i*1 and *i*2 as shown in Fig. 2-1(a) with member length L_i. The random perturbations are firstly added to the locations of the end nodes *i*1 and *i*2 in *x*- and *y*-coordinates, and the corresponding uncertain nodal locations are expressed as

$$\left(x_j', y_j'\right) = \left(x_j, y_j\right) + \left(\Delta x_j, \Delta y_j\right) \quad \text{for} \quad j = i1,\ i2 \tag{2.17}$$

where $\left(x_j', y_j'\right)$ is the uncertain location of node *j* after adding perturbations and $\left(x_j, y_j\right)$ is the nominal location of node *j* before adding perturbations, which are denoted as blue and red dots in Fig. 2-1(a), respectively; $\left(\Delta x_j, \Delta y_j\right)$ are the random perturbations of uncertainty in nodal locations.

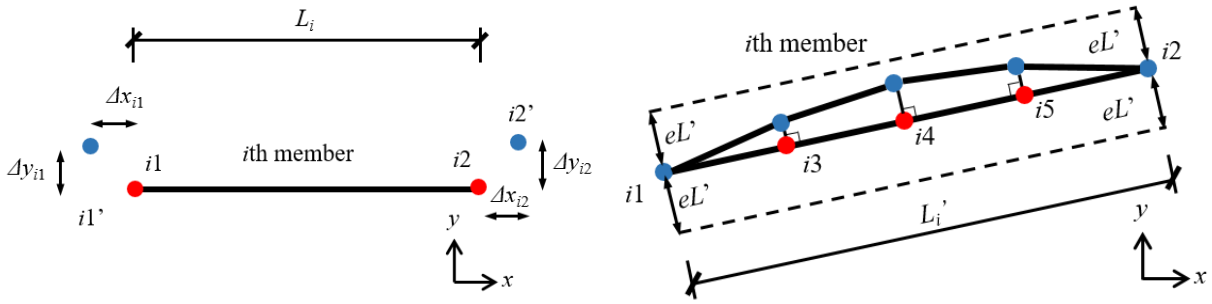

(a) (b)

Fig. 2-1 Uncertainty in nodal locations of the *i*th member on (a) end nodes; (b) intermediate nodes

After determining the uncertain locations of the end nodes, the member length is changed from L_i to L_i'. When no global stability constraint is considered or L_i' is small enough, the *i*th member is simulated by only one Euler-Bernoulli beam element, otherwise it is simulated by four Euler-Bernoulli beam elements with the same element length, which are distinguished by three intermediate nodes *i*3, *i*4 and *i*5 as shown by the red dots in Fig. 2-1(b). Interpolating between the uncertain locations $\left(x_{i1}', y_{i1}'\right)$ and $\left(x_{i2}', y_{i2}'\right)$ of nodes *i*1 and *i*2 obtained by Eq. (2-17), the locations of the three intermediate nodes are calculated as follows:

$$\left(x_j', y_j'\right) = \left(x_{i1}', y_{i1}'\right) + k\left[\frac{\left(x_{i2}', y_{i2}'\right) - \left(x_{i1}', y_{i1}'\right)}{4}\right],\ k=1,2,3 \tag{2.18}$$

where k = 1, 2 and 3 correspond to the locations of i3, i4 and i5, respectively. For the given eccentricity e of the ith member, which is the maximum deviation from the straight line connected the two end nodes i1' and i2' and can be considered as initial imperfection shape, the random perturbations are added to nodes i3, i4 and i5 perpendicular to the ith member, and the uncertain locations of these three nodes are calculated as

$$\begin{aligned} &\left(x_j'', y_j''\right) = \left(x_j', y_j'\right) + \left(\Delta x_j, \Delta y_j\right) \text{ for } j = i3,\ i4,\ i5 \\ &\sqrt{\Delta x_j{}^2 + \Delta y_j{}^2} \le eL_i';\quad \left(\Delta x_j, \Delta y_j\right) \perp \left(x_{i2}' - x_{i1}', y_{i2}' - y_{i1}'\right) \end{aligned} \tag{2.19}$$

where $\left(x_j'', y_j''\right)$, $(j = i3,\ i4,\ i5)$ are the uncertain locations of nodes i3, i4 and i5 as shown by the blue dots in Fig. 2-1(b), and $\left(\Delta x_j, \Delta y_j\right)$, $j = i3,\ i4,\ i5$ are the random perturbations on the locations of nodes i3, i4 and i5. It can be seen from Figs 2-1(a) and (b) that the final imperfect geometry of the ith member is obtained through the uncertain locations of two end nodes i1 and i2 and three intermediate nodes i3 to i5. Moreover, in order to consider the correlation relationships among uncertainties in locations of end nodes and intermediate nodes, the following exponential decay function is used to calculate the correlation coefficient [66]:

$$c_{j1j2} = \exp\left(-\frac{\left\|\left(x_{j1}, y_{j1}\right) - \left(x_{j2}, y_{j2}\right)\right\|}{L_{\exp}}\right),\ j1,\ j2 = i1,\ i2, \ldots,\ i5 \tag{2.20}$$

where c_{j1j2} is the correlation coefficient between uncertainties in locations of nodes j1 and j2, and $L_{\exp}$ is the user-defined correlation length. As discussed in Ref. [66], since the correlation among uncertainties in frame structures is weaker than that in continuum structure, a small value will be assigned to $L_{\exp}$ in numerical examples.

Similarly, by denoting the nominal values of cross-sectional area and Young's modulus as A_i and E_i, respectively, the random perturbations are added in a similar manner as in Eq. (2-17) as

$$A_i' = A_i + \Delta A_i;\ E_i' = E_i + \Delta E_i \tag{2.21}$$

where A_i' and E_i' are the corresponding uncertain cross-sectional area and Young's modulus of ith member after adding random perturbations. It is worth noting that the four beam elements in Fig. 2-1(b) share the same A_i' and E_i'.

2.5 Singularity phenomenon in global stability

As discussed in the research background in Chapter 1, the singularity phenomenon in global stability would result in pseudo local buckling which have negative effects on calculating the linear buckling load factor [36][37]. To illustrate the singularity phenomenon of the stability constraint, the buckling load factor of a simple frame structure is investigated as shown in Fig. 2-2(a), where the node number and the member number are indicated by those with and without parentheses,

respectively. The frame is pin-supported at nodes 1 and 2, and a downward vertical load F with magnitude 2000 N is applied at node 3. Each member is divided into four Euler-Bernoulli beam elements with Young's modulus 3×10^{11} Pa, and their cross-sectional areas are listed in Table 2-1. Note that the crossing members 3 and 4 are not connected at their intersection. As a result, there are 20 beam elements in total in the structure. For comparison purpose, the frame structure after removing the thin members, i.e., members 2, 3 and 5, is also investigated and shown in Fig. 2-2(b). The linear buckling load factor λ^{cr} before removing thin members is 0.7971, whereas the value of λ^{cr} after removing thin members is 238440.64. This enormous difference demonstrates that global geometrical stiffness matrix of the structure is highly dependent on its thin members; therefore, the accurate value of λ^{cr} cannot be obtained without removing the thin members which may have pseudo member buckling and violate the global stability constraint.

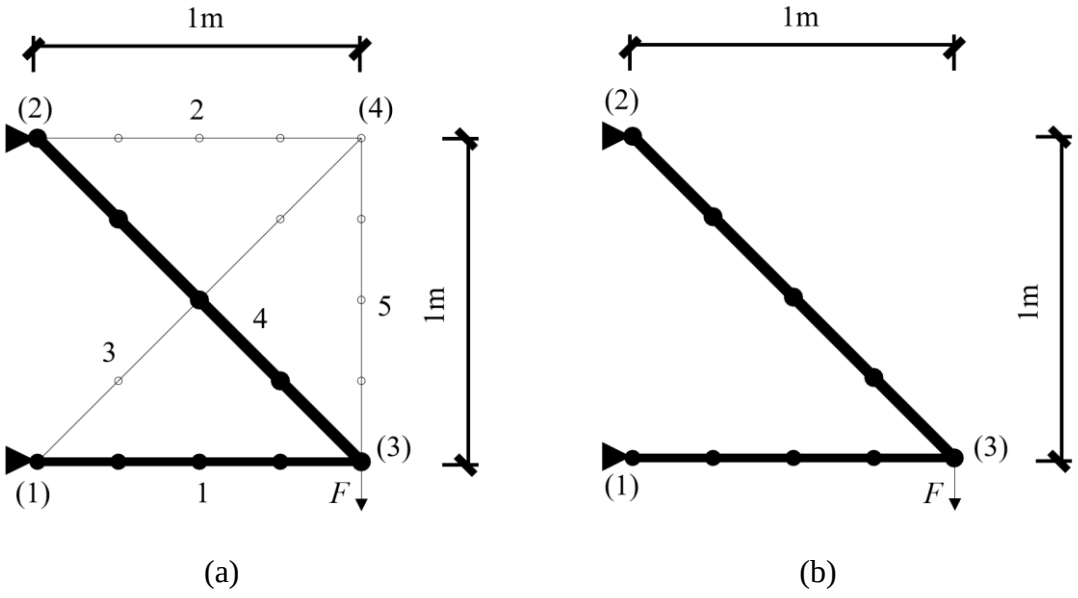

Fig. 2-2 Simple frame structure: (a) before removing thin elements; (b) after removing thin elements

Table 2-1 Cross-sectional areas of structure in Fig. 2-2(a)

Member number	Cross-sectional area (m^2)
1	0.03478
2	1×10^{-7}
3	1×10^{-7}
4	0.04611
5	1×10^{-7}

Chapter 3

Shape and topology optimization

3.1 Brief introduction

Chapter 3 is to present a method for simultaneous shape and topology optimization of plane frames, in which the FDM is used to prevent the generation of extremely short members, and a brief introduction of this chapter is given as follows.

In Section 3.2, the idea of shape optimization using FDM is explained. The shape of frame structure to be optimized is determined by the auxiliary pin-jointed structure to which the FDM is applied, and finite element analysis (FEA) is implemented on the frame structure only. Thus, the loading and boundary conditions of the auxiliary pin-jointed structure are not related to the true conditions for the frame structure to be optimized.

In Section 3.3, the shape and topology optimization problem of plane frame is formulated. Based on FDM, The design variables are the force densities and cross-sectional properties of members in the frame structure, and the details of how FDM indirectly controls the member length to avoid melting node is also given.

In Section 3.4, the sensitivity coefficients with respect to design variables are derived, and in order to obtain a distinct structural shape, an optimization problem is solved after removing the thin elements and merging the closely spaced nodes in the result obtained in Section 3.3, where the design variables are the nodal locations and the cross-sectional properties of members.

In Section 3.5, three numerical examples are investigated to illustrate the effectiveness of proposed method, and each example is solved 100 times with different initial values of design variables to obtain the optimal result. Finally, some conclusions are drawn in Section 3.6.

3.2 Shape optimization using FDM

Firstly, consider a plane frame structure discretized by Euler–Bernoulli beam element [119]. The global coordinates, node numbers, local coordinates and local displacement numbers of the *i*th beam element are shown in Fig. 3-1. Each element has six degrees of freedom (DOF) due to the consideration of bending deformation.

Let α be the angle between the ξ-axis of the beam element and the x-axis of the global

coordinates, where ξ-axis is directed from node 1 to node 2. The local stiffness equation of the ith element can be written as

$$\bar{\boldsymbol{k}}_i \bar{\boldsymbol{u}}_i = \bar{\boldsymbol{f}}_i \tag{3.1}$$

where $\bar{\boldsymbol{k}}_i \in R^{6\times 6}$, $\bar{\boldsymbol{u}}_i \in R^6$ and $\bar{\boldsymbol{f}}_i \in R^6$ are the stiffness matrix, nodal displacement vector and nodal force vector, respectively, with respect to the local coordinates. Note that the components in $\bar{\boldsymbol{f}}_i$ correspond to those in $\bar{\boldsymbol{u}}_i$, in which the displacement numbers are specified in Fig. 3-1. By introducing transformation matrix $\boldsymbol{T}_i \in R^{6\times 6}$ for the ith element, the relation between the local stiffness matrix and the global stiffness matrix of the ith beam element can be obtained as

$$\boldsymbol{k}_i = \boldsymbol{T}_i^T \bar{\boldsymbol{k}}_i \boldsymbol{T}_i \tag{3.2}$$

where $\boldsymbol{k}_i \in R^{6\times 6}$ represents the element stiffness matrix with respect to the global coordinates.

The vectors of nodal displacements and nodal forces with respect to the global coordinates are denoted by $\boldsymbol{u}_i \in R^6$ and $\boldsymbol{f}_i \in R^6$, respectively. Relation between $\boldsymbol{u}_i$ and $\boldsymbol{f}_i$ can be expressed using $\boldsymbol{k}_i$ as

$$\boldsymbol{k}_i \boldsymbol{u}_i = \boldsymbol{f}_i \tag{3.3}$$

Assembling all the elements of $\boldsymbol{k}_i$, we can derive the n_{dof}-by-n_{dof} global stiffness matrix $\boldsymbol{K}$ of the frame structure, where n_{dof} is the number of DOFs of the structure with appropriate boundary conditions. Accordingly, the nodal force vector $\boldsymbol{F} \in R^{n_{\text{dof}}}$ and the nodal displacement vector $\boldsymbol{U} \in R^{n_{\text{dof}}}$ can be constructed by assembling $\boldsymbol{f}_i$ and $\boldsymbol{u}_i$. Therefore, $\boldsymbol{U}$ is obtained by solving the following stiffness equation:

$$\boldsymbol{K}\boldsymbol{U} = \boldsymbol{F} \tag{3.4}$$

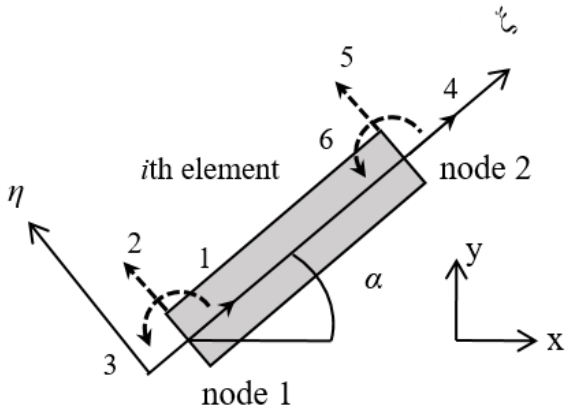

Fig. 3-1 Definition of displacement/force components and global/local coordinates of ith beam element

Then the FDM discussed in Section 2.2 is introduced for shape optimization of the frame structure. Since not only axial force, but also shear force and bending moment exist in the beam element, the FDM is applied to an auxiliary pin-jointed structure to define the nodal locations of the frame that is to be optimized. Therefore, it is important to note that in the following section of problem formulation, the shape of frame structure to be optimized is determined by the auxiliary pin-jointed structure to which the FDM is applied, and the FEA for obtaining the structural response is implemented on the frame structure only. Fig. 3-2 illustrates how FDM is applied to shape optimization of frame structure. The loading and boundary conditions are given to the frame structure only, whereas the corresponding nodes are classified into fixed and free nodes in the auxiliary pin-jointed structure to which the FDM is applied. After determining the locations of nodes in the auxiliary pin-jointed structure using FDM, the shape of frame structure is correspondingly modified and the FEA is implemented to obtain the structure response.

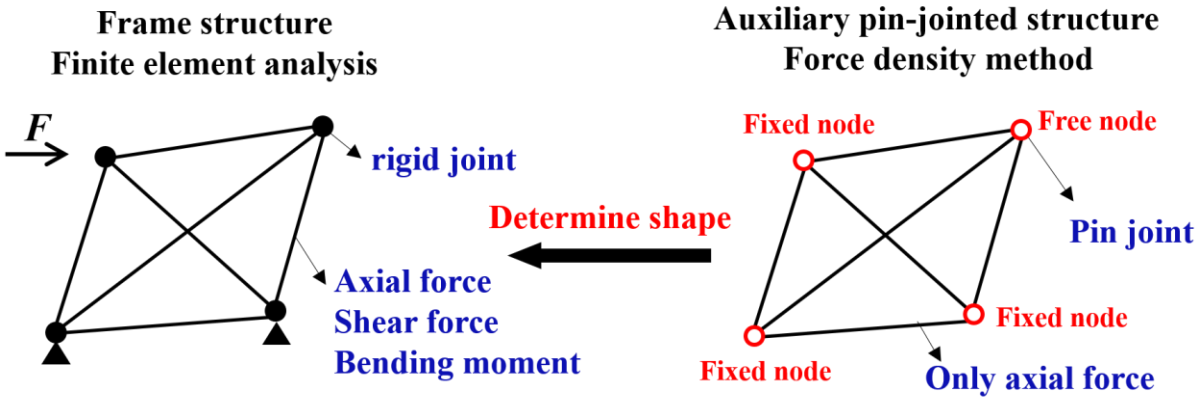

Fig. 3-2 Introduction of FDM to shape optimization of frame structure

It is worth noting that in Refs. [59][60] a two-step algorithm is proposed for the optimization of a shear wall consisting of latticed block, where the lattice members are discretized with plane stress shell elements. In the first step of the algorithm the shape of lattice is optimized with fixed width of lattice members, and FDM is used to define the nodes of lattices to avoid the difficulty of overlapping nodes; in the second step the widths of lattice members are optimized with fixed geometry of lattice. Each step is alternatively repeated until the lattice converges to an optimal configuration, and the thin lattice members will be removed after step 2 every time to modify the topology. However, in such cases the FDM is only applied to a very specific problem, i.e., the shape optimization of lattice, and the general application to simultaneous shape and topology optimization of plane frames are not considered. Besides, the indirect control of member length to avoid singularity in stiffness matrix, which will be presented in the next section, is also not discussed, and the effectiveness of applying FDM to an auxiliary truss or cable-net structure is not fully explored yet.

3.3 Problem formulation

Consider an optimization problem of minimizing the compliance J defined as follows:

$$J = \boldsymbol{U}^T \boldsymbol{K} \boldsymbol{U} \tag{3.5}$$

which is equal to the external work that is converted into the form of Eq. (3.5) using Eq. (3.4). Let $\boldsymbol{D} = \left(D_1, D_2, \ldots D_m\right)$ denote the vector of design variables defining the cross-sectional properties of members, and the upper bound $\overline{V}$ is given for the total structural volume. Then, the conventional optimization problem with respect to the locations of free nodes and the cross-sectional properties as variables is formulated as follows:

$$\begin{aligned} &\text{Minimize} \quad J\left(\boldsymbol{D}, \boldsymbol{x}_{\text{free}}, \boldsymbol{y}_{\text{free}}\right) = \boldsymbol{U}^T \boldsymbol{K}\left(\boldsymbol{D}, \boldsymbol{x}_{\text{free}}, \boldsymbol{y}_{\text{free}}\right)\boldsymbol{U} \\ &\text{subject to} \quad \underline{D}_i \le D_i \le \overline{D}_i, \ i = 1, 2, \ldots, m; \\ &\qquad\qquad \underline{x}_j \le x_j \le \overline{x}_j, \ \underline{y}_j \le y_j \le \overline{y}_j, \ j = 1, 2, \ldots, n_{\text{free}} \\ &\qquad\qquad V\left(\boldsymbol{D}, \boldsymbol{x}_{\text{free}}, \boldsymbol{y}_{\text{free}}\right) \le \overline{V} \end{aligned} \tag{3.6}$$

where n_{free} is the number of free nodes, $\underline{D}_i$ and $\overline{D}_i$ are the lower and upper bounds of D_i, and $\underline{x}_j$, $\overline{x}_j$, $\underline{y}_j$ and $\overline{y}_j$ are the lower and upper bounds of x- and y-coordinates of the jth node. Note that $\boldsymbol{K}$ is a function of $\boldsymbol{D}$, $\boldsymbol{x}_{\text{free}}$ and $\boldsymbol{y}_{\text{free}}$, while $\boldsymbol{U}$ is an implicit function of $\boldsymbol{D}$, $\boldsymbol{x}_{\text{free}}$ and $\boldsymbol{y}_{\text{free}}$ which is obtained by solving Eq. (3.4). It should be noted here that since the stiffness matrix of rigidly-jointed frame structure differs from that of the pin-jointed truss structure, the compliance minimization problem (3.6) is not equivalent to the volume minimization under stress constraints, and cannot be solved by the existing methods for truss structures [120].

One of the difficulties in solving problem (3.6) is the existence of melting or coalescent nodes, which will result in the singularities in $\boldsymbol{K}$ [51]. This can be handled by adding constraints to limit the lower bound of the member length. However, as pointed out by Achtziger [51], directly introducing such constraints to avoid geometries without melting nodes will in return cause intractable definition of feasible region of the nodal location. By contrast, the solution space becomes too small if a tight bound is given for the nodal coordinates, and large bound will lead to unfavorable intersection of members. Hence, we next incorporate FDM for defining the nodal locations of the plane frame structure by solving Eq. (2.4) of the corresponding auxiliary truss or cable-net structure. The side constraints for the locations of free nodes which are assigned in problem (3.6) to prevent divergence in the optimization process, however, are no longer needed when the nodal coordinates can be calculated by Eq. (2.4). Accordingly, the optimization problem (3.6) is restated as

$$\begin{aligned} &\text{Minimize} \quad J\left(\boldsymbol{D}, \boldsymbol{x}_{\text{free}}\left(\boldsymbol{t}\right), \boldsymbol{y}_{\text{free}}\left(\boldsymbol{t}\right)\right) = \boldsymbol{U}^T \boldsymbol{K}\left(\boldsymbol{D}, \boldsymbol{x}_{\text{free}}\left(\boldsymbol{t}\right), \boldsymbol{y}_{\text{free}}\left(\boldsymbol{t}\right)\right)\boldsymbol{U} \\ &\text{subject to} \quad \underline{D}_i \le D_i \le \overline{D}_i, \ \underline{t}_i \le t_i \le \overline{t}_i, \ i = 1, 2, \ldots, m; \\ &\qquad\qquad V\left(\boldsymbol{D}, \boldsymbol{x}_{\text{free}}\left(\boldsymbol{t}\right), \boldsymbol{y}_{\text{free}}\left(\boldsymbol{t}\right)\right) \le \overline{V} \end{aligned} \tag{3.7}$$

where $\underline{t}_i$ and $\overline{t}_i$ are the lower and upper bounds for force density of the ith member. We can observe from Eqs. (3.6) and (3.7) that these two formulations of optimization problem are basically the same, and they will lead to the same solution if a set of $\boldsymbol{t}$ in problem (3.7) can define the optimal solution of problem (3.6). In other words, if the optimal solution of problem (3.6) is included in the feasible domain of problem (3.7), it can be found by solving the optimization problem (3.7). Recall that in Eq. (3.7) the structural compliance is calculated for the rigidly-jointed frame model with Euler-Bernoulli beam elements.

Substituting t_i in Eq. (2.2) into the constraints on t_i in problem (3.7), we obtain

$$\underline{t}_i \le \frac{N_i}{L_i} \le \overline{t}_i \tag{3.8}$$

If we assume the absolute value of $\underline{t}_i$ is equal to $\overline{t}_i$, i.e., $\left|\underline{t}_i\right| = \left|\overline{t}_i\right| = t_{i,\mathrm{abs}} \left(>0\right)$, Eq. (3.8) can be simplified as

$$\left|\frac{N_i}{L_i}\right| \le t_{i,\mathrm{abs}} \tag{3.9}$$

Because the member lengths are positive, we can derive the lower-bound constraint for member length, if N_i is not equal to 0, by transforming Eq. (3.9) to

$$\frac{\left|N_i\right|}{t_{i,\mathrm{abs}}} \le L_i \tag{3.10}$$

Since t_i can have either positive or negative value, the nodal locations obtained from Eq. (2.4) will have drastic variation due to the change of sign of force density. Therefore, we next assume that lower bound of t_i is a small positive value ε, namely, $\underline{t}_i = \varepsilon$, and $\overline{t}_i$ is a sufficiently large real number. Then Eq. (3.8) can be rewritten as

$$\varepsilon \le \frac{N_i}{L_i} \le \overline{t}_i \tag{3.11}$$

which means $t_i = N_i / L_i$ are positive for all members like a cable net during the optimization process. Since $N_i > 0$ for all the members, we can reformulate Eq. (3.11) with respect to L_i as

$$\frac{N_i}{\overline{t}_i} \le L_i \le \frac{N_i}{\varepsilon} \tag{3.12}$$

Hence, the length of ith member is indirectly controlled by the side constraints of its corresponding force density. If $\overline{t}_i$ is appropriately chosen and the shape of the frame is modeled by an auxiliary cable net that can be at self-equilibrium state with positive forces in all the members, then the existence of extremely short member can be avoided by using Eq. (3.12).

Furthermore, for the auxiliary structure of cable net without external load, nodal locations are determined only by the ratios of force densities, and the nodal locations do not change when the force densities are scaled with the same factor. Therefore, to prevent poor convergence of optimization process due to non-uniqueness of the solution, an additional norm constraint with a positive constant *c* is given for the force densities. Hence, the optimization problem is rewritten as

$$\begin{aligned}
&\text{Minimize} \quad J\left(\boldsymbol{D}, \boldsymbol{x}_{\text{free}}(\boldsymbol{t}), \boldsymbol{y}_{\text{free}}(\boldsymbol{t})\right) = \boldsymbol{U}^T \boldsymbol{K}\left(\boldsymbol{D}, \boldsymbol{x}_{\text{free}}(\boldsymbol{t}), \boldsymbol{y}_{\text{free}}(\boldsymbol{t})\right)\boldsymbol{U} \\
&\text{subject to} \quad \underline{D}_i \le D_i \le \overline{D}_i,\ \underline{t}_i \le t_i \le \overline{t}_i,\ i = 1, 2, \ldots, m \\
&\qquad\qquad V\left(\boldsymbol{D}, \boldsymbol{x}_{\text{free}}(\boldsymbol{t}), \boldsymbol{y}_{\text{free}}(\boldsymbol{t})\right) \le \overline{V}; \\
&\qquad\qquad \sum_{i=1}^{m} (t_i)^2 = c
\end{aligned} \tag{3.13}$$

where $\boldsymbol{t} = (t_1, t_2, \ldots, t_m)$ and $\boldsymbol{D} = (D_1, D_2, \ldots, D_m)$ are the *2m* design variables, and the difficulties caused by the melting nodes are avoided by indirectly adding the side constraints on the force densities, which in return controls the upper and lower bounds of member lengths. Note that optimization problems (3.7) and (3.13) are classified as nonlinear programming (NLP) problem, in which all functions are differentiable with respect to ***t*** and ***D***. We will exploit this good nature to carry out the sensitivity analysis in the next section.

3.4 Sensitivity analysis and further improvement

To solve problems (3.7) and (3.13) using a gradient-based algorithm, sensitivity coefficients of objective and constraint functions are analytically derived for reducing computational effort [121][122]. By differentiating the compliance with respect to t_i, we can obtain

$$\frac{\partial J}{\partial t_i} = \sum_{j=1}^{n_{\text{free}}} \left(\frac{\partial J}{\partial x_{\text{free},j}} \frac{\partial x_{\text{free},j}}{\partial t_i} + \frac{\partial J}{\partial y_{\text{free},j}} \frac{\partial y_{\text{free},j}}{\partial t_i} \right),\ i = 1, 2, ..., m \tag{3.14}$$

The differential coefficients $\partial J / \partial x_{\text{free},j}$ and $\partial J / \partial y_{\text{free},j}$ are called shape sensitivity coefficients, and the derivatives of the coordinates of free nodes $\boldsymbol{x}_{\text{free}}$ and $\boldsymbol{y}_{\text{free}}$ with respect to force density vector ***t*** can be computed from the equilibrium equation Eq. (2.4), and details can be found in Ref [55]. By directly differentiating Eq. (3.5) with respect to $x_{\text{free},j}$ and $y_{\text{free},j}$, we can have the following equations

$$\frac{\partial J}{\partial x_{\text{free},j}} = -\boldsymbol{U}^T \frac{\partial \boldsymbol{K}}{\partial x_{\text{free},j}} \boldsymbol{U}, \quad \frac{\partial J}{\partial y_{\text{free},j}} = -\boldsymbol{U}^T \frac{\partial \boldsymbol{K}}{\partial y_{\text{free},j}} \boldsymbol{U},\ j = 1, 2, \ldots, n_{\text{free}} \tag{3.15}$$

The expression of design sensitivity coefficients with respect to D_i is given as

$$\frac{\partial J}{\partial D_i} = -\boldsymbol{U}^T \frac{\partial \boldsymbol{K}}{\partial D_i} \boldsymbol{U}, \quad i = 1, 2, \ldots, m \tag{3.16}$$

Let $\left(x_{1,i}, y_{1,i}\right)$ and $\left(x_{2,i}, y_{2,i}\right)$ denote the coordinates of the two end nodes of *i*th member. Differentiation of the total structural volume with respect to t_i and D_i, respectively, leads to

$$\frac{\partial V}{\partial t_i} = \sum_{j=1}^{m}\sum_{k=1}^{2} A_j \left(\frac{\partial L_j}{\partial x_{k,j}} \frac{\partial x_{k,j}}{\partial t_i} + \frac{\partial L_j}{\partial y_{k,j}} \frac{\partial y_{k,j}}{\partial t_i} \right), \quad \frac{\partial V}{\partial D_i} = L_i \frac{\partial A_i}{\partial D_i}, \; i = 1, 2, \ldots, m \tag{3.17}$$

where A_j is the cross-sectional area of the *j*th member. Because the locations of fixed nodes are invariant to the force densities, the derivatives of member length L_i with respect to $x_{k,i}$ and $y_{k,i}$ $\left(k = 1, 2\right)$ vanish if $x_{k,i}$ and $y_{k,i}$, respectively, are the coordinates of a fixed node. The sensitivity coefficients of objective and constraint functions can be computed by using Eqs. (3.14)−(3.17).

Furthermore, since problems (3.7) and (3.13) may have many local optimal solutions, we carry out optimization many times from randomly generated different initial values of design variables, and select the best local optimal solution as an optimal solution. However, the optimal solution may have closely spaced nodes and/or very thin members, causing ambiguity in structural layout. Therefore, we further optimize the cross-sectional properties and nodal locations by solving the following problem:

$$\begin{aligned} &\text{Minimize} \;\; J\left(\boldsymbol{D}, \boldsymbol{x}_{\text{free}}, \boldsymbol{y}_{\text{free}}\right) = \boldsymbol{U}^T \boldsymbol{K}\left(\boldsymbol{D}, \boldsymbol{x}_{\text{free}}, \boldsymbol{y}_{\text{free}}\right)\boldsymbol{U} \\ &\text{subject to} \;\; \underline{D}_i \le D_i \le \overline{D}_i, \; i = 1, 2, \ldots, \hat{m}; \\ &\qquad\qquad \underline{x}_j \le x_j \le \overline{x}_j, \; \underline{y}_j \le y_j \le \overline{y}_j, \; j = 1, 2, \ldots, \hat{n}_{\text{free}} \\ &\qquad\qquad V\left(\boldsymbol{D}, \boldsymbol{x}_{\text{free}}, \boldsymbol{y}_{\text{free}}\right) \le \overline{V} \end{aligned} \tag{3.18}$$

where $\hat{n}_{\text{free}}$ and $\hat{m}$ are the numbers of free nodes and members, respectively, after merging the closely spaced nodes and removing the thin elements of the optimal solution of problem (3.7) or (3.13), which may have different values from the corresponding *n* and *m* in problem (3.7). The same symbols in Sec. 3.3 are used for variables for brevity, and sensitivity analysis of the objective and constraint functions in problem (3.18) can be carried out in a similar manner as given above.

Note that in Section 3.3 the lower bound of member length is indirectly assigned in order to prevent the existence of a zero-length member; however, the closely spaced nodes may still exist if the ratio of $|N_i|$ to $t_{i,\text{abs}}$ or to $\underline{t}_i$ is small. The lower bound $\underline{D}_i$ for D_i is a sufficiently small positive value, and owing to the fact that optimization problem of minimizing compliance is continuously dependent on the bounds of member sizes [123], optimal topology is further enhanced and obtained by removing some of the members whose member size reaches the lower bound $\underline{D}_i$.

3.5 Numerical examples

In this section, we will present three numerical examples in order to illustrate the effectiveness of proposed method, and for each example the node number and the member number shown in the

initial structure are indicated by those with and without parentheses, respectively. The NLP problem is solved using the sequential quadratic programming (SQP) algorithm in the *fmincon* of Optimization Toolbox of MATLAB 2018a [124]. Each member is assumed to have solid circular cross-section, and thereby the cross-sectional area and second moment of inertia can be expressed by its diameter, i.e., the design variable D_i is the diameter of member i. Without loss of generality, Young's modulus is assumed to be the same for all the members.

Optimal solutions are found for the following Cases N and P with negative and positive lower bounds, respectively, of force density:

Case N: Solve problem (3.7) with $-t_{i,\mathrm{abs}} \le t_i \le t_{i,\mathrm{abs}},\ t_{i,\mathrm{abs}} = 1000\,\mathrm{N/m}$.

Case P: Solve problem (3.13) with $\varepsilon \le t_i \le t_{i,\mathrm{abs}},\ t_{i,\mathrm{abs}} = 1000\,\mathrm{N/m},\ \varepsilon = 0.0001\,\mathrm{N/m}$.

Note that the value of $t_{i,\mathrm{abs}}$ is determined such that the lower bound of member length is around 0.001 m for a member with the axial force about 1 N. For the diameter, the lower bound is 0.001 m, and no upper bound is given. We select the best result out of 100 solutions obtained from 100 different random seeds, and the average computational time, denoted as t_{ave}, of these 100 runs is also presented for each example.

3.5.1 Example 1

The first example is optimization of a two-dimensional cantilever frame. The initial ground structure consists of a 3×2 grid, with 12 nodes and 27 members, as shown in Fig. 3-3. The frame is pin-supported at three left nodes 1, 2, 3, and a downward vertical load F with unit magnitude 1 N is applied at node 11. Note that the magnitude of load is not important, because the compliance is proportional to the load for the same optimal solution. According to Section 2.2, these four nodes, i.e., nodes 1, 2, 3 and 11 are the fixed nodes and the remaining eight nodes are the free nodes.

First consider Case N to solve problem (3.7) with the upper bound volume $\bar{V}$ equal to 1 m^3. The best result among 100 trials is shown in Fig. 3-4(a) that has the compliance J = 81.957 Nm. Note that the width of each member in the following figures is proportional to its diameter, which is scaled appropriately for each figure. The locations of nodes are listed in Table 3-1, and the values of force density vector $\boldsymbol{t}$, member diameter vector $\boldsymbol{D}$ and member length vector $\boldsymbol{L}$ of the best result are listed in Table 3-2.

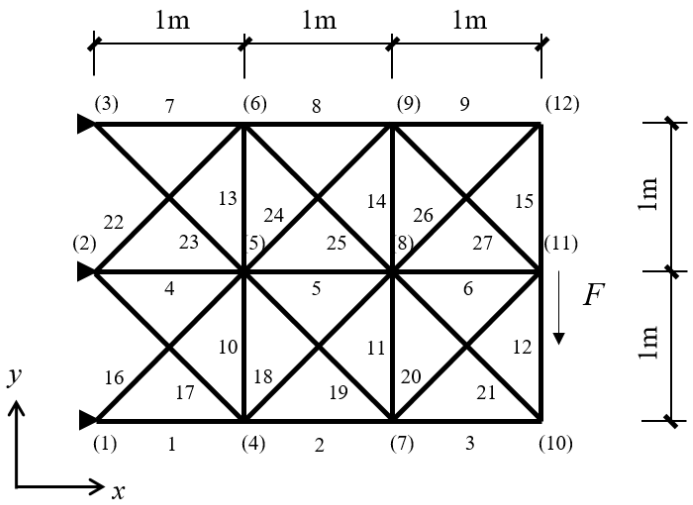

Fig. 3-3 Initial ground structure of Example 1

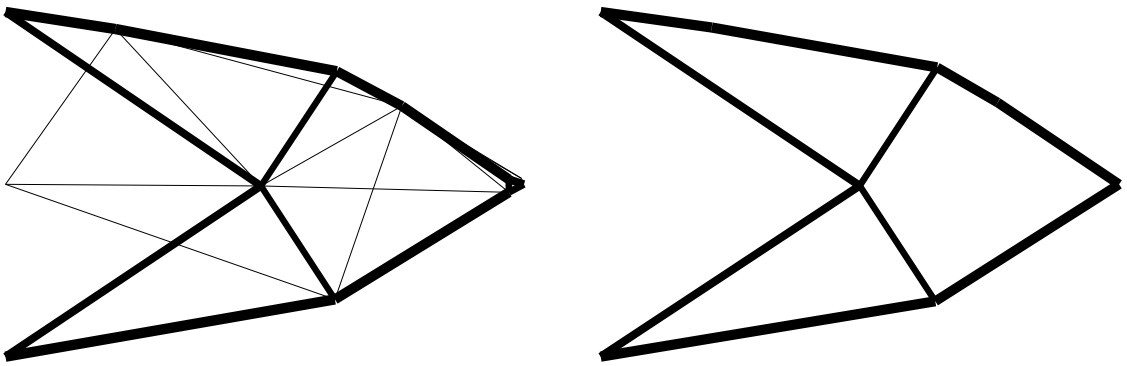

(a) (b)

Fig. 3-4 Optimal shapes of Example 1 for Case N and $\bar{V} = 1\text{m}^3$; (a) best result of problem (3.7), (b) optimal solution after solving problem (3.18)

In order to obtain a distinct structural shape and topology, this best result is further optimized by solving problem (3.18) with volume constraint $\bar{V} = 1\text{m}^3$ and $D_i \in [0.001, +\infty](\text{m})$, $i = 1, 2, \ldots, \hat{m}$. The four nodes 7, 10, 11 and 12 are combined to a single node and members 4, 6, 13, 17, 18, 19, 22, 25 and 27, which reach the lower bound of member diameter, are removed before further optimization. The optimal solution of problem (3.18) is shown in Fig. 3-4(b), with the removal of members whose D_i is equal to $\underline{D}_i$. The compliance, denoted as Final J in Table 3-3, is slightly increased to $J = 83.095$ Nm. As we can see from Fig. 3-4, the procedure of further optimization "filters" the result and presents a more distinct solution.

Table 3-1 Nodal location of best result of Example 1 with $\bar{V} = 1\text{m}^3$

Node	Case N		Case P	
	x (m)	y (m)	x (m)	y (m)
1	0	0	0	0
2	0	1	0	1
3	0	2	0	2
4	1.9065	0.3324	0.3396	0.0567
5	1.4783	0.9906	1.5071	1.0066
6	0.6368	1.9009	0.6521	1.8924
7	2.9136	0.9536	1.9760	0.3278
8	2.2941	1.4542	1.5457	1.0069
9	1.9173	1.6558	1.9596	1.6778
10	2.9127	1.0291	3	0
11	3	1	3	1
12	2.9849	1.0351	3	2

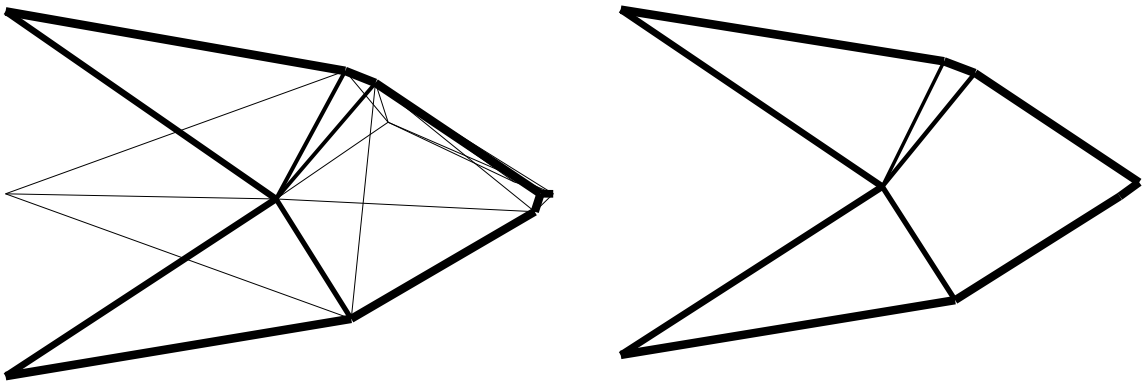

(a) (b)

Fig. 3-5 Optimal shapes of Example 1 for Case N and $\bar{V} = 0.7\text{m}^3$; (a) best result of problem (3.7), (b) optimal solution after solving problem (3.18)

Table 3-2 Force density, diameter and length of best result of Example 1 with $\bar{V} = 1\text{m}^3$

Member	End nodes		Case N			Case P		
			t_i (N/m)	D_i (m)	L_i (m)	t_i (N/m)	D_i (m)	L_i (m)
1	1	4	–0.0953	0.379	1.935	0.632	0.374	0.344
2	4	7	0.114	0.364	1.183	0.131	0.373	1.658
3	7	10	–0.124	0.243	0.075	0.283	0.001	1.075
4	2	5	–0.147	0.001	1.478	0.0001	0.001	1.507
5	5	8	0.297	0.00399	0.938	0.192	0.186	0.038
6	8	11	–0.274	0.001	0.839	0.125	0.001	1.454
7	3	6	–0.380	0.380	0.644	0.456	0.371	0.661
8	6	9	0.509	0.382	1.304	0.227	0.371	1.325
9	9	12	0.325	0.00554	1.235	0.339	0.001	1.089
10	4	5	–0.220	0.232	0.785	0.0001	0.00108	1.505
11	7	8	0.174	0.00163	0.796	0.00284	0.240	0.804
12	10	11	–0.300	0.295	0.092	0.0734	0.001	1
13	5	6	–0.237	0.001	1.240	0.0001	0.00193	1.231
14	8	9	–0.331	0.365	0.427	0.0001	0.238	0.788
15	11	12	–0.336	0.0352	0.038	0.0533	0.001	1
16	1	5	0.0116	0.287	1.780	0.0148	0.295	1.812
17	2	4	0.190	0.001	2.020	0.0001	0.001	1.002
18	4	8	–0.0752	0.001	1.187	0.0001	0.00308	1.535
19	5	7	–0.156	0.001	1.436	0.177	0.0121	0.825
20	7	11	–0.0187	0.255	0.098	0.00878	0.356	1.225
21	8	10	–0.0425	0.367	0.751	0.0005.74	0.001	1.768
22	2	6	0.224	0.001	1.103	0.0001	0.001	1.105
23	3	5	0.132	0.285	1.790	0.00141	0.296	1.805
24	5	9	–0.291	0.234	0.797	0.201	0.00782	0.809
25	6	8	–0.333	0.001	1.716	0.0001	0.00492	1.258
26	8	12	–0.509	0.0109	0.808	0.00253	0.001	1.761
27	9	11	0.280	0.001	1.266	0.0343	0.355	1.241

Furthermore, we change the value of $\bar{V}$ to 0.7, 0.4 and 0.1 (m^3), and find the optimal solutions as shown in Figs. 3-5, 3-6 and 3-7, respectively. The compliance values of optimal solutions of problem (3.18) are listed in Table 3-3 as Final *J*. As seen from these figures, layouts of the optimal solutions corresponding to different values of $\bar{V}$ are similar, although they are not exactly the same. The optimal solution for $\bar{V} = 0.7\text{m}^3$ is asymmetric, which is similar to the case of optimal truss in Ref. [55]. Since the members of a frame are rigidly jointed, the existence of collinear members connected to one node, which may cause singularity in stiffness matrix of pin-jointed structure, is permitted. Thus, once the bounds of force density are carefully determined, the generation of extremely short members can be prevented, keeping regularity of the stiffness matrix of the structure.

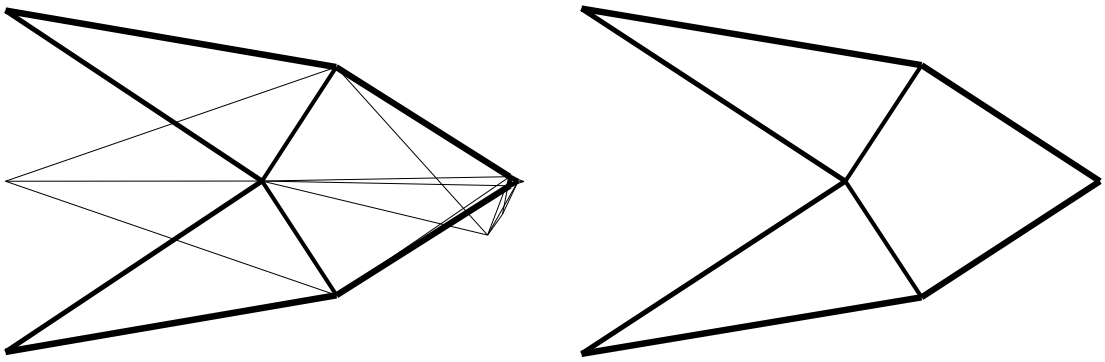

(a) (b)

Fig. 3-6 Optimal shapes of Example 1 for Case N and $\bar{V} = 0.4\text{m}^3$; (a) best result of problem (3.7), (b) optimal solution after solving problem (3.18)

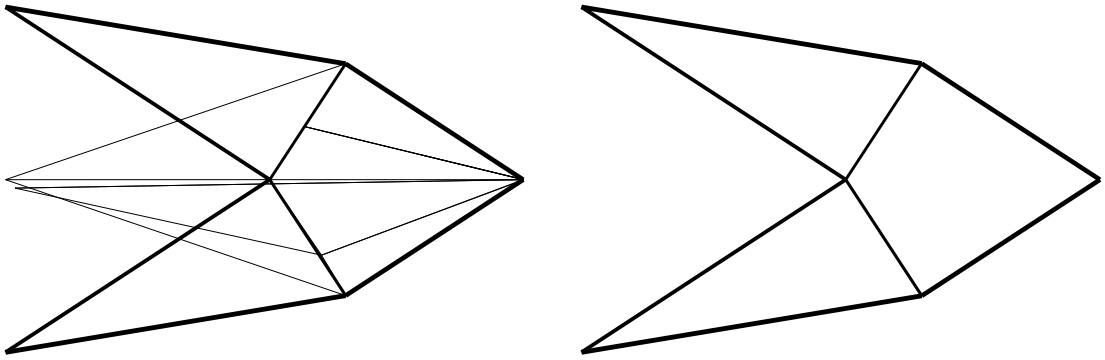

(a) (b)

Fig. 3-7 Optimal shapes of Example 1 for Case N and $\bar{V} = 0.1\text{m}^3$; (a) best result of problem (3.7), (b) optimal solution after solving problem (3.18)

We further investigate the effectiveness of proposed method of Case P with different values of $\bar{V}$. In this case, nodes 10 and 12 together with nodes 1, 2 and 3 in Fig. 3-3 are pin-supported for ensuring each member is in tension at self-equilibrium state to represent an auxiliary cable net, and no load is applied to the cable net for finding the nodal location using the FDM. The loading condition of the frame to be optimized is the same as Case N.

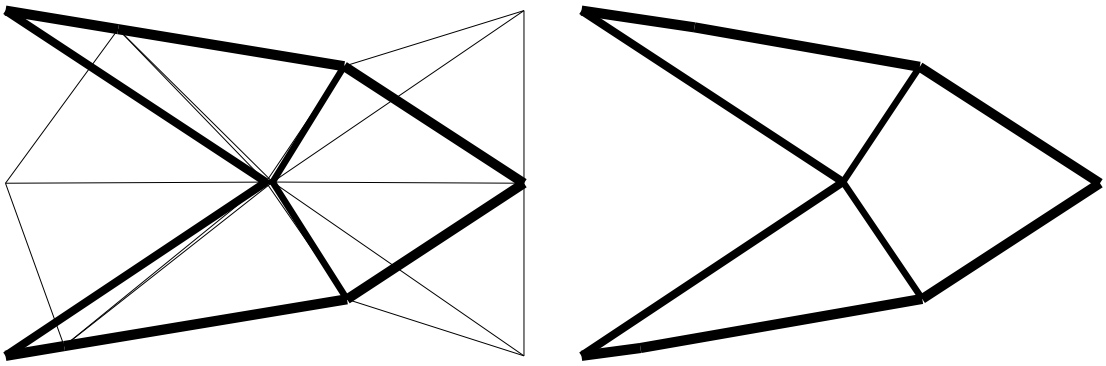

(a) (b)

Fig. 3-8 Optimal shapes of Example 1 for Case P and $\bar{V}=1\text{m}^3$; (a) best result of problem (3.13), (b) optimal solution after solving problem (3.18)

The results of solving problems (3.13) for $\bar{V}=1.0$, 0.7, 0.4 and 0.1 (m^3), are listed in Table 3-3. The optimal solutions of problems (3.13) and (3.18) with $\bar{V}=1\ \text{m}^3$ are shown in Fig. 3-8, and the nodal locations of optimal solution of problems (3.13) are listed in Table 3-1, while the corresponding member diameters, force densities and member lengths are listed in Table 3-2. The values of J after improvement, denoted as Final J, are listed in Table 3-3 to show that the compliance values are close to those with the same values of $\bar{V}$ before improvement, respectively, for $\bar{V}=1.0$, 0.7, 0.4 and 0.1 (m^3). Note that the optimal shapes of Case P with $\bar{V}=0.7$, 0.4 and 0.1 (m^3) are almost the same as Fig. 3-8(a) before further optimization, and similar to those in Figs. 3-5(b), 3-6(b) and 3-7(b) after further optimization. Therefore, those figures are not shown here. It is seen from Fig. 3-8(a) that the optimal shape is defined using some members in the auxiliary cable net with supports in left and right boundaries.

Table 3-3 Statistical result, final values of compliance J (Nm) and CPU time (sec) of 100 results of Example 1 with different $\bar{V}$ (m^3)

$\bar{V}$	1.0		0.7		0.4		0.1	
Case	N	P	N	P	N	P	N	P
Max. J	99.050	87.661	186.185	123.573	247.511	218.988	997.379	876.403
Min. J	81.987	82.930	117.481	118.769	206.680	208.012	833.479	832.460
Average J	86.544	83.814	123.801	119.474	215.292	210.070	847.479	845.779
Std. Dev.	3.941	1.194	9.073	1.305	6.723	3.304	35.955	16.568
Final J	83.095	82.796	118.721	118.650	208.412	207.949	833.855	832.267
t_{ave}	10.95	25.22	7.71	19.36	7.80	12.87	5.83	10.18
Converged solutions	76	86	72	83	68	79	61	72

Table 3-3 also shows the maximum, minimum, average and standard deviation of J of problem (3.13) of 100 runs for each values of $\bar{V}$. It is seen from the table that the difference between the maximum J and the minimum J with Case N is greater than that of Case P, and the standard deviation also has larger value, indicating a wide range of variation in the solutions. This is mainly because if the force density is allowed to change from negative to positive real number or vice versa for Case N, the free nodes move drastically and the possibility of convergence to a local optimal solution increases.

On the other hand, if all the members are allowed in tension only, the movement of free nodes become smooth due to invariant sign in force density and every node for Case P is balanced in tension. It is important to note for Case P that since only positive force density is allowed to exist, the fixed nodes may be different from those for Case N; however, it has little influence on finding the optimal solution of problem (3.13) if the optimal shape can be successfully determined by a set of positive force densities. Some shapes during the optimization procedure are presented and illustrated in Appendix A1 for a better interpretation of the proposed method with Cases N and P. The average computation time t_{ave} of Example 1 among 100 random seeds are listed in Table 3-3, with a computer configuration of Intel Core i5 processor and 4GB RAM. As explained in Appendix A1, Case P has smoother convergence property than Case N; e.g., for $\bar{V} = 1\text{m}^3$; therefore, nearly optimal solution can be easily obtained in Case P. However, the number of major iterations of SQP algorithm is 644 for Case P and 517 for Case N, and the Case P needs more computation time than Case N. This is mainly because the norm constraint for force density in problem (3.13) is to be satisfied and the feasible region in Case P is smaller than Case N. Although the optimization procedure of Case P is less oscillatory, the step length can often be taken as a small value for satisfying the side constraints for t_{i}, requiring more iterations.

3.5.2 Example 2

In the second example, we investigate the optimal shape and topology of a 2-dimensional bridge frame with a 6×1 grid, where the 14 nodes are connected by 31 members, and the initial ground structure is shown in Fig. 3-9. The structure is pin-supported at node 1 and roller-supported at node 13. At each of the nodes 3, 5, 7, 9 and 11, a downward vertical load F with unit magnitude 1 N is applied. Accordingly, these seven nodes are regarded as fixed nodes during the optimization procedure.

Again, $\bar{V} = 1\text{m}^3$ is first assigned for this example. Because the summation of entries of each row in force density matrix is zero and y-coordinates of all fixed nodes are zero, one of the trivial solutions for $\boldsymbol{y}_{\text{free}}$ is the zero-vector. Therefore, we assign upward reaction force 2.5 N at the supports 1 and 13 and include the y-directional equilibrium equations at the supports to be solved for $\boldsymbol{y}_{\text{free}}$. The best result of problem (3.7) of Case N is presented in Fig. 3-10(a), with the compliance J = 1221.03 Nm. The nodal locations are listed in Table 3-4, and the corresponding values of $\boldsymbol{t}$, $\boldsymbol{D}$ and $\boldsymbol{L}$ for all members are listed in Table 3-5. As seen from Fig. 3-10(a) and Table 3-5, the free nodes are separately located such that no extremely short member exists.

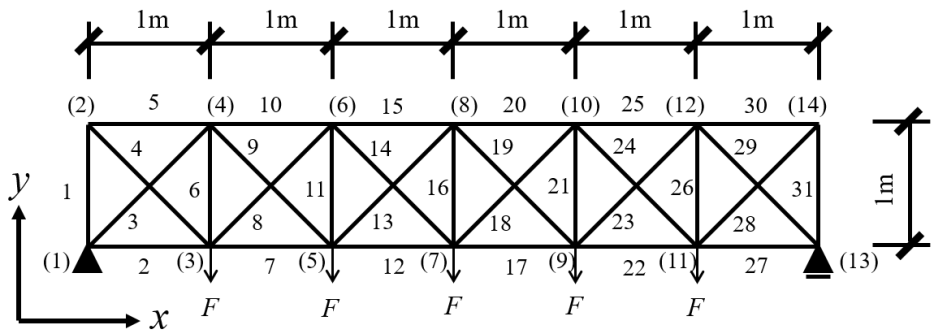

Fig. 3-9 Initial ground structure of Example 2

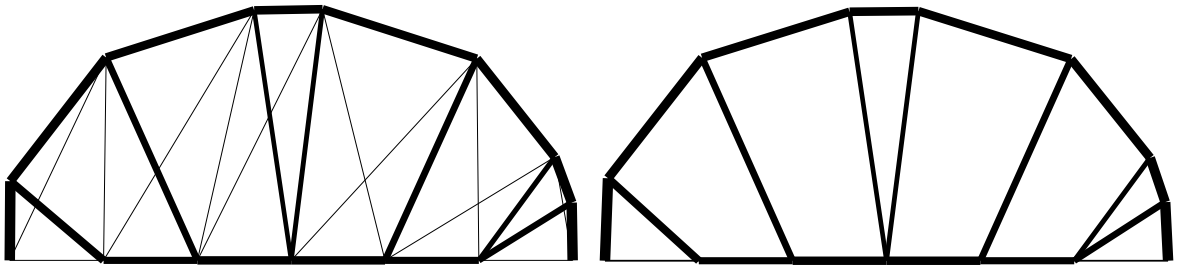

(a) (b)

Fig. 3-10 Optimal shapes of Example 2 for Case N and $\bar{V} = 1\text{m}^3$; (a) best result of problem (3.7), (b) optimal solution after solving problem (3.18)

The improved optimal solution is obtained by solving problem (3.18) with $\bar{V} = 1\text{m}^3$ as shown in Fig. 3-10(b). After removal of thin members with $\underline{D}_i = 0.001\text{m}$, the compliance J is reduced to 1219.22 Nm. It should be noted that members 2 and 27 connecting nodes (1, 3) and nodes (11, 13), respectively, do not vanish in Fig. 3-10(b), making the structure globally stable. This property is different from the optimal shape of pin-jointed truss [51][55], where members 2 and 27 do not exist. This is because only axial force equilibrium condition has to be satisfied for truss structure; however, for rigidly-jointed frame structure, axial force, shear force and bending moment simultaneously exist in the member, leading to the slight inclination of members 1 and 31 as shown in Fig. 3-11. Therefore, the forces in members 2 and 27 are not zero, and these members are necessary to exist for satisfying the equilibrium conditions at the supports.

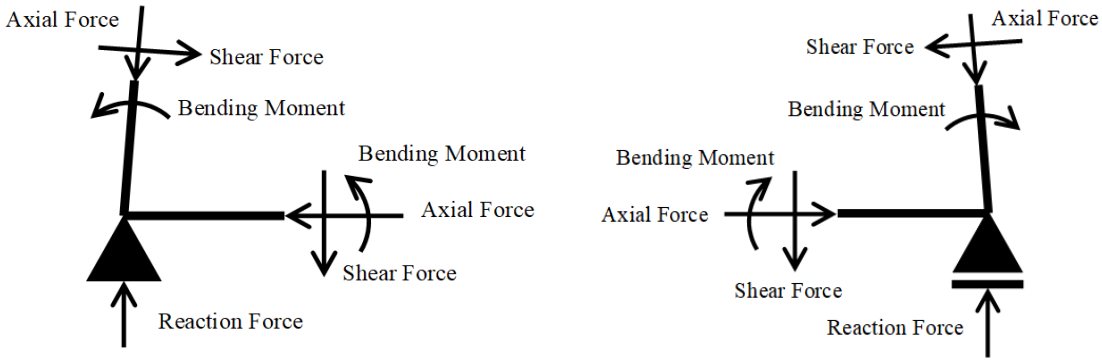

(a) (b)

Fig. 3-11 Illustration of equilibrium condition; (a) pin-supported node 1 and (b) roller-supported node 31

Table 3-4 Nodal location of best result of Example 2 with $\bar{V} = 1\text{m}^3$

Node	Case N		Case P	
	x (m)	y (m)	x (m)	y (m)
1	0	0	0	0
2	0.0062	0.7462	0.0064	0.7583
3	1	0	1	0
4	1.0273	2.0677	0.7234	1.7475
5	2	0	2	0
6	2.6053	2.5714	1.3496	2.1902
7	3	0	3	0
8	3.3339	2.5842	3.0004	2.6822
9	4	0	4	0
10	4.978	2.0556	4.6505	2.1903
11	5	0	5	0
12	5.8098	1.0044	5.2764	1.7477
13	6	0	6	0
14	5.9893	0.5174	5.9936	0.7583
15	--	--	0	3
16	--	--	1	3
17	--	--	2	3
18	--	--	3	3
19	--	--	4	3
20	--	--	5	3
21	--	--	6	3

Table 3-5 Force density, diameter and length of best result of Example 2 with $\bar{V} = 1\text{m}^3$

Member	End nodes		Case N			Case P		
			t_i (N/m)	D_i (m)	L_i (m)	t_i (N/m)	D_i (m)	L_i (m)
1	1	2	–2.08	0.304	0.846	0.381	0.302	0.858
2	1	3	0.365	0.00431	1.000	0.122	0.00300	1.000
3	1	4	–0.343	0.00402	2.399	0.227	0.001	1.984
4	2	3	–0.398	0.238	1.305	0.00128	0.2341	1.312
5	2	4	–0.144	0.266	1.670	0.000790	0.264	1.221
6	3	4	1.21	0.001	2.168	0.161	0.001	1.868
7	3	5	0.706	0.207	1.000	0.102	0.203	1.000
8	3	6	–0.479	0.001	3.117	0.135	0.001	2.316
9	4	5	0.0495	0.198	2.376	0.0227	0.145	2.245
10	4	6	–0.177	0.248	1.656	0.164	0.255	0.767
11	5	6	–0.276	0.001	2.739	0.000687	0.145	2.380
12	5	7	0.111	0.244	1.000	0.203	0.244	1.000
13	5	8	0.607	0.001	2.997	0.0164	0.001	2.956
14	6	7	–0.553	0.134	2.700	0.0135	0.001	2.823
15	6	8	0.142	0.248	0.729	0.0231	0.247	1.722
16	7	8	1.23	0.141	2.705	0.0318	0.187	2.782
17	7	9	0.234	0.244	1.000	0.00720	0.244	1.000
18	7	10	–0.379	0.001	2.926	0.000117	0.001	2.823
19	8	9	0.616	0.00424	2.766	0.00911	0.001	2.956
20	8	10	0.224	0.247	1.727	0.0001.95	0.247	1.721
21	9	10	–0.477	0.196	2.367	0.00513	0.145	2.381
22	9	11	0.495	0.206	1.000	0.0991	0.203	1.000
23	9	12	0.340	0.0116	2.120	0.0759	0.145	2.245
24	10	11	0.494	0.001	2.156	0.165	0.001	2.317
25	10	12	–0.181	0.261	1.340	0.219	0.255	0.767
26	11	12	–0.224	0.152	1.369	0.0347	0.001	1.868
27	11	13	0.396	0.00409	1.000	0.0940	0.003	1.000
28	11	14	0.295	0.183	1.166	0.00310	0.234	1.313
29	12	13	–2.06	0.001	1.121	0.234	0.001	1.984
30	12	14	–0.0650	0.283	0.519	0.000239	0.264	1.222
31	13	14	–0.363	0.303	0.618	0.433	0.302	0.858
32	2	15	--	--	--	0.144	0.001	2.241
33	2	16	--	--	--	0.00156	0.001	2.452
34	15	4	--	--	--	0.270	0.001	1.446
35	15	16	--	--	--	0.0706	0.001	1.000
36	4	16	--	--	--	0.171	0.001	1.282
37	4	17	--	--	--	0.107	0.001	1.788
38	16	6	--	--	--	0.284	0.001	0.882
39	16	17	--	--	--	0.139	0.001	1.000
40	6	17	--	--	--	0.163	0.001	1.038
41	6	18	--	--	--	0.0498	0.001	1.838

42	17	8	--	--	--	0.197	0.001	1.049
43	17	18	--	--	--	0.0803	0.001	1.000
44	8	18	--	--	--	0.0997	0.001	0.318
45	8	19	--	--	--	0.242	0.001	1.049
46	18	10	--	--	--	0.142	0.001	1.838
47	18	19	--	--	--	0.217	0.001	1.000
48	10	19	--	--	--	0.116	0.001	1.038
49	10	20	--	--	--	0.342	0.001	0.882
50	19	12	--	--	--	0.0582	0.001	1.788
51	19	20	--	--	--	0.222	0.001	1.000
52	12	20	--	--	--	0.123	0.001	1.282
53	12	21	--	--	--	0.251	0.001	1.446
54	20	14	--	--	--	0.000616	0.001	2.452
55	20	21	--	--	--	0.0738	0.001	1.000
56	14	21	--	--	--	0.166	0.001	2.242

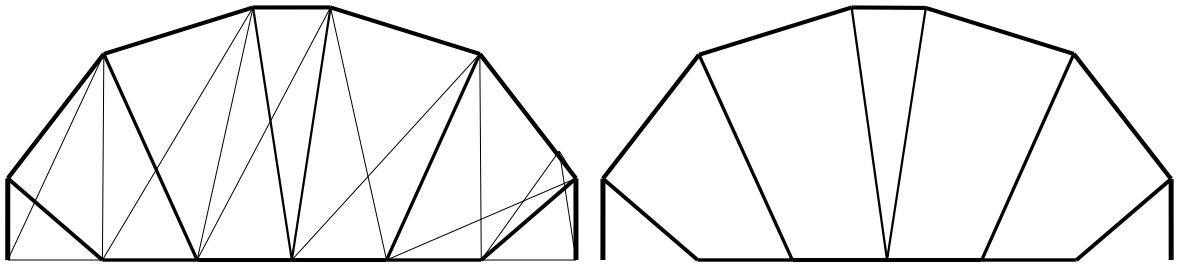

(a) (b)

Fig. 3-12 Optimal shapes of Example 2 for Case N and $\bar{V} = 0.1\mathrm{m}^3$; (a) best result of problem (3.7), (b) optimal solution after solving problem (3.18)

The same optimization procedure is carried out with $\bar{V} = 0.1\mathrm{m}^3$, and compliance of the improved optimal solution is listed in Table 3-6 as Final *J*. It can also be found from Fig. 3-12 that no melting nodes exist for this case. Although the frame in Fig. 3-12 has only six upper nodes, members 25 and 30 connecting nodes (10, 12) and (12, 14), respectively, are colinear, and node 12 exists on the member connecting nodes (10, 14). Furthermore, with the decrease of upper bound volume, the diameters of members 2 and 27 are close to $\underline{D}_i$ and these members are removed after further optimization. However, the stiffness matrix of the optimal solution after solving problem (3.18) is determinate owing to small bending stiffness in members 1 and 31.

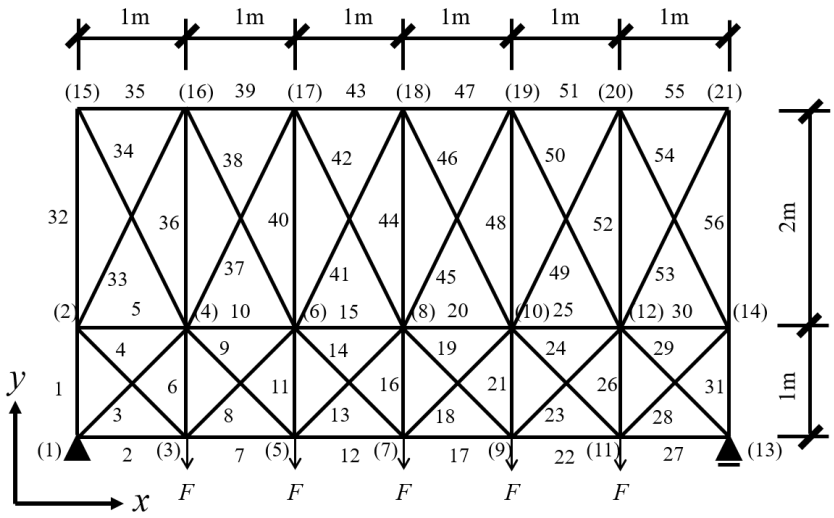

Fig. 3-13 Modified initial ground structure for Case P of Example 2

Optimization problems (3.13) and (3.18) for Example 2 are solved also with Case P. Seven additional nodes 15–21 exist at the top of the initial structure as shown in Fig. 3-13. By fixing the locations of nodes 1, 3, 5, 7, 9, 11, 13, 15–21, we have an auxiliary cable net to define the nodal locations of free nodes. In order to allow the free nodes to move in a wide range, y-coordinates of the seven additional nodes have a large value 3 m. In this way, a kind of cable net is generated for solving Eq. (2.4) to obtain x_{free} and y_{free}.

The compliance values of improved optimal solutions are listed in Table 3-6 as Final J, and Figs. 3-14 and 3-15 show the optimal solutions for $\bar{V} = 1$ and 0.1 (m^3), respectively. Although the final structural layouts of these four solutions are symmetric with respect to the middle vertical axis, symmetry constraints are not enforced explicitly. Through observation from Table 3-6, one can realize that the values of J of improved optimal solutions with the same $\bar{V}$ are very close in both cases. It is worth noting that the initial ground structures for Cases N and P are different; however, the purpose of adding nodes and members for Case P is merely to obtain a self-equilibrium state of free nodes with tension state, and none of the additional nodes are allowed to move. Therefore, the optimal shapes of both cases are still controlled by the same free nodes, i.e., nodes 2, 4, 6, 8 and 10, and similar optimal solutions can be found by the proposed method if the coordinates of free nodes of optimal shape can be determined in their feasible domain of the force density vector.

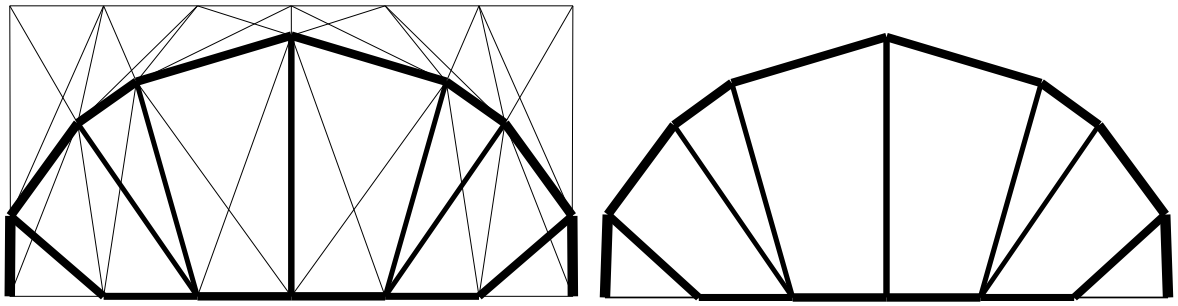

(a) (b)

Fig. 3-14 Optimal shapes of Example 2 for Case P and $\bar{V} = 1\text{m}^3$; (a) best result of problem (3.13), (b) optimal solution after solving problem (3.18)

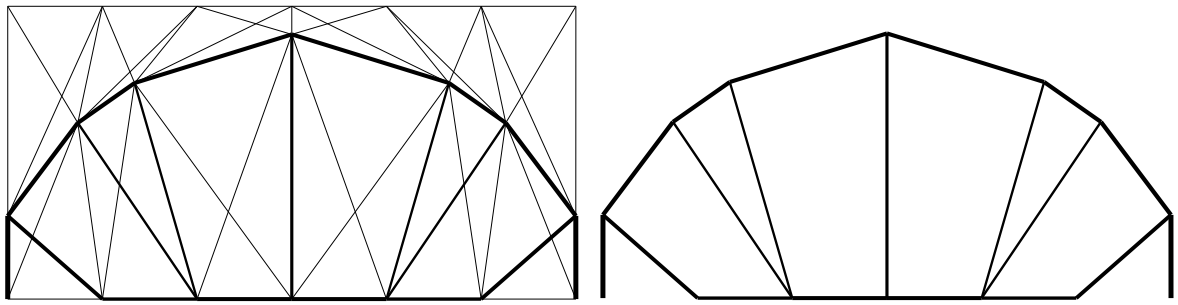

(a) (b)

Fig. 3-15 Optimal shapes of Example 2 for Case P and $\bar{V} = 0.1\text{m}^3$; (a) best result of problem (3.13), (b) optimal solution after solving problem (3.18)

Table 3-6 Statistical result, final values of compliance J (Nm) and CPU time (sec) of 100 results of Example 2 with different $\bar{V}$ (m^3)

$\bar{V}$ (m^3)	1.0		0.1	
Case	N	P	N	P
Max J	7898.12	1276.47	47039.81	13405.61
Min J	1221.03	1217.43	12255.81	12232.50
Average J	2252.89	1232.22	15520.27	12448.70
Std. Dev.	1912.16	21.2445	6842.66	310.84
Final J	1219.22	1217.07	12255.04	12230.92
t_{ave}	22.65	25.99	12.47	16.01
Converged solutions	85	97	82	93

Table 3-6 also lists the statistical result of 100 runs, computation time t_{ave} with the same computer configuration as Example 1 and number of converged solutions within 100 different trials. It can be observed that the value of maximum J among 100 runs can be 5 or 6 times the value of minimum J for Case N, indicating the tendency of being trapped in a local optimal solution or even diverged to some extent. Its standard deviation is also greater than that of Case P. However, the values of average J for both cases are within an acceptable range, which are about 20% larger than the minimum J.

3.5.3 Example 3

The third example is an optimization of a grid-like shear wall subjected to a horizontal force of 1 N at node 5 as shown in Fig. 3-16. The structure is pin-supported at nodes 1 and 31. Because the border of shear wall is usually required to keep rectangle after optimization, nodes on the border frame, i.e., 2, 3, 4, 5, 6, 10, 11, 15, 16, 20, 21, 25, 26, 30, 32, 33, 34 and 35, as well as nodes 1 and 31, are classified as fixed nodes, and the remaining 15 nodes are the free nodes. Members of border and inner lattice are depicted by thick and thin black lines in Fig. 3-16, respectively. The cross-section diameters of border frame members are fixed at 0.1 m and remain unchanged during the optimization procedure. Design variables are the cross-section diameters and force densities of all the inner lattice members. In this example, only Case P is considered, Fig. 3-17 shows the optimization results by solving problems (3.13) and (3.18) with $\bar{V} = 1\text{m}^3$. It should be noted that in this example there is no intention to optimize a practical shear structure which could be subjected to the horizontal load from both directions, but rather a structure similar to shear wall, and therefore symmetry condition is not applied in this example.

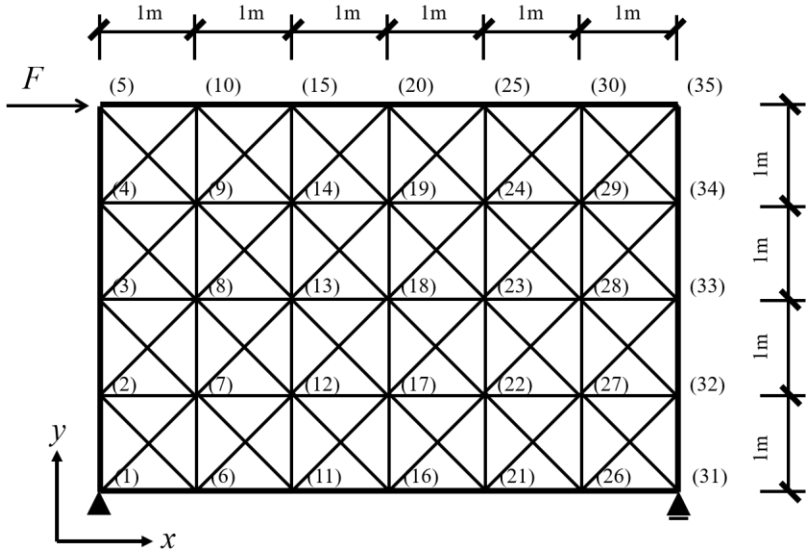

Fig. 3-16 Initial ground structure of Example 3

It can be observed from Fig. 3-17(a) that no extremely short member exists, although some of the nodes are closely spaced and connected mainly due to the low axial force in the self-equilibrium state, and the diameters of many members reach $\underline{D}_i$. Then, the final optimal solution is obtained as shown in Fig. 3-17(b) by further solving problem (3.18), where the compliance value is 103.0494 Nm. Next, problems (3.13) and (3.18) are solved with the change of upper-bound volume $\bar{V}$ to 0.7, 0.4 and 0.1 (m^3). The optimal solutions are shown in Figs. 3-18 to 3-20, respectively, and the corresponding compliances after further optimization are listed in Table 3-7 as final *J*. For $\bar{V} = 1$ and 0.7 (m^3), the optimal solutions are similar; however, the shape and topology of optimal solution becomes different when $\bar{V}$ decrease to 0.4 and 0.1 (m^3). This is mainly because long members cannot exist if the diameter becomes small as $\bar{V}$ is decreased.

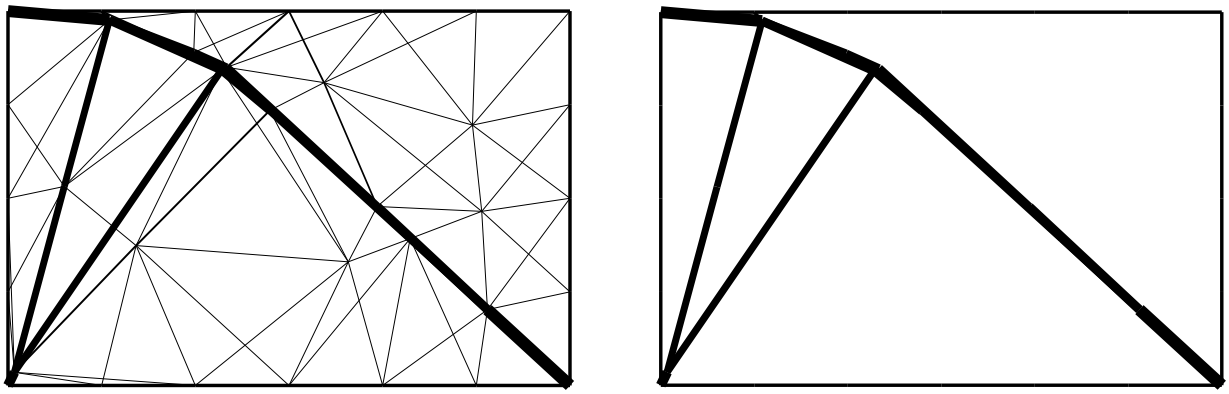

(a) (b)

Fig. 3-17 Optimal shapes of Example 3 for Case P and $\bar{V} = 1\text{m}^3$; (a) best result of problem (3.13), (b) optimal solution after solving problem (3.18)

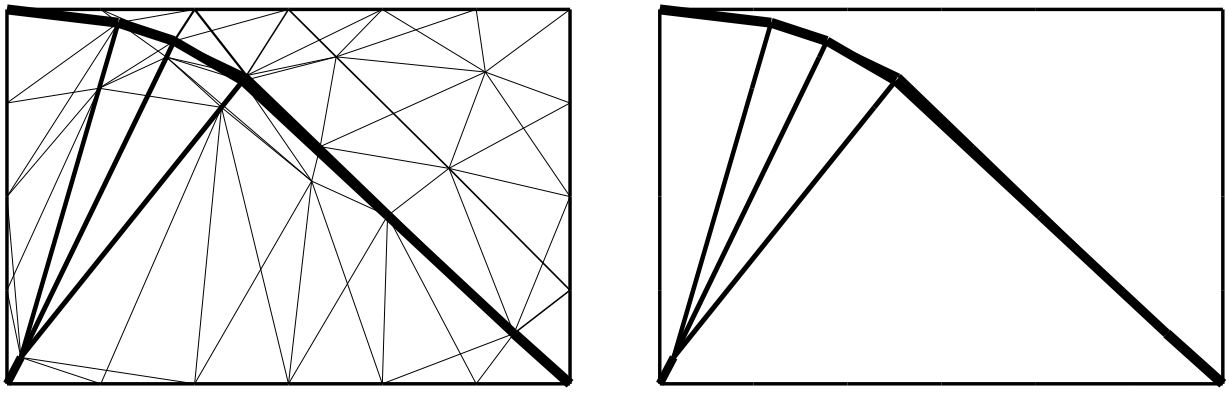

(a) (b)

Fig. 3-18 Optimal shapes of Example 3 for Case P and $\bar{V} = 0.7\text{m}^3$; (a) best result of problem (3.13), (b) optimal solution after solving problem (3.18)

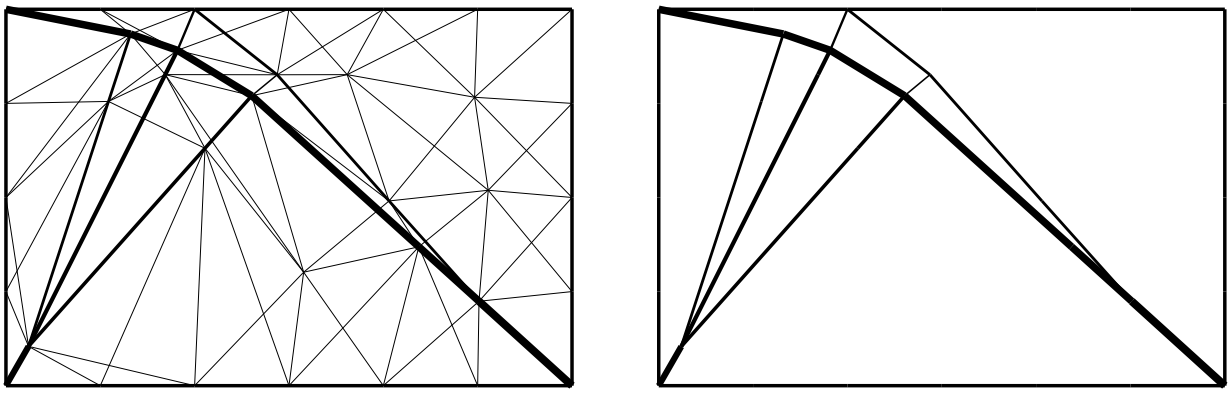

(a) (b)

Fig. 3-19 Optimal shapes of Example 3 for Case P and $\bar{V} = 0.4\text{m}^3$; (a) best result of problem (3.13), (b) optimal solution after solving problem (3.18)

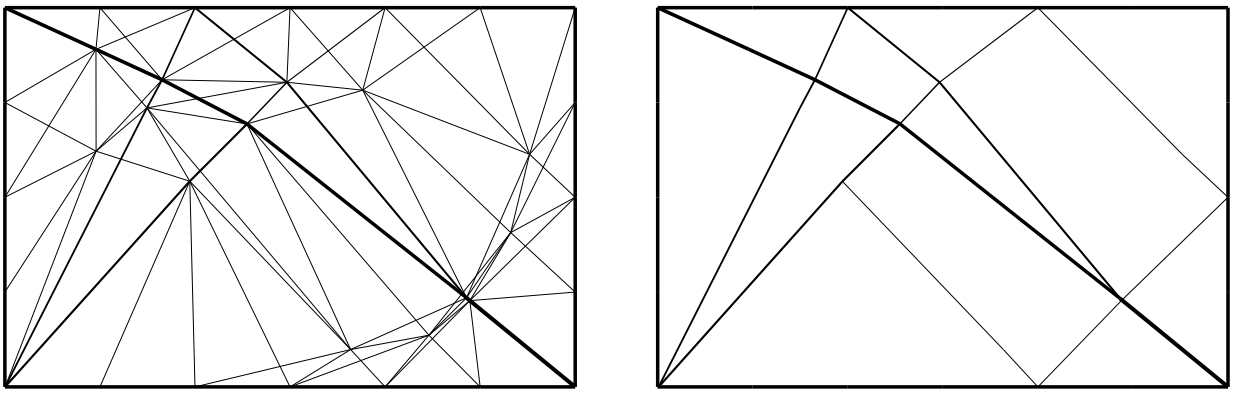

(a) (b)

Fig. 3-20 Optimal shapes of Example 3 for Case P and $\bar{V} = 0.1\text{m}^3$; (a) best result of problem (3.13), (b) optimal solution after solving problem (3.18)

Table 3-7 Statistical result, initial and final values of compliance J (Nm) and CPU time (sec) of 100 results of Example 3 with different $\bar{V}$ (m^3)

$\bar{V}$	1.0	0.7	0.4	0.1
Max J	107.595	146.811	245.683	889.966
Min J	103.829	144.110	242.160	840.453
Average J	105.315	145.700	244.180	851.771
Std. Dev.	0.9778	0.4579	0.6406	10.814
Final J	103.050	143.794	242.142	840.231
Initial J	388.792	465.937	626.432	1517.843
t_{ave}	27.45	27.44	22.30	21.47

The maximum, minimum, average and standard deviation of J among 100 random seeds, as well as t_{ave}, are shown in Table 3-7. Compliance of initial ground structure where the inner lattice members are evenly distributed is also calculated and listed in Table 3-7 as Initial J for comparison purpose. It can be seen from Table 3-7 that the compliance is significantly decreased through optimization by the proposed method.

3.6 Conclusions

In this chapter a new method has been presented for shape and topology optimization of plane frame structures using force density to define the nodal locations of free nodes. An auxiliary truss or cable net with different boundary and loading conditions is introduced to which the FDM is applied. In order to prevent generation of melting nodes in the structure, the side constraint on member length is indirectly assigned by limiting the force density value of each member. Two cases of lower bound of force density are given; namely, Case N for negative lower bound and Case P for small positive lower bound, which correspond to truss and cable net, respectively, for the definition of auxiliary structure. Sensitivity coefficients of the objective and constraint functions with respect to the force density and the member diameter are also derived to accelerate the optimization procedure. After obtaining the optimization results, the shape and topology of the structure are further improved in order to achieve a distinct final solution without extremely thin member or closely space nodes. Three numerical examples are presented to illustrate the effectiveness of proposed method, and the conclusions are drawn as follows:

(1) Good approximate optimal solutions of shape and topology of frames can be successfully found for both Case N and Case P. However, comparison of results obtained from 100 different trials shows that Case P is more stable, i.e., has smaller standard deviation, than Case N.

(2) Lower bounds for member lengths can be indirectly assigned by the upper- and lower-bound constraints on the force densities. An approximate optimal solution can be obtained smoothly by assigning a positive lower bound for force density, although convergence to a strict optimal solution is slow.

(3) In the example of bridge frame (Example 2), a thin horizontal member is needed at the roller support to be at equilibrium with the shear force of the thick vertical member, although such member is not needed for a truss or a frame with thin vertical member corresponding to a small upper bound of structural volume.

(4) If the vertical coordinates of fixed nodes have the same value, then the coordinates of free nodes cannot be determined using FDM. In this case, an equilibrium condition with the reaction force at a support is included to successfully obtain the nodal coordinates of free nodes.

Chapter 4

Robust optimization

4.1 Brief introduction

Chapter 4 is to present a worst case approach to RSO of plane frames, in which the structural robustness is represented by using order statistics and the corresponding order, and a brief introduction of this chapter is given as follows.

In Section 4.2, details of defining the structural robustness using order statistics are given. The accurate evaluation of the exact worst structural response is relaxed to 100βth percentile response, which is further approximated by the kth order statistic using the theory of distribution-free one-side tolerance interval. Therefore, the structural robustness is represented by the order k and the corresponding order statistic.

In Section 4.3, two kinds of WCO problem formulations are presented. The first is to minimize the structural stress with volume and global stability constraints, where the penalization method is used to alleviate the singularity phenomenon; the second is a multi-objective optimization problem with volume constraint, where several stress values with different robustness levels are considered as objectives to be minimized.

In Section 4.4, the penalization method is implemented to avoid singularity phenomenon. The element stress and geometrical stiffness matrix are penalized with respect to the cross-sectional areas for the thin elements, and a simple example is investigated for verification of the proposed penalization method.

In Section 4.5, four numerical examples are explored to demonstrate effectiveness of the two methods proposed in Section 4.3, and the solution of deterministic optimization is also given in each example for comparison purpose. Finally, some conclusions are drawn in Section 4.6.

4.2 Robustness definition using order statistics

Consider an RSO problem corresponding to the design variables $\boldsymbol{d}$ and the uncertain parameters $\boldsymbol{\theta}$. Based on the definition of order statistics and the corresponding statistical inference theory in

Section 2.3, the probability α_k of 100β% of the stochastic structural response $g(\boldsymbol{d};\boldsymbol{\theta})$ less than the kth order statistic $Z_{k:m_s}$ can be calculated as

$$\alpha_k = \Pr\left\{F\left(Z_{k:m_s}\right) \geq \beta\right\} = \Pr\left\{U_{k:m_s} \geq \beta\right\} = \sum_{r=0}^{m_s-k} \binom{m_s}{r} \beta^r \left(1-\beta\right)^{m_s-r} = 1 - I_\beta\left(m_s - k + 1, k\right) \quad (4.1)$$

where $U_{k:m_s}$ is the kth order statistic from m_s i.i.d. standard uniform random variables as defined in Section 2.3, and $I_\beta\left(m_s - k + 1, k\right)$ is the incomplete beta function [77][117]. Because the probability of the structural response falling into the one-side interval $\left(-\infty, Z_{k:m_s}\right)$ is independent of the distribution $F(z)$, Eq. (4.1) is also called distribution-free one-side tolerance interval, and $Z_{k:m_s}$ can be seen as the 100βth percentile structural response in probabilistic sense with the confidence level α_k.

In order to enable $Z_{k:m_s}$ to be accurate as a percentile estimator of the structural response, the value of confidence level α_k in Eq. (4.1) should be close to 1; e.g., 0.9 or 0.95 [117]. Furthermore, according to Prescott *et al*. [117] , α_k will monotonically increase to 1 as the sample size m_s is increased. Therefore, if the values of k, α_k and β are specified, one can obtain the threshold (minimum) value of sample size m_s such that α_k is not less than its preassigned value; on the other hand, if sample size m_s is specified as the threshold value satisfying Eq. (4.1) and the value of k is also given, the relation between α_k and β can also be derived by solving Eq. (4.1). As demonstrated by Ohsaki *et al*. [77], the relation between α_k and β can be obtained for some fixed values of m_s and various specified values of $k\,(=1,2,\ldots,20)$, which is shown in Fig. 4-1. Note that the curves in top-right and bottom-left of each figure in Fig. 4-1 correspond to k=1 and 20, respectively. The relations between k and β with $\alpha_k = 0.9$ are also given in Tables 4-1 and 4-2 for m_s = 100 and 200, respectively. It can be seen from these tables that β is a decreasing function of k, in other words, the portion of the structural response less than $Z_{k:m_s}$ will decrease as the value of k increases with the same α_k. Therefore, for given α_k and m_s, a higher order k corresponds to a less structural response under uncertainty exceeding 100βth percentile response, and the order k and its corresponding order statistic $Z_{k:m_s}$ approximating the percentile response can be regarded as representing the robustness level of the structure.

Table 4-1 Relation between k and β (α_k = 0.9, m_s = 100)

k	1	2	3	4	5	6	7	8	9	10
β	0.977	0.962	0.948	0.934	0.922	0.909	0.897	0.885	0.873	0.862
k	11	12	13	14	15	16	17	18	19	20
β	0.850	0.839	0.827	0.816	0.805	0.794	0.783	0.772	0.761	0.750

Table 4-2 Relation between k and β (α_k = 0.9, m_s = 200)

k	1	2	3	4	5	6	7	8	9	10
β	0.989	0.981	0.974	0.967	0.960	0.954	0.948	0.942	0.936	0.930
k	11	12	13	14	15	16	17	18	19	20
β	0.924	0.918	0.912	0.907	0.901	0.895	0.890	0.884	0.878	0.873

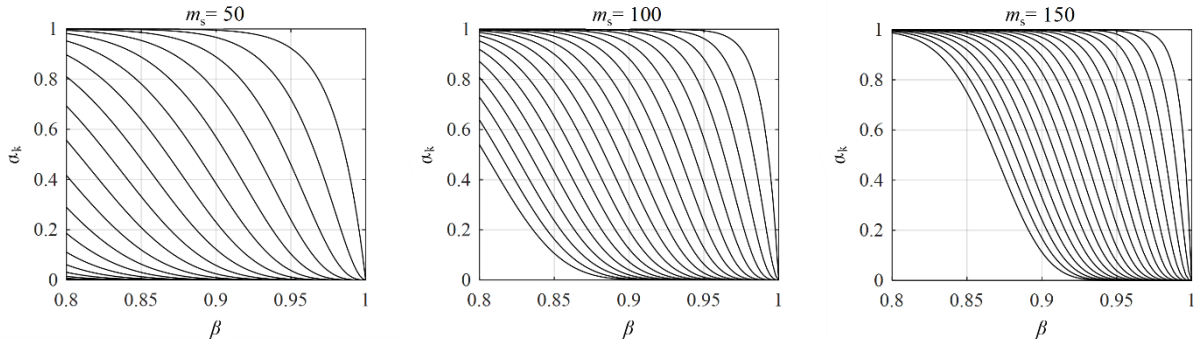

(a) (b) (c)

Fig. 4-1 Relation between α_k and β for some fixed values of m_s and various values of k: (a) m_s = 50; (b) m_s = 100; (c) m_s = 150

4.3 Problem formulation

In this section, two formulations for robust optimization of plane frames under uncertainty are presented. One is a single-objective optimization to minimize the maximum stress under volume and global stability constraints, and the other is a multi-objective optimization to simultaneously minimize the maximum stress with different robustness levels under volume constraint.

4.3.1 Shape and topology optimization with global stability constraint

We begin with the deterministic shape and topology optimization problem of minimizing the stress of a plane frame under global stability and volume constraints, which is formulated as follows:

$$\begin{aligned}
&\text{Minimize } \sigma = \max_{\substack{i=1,2,\cdots m_e \\ j=1,2,\cdots p}} \left(\sigma_{V,ij}\left(\boldsymbol{x}_{\text{free}}, \boldsymbol{y}_{\text{free}}, \boldsymbol{A}\right)\right) \\
&\text{subject to } \frac{1}{\lambda^{\text{cr}}\left(\boldsymbol{x}_{\text{free}}, \boldsymbol{y}_{\text{free}}, \boldsymbol{A}\right)} \le \frac{1}{\underline{\lambda}}; \\
&\quad V\left(\boldsymbol{x}_{\text{free}}, \boldsymbol{y}_{\text{free}}, \boldsymbol{A}\right) \le \bar{V}; \\
&\quad \underline{\boldsymbol{x}}_{\text{free}} \le \boldsymbol{x}_{\text{free}} \le \bar{\boldsymbol{x}}_{\text{free}}; \quad \underline{\boldsymbol{y}}_{\text{free}} \le \boldsymbol{y}_{\text{free}} \le \bar{\boldsymbol{y}}_{\text{free}}; \quad \underline{\boldsymbol{A}} \le \boldsymbol{A} \le \bar{\boldsymbol{A}}
\end{aligned} \tag{4.2}$$

where $\boldsymbol{x}_{\text{free}}$, $\boldsymbol{y}_{\text{free}}$ and $\boldsymbol{A}$ are the vectors of x- and y-coordinates of the free nodes and the cross-sectional areas of the Euler-Bernoulli beam elements, respectively, which serve as design variables in problem (4.2), and the lower and upper bars in the constraints represent the lower and upper bounds of the corresponding design variables; m_{e} is the number of beam elements in the frame; p is the number of points for stress evaluation within each element, and their selections will be explained in Section 4.4, together with the penalization method for stress and global stability singularities; $\sigma_{V,ij}$ is the von Mises stress evaluated at point j of the ith element, and the detailed implementation of calculating the von Mises stress of beam element is referred to Ref. [125]; $\overline{V}$ and $\underline{\lambda}$ are the upper bound for the structural volume and the lower bound for the global linear buckling load factor λ^{cr}, respectively. Note that λ^{cr} is defined as the smallest positive eigenvalue of the following eigenvalues problem:

$$\left(\boldsymbol{K}\left(\boldsymbol{x}_{\text{free}},\boldsymbol{y}_{\text{free}},\boldsymbol{A}\right)+\lambda\boldsymbol{K}_{G}\left(\boldsymbol{x}_{\text{free}},\boldsymbol{y}_{\text{free}},\boldsymbol{A}\right)\right)\boldsymbol{\Phi}=\boldsymbol{0} \tag{4.3}$$

where $\boldsymbol{K}$ and $\boldsymbol{K}_G$ are the n_{dof}-by-n_{dof} global elastic stiffness matrix and the geometrical stiffness matrix corresponding to the unit load factor, respectively [126]. In Eq. (4.2) the global stability constraint is written with respect to the reciprocals of λ^{cr} and $\underline{\lambda}$ to ensure that λ^{cr} is either larger than $\underline{\lambda}$ or negative [108], and for simplicity we hereafter denote the reciprocals as $\gamma^{\text{cr}}=1/\lambda^{\text{cr}}$ and $\overline{\gamma}=1/\underline{\lambda}$, respectively.

By incorporating the FDM as discussed in Chapter 3, the locations of free nodes of a plane frame can be derived by solving Eq. (2.4) of the corresponding auxiliary truss, and the optimization problem (4.2) is restated as

$$\begin{aligned}
&\text{Minimize } \sigma=\max_{\substack{i=1,2,\cdots m_{\text{e}}\\ j=1,2,\cdots p}}\left(\sigma_{V,ij}\left(\boldsymbol{x}_{\text{free}}\left(\boldsymbol{t}\right),\boldsymbol{y}_{\text{free}}\left(\boldsymbol{t}\right),\boldsymbol{A}\right)\right)\\
&\text{subject to } \gamma^{\text{cr}}\left(\boldsymbol{x}_{\text{free}}\left(\boldsymbol{t}\right),\boldsymbol{y}_{\text{free}}\left(\boldsymbol{t}\right),\boldsymbol{A}\right)\le\overline{\gamma};\\
&\qquad V\left(\boldsymbol{x}_{\text{free}}\left(\boldsymbol{t}\right),\boldsymbol{y}_{\text{free}}\left(\boldsymbol{t}\right),\boldsymbol{A}\right)\le\overline{V}\\
&\qquad \underline{\boldsymbol{t}}\le\boldsymbol{t}\le\overline{\boldsymbol{t}};\quad \underline{\boldsymbol{A}}\le\boldsymbol{A}\le\overline{\boldsymbol{A}}
\end{aligned} \tag{4.4}$$

where $\boldsymbol{t}$ is the force density vector. As discussed in Chapter 3, problems (4.2) and (4.4) are basically the same and will lead to the same solution if a set of $\boldsymbol{t}$ in problem (4.4) can define the optimal solution of problem (4.2), which means the optimal solution of problem (4.2) can be found by solving problem (4.4) if it is included in the feasible domain of problem (4,4). Note again that in problem (4.4) the stress are calculated for the rigidly-jointed frame model with Euler-Bernoulli beam elements.

When uncertainty is introduced to problem (4.4), the optimization problem considering uncertainty takes the following form:

$$
\begin{aligned}
&\text{Minimize } \sigma^{\max} = \max_{\boldsymbol{\theta}\in\Omega} \sigma\left(\boldsymbol{x}_{\text{free}}(\boldsymbol{t}), \boldsymbol{y}_{\text{free}}(\boldsymbol{t}), \boldsymbol{A}; \boldsymbol{\theta}\right) \\
&\text{subject to } \gamma^{\text{cr,max}} = \max_{\boldsymbol{\theta}\in\Omega} \left(\gamma^{\text{cr}}\left(\boldsymbol{x}_{\text{free}}(\boldsymbol{t}), \boldsymbol{y}_{\text{free}}(\boldsymbol{t}), \boldsymbol{A}; \boldsymbol{\theta}\right)\right) \le \bar{\gamma}; \\
&\qquad V\left(\boldsymbol{x}_{\text{free}}(\boldsymbol{t}), \boldsymbol{y}_{\text{free}}(\boldsymbol{t}), \boldsymbol{A}\right) \le \bar{V}; \\
&\qquad \underline{\boldsymbol{t}} \le \boldsymbol{t} \le \bar{\boldsymbol{t}}; \quad \underline{\boldsymbol{A}} \le \boldsymbol{A} \le \bar{\boldsymbol{A}}
\end{aligned}
\tag{4.5}
$$

where σ and γ^{cr} are the same as problem (4.4); $\boldsymbol{\theta} = (\Delta\boldsymbol{x}, \Delta\boldsymbol{y}, \Delta\boldsymbol{A})$ is the vector representing the uncertainty in nodal locations and cross-sectional areas as described in Section 2.4; Ω is the corresponding uncertain parameter space of $\boldsymbol{\theta}$; $\sigma^{\max}$ and $\gamma^{\text{cr,max}}$ are the values of maximum von Mises stress and reciprocal of global linear buckling load factor within the space Ω, respectively. It is worth noting that problem (4.5) can be regarded as a WCO problem with semi-infinite constraint for design variables and uncertain parameters, since it can be equivalently transformed into

$$
\begin{aligned}
&\text{Minimize } \sigma^{\max} = \max_{\boldsymbol{\theta}\in\Omega} \sigma\left(\boldsymbol{x}_{\text{free}}(\boldsymbol{t}), \boldsymbol{y}_{\text{free}}(\boldsymbol{t}), \boldsymbol{A}; \boldsymbol{\theta}\right) \\
&\text{subject to } \gamma^{\text{cr}} = \left(\gamma^{\text{cr}}\left(\boldsymbol{x}_{\text{free}}(\boldsymbol{t}), \boldsymbol{y}_{\text{free}}(\boldsymbol{t}), \boldsymbol{A}; \boldsymbol{\theta}\right)\right) \le \bar{\gamma} \text{ for } \forall\boldsymbol{\theta}\in\Omega; \\
&\qquad V\left(\boldsymbol{x}_{\text{free}}(\boldsymbol{t}), \boldsymbol{y}_{\text{free}}(\boldsymbol{t}), \boldsymbol{A}\right) \le \bar{V}; \\
&\qquad \underline{\boldsymbol{t}} \le \boldsymbol{t} \le \bar{\boldsymbol{t}}; \quad \underline{\boldsymbol{A}} \le \boldsymbol{A} \le \bar{\boldsymbol{A}}
\end{aligned}
\tag{4.6}
$$

Problem (4.6) can be classified as an RSO problem. To see this, we introduce the slack variable *s* and problem (4.6) can be further reformulated as follows, where the constraints are to be satisfied for all possible set of uncertain parameters:

$$
\begin{aligned}
&\text{Minimize } s \\
&\text{subject to } \sigma\left(\boldsymbol{x}_{\text{free}}(\boldsymbol{t}), \boldsymbol{y}_{\text{free}}(\boldsymbol{t}), \boldsymbol{A}; \boldsymbol{\theta}\right) \le s \text{ for } \forall\boldsymbol{\theta}\in\Omega; \\
&\qquad \gamma^{\text{cr}} = \left(\gamma^{\text{cr}}\left(\boldsymbol{x}_{\text{free}}(\boldsymbol{t}), \boldsymbol{y}_{\text{free}}(\boldsymbol{t}), \boldsymbol{A}; \boldsymbol{\theta}\right)\right) \le \bar{\gamma} \text{ for } \forall\boldsymbol{\theta}\in\Omega; \\
&\qquad V\left(\boldsymbol{x}_{\text{free}}(\boldsymbol{t}), \boldsymbol{y}_{\text{free}}(\boldsymbol{t}), \boldsymbol{A}\right) \le \bar{V}; \\
&\qquad \underline{\boldsymbol{t}} \le \boldsymbol{t} \le \bar{\boldsymbol{t}}; \quad \underline{\boldsymbol{A}} \le \boldsymbol{A} \le \bar{\boldsymbol{A}}
\end{aligned}
\tag{4.7}
$$

Therefore, we solve an RSO problem using the randomized or stochastic approach for estimating the worst values of the responses of the WCO problem. However, it is difficult to directly solve problem (4.7) because the exact worst values of structural responses are difficult to find. Therefore, the exact worst responses are relaxed to the 100βth percentile structural responses which are approximated by order statistics, and the procedure will be illustrated as follows.

Let $\boldsymbol{\theta}_1, \boldsymbol{\theta}_2, \cdots, \boldsymbol{\theta}_{m_s}$ be the m_s samples of i.i.d. vectors of uncertainties in nodal locations and cross-sectional areas with unknown distributions, and $(\boldsymbol{t}, \boldsymbol{A})$ be the design variable vectors of force densities and cross-sectional areas. The corresponding m_s structural responses in Eq. (4.7) with respect to $\boldsymbol{\theta}_1, \boldsymbol{\theta}_2, \cdots, \boldsymbol{\theta}_{m_s}$ and $(\boldsymbol{t}, \boldsymbol{A})$ are denoted by $\sigma_1 = \sigma\left(\boldsymbol{t}, \boldsymbol{A}; \boldsymbol{\theta}_1\right), ..., \sigma_{m_s} = \sigma\left(\boldsymbol{t}, \boldsymbol{A}; \boldsymbol{\theta}_{m_s}\right)$ and

$\gamma_1^{\mathrm{cr}} = \gamma^{\mathrm{cr}}\left(\boldsymbol{t}, \boldsymbol{A}; \boldsymbol{\theta}_1\right), ..., \gamma_{m_\mathrm{s}}^{\mathrm{cr}} = \gamma^{\mathrm{cr}}\left(\boldsymbol{t}, \boldsymbol{A}; \boldsymbol{\theta}_{m_\mathrm{s}}\right)$, respectively. Similar to the order statistics defined in Section 2.2, the *k*th maximum stress $\sigma_{k:m_\mathrm{s}}$ is called the *k*th order statistic of the stress where $\sigma_{1:m_\mathrm{s}} \geq \sigma_{2:m_\mathrm{s}} \geq ... \geq \sigma_{m_\mathrm{s}:m_\mathrm{s}}$, and the $\gamma_{1:m_\mathrm{s}}^{\mathrm{cr}}, \gamma_{2:m_\mathrm{s}}^{\mathrm{cr}}, ..., \gamma_{m_\mathrm{s}:m_\mathrm{s}}^{\mathrm{cr}}$ and $\gamma_{k:m_\mathrm{s}}^{\mathrm{cr}}$ are also defined in the same manner.

As stated in Section 4.2, the order *k* and its corresponding order statistic approximating the 100βth percentile of structural response can be regarded as representing the robustness level of the structure. Suppose the worst values of the responses in the parameter space in problem (4.7) are approximated by the *k*th order statistics $\sigma_{k:m_\mathrm{s}}$ and $\gamma_{k:m_\mathrm{s}}^{\mathrm{cr}}$ among m_s realizations at confidence level α_k. Then problem (4.7) can be rewritten as

$$
\begin{aligned}
&\text{Minimize } s \\
&\text{subject to } \sigma_{k:m_\mathrm{s}}\left(\boldsymbol{x}_{\mathrm{free}}\left(\boldsymbol{t}\right), \boldsymbol{y}_{\mathrm{free}}\left(\boldsymbol{t}\right), \boldsymbol{A}; \boldsymbol{\Theta}\right) \leq s; \\
&\qquad \gamma_{k:m_\mathrm{s}}^{\mathrm{cr}}\left(\boldsymbol{x}_{\mathrm{free}}\left(\boldsymbol{t}\right), \boldsymbol{y}_{\mathrm{free}}\left(\boldsymbol{t}\right), \boldsymbol{A}; \boldsymbol{\Theta}\right) \leq \bar{\gamma}; \\
&\qquad V\left(\boldsymbol{x}_{\mathrm{free}}\left(\boldsymbol{t}\right), \boldsymbol{y}_{\mathrm{free}}\left(\boldsymbol{t}\right), \boldsymbol{A}\right) \leq \bar{V}; \\
&\qquad \underline{\boldsymbol{t}} \leq \boldsymbol{t} \leq \bar{\boldsymbol{t}}; \quad \underline{\boldsymbol{A}} \leq \boldsymbol{A} \leq \bar{\boldsymbol{A}}
\end{aligned}
\tag{4.8}
$$

where $\boldsymbol{\Theta} = \left(\boldsymbol{\theta}_1, \cdots, \boldsymbol{\theta}_{m_\mathrm{s}}\right)$ denotes the set of m_s sample vectors of uncertain parameters. The difference between the approximated worst values in problem (4.8) and the exact worst values in problem (4.7) will become smaller if the value of *k* is closer to 1, and the robustness levels of both maximum stress and global stability also increase as the order *k* decreases. Note that the constraints in RSO problem (4.7) are relaxed, i.e., the robustness for satisfying the constraints is relaxed, by using order statistics in problem (4.8) at specified confidence level α_k, and such robustness can be referred to as statistical feasibility robustness which handles the semi-infinite constraints stochastically [20]. Although similar formulation to incorporate uncertainty in constraint can be found in RBSO problem and referred to as risk or chance constraint [127–129], there is no general consensus that RBSO should not be considered as part of the robust optimization methodology, and vice versa [20], and the connection between robustness and the stochastic or probability theory are also exploited recently by some researchers [130]. The equivalence between the probabilistic optimization problem and the robust optimization with uncertain-but-bounded variables are also discussed by Elishakoff and Ohsaki [17]. Hence, we consider problem (4.8) as robust optimization problem due to the fact that it is a relaxed version of the WCO problem (4.7), and problem (4.8) serves as the RSO problem to be solved in the numerical examples of this chapter.

Moreover, as stated in Section 3.3, although the member length is indirectly controlled by the bounds of force densities to prevent zero-length member, closely spaced nodes may exist when the value of N_i is small, which can be derived by Eq. (3.10) or Eq. (3.12). Besides, if the cross-sectional area of the short member is moderately large, unexpectedly large von Mises stress may appear due to its large bending stiffness. However, the closely spaced nodes in the final solution will be merged into one node to obtain a simplified structural layout without short members. Therefore, in order to find the appropriate maximum stress to be minimized, the stress of the short

member is ignored for computing the objective function during the optimization process. In addition, the short member is modeled by only one beam element to avoid singularity caused by its large stiffness, and the nodal uncertainty is then applied only at the end nodes of a short member.

Problem (4.8) is solved using CONOPT in the MATLAB interface of TOMLAB with default settings [131]. The correlated nodal uncertainty values in each member are generated by using copulas [132] [133] in MATLAB 2018a [134], and their correlation coefficients are calculated by Eq. (2.20) in Section 2.4. Furthermore, the frame member is modeled by only one beam element if its length is less than 0.1 m; otherwise the frame member is evenly divided into four beam elements as explained in Section 2.4. Flowchart of the optimization procedure with global stability constraint is shown in Fig. 4-2.

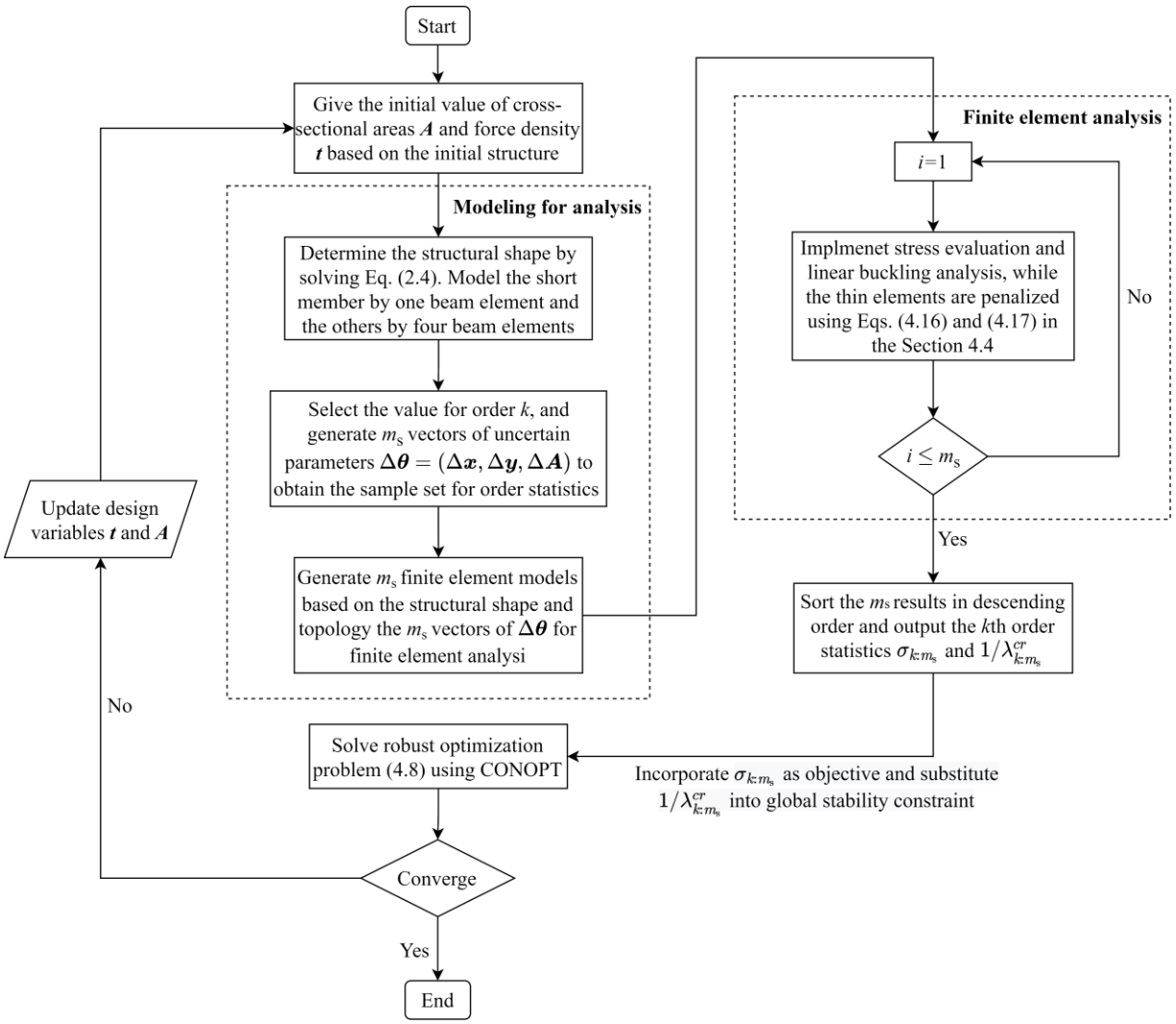

Fig. 4-2 Flowchart of robust optimization in Section 4.3.1

4.3.2 Multi-objective optimization

Due to the trade-off relationship between robustness level and structural performance [135], the selection of order k is not evident, and one may decide the value of k to meet the practical robustness. Because the exact extreme value corresponds to extremely rare event, for some cases it may be important to minimize not only the worst (i.e., k close to 1), but also the median and/or other percentile values of the response. Therefore, it is of interest to consider the structural responses with different values of k as multiple objective functions. Moreover, for comparison purpose the structural response without considering uncertainty is also included. The details of formulating multi-objective optimization problem are given as follows.

Let design variables be the vectors of nodal coordinate $\boldsymbol{x}=\left(x_1,x_2,\ldots,x_{n_x}\right)$, $\boldsymbol{y}=\left(y_1,y_2,\ldots,y_{n_y}\right)$ and cross-sectional areas $\boldsymbol{A}=\left(A_1,A_2,\ldots,A_{m_e}\right)$, where n_x and n_y are the numbers of variables in x- and y-coordinates, respectively. The structural optimization problem without considering uncertainty can be formulated as

$$\begin{aligned}&\text{Minimize } \sigma=\max_{\substack{i=1,2,\cdots m_e\\ j=1,2,\cdots p}}\left(\sigma_{V,ij}\left(\boldsymbol{x},\boldsymbol{y},\boldsymbol{A}\right)\right)\\ &\text{subject to } V\left(\boldsymbol{x},\boldsymbol{y},\boldsymbol{A}\right)\le\bar{V};\\ &\qquad\underline{\boldsymbol{x}}\le\boldsymbol{x}\le\bar{\boldsymbol{x}};\ \underline{\boldsymbol{y}}\le\boldsymbol{y}\le\bar{\boldsymbol{y}};\ \underline{\boldsymbol{A}}\le\boldsymbol{A}\le\bar{\boldsymbol{A}}\end{aligned}\tag{4.9}$$

It is worth noting that in problem (4.9) tight bounds $\underline{\boldsymbol{x}}$, $\bar{\boldsymbol{x}}$, $\underline{\boldsymbol{y}}$ and $\bar{\boldsymbol{y}}$ are given for the design variables of coordinates $\boldsymbol{x}$ and $\boldsymbol{y}$, and therefore FDM is not used here for shape optimization. After solving problem (4.9), the topology of the structure is modified by removing the elements which have small cross-sectional areas and are considered to have little contribution to the reduction of structural response. However, such unnecessary elements may become useful for a solution to an RSO problem to minimize the worst structural response under uncertainty. Therefore, based on the optimal shape obtained by solving problem (4.9), we further choose the cross-sectional areas as the design variables for RSO problem formulated as follows:

$$\begin{aligned}&\text{Minimize } \sigma^{\max}=\max_{\boldsymbol{\theta}\in\Omega}\sigma\left(\boldsymbol{A};\boldsymbol{\theta}\right)\\ &\text{subject to } V\left(\boldsymbol{A}\right)\le\bar{V};\\ &\qquad\underline{\boldsymbol{A}}\le\boldsymbol{A}\le\bar{\boldsymbol{A}}\end{aligned}\tag{4.10}$$

Note that in problem (4.10) no uncertainty is considered in the constraint for simplicity. According to Section 4.2, the worst value $\sigma^{\max}$ is relaxed to 100βth ($0<\beta<1$) percentile response which is approximated by the kth order statistic, and problem (4.10) is rewrite as

$$\begin{aligned}&\text{Minimize } \sigma_{k:m_s}\left(\boldsymbol{A};\boldsymbol{\theta}\right)\\ &\text{subject to } V\left(\boldsymbol{A}\right)\le\bar{V};\\ &\qquad\underline{\boldsymbol{A}}\le\boldsymbol{A}\le\bar{\boldsymbol{A}}\end{aligned}\tag{4.11}$$

where m_s is the sample size of order statistics. By selecting different values of k in problem (4.11), and including the response without considering uncertainty denoted by $\bar{\sigma}(\boldsymbol{A}) = \max_{\substack{i=1,2,\cdots m_e \\ j=1,2,\cdots p}} \left(\sigma_{V,ij}(\boldsymbol{A})\right)$, the multi-objective optimization problem is formulated as

$$\begin{aligned} &\text{Minimize } \bar{\sigma}(\boldsymbol{A}),\ \sigma_{k_1:m_s}(\boldsymbol{A};\boldsymbol{\theta}),\ \sigma_{k_2:m_s}(\boldsymbol{A};\boldsymbol{\theta}),\ldots,\ \sigma_{k_f:m_s}(\boldsymbol{A};\boldsymbol{\theta}) \\ &\text{subject to } V(\boldsymbol{A}) \le \bar{V}; \\ &\qquad \underline{\boldsymbol{A}} \le \boldsymbol{A} \le \bar{\boldsymbol{A}} \end{aligned} \tag{4.12}$$

where $k_1, k_2, \ldots, k_f \ (1 \le k_1 < k_2 < \ldots < k_f \le m_s)$ are the selected values of order k.

According to the dependence properties of order statistics [136] [137], two order statistics are non-negatively correlated if they are i.i.d. random variables. Since the probability distribution of structural response is unknown, only distribution-free measurements of dependence, like Spearman's correlation and Kendall's tau can be applied, and their explicit calculations have been exploited by Navarro and Balakrishnan [138]. However, it is known that the value of $\sigma_{k:m_s}(\boldsymbol{A};\boldsymbol{\theta})$ strongly depends on the choice of random numbers, especially when k is close to 1. Therefore, in some cases the linear statistic (L-statistic), which is a linear combination of order statistics, is also used as an estimator due to its simplicity and stability [117]. We use the simple trimmed mean $S_{\bar{k}:m_s}(\boldsymbol{A};\boldsymbol{\theta})$, defined as follows, for smoothing the quantile response:

$$S_{\bar{k}:m_s}(\boldsymbol{A};\boldsymbol{\theta}) = \frac{1}{[m_s p_2] - [m_s p_1]} \sum_{k=[m_s p_1]+1}^{[m_s p_2]} \sigma_{k:m_s}(\boldsymbol{A};\boldsymbol{\theta}) \tag{4.13}$$

where p_1 and $1 - p_2$ $(0 \le p_1 < p_2 \le 1)$ are the preassigned portions of the samples trimmed at the lower and upper ends, and $[m_s p_1]$ and $[m_s p_2]$ are the greatest integer less than $m_s p_1$ and $m_s p_2$, respectively. The subscript $\bar{k}$ represents the arithmetic mean of all orders k in the set $\{[m_s p_1]+1, \ldots, [m_s p_2]\}$.

It is obvious that if p_1 and p_2 in Eq. (4.13) are properly selected such that

$$S_{\bar{k}:m_s}(\boldsymbol{A};\boldsymbol{\theta}) = \frac{1}{3}\left(\sigma_{k-1:m_s}(\boldsymbol{A};\boldsymbol{\theta}) + \sigma_{k:m_s}(\boldsymbol{A};\boldsymbol{\theta}) + \sigma_{k+1:m_s}(\boldsymbol{A};\boldsymbol{\theta})\right) \tag{4.14}$$

then the trimmed mean $S_{\bar{k}:m}(\boldsymbol{X};\boldsymbol{\theta})$ is a function of order k, and can also be used as an approximation of quantile response $\sigma_{k:m_s}(\boldsymbol{A};\boldsymbol{\theta})$ to meet the various robustness levels. We denote the trimmed mean defined as Eq. (4.14) by $S_{k:m}$ for the implication of function of order k hereafter. Then, the multi-objective optimization problem to minimize $S_{k:m}$ can be formulated as

$$\begin{aligned} &\text{Minimize } \bar{\sigma}(\boldsymbol{A}),\ S_{k_1:m_s}(\boldsymbol{A};\boldsymbol{\theta}),\ S_{k_2:m_s}(\boldsymbol{A};\boldsymbol{\theta}),\ldots,\ S_{k_f:m_s}(\boldsymbol{A};\boldsymbol{\theta}) \\ &\text{subject to } V(\boldsymbol{A}) \le \bar{V}; \\ &\qquad \underline{\boldsymbol{A}} \le \boldsymbol{A} \le \bar{\boldsymbol{A}} \end{aligned} \tag{4.15}$$

where $k_1, k_2, \ldots k_f \ \left(2 \le k_1 < k_2 < \ldots < k_f \le m_s - 1\right)$ are the selected values of order k in $S_{k:m_s}(\boldsymbol{A};\boldsymbol{\theta})$.

Problems (4.9), (4.12) and (4.15) are solved using genetic algorithms (GAs), which is one of the standard methods for solving multi-objective optimization problem. It is well known for GAs that the diversity of the initial population has great influence on the final solution and convergence property. Therefore, we use Latin hypercube sampling (LHS) method to generate the initial population for all of the three problems to maintain diversity, and the optimal solution of problem (4.9) is also added into the initial population of multi-objective optimization problems (4.12) and (4.15).

The flowchart of multi-objective optimization procedure is summarized in Fig. 4-3, which consists of the following steps:

Step 1: Select the design variables from the sets of nodal coordinates and cross-sectional areas, and specify the nominal values of uncertain parameters for problem (4.9). Generate the initial population using LHS method. Solve problem (4.9) using GA and obtain the optimal solution.

Step 2: Based on the shape of optimal solution of Step 1, select the cross-sectional areas as design variables for multi-objective optimization problems (4.12) and (4.15). Generate the initial population using LHS method and add the optimal solution of problem (4.9) into it.

Step 3: Select the multiple values of order k to determine the objective functions of problems (4.12) and (4.15) according to various robustness levels. Generate m_s vectors of random values $\boldsymbol{\theta}$ to obtain the sample set for order statistics.

Step 4: Solve problems (4.12) and (4.15) using a multi-objective GA. For each individual, compute m_s response values corresponding to the m_s vectors of $\boldsymbol{\theta}$, and rearrange the responses in a descending order to compute the objective function values based on the multiple selected orders k.

Step 5: Obtain the Pareto optimal solutions, and remove the elements whose cross-sectional areas are small enough.

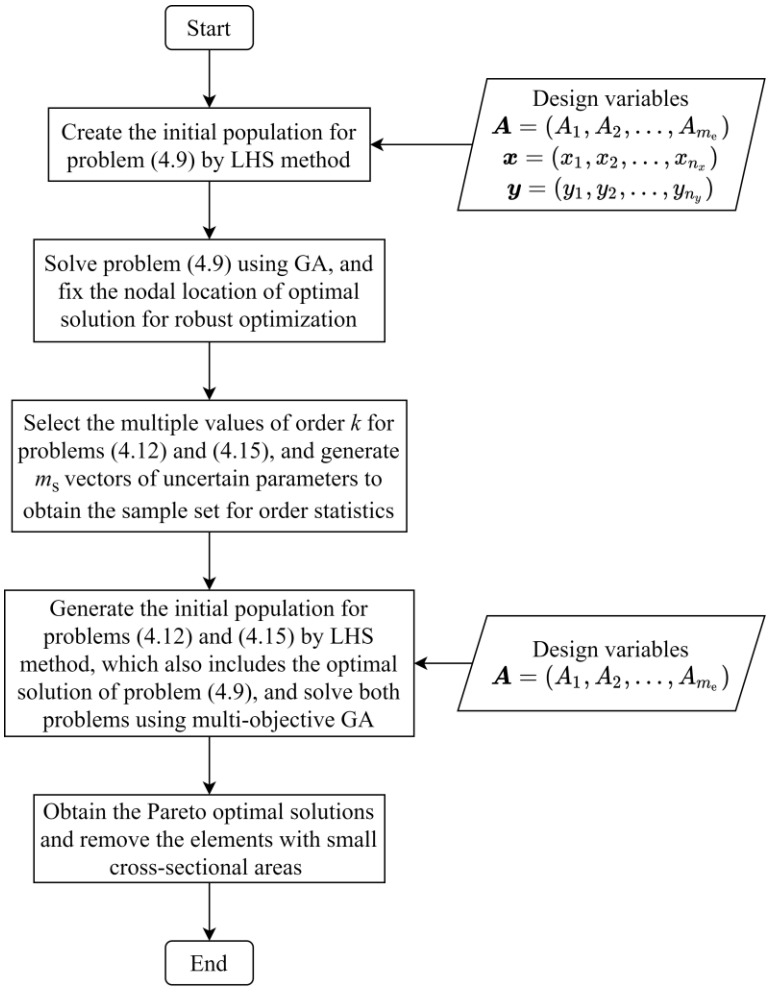

Fig. 4-3 Flowchart of multi-objective robust optimization in Section 4.3.2

4.4 Penalization method

When the cross-sectional areas of some members are close to 0, the accuracy of stress and eigenvalue analyses of the structure would be affected due to the existence of these thin elements, resulting in a disconnected feasible domain for the optimization problem which may have some degenerate sub-domains such as half lines [139][140], and this behavior is usually regarded as singularity phenomena in structural optimization [8][113][141]. Since singularity phenomenon might emerge in the maximum stress and the global buckling load factor and influence the optimization result, the penalization method is used for both stress singularity problem and singularity in global buckling load factor. Firstly, based on the method for stress-based optimization [140], the element stress is penalized as follows if the cross-sectional area of the *i*th element is small enough:

$$\hat{\sigma}_{V,i} = \left(A_i / \bar{A}_i \right)^{\eta} \max_{j=1,2,\cdots p} \left(\sigma_{V,ij} \right) \tag{4.16}$$

where i, j , p and $\sigma_{V,ij}$ have the same meaning as Eqs. (4.2) and (4.4); $\bar{A}_i$ is the ith element of $\bar{\boldsymbol{A}}$ defined in Eq. (4.8); η is the penalization parameter to underestimate the stress of a thin element. According to Ref. [140], the value of η should be greater than 0 and less than 1, and in this research we select $\eta = 0.5$ which is the same as in Ref. [140].

To verify the effectiveness of using Eq. (4.16), a simple example of stress minimization problem under volume constraint is to be solved where uncertainty is not taken into consideration. The initial structure of a simple frame is shown in Fig. 4-4(a), in which the node number and the member number are indicated by those with and without parentheses, respectively. The frame is pin-supported at nodes 1 and 2, and a downward vertical load F with magnitude 2000 N is applied at node 3. The design variables are the cross-sectional areas of the five members, and each member is divided into four Euler-Bernoulli beam elements. Note that the crossing members 3 and 4 are not connected at their intersection. As a result, there are 20 beam elements in the structure. The Young's modulus is 3×10^{11} Pa, and the von Mises stress is calculated at the neutral axis and the upper and lower edges of the cross-section at the two end nodes of each element, which are illustrated in Fig. 4-4(b). The optimization problem is formulated based on Eq. (4.4) in Section 4.3.1 without global buckling constraint and considering only $\boldsymbol{A}$ as design variables, where m_e = 20, p = 6, and the upper and lower bounds of cross-sectional areas for all members are 0.05 and 1×10^{-7} (m^2), respectively. The stress of a thin element is penalized using Eq. (4.16), and the thin elements are defined as those whose cross-sectional areas are less than 1% of A_{max}, where A_{max} is the maximum cross-sectional area of the frame. The problem is solved by the generalized reduced gradient (GRG) method of CONOPT in the MATLAB interface of TOMLAB with default settings [131]. The optimal solution and the corresponding cross-sectional areas are shown in Fig. 4-5(a) and Table 4-3, which is the same as Fig. 2-4(a) and Table 2-1 in Section 2.4, and the result after removing the thin elements is shown in Fig. 4-5(b). The maximum von Mises stresses before and after removing thin elements are 68199.41 and 68199.54 (Pa), respectively, which are almost the same, indicating that the stress singularity phenomenon can be avoided by using Eq. (4.16).

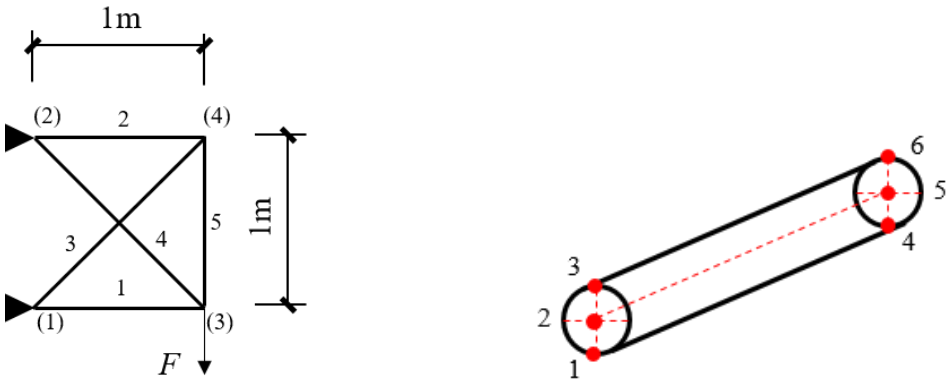

(a) (b)

Fig. 4-4 A simple frame model: (a) initial structure; (b) stress evaluation points of each element

Table 4-3 Cross-sectional areas of optimal solution of simple frame model

Member number	Cross-sectional area (m^2)
1	0.03478
2	1×10^{-7}
3	1×10^{-7}
4	0.04611
5	1×10^{-7}

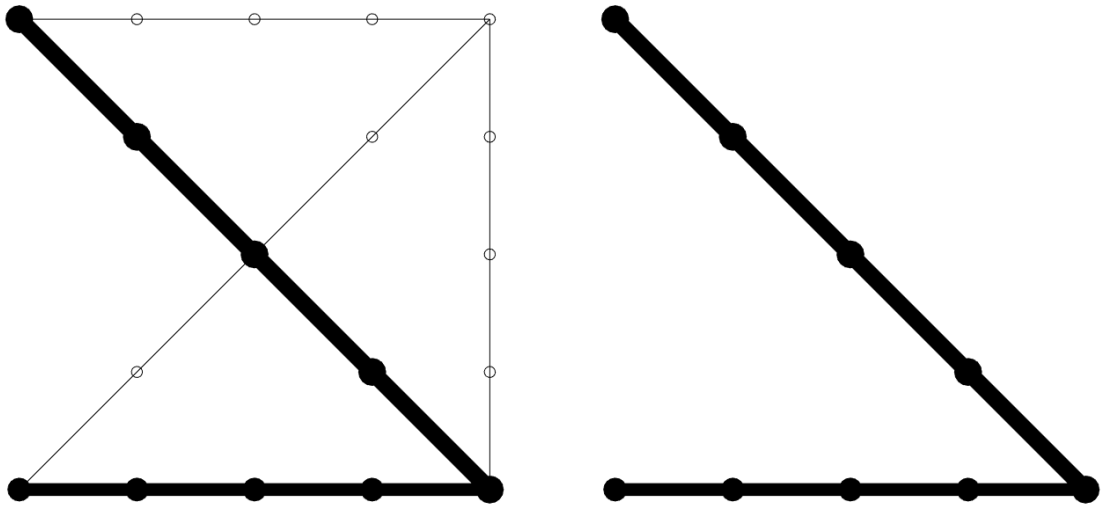

(a) (b)

Fig. 4-5 Optimal solution of simple frame model: (a) before removing thin elements; (b) after removing thin elements

The penalization approach to alleviate stress singularity is also used for singularity phenomenon in global instability. It has been pointed out that the emergence of slender member in compression will lead to a violation of global stability constraint due to their negative contributions in global geometrical stiffness matrix [36]. Therefore, in order to obtain the accurate linear buckling load factor of the structure when thin elements are involved, the geometrical stiffness matrix of the thin element, say the *i*th element, is penalized as follows:

$$\hat{\boldsymbol{K}}_{G,i} = \left(A_i / \bar{A}_i \right)^{\rho} \times \boldsymbol{K}_{G,i} \tag{4.17}$$

where $\boldsymbol{K}_{G,i}$ is the original geometrical stiffness matrix of the *i*th element and ρ is the penalization parameter. Eq. (4.17) is inspired by the standard SIMP method where the elastic element stiffness matrix with intermediate density is penalized by the corresponding density design variable [3, 142]. The main purpose of using Eq. (4.17) is to exclude the superficial buckling without removing any thin element and keeping the connection of nodes unchanged.

To illustrate the effectiveness of Eq. (4.17), we investigate the linear buckling load factor of the solution of the same optimization problem. As discussed in Section 2.4, the linear buckling load factor before removing thin elements is much smaller than that after removing the thin elements. However, if the geometrical stiffness matrices of the thin elements are penalized using Eq. (4.17), we can eliminate such negative effect in the global geometrical stiffness matrix and obtain the accurate value of λ^{cr} without removing the thin elements. Figure. 4-6 shows the relationship between λ^{cr} before removing thin elements and the penalization parameter ρ in Eq. (4.17). The value of λ^{cr} after removing the thin elements is also plotted with red line for comparison. As we can see from Fig. 4-6, the value of λ^{cr} before removing the thin elements increases as ρ is increased, and becomes close to 238440.64 when ρ is greater than 1, indicating that the global stability of the structure can be evaluated by using Eq. (4.17) with a value of ρ larger than 1. Therefore, for the single-objective optimization problem in Section 4.3.1 we choose $\rho = 2$ in Eq. (4.17) to penalize the geometrical stiffness matrix of a thin element.

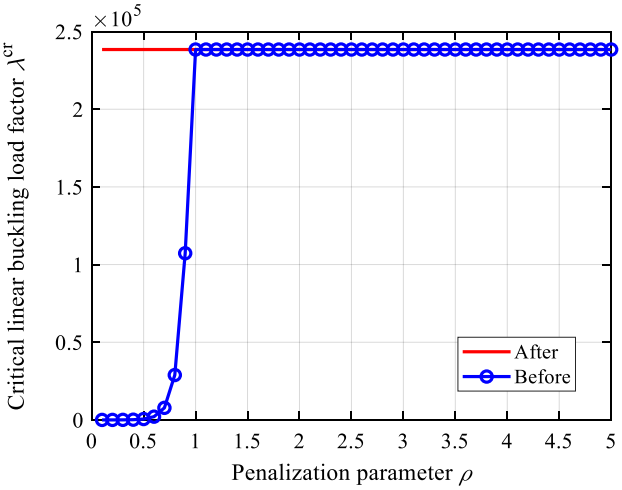

Fig. 4-6 Variation of linear buckling load factor with respect to penalization parameter

4.5 Numerical examples

In this section four numerical examples are investigated to demonstrate the effectiveness of the proposed methods as discussed in Sections 4.3, and the details of parameter settings for the both problem formulations will be given in Section 4.4.1. On the one hand, examples 1 and 2 are presented for the single-objective problem formulation in Section 4.3.1, and they are solved using CONOPT in the MATLAB interface of TOMLAB with default settings [56]. On the other hand, examples 3 and 4 are presented for the multi-objective problem formulation in Section 4.3.2, and they are solved by a multi-objective GA in Global Optimization Toolbox of MATLAB 2018a [124] with crossover rate 0.7 by default. Besides, we assume that in the following examples each member has solid circular cross-section, and the crossing members are not connected at their intersection.

For each example the node number and the member number shown in the initial structure are indicated by those with and without parentheses, respectively.

4.5.1 Parameter settings

As for the single-objective problem formulation in 4.3.1, since the robustness level β is a decreasing function of order k with given sample size m_s, and higher values of β and confidence level α_k lead to a better approximation of the worst structural response, we assume k = 1, m_s = 150 and $\alpha_k = 0.9995$ for problem (4.8) in examples 1 and 2, i.e., the $\sigma_{k:m_s}$ and $\gamma^{cr}_{k:m_s}$ in problem (4.8) are written as $\sigma_{1:150}$ and $\gamma^{cr}_{1:150}$, respectively, and the corresponding robustness β of both maximum stress and global buckling load factor is 0.95. The eccentricity e in Section 2.4 is 0.01 for each member in accordance with Ref. [143], and the entries of vector $\boldsymbol{\theta} = (\Delta\boldsymbol{x}, \Delta\boldsymbol{y}, \Delta\boldsymbol{A})$ are characterized by uniformly distributed interval variables with the increments indicated by Δ, i.e., $\Delta\boldsymbol{x} \in \left[\Delta\boldsymbol{x}_{\text{lower}}, \Delta\boldsymbol{x}_{\text{upper}}\right]$, $\Delta\boldsymbol{y} \in \left[\Delta\boldsymbol{y}_{\text{lower}}, \Delta\boldsymbol{y}_{\text{upper}}\right]$, $\Delta\boldsymbol{A} \in \left[\Delta\boldsymbol{A}_{\text{lower}}, \Delta\boldsymbol{A}_{\text{upper}}\right]$. The feasible region Ω is then defined as $\left[\Delta\boldsymbol{x}_{\text{lower}}, \Delta\boldsymbol{x}_{\text{upper}}\right] \times \left[\Delta\boldsymbol{y}_{\text{lower}}, \Delta\boldsymbol{y}_{\text{upper}}\right] \times \left[\Delta\boldsymbol{A}_{\text{lower}}, \Delta\boldsymbol{A}_{\text{upper}}\right]$, where the subscripts lower and upper represent the lower and upper bounds for the corresponding uncertain parameters, respectively. Note that the same set of uncertain parameters is used at each iteration during optimization process. Validity of this procedure is explained in Appendix A2. Because the variation range of uncertain locations of intermediate nodes can be derived with prescribed uncertain nodal locations of free nodes and the eccentricity e, only the bounds for free nodes, denoted by $\Delta\boldsymbol{x}_{\text{free,lower}}$, $\Delta\boldsymbol{x}_{\text{free,upper}}$, $\Delta\boldsymbol{y}_{\text{free,lower}}$ and $\Delta\boldsymbol{y}_{\text{free,upper}}$, are given in each example, and we assume that the nodal uncertainty does not exist in the fixed nodes. The correlated nodal uncertainty values in each member are generated by using copulas [132][133] in MATLAB 2018a [134], and their correlation coefficients are calculated by Eq. (2.20) with correlation length L_{exp}=0.1m. It should be noted that in problem (4.8) no assumption is made on the distribution type of the uncertain parameters; however, in the numerical examples we choose the uniform distribution as the sample-generating mechanism for conveniently constructing the random sample set for order statistics [79].

Furthermore, since closely spaced nodes may still exist in the optimization process, we hereafter do not divide the frame member if its length is less than 0.1 m; otherwise the frame member is evenly divided into four beam elements as explained in Section 2.4. An element is regarded as thin if its cross-sectional area is less than 1% of the maximum cross-sectional area of the frame. The stress and geometrical stiffness of a thin element are penalized using Eqs. (4.16) and (4.17), respectively. The number of evaluation points p within each element is 6, and their positions are shown in Fig. 4-4(b). The parameter values listed in Table 4-4 are used in examples 1 and 2 if not specified explicitly, where $\boldsymbol{I}$ is the vector with all entries equal to 1. Note that $\underline{\boldsymbol{A}}$ in Table 4-4 is the lower bound of cross-sectional area without considering uncertainty, i.e., $\boldsymbol{A} \geq \underline{\boldsymbol{A}}$, and the number of nodes n does not include the intermediate nodes in each member. The deterministic optimization problem (4.4) is also solved in examples 1 and 2 for comparison

purpose, and the solution of robust optimization problem (4.8) and deterministic optimization problem (4.4) are denoted as solutions R and D, respectively.

Table 4-4 Parameter settings of examples 1 and 2

Parameters	Example 1	Example 2
Lower bound of $\Delta \boldsymbol{x}_{\text{free,lower}}$ (m)	$-0.02\boldsymbol{I}$	$-0.02\boldsymbol{I}$
Upper bound of $\Delta \boldsymbol{x}_{\text{free,upper}}$ (m)	$0.02\boldsymbol{I}$	$0.02\boldsymbol{I}$
Lower bound of $\Delta \boldsymbol{y}_{\text{free,lower}}$ (m)	$-0.02\boldsymbol{I}$	$-0.02\boldsymbol{I}$
Upper bound of $\Delta \boldsymbol{y}_{\text{free,lower}}$ (m)	$0.02\boldsymbol{I}$	$0.02\boldsymbol{I}$
Lower bound of $\Delta \boldsymbol{A}_{\text{lower}}$ (m^2)	$-0.02\boldsymbol{A}$	$-0.02\boldsymbol{A}$
Upper bound of $\Delta \boldsymbol{A}_{\text{upper}}$ (m^2)	$0.02\boldsymbol{A}$	$0.02\boldsymbol{A}$
Nominal value of $\boldsymbol{E}$ (Pa)	$2\times10^{11}\boldsymbol{I}$	$2\times10^{11}\boldsymbol{I}$
Sample size m_s	150	150
Order k in problem (4.8)	1	1
Confidence level α_k	0.9995	0.9995
Robustness β	0.95	0.95
Upper bound $\bar{\boldsymbol{A}}$ (m^2)	$0.05\boldsymbol{I}$	$0.05\boldsymbol{I}$
Lower bound $\underline{\boldsymbol{A}}$ (m^2)	$1\times10^{-7}\boldsymbol{I}$	$1\times10^{-7}\boldsymbol{I}$
Upper bound $\bar{\boldsymbol{t}}$ (N/m)	$1000\boldsymbol{I}$	$1000\boldsymbol{I}$
Lower bound $\underline{t}$ (N/m)	$-1000\boldsymbol{I}$	$-1000\boldsymbol{I}$
Upper bound $\bar{V}$ (m^3)	0.02	0.1
Lower bound $\underline{\lambda}$	3.4	50
Upper bound $\bar{\gamma}$	0.29	0.02
Correlation length L_{exp} (m)	0.1	0.1
Number of members m	10	27
Number of nodes n	6	12
Eccentricity e	0.01	0.01

As for multi-objective formulation in Section 4.3.2, the uncertain parameters $\boldsymbol{\theta} = (\Delta \boldsymbol{x}, \Delta \boldsymbol{y}, \Delta \boldsymbol{E})$ are also characterized by the uniformly distributed interval variables, i.e., $\Delta \boldsymbol{E} \in \left[\Delta \boldsymbol{E}_{\text{upper}}, \Delta \boldsymbol{E}_{\text{lower}}\right]$, $\Delta \boldsymbol{x} \in \left[\Delta \boldsymbol{x}_{\text{lower}}, \Delta \boldsymbol{x}_{\text{upper}}\right]$ and $\Delta \boldsymbol{y} \in \left[\Delta \boldsymbol{y}_{\text{lower}}, \Delta \boldsymbol{y}_{\text{upper}}\right]$. To illustrate effectiveness of the proposed method, the range of uncertain interval parameters are given as approximately 10% from the nominal value in the similar manner as the examples by Guest and Igusa [62]. It is worth noting that the elements of design variables $\boldsymbol{x}$ and $\boldsymbol{y}$ in problem (4.9) do not exactly correspond to the uncertain parameters $\Delta \boldsymbol{x}$ and $\Delta \boldsymbol{y}$ in problems (4.12) and (4.15); $\boldsymbol{x}$ and $\boldsymbol{y}$ may have more or less elements than $\Delta \boldsymbol{x}$ and $\Delta \boldsymbol{y}$, respectively, and vice versa.

Furthermore, since our purpose is to minimize the structural response at different robustness levels, we hereafter select the maximum and median structural responses as the desired percentiles to be minimized [135], and the upper quartile, which is defined as the middle between the maximum and median, is also included to investigate the variation trend of objective function values and their statistical values. A small positive lower bound of cross-sectional area is given for a non-existing member to prevent numerical difficulty. The values of parameters in examples 3 and 4 are listed in Table 4-5, if not specified explicitly

Table 4-5 Parameter settings of examples 3 and 4

Parameters	Example 3	Example 4
Lower bound of $\Delta \boldsymbol{x}_{\text{lower}}$ (m)	$-0.6\boldsymbol{I}$	$-0.1\boldsymbol{I}$
Upper bound of $\Delta \boldsymbol{x}_{\text{upper}}$ (m)	$0.6\boldsymbol{I}$	$0.1\boldsymbol{I}$
Lower bound of $\Delta \boldsymbol{y}_{\text{lower}}$ (m)	$-0.6\boldsymbol{I}$	$-0.1\boldsymbol{I}$
Upper bound of $\Delta \boldsymbol{y}_{\text{lower}}$ (m)	$0.6\boldsymbol{I}$	$0.1\boldsymbol{I}$
Lower bound of $\Delta \boldsymbol{E}_{\text{lower}}$	$-0.1\boldsymbol{E}$	$-0.1\boldsymbol{E}$
Upper bound of $\Delta \boldsymbol{E}_{\text{upper}}$	$0.1\boldsymbol{E}$	$0.1\boldsymbol{E}$
Nominal value of $\boldsymbol{E}$ (Pa)	2.1×10^{11}	2.1×10^{11}
Upper bound $\bar{\boldsymbol{A}}$ (m^2)	$0.1\boldsymbol{I}$	$0.05\boldsymbol{I}$
Lower bound $\underline{\boldsymbol{A}}$ (m^2)	$1\times10^{-7}\boldsymbol{I}$	$1\times10^{-7}\boldsymbol{I}$
Upper bound of $\bar{V}$ (m^3)	1	0.2
Order k in problem (4.12)	1, 50, 100	1, 50, 100
Order k in problem (4.15)	2, 50, 100	2, 50, 100
Confidence level α_k	0.9	0.9
Sample size m_s	200	200

4.5.2 Example 1: single-objective problem formulation in 4.3.1

The first example is a plane frame with two square units, and the initial frame is shown in Fig. 4-7. The frame is pin-supported at nodes 1 and 2, and a downward vertical load F = 200 kN is applied at node 5. The fixed nodes for FDM are selected as nodes 1, 2 and 5, and the others are free nodes. The robust and deterministic solutions R and D are obtained by solving optimization problems (4.8) and (4.4), respectively.

The solutions R and D are shown in Fig. 4-8, where the contour represents the value of von Mises stress without adding uncertainty. The nodal locations, force densities, cross-sectional areas and member lengths of solutions R and D are listed in Tables 4-6 and 4-7. In order to give a more intuitive comparison, the worst case of stress distributions of solutions R and D are shown in Fig. 4-9, where uncertainties are considered in nodal locations and cross-sectional areas, and the values of σ, $\sigma_{1:150}$, γ^{cr}, λ^{cr}, $\gamma^{\text{cr}}_{1:150}$, $\lambda^{\text{cr}}_{1:150}$ and V are also listed in Table 4-8. It is worth noting that Figs.

4-8 and 4-9 show the performances of solutions R and D with and without adding uncertainties, respectively, under the same loading and boundary conditions.

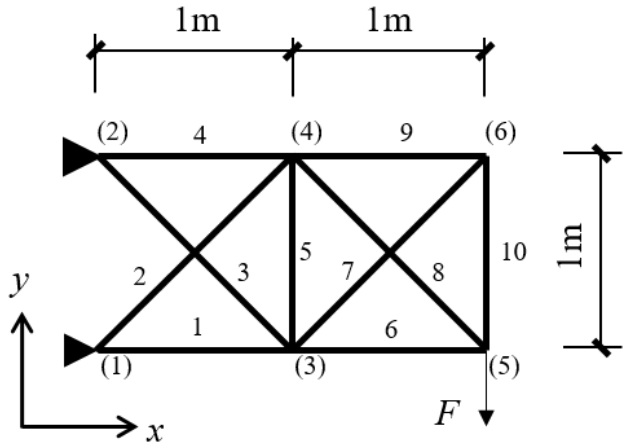

Fig. 4-7 Initial frame of Example 1

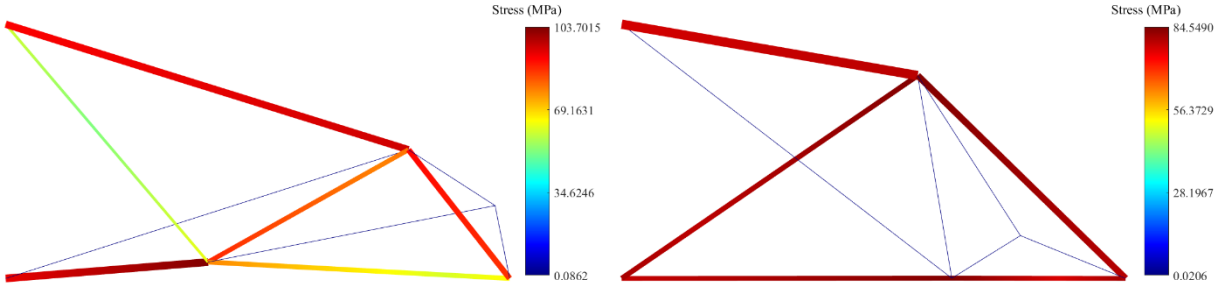

(a) (b)

Fig. 4-8 Solutions of Example 1 and stress distribution without uncertainty: (a) Solution R; (b) Solution D

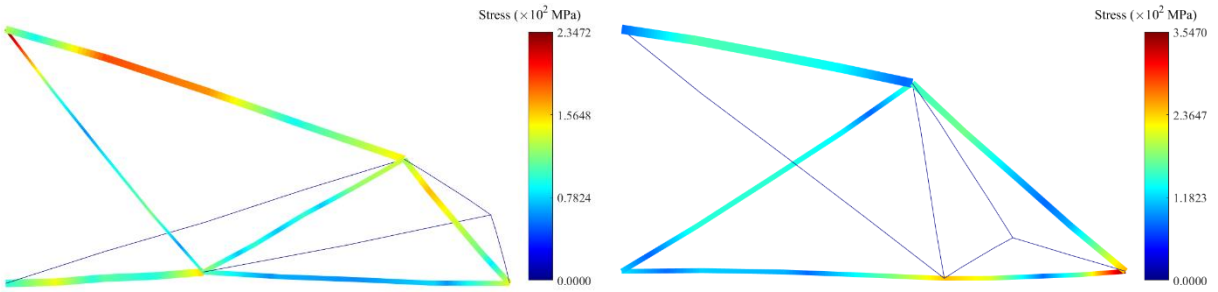

(a) (b)

Fig. 4-9 Solutions of Example 1 and worst stress distribition: (a) Solution R; (b) Solution D

It can be seen from Fig. 4-8 and Table 4-8 that solution D has a smaller σ than solution R, and the linear buckling load factor of solution D is close to $\underline{\lambda}$. Moreover, for solution D the von Mises stresses in the elements with moderate cross-sectional areas are at the similar magnitude and close to σ, which means that the limited material is fully utilized in solution D. However, as we can see from Tables 4-6 and 4-7, the cross-sectional areas of members 1 and 6 in solution D are almost the same, and nodes 1, 3 and 5 are almost located at the same horizontal line; therefore members 1 and 6 can be considered as a long member connecting nodes 1 and 5, resulting in a much higher $\sigma_{1:150}$ and a violation on global stability constraint when uncertainty is involved, as observed in Fig. 4-9(b) and Table 4-8.

Table 4-6 Nodal location of solutions of Example 1

Node number	Solution R		Solution D	
	x-coordinate (m)	*y*-coordinate (m)	*x*-coordinate (m)	*y*-coordinate (m)
1	0	0	0	0
2	0	1	0	1
3	0.8011	0.0631	1.3101	0.0008
4	1.6003	0.5087	1.1747	0.7980
5	2	0	2	0
6	1.9439	0.2882	1.5822	0.1685

Table 4-7 Cross-sectional area, force density and member length of solutions of Example 1

Member number	Solution R			Solution D		
	Cross-sectional area (m^2)	Force density (N/m^2)	Length (m)	Cross-sectional area (m^2)	Force density (N/m^2)	Length (m)
1	0.004302	0.2617	0.8059	0.002678	0.4489	1.3101
2	1×10^{-7}	0.0933	1.6767	0.002933	-0.4132	1.4202
3	0.001560	0.1924	1.2332	1×10^{-7}	-0.1647	1.6476
4	0.004069	0.1263	1.6729	0.005220	0.7074	1.1920
5	0.002682	-0.2225	0.9096	1×10^{-7}	0.0980	0.8085
6	0.002719	0.5726	1.1983	0.002675	0.3539	0.6898
7	1×10^{-7}	-0.1260	1.1603	1×10^{-7}	0.5198	0.3196
8	0.003228	0.0078	0.6462	0.003710	0.2497	1.1480
9	1×10^{-7}	0.4978	0.4081	1×10^{-7}	0.3099	0.7499
10	1×10^{-7}	0.4798	0.2921	1×10^{-7}	0.6410	0.4504

Table 4-8 Values of σ, $\sigma_{1:150}$, γ^{cr}, λ^{cr}, $\gamma^{cr}_{1:150}$, $\lambda^{cr}_{1:150}$ and V of solutions of Example 1

Solution	σ (MPa)	$\sigma_{1:150}$ (MPa)	γ^{cr}	λ^{cr}	$\gamma^{cr}_{1:150}$	$\lambda^{cr}_{1:150}$	V (m^3)
R	103.7015	234.7208	0.0868	11.5117	0.0914	10.9328	0.02
D	84.5490	354.7003	0.2899	3.4490	0.3193	3.1314	0.02

While the stress distribution in solution R has several different stress levels and some of these elements has much smaller von Mises stress than σ, the long member in solution D no longer exists in solution R and node 3 is connected by more elements, increasing the redundancy of the structure to reduce the effect of uncertainty on structural performance. In addition, compared to solution D, the overall height of solution R is smaller. It is observed from Fig. 4-9 that at the worst case more elements in solution R have high stress level close to $\sigma_{1:150}$, while in solution D the high stress level only exists in the elements at the bottom, which demonstrates that the elements in solution R cooperate with each other to reduce the maximum stress. Table 4-8 also indicates that $\sigma_{1:150}$ of solution R is smaller than that of solution D, and the global stability constraint is satisfied under uncertainty which is far from being active. Specifically, $\sigma_{1:150}$ of solution R increases about 126.34% from σ and $\lambda_{1:150}^{\mathrm{cr}}$ decreases about 5.02% from λ^{cr}, whereas $\sigma_{1:150}$ of solution D increases about 319.52% from σ and $\lambda_{1:150}^{\mathrm{cr}}$ decreases about 9.02% from λ^{cr}. This result indicates that solution R is more robust and stable than solution D with respect to reducing the influence of uncertainty in nodal locations and cross-sectional areas on structural performance. Although the details are not shown, a similar solution as solution D is obtained if global stability constraint is not considered. This fact emphasizes the importance of the proposed penalization method of the geometrical stiffness matrix to obtain the optimal solution neglecting the superficial buckling of the thin members.

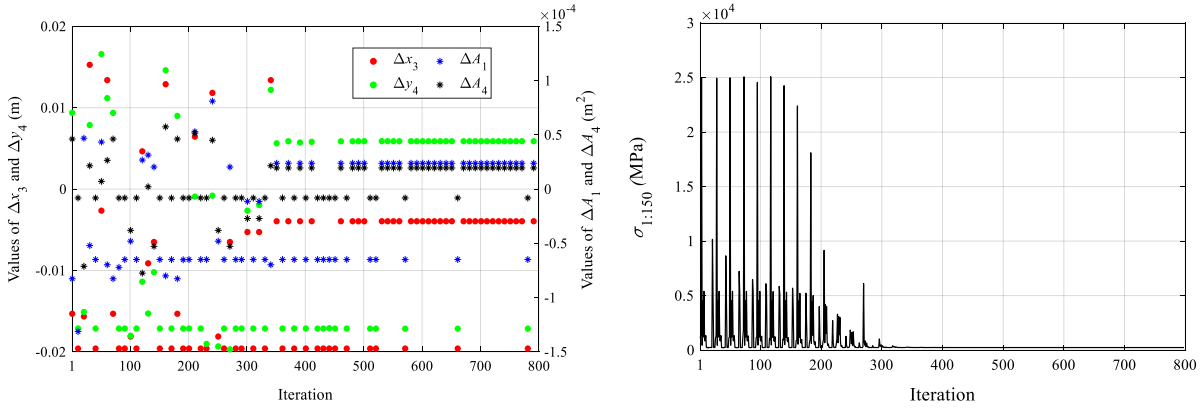

(a) (b)

Fig. 4-10 Iteration history of Example 1: (a) Values of Δx_3, Δy_4, ΔA_1 and ΔA_4 in worst case scenario; (b) First order statistic $\sigma_{1:150}$

Furthermore, the iteration histories of values of uncertainties in the *x*-coordinate of node 3 and *y*-coordinate of node 4, denoted by Δx_3 and Δy_4, respectively, and cross-sectional areas of members 1 and 4, denoted by ΔA_1 and ΔA_4, respectively, in the worst case scenario are presented

in Fig. 4-10(a), and the iteration history of $\sigma_{1:150}$ is also presented in Fig. 4-10(b). Note that for simplicity in Fig. 4-10(a) only the values of every 10 iterations are shown. It can be observed from Fig. 4-10(a) that the values of uncertainties in nodal coordinates and cross-sectional areas in the worst case scenario change during the optimization procedure, indicating that the worst case scenarios would switch with respect to the variations of uncertain parameters. Moreover, in Fig. 4-10(b) there are several humps in the iteration history of $\sigma_{1:150}$ which increase rapidly to a very large value. The main reason would be that since the optimization problem is nonlinear with respect to the design variables, solutions that are sensitive to uncertain parameters are sometimes evaluated during optimization, resulting in a large value of $\sigma_{1:150}$. However, in this example the values of humps are gradually decreased and the worst case scenario converged as the optimization procedure converged to a local minimum with an appropriate shape and topology. In addition, we further investigate the effect of using different sampling sets for constructing the order statistics on final design, and the results are presented in Appendix A2.

4.5.3 Example 2: single-objective problem formulation in 4.3.1

The second example is another cantilever plane frame structure with 3×2 units. The structure is pin-supported at nodes 1, 2 and 3, and a downward vertical load F = 100 kN is applied at node 11 as shown in Fig. 4-11.

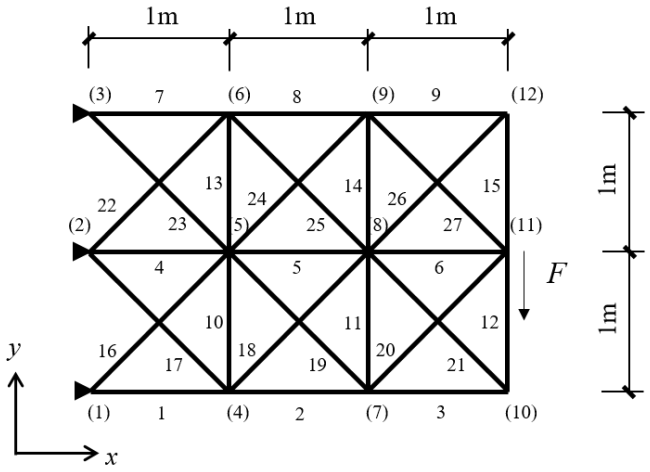

Fig. 4-11 Initial frame of Example 2

In a similar manner as Example 1, we solve both the robust and deterministic optimization problems (4.8) and (4.4) for Example 2. The nodal locations, cross-sectional areas, force densities and member lengths of solutions R and D are listed in Tables 4-9 and 4-10, and Table 4-11 lists the values of σ, $\sigma_{1:150}$, γ^{cr}, λ^{cr}, $\gamma^{\mathrm{cr}}_{1:150}$, $\lambda^{\mathrm{cr}}_{1:150}$ and V. Solutions R and D are shown in Fig. 4-12 and

the stress contours are obtained without considering uncertainty, while Fig. 4-13 shows the worst stress distributions of solutions R and D. It should be noted that since the stresses of short members are ignored during the optimization, the stresses of short member 6 in solution R and short members 1 and 7 in solution D are represented as 0 in Figs. 4-12 and 4-13.

Table 4-9 Nodal location of solutions of Example 2

Node number	Solution R		Solution D	
	x-coordinate (m)	*y*-coordinate (m)	*x*-coordinate (m)	*y*-coordinate (m)
1	0	0	0	0
2	0	1	0	1
3	0	2	0	2
4	0.9342	0.1628	0.0249	0.0060
5	1.4275	1.0654	1.3000	1.0004
6	0.6667	1.9573	0.0250	1.9939
7	1.9891	0.3623	1.8630	0.2935
8	2.9738	0.8939	1.4999	1.0004
9	1.8244	1.8063	1.8622	1.7067
10	2.7641	1.2496	2.7868	1.2748
11	3	1	3	1
12	2.8315	1.0208	2.2953	1.9169

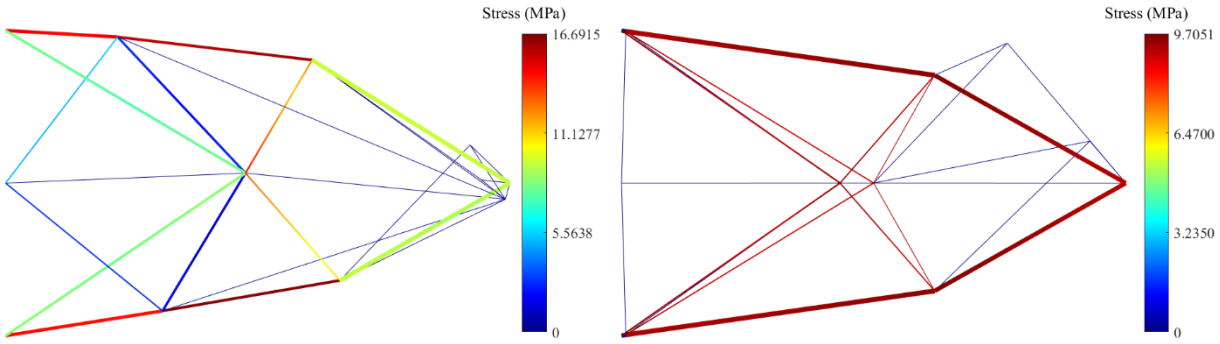

(a) (b)

Fig. 4-12 Solutions of Example 2 and stress distribution without uncertainty: (a) Solution R; (b) Solution D

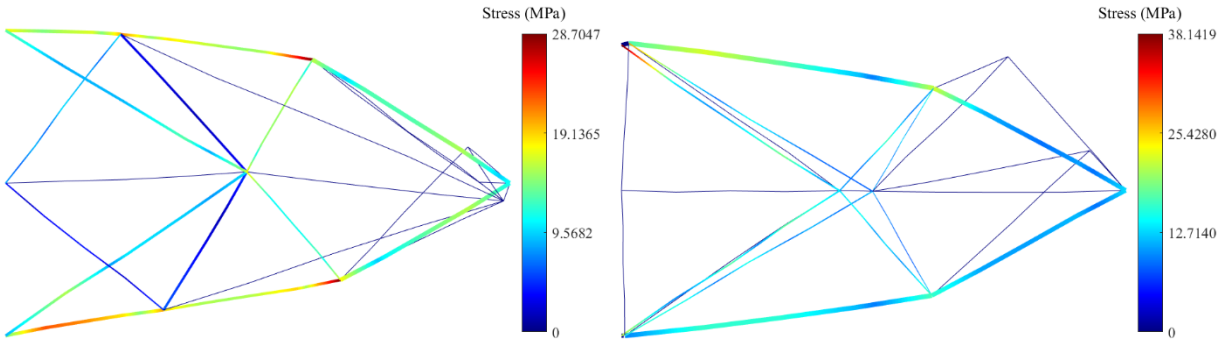

(a) (b)

Fig. 4-13 Solutions of Example 2 and worst stress distribition: (a) Solution R; (b) Solution D

Table 4-10 Cross-sectional area and force density of solutions of Example 2

Member number	Solution R			Solution D		
	Cross-sectional area (m^2)	Force density (N/ m)	Length (m)	Cross-sectional area (m^2)	Force density (N/ m)	Length (m)
1	0.0077	0.8088	0.9483	0.0099	0.0114	0.0257
2	0.0064	-0.8207	1.0735	0.0114	0.0659	1.8603
3	5.52×10^{-7}	0.0845	1.1781	1×10^{-7}	-0.0595	1.3477
4	1.87×10^{-7}	-0.0556	1.4290	1×10^{-7}	0.07949	1.3000
5	1.83×10^{-7}	0.0867	1.5557	1×10^{-7}	-0.4249	0.1999
6	9.49×10^{-7}	-0.9537	0.1000	1×10^{-7}	-0.4484	1.5000
7	0.0077	1.3707	0.6681	0.0099	0.0383	0.0257
8	0.0064	0.0208	1.1674	0.0113	0.2297	1.8595
9	1.85×10^{-7}	0.0864	1.2772	1×10^{-7}	-0.1393	0.4814
10	0.0056	0.5636	1.0286	1×10^{-7}	0.1459	1.6169
11	3.51×10^{-6}	-0.8759	1.1191	0.0017	-0.1890	0.7946
12	2.99×10^{-7}	1.2386	0.3434	1×10^{-7}	0.1458	0.3478
13	0.0054	1.1569	1.1722	1×10^{-7}	-0.0752	1.6164
14	1.84×10^{-7}	0.4991	1.4675	0.0017	-0.2745	0.7937
15	1.84×10^{-7}	0.0748	0.1697	1×10^{-7}	-0.0232	1.1564
16	0.0061	-0.1373	1.7813	0.0036	-0.2397	1.6403
17	0.0032	-0.5928	1.2544	1×10^{-7}	0.0424	0.9943
18	1.86×10^{-7}	0.3870	2.1667	0.0028	-0.2074	1.7789
19	0.0036	0.2556	0.8998	0.0028	0.1364	0.9036
20	0.0098	0.0740	1.1952	0.0103	0.1622	1.3385
21	1.78×10^{-7}	-1.0804	0.4129	1×10^{-7}	0.0669	1.3158
22	0.0031	-0.7756	1.1666	1×10^{-7}	0.2256	0.9943
23	0.0061	-0.4466	1.7062	0.0036	0.0815	1.6398
24	0.0039	-0.0823	0.8404	0.0028	-0.0069	0.9027
25	1.85×10^{-7}	-0.2199	2.5403	0.0028	-0.2167	1.7783
26	1.83×10^{-7}	0.5229	0.1906	1×10^{-7}	0.0552	1.2134
27	0.0098	-0.5693	1.4255	0.0102	0.3332	1.3393

It can be seen from Fig. 4-12 and Tables 4-9 and 4-10 that compared to solution D, the nodal locations and cross-sectional areas of solution R are asymmetric with respect to the center line parallel to the *x*-axis, and σ of solution R is almost twice of that of solution D. However, when uncertainty is added to the nodal locations and cross-sectional areas, $\sigma_{1:150}$ of solution D significantly increases about 293% from 9.7051 MPa to 38.1419 MPa, and $\lambda_{1:150}^{cr}$ is also decreases about 7.67% from λ^{cr} violating the global stability constraint. This is mainly because the existences of long members in solution D make the structure more sensitive to the asymmetric uncertainties. By contrast, $\sigma_{1:150}$ of solution R is smaller than that of solution D as more members have increased their cross-sectional areas and connect to the support node 2, avoiding the existence of long members and increasing the structural stability. In addition, we can see from Table 4-11 that $\lambda_{1:150}^{cr}$ of solution R decreases only about 5.3% from λ^{cr} and the global stability constraint is also satisfied under uncertainty, which indicates solution R has more stability than solution D.

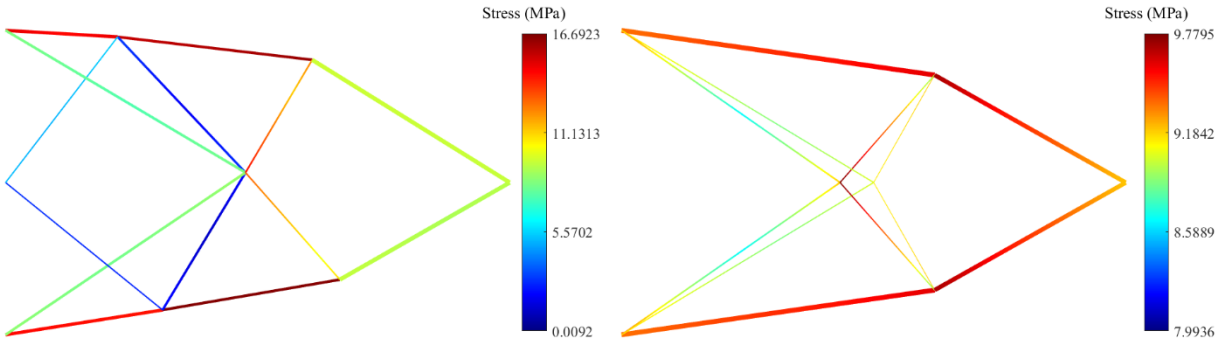

Fig. 4-14 Solutions of Example 2 and stress distribution without uncertainty after merging the closely spaced nodes and removing thin elements: (a) Solution R; (b) Solution D

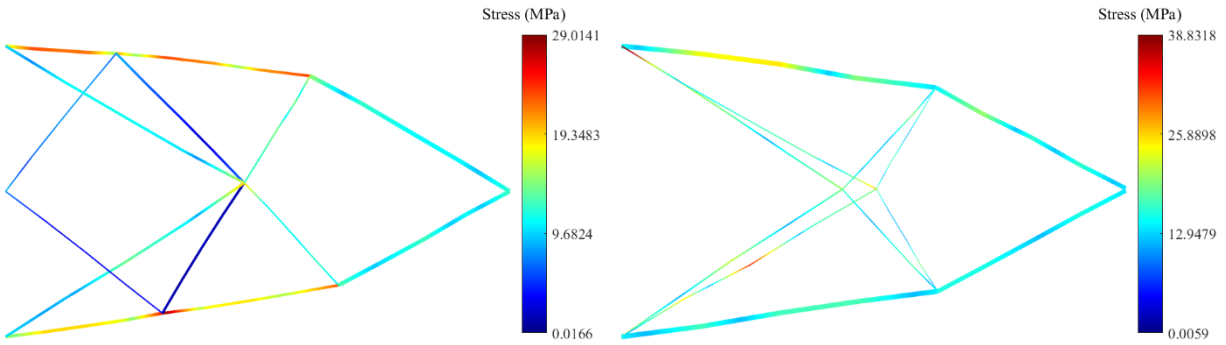

Fig. 4-15 Solutions of Example 2 and worst stress distribution after merging the closely spaced nodes and removing thin elements: (a) Solution R; (b) Solution D

Figures. 4-14 and 4-15 show the stress contours of solutions R and D without considering uncertainty and the corresponding worst stress distributions, respectively, after merging the closely spaced nodes and removing thin elements. The values of σ, $\sigma_{1:150}$, γ^{cr}, λ^{cr}, $\gamma^{cr}_{1:150}$, $\lambda^{cr}_{1:150}$ and V of solutions in Figs. 4-14 and 4-15 are listed in Table 4-12. It can be found that the differences between Tables 4-11 and 4-12 for solutions R and D are about 1.5% or less, however, as stated in Section 4.3.1, unexpectedly large stress might exist in a short member with moderate cross-sectional area due to its large bending stiffness, and would provide an inaccurate stress to be minimized if it is considered during optimization procedure. For example, the von Mises stress of members 1 and 7 without uncertainty in solution D are both 13.0781 MPa, which is much larger than the stress after merging the closely spaced nodes and removing thin elements. Therefore, the stress in short member is set to 0 during the optimization procedure to avoid such inaccurate stress to be minimized.

Table 4-11 Values of σ, $\sigma_{1:150}$, γ^{cr}, λ^{cr}, $\gamma^{cr}_{1:150}$, $\lambda^{cr}_{1:150}$ and V of solutions of Example 2 before merging the closely spaced nodes and removing thin elements

Solution	σ (MPa)	$\sigma_{1:150}$ (MPa)	γ^{cr}	λ^{cr}	$\gamma^{cr}_{1:150}$	$\lambda^{cr}_{1:150}$	V (m^3)
R	16.6915	28.7047	0.0102	97.9790	0.0107	92.7861	0.1
D	9.7051	38.1419	0.0195	51.1818	0.0216	47.2584	0.1

Table 4-12 Values of σ, $\sigma_{1:150}$, γ^{cr}, λ^{cr}, $\gamma^{cr}_{1:150}$, $\lambda^{cr}_{1:150}$ and V of solutions of Example 2 after merging the closely spaced nodes and removing thin elements

Solution	σ (MPa)	$\sigma_{1:150}$ (MPa)	γ^{cr}	λ^{cr}	$\gamma^{cr}_{1:150}$	$\lambda^{cr}_{1:150}$	V (m^3)
R	16.6923	29.0141	0.0102	97.9778	0.0108	92.2404	0.1
D	9.7795	38.8318	0.0197	50.7112	0.0211	47.4364	0.1

It can be seen from Tables 4-9 to 4-11 that solutions R and D have the same structural volume that is equal to its upper bound; however, they have different structural geometries and distributions of cross-sectional areas, leading to a trade-off relationship between structural robustness and performance. Specifically, solution D has a smaller σ at deterministic condition, while the $\sigma_{1:150}$ of solution R increases less from σ and has larger λ^{cr} and $\lambda^{cr}_{1:150}$ than those of solution D.

4.5.4 Example 3: multi-objective problem formulation in 4.3.2

The third example is a 14-node bridge frame with 6×1 grid and 31 beam elements, which is pin-supported at nodes 1 and 13. The initial ground structure is shown in Fig. 4-16. There are five downward loads with magnitude of $F = 3\times10^6$ N applied at nodes 3, 5, 7, 9 and 11.

Firstly, to investigate the difference between optimal designs of truss and frame, we first minimize the structural volume under stress constraints on each element and *y*-directional displacement at each node except nodes 1 and 13. This problem has been studied in Ref. [144] using truss elements. Note that uncertainty is not considered here, and Young's modulus for each beam element is 2.1×10^{11} Pa.

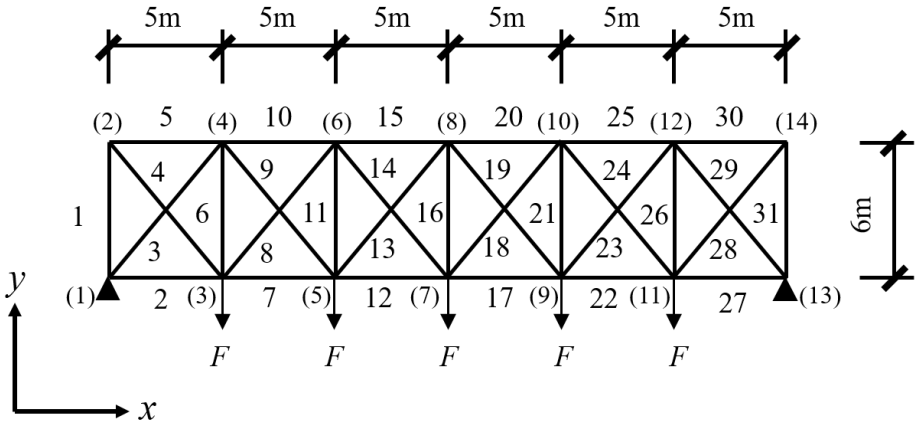

Fig. 4-16 Initial frame of Example 3

The design variables are the cross-sectional area of each element and the *y*-coordinates of the upper nodes 2, 4, 6, 8, 10, 12 and 14. Because the structural shape, loading and boundary conditions are symmetric with respect to the center line parallel to the *y*-axis, the number of design variables is reduced from 38 to 20, with 16 design variables $\boldsymbol{A}=(A_1,A_2,\ldots,A_{16})$ representing the cross-sectional areas of elements 1 to 16, and four design variables $\boldsymbol{y}=(y_2,y_4,y_6,y_8)$ representing the *y*-coordinates of nodes 2, 4, 6 and 8. Since both bending moment and axial force exist in the frame structure, we have to ensure that both of the tensile and compressive stresses at the edge of element ends should not exceed the allowable stress. Therefore, we increase the upper bound of cross-sectional area from 0.1 m^2, which is used in Ref. [144], to 0.2 m^2 such that the cross-sectional area does not reach the upper bound. The optimization problem to minimize the total structural volume $V(\boldsymbol{A},\boldsymbol{y})$ is formulated as follows:

$$
\begin{aligned}
&\text{Minimize} \quad V(\boldsymbol{A},\boldsymbol{y}) \\
&\text{subject to} \quad \delta_i(\boldsymbol{A},\boldsymbol{y}) \le \delta_{\mathrm{U}}, \quad i=2,3,\ldots,12,14 \\
&\quad \begin{cases} \sigma_l^{\text{max-t}}(\boldsymbol{A},\boldsymbol{y}) \le \sigma_{\mathrm{t,U}} \\ \sigma_l^{\text{max-c}}(\boldsymbol{A},\boldsymbol{y}) \le \sigma_{\mathrm{c,U}} \end{cases}, \\
&\quad \underline{A} \le A_l \le \overline{A}, \quad l=1,2,\ldots,16 \\
&\quad \underline{y} \le y_j \le \overline{y}, \quad j=2,4,6,8
\end{aligned}
\tag{4.18}
$$

where $\delta_i(\boldsymbol{A},\boldsymbol{y})$ is the downward displacement of node i, and $\delta_{\mathrm{U}}=0.1$ m is its upper bound; $\sigma_l^{\text{max-t}}(\boldsymbol{A},\boldsymbol{y})$ and $\sigma_l^{\text{max-c}}(\boldsymbol{A},\boldsymbol{y})$ represent the maximum tension and compressive edge stresses (>0) of lth element; $\sigma_{\mathrm{t,U}}=1.30\times10^{8}$ Pa and $\sigma_{\mathrm{c,U}}=1.04\times10^{8}$ Pa are the upper bounds of edge stress in tension and compression, respectively. Bounds for the design variables are $\underline{y}=2$ m, $\overline{y}=8$ m, $\overline{A}=0.2$ m^2 and $\underline{A}=1.0\times10^{-7}$ m^2.

Problem (4.18) is solved by GA, and the optimal solution is shown in Fig. 4-17(a). The structural volume is 5.42 m^3, which is about 6.4% larger than the result in Ref. [144]. The main reason is that the truss structure has only axial force and the element is either under uniaxial tension or compression. On the other hand, the edge stresses of frame element consists of bending stress and uniaxial tensile or compressive stress, which are illustrated in Fig. 4-18, and the cross-sectional area need to be larger than that of the truss element in order not to violate the stress constraints, leading to a little increase of the total structural volume.

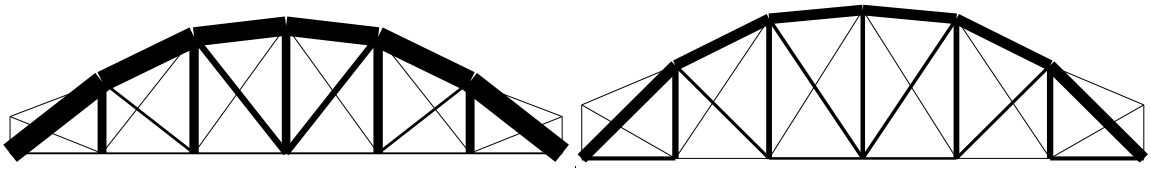

(a) (b)

Fig. 4-17 Optimal solutions of Example 3: (a) problem (4.18); (b) problem (4.19)

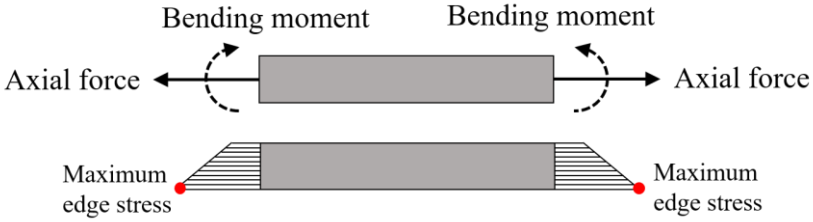

Fig. 4-18 Illustration of internal force and maximum edge stress of beam element

Next, we select Young's modulus of each element and x- and y-coordinates of nodes 2, 4, 6, 8, 10, 12 and 14 as uncertain parameters, and minimize the maximum stress under volume constraint. The initial structure is the same as shown in Fig. 4-16 and design variables are $\boldsymbol{A}=(A_1,A_2,\ldots,A_{16})$ and $\boldsymbol{y}=(y_2,y_4,y_6,y_8)$. Based on Eq. (4.9) and the parameter values listed in Table 4-5, the optimization problem without uncertainty is formulated as follows:

$$\begin{aligned}
&\text{Minimize} \quad \sigma^{\max} = \max_{i=1,2,\ldots,16} \sigma_i^{\max}\left(\boldsymbol{A}, \boldsymbol{y}\right) \\
&\text{subject to} \quad V\left(\boldsymbol{A}, \boldsymbol{y}\right) \le \bar{V} \\
&\qquad\qquad \underline{A} \le A_l \le \bar{A}, \;\; l = 1, 2, \ldots, 16; \\
&\qquad\qquad \underline{y} \le y_j \le \bar{y}, \;\; j = 2, 4, 6, 8
\end{aligned} \tag{4.19}$$

Problem (4.19) is solved using GA, and the optimal solution is shown in Fig. 4-17(b). Then based on the optimal shape in Fig. 4-17(b), we choose the cross-sectional areas as design variables and consider the variation in uncertain parameters. The multi-objective optimization problem reads

$$\begin{aligned}
&\text{Minimize} \quad \sigma^{\max}\left(\boldsymbol{A}\right), \; \sigma_{1:200}^{\max}\left(\boldsymbol{A};\boldsymbol{\theta}\right), \; \sigma_{50:200}^{\max}\left(\boldsymbol{A};\boldsymbol{\theta}\right), \; \sigma_{100:200}^{\max}\left(\boldsymbol{A};\boldsymbol{\theta}\right) \\
&\text{subject to} \quad V\left(\boldsymbol{A}\right) \le \bar{V}; \\
&\qquad\qquad \underline{A} \le A_l \le \bar{A}, \;\; l = 1, 2, \ldots, 16
\end{aligned} \tag{4.20}$$

As a result of optimization, the 200 solutions converged to a set of 70 different Pareto optimal solutions, and the total computational efforts for solving problems (4.19) and (4.20), including the iteration steps, number of function analyses and computation time, are listed in Table 4-13. Since FEA can be avoided if the individuals in the current population have appeared in the previous iterations and thus computational efforts can be saved, the following criterion is adopted to determine whether the analysis for the current individual is needed or not:

$$\frac{\left\|\boldsymbol{p}_1 - \boldsymbol{p}_i\right\|}{\left\|\boldsymbol{p}_i\right\|} \le 0.001, \;\; i = 1, 2, \ldots, n_{\mathrm{a}} \tag{4.21}$$

where $\boldsymbol{p}_1$ is the current individual to be evaluated, $\boldsymbol{p}_i$ is the individual that has appeared before and n_{a} is the number of individuals that have appeared before without duplication. By using Eq. (4.21) the number of analyses for solving problems (4.19) and (4.20) without duplication can be obtained as listed in Table 4-13. Note that the computation time is calculated for the total number of analyses.

Table 4-13 Computational efforts of Examples 1 to 4

Example	Iteration steps	Number of analyses	Number of analyses without duplication	Computation time
1	798	600,150 (problem 4.8)	--	3201.61 sec
2	1806	1,357,650 (problem 4.8)	--	5450.08 sec
3	621	400,200 (problem 4.19) 7,880,000 (problem 4.20)	45,533 (problem 4.19) 4,345,000 (problem 4.20)	4243.78 sec
4	951	115,600 (problem 4.23) 15,320,000 (problem 4.24)	37,605 (problem 4.23) 11,302,600 (problem 4.24)	5782.27 sec

The Pareto optimal solutions at different steps are plotted in Figs. 4-19, 4-20 and 4-21, respectively, in the planes of $\sigma^{\max}$ and one of $\sigma_{1:200}^{\max}$, $\sigma_{50:200}^{\max}$ and $\sigma_{100:200}^{\max}$, where the solutions on the Pareto front are denoted by PF followed by the step number in the parentheses. It can be observed from Fig. 4-

19(a) that the Pareto front is generated with good accuracy after step 30, and the optimal value of $\sigma^{\max}$ remains the same due to the addition of optimal solution of problem (4.19) into the initial population of problem (4.20). Figure 4-19(b) plots the detailed view of the Pareto optimal solutions and their corresponding trade-off relationships. We can see that the variation of $\sigma^{\max}_{1:200}$ at the Pareto front is greater than that of $\sigma^{\max}$. The same conclusions can be drawn from Figs. 4-20 and 4-21.

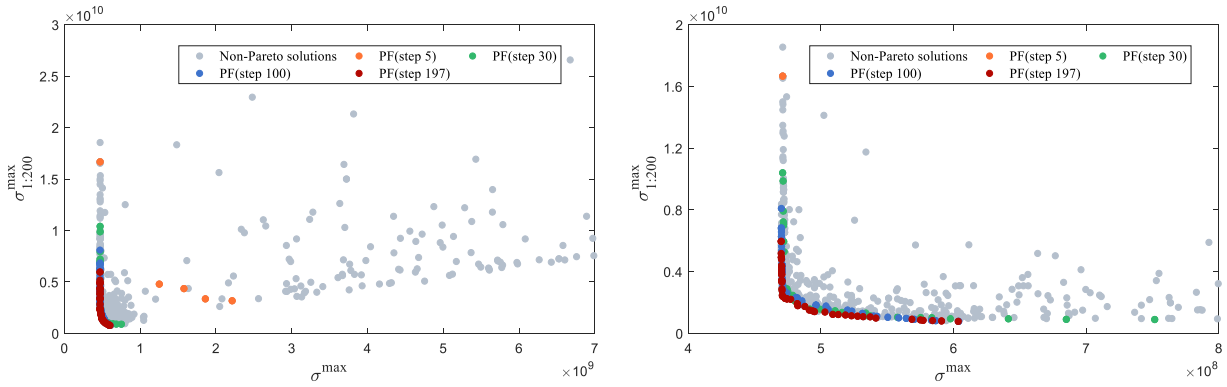

(a) (b)

Fig. 4-19 Stepwise Pareto front of objectives $\sigma^{\max}$ and $\sigma^{\max}_{1:200}$: (a) Overall review; (b) Detailed view

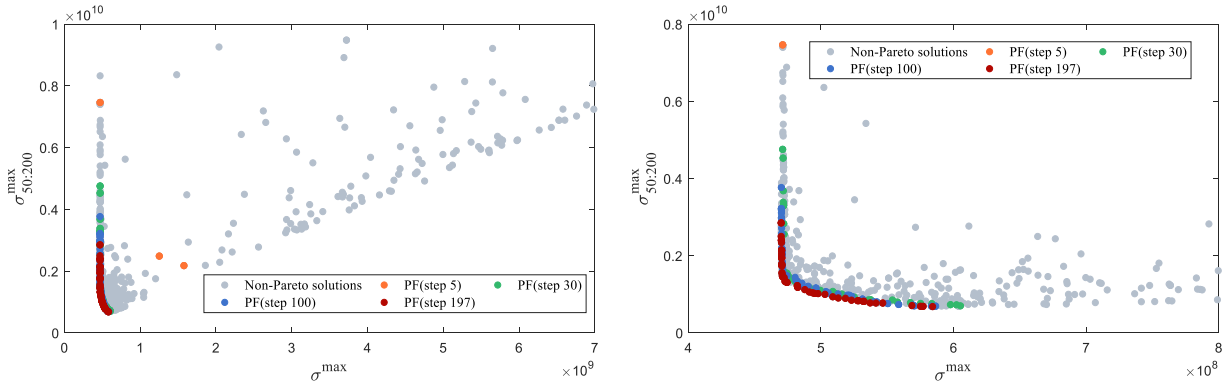

(a) (b)

Fig. 4-20 Stepwise Pareto front of objectives $\sigma^{\max}$ and $\sigma^{\max}_{50:200}$: (a) Overall review; (b) Detailed view

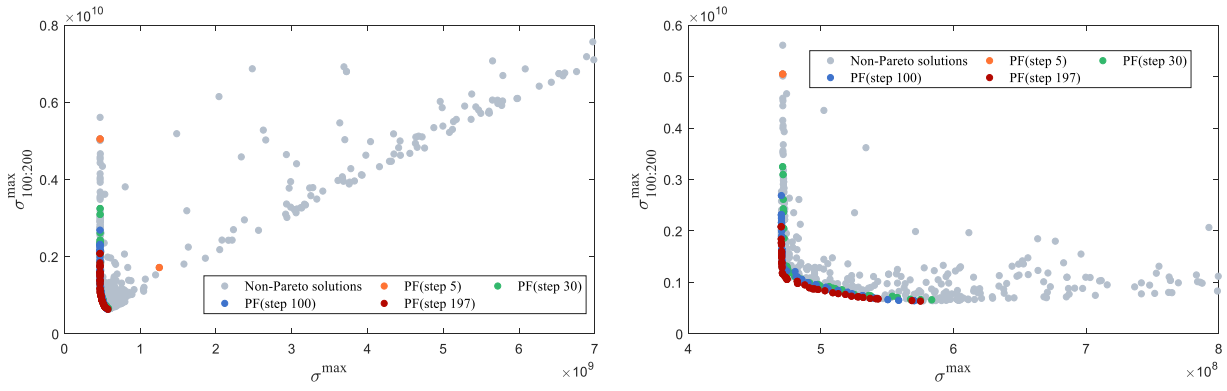

(a) (b)

Fig. 4-21 Stepwise Pareto front of objectives $\sigma^{\max}$ and $\sigma^{\max}_{100:200}$: (a) Overall review; (b) Detailed view

Table 4-14 Objective values and structural volume of solutions A, B, C and D of problem (4.21) in Example 3 before removing thin elements

Solution	$\sigma^{\max}$ (Pa)	$\sigma^{\max}_{1:200}$ (Pa)	$\sigma^{\max}_{50:200}$ (Pa)	$\sigma^{\max}_{100:200}$ (Pa)	V (m^3)
A	4.7001×10^{8}	5.9733×10^{9}	2.8549×10^{9}	2.0861×10^{9}	1.0
B	6.0353×10^{8}	7.7531×10^{8}	6.9560×10^{8}	6.5546×10^{8}	1.0
C	5.8417×10^{8}	8.2934×10^{8}	6.8127×10^{8}	6.4418×10^{8}	1.0
D	5.7499×10^{8}	8.7466×10^{8}	6.9079×10^{8}	6.3814×10^{8}	1.0

Table 4-15 Objective values and structural volume of solutions A, B, C and D of problem (4.21) in Example 3 after removing thin elements

Solution	$\sigma^{\max}$ (Pa)	$\sigma^{\max}_{1:200}$ (Pa)	$\sigma^{\max}_{50:200}$ (Pa)	$\sigma^{\max}_{100:200}$ (Pa)	V (m^3)
A	4.7080×10^{8}	1.7213×10^{10}	7.3785×10^{9}	4.1258×10^{9}	1.0
B	6.0929×10^{8}	7.7872×10^{8}	6.9805×10^{8}	6.6848×10^{8}	1.0
C	5.8482×10^{8}	8.3908×10^{8}	6.8469×10^{8}	6.4775×10^{8}	1.0
D	5.8070×10^{8}	8.8895×10^{8}	6.9200×10^{8}	6.4595×10^{8}	1.0

The Pareto optimal solutions that have the smallest values of $\sigma^{\max}$, $\sigma^{\max}_{1:200}$, $\sigma^{\max}_{50:200}$ and $\sigma^{\max}_{100:200}$, respectively, are denoted by solutions A, B, C and D, and shown in Fig. 4-22. The maximum edge stress of each element, which is calculated without considering uncertainty, are also depicted. Note that the thin elements, whose cross-sectional areas are less than 0.0001 m^2, are removed from the optimal solutions in Fig. 4-22, and their objective values before and after removing the thin

elements are listed in Tables 4-14 and 4-15, respectively, together with their structural volume. The distribution of cross-sectional areas are plotted in Fig. 4-23.

We can see from Fig. 4-22 and Tables 4-14 and 4-15 that solution A has obviously large values of objective functions $\sigma_{1:200}^{\max}$, $\sigma_{50:200}^{\max}$ and $\sigma_{100:200}^{\max}$. Solution B has the minimum value of $\sigma_{1:200}^{\max}$ and some of the elements, which do not exist in solution A, have moderately large cross-sectional areas to reduce the effect of uncertainties in Young's modulus and nodal locations, resulting in a large stiffness of the frame.

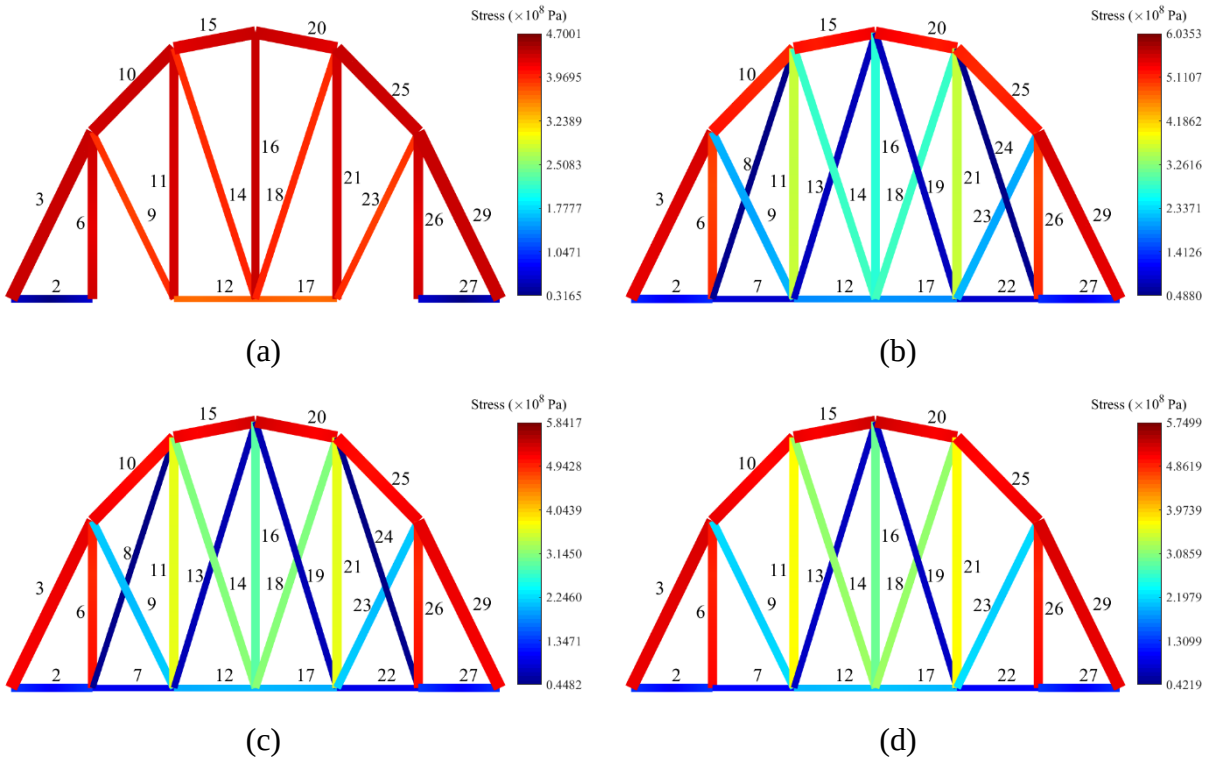

Fig. 4-22 Pareto optimal solutions of problem (4.20): (a) Solution A; (b) Solution B; (c) Solution C; (d) Solution D

Moreover, as seen from Tables 4-14 and 4-15, the objective values of solutions B, C, and D as well as the objective value of $\sigma^{\max}$ in solution A before and after removing thin elements are very close. However, the objective values of $\sigma_{1:200}^{\max}$, $\sigma_{50:200}^{\max}$ and $\sigma_{100:200}^{\max}$ in solution A after removing thin elements are greater than those before removal. This is mainly because although solution A has the minimum value of $\sigma^{\max}$ among 70 Pareto optimal solutions, it is unstable if bending stiffness is very small and become worse when the thin elements are removed, making it more sensitive to the uncertainties. Thus, its maximum stress increases rapidly as deformation becomes asymmetric.

It is confirmed that solutions C and D have the smallest values of $\sigma_{50:200}^{\max}$ and $\sigma_{100:200}^{\max}$, respectively, and elements 8 and 24 are removed in solution D. We can also observe from Tables 4-14 and 4-15 that the nominal objective value $\sigma^{\max}$ decreases as order *k* is increased. However, the solutions A and D that minimize the nominal and median values are very different, indicating that a small asymmetric property leads to a large increase of the maximum stress, and accordingly leads to a significant difference in the optimal solutions. By contrast, the extreme value $\sigma_{1:200}^{\max}$ increases as order *k* is increased. However, the increase is not very significant. The cross-sectional areas of solutions B, C and D have similar distribution as shown in Fig. 4-23.

Solutions A, B, C and D have the same structural volume of 1.0 m^3; however, they have different distributions of cross-sectional areas after solving problem (4.20), leading to different performances on minimizing the maximum stress. Furthermore, it can be seen that none of these four solutions has the minimum values for any of the two objectives, indicating that the optimal solution may vary with robustness level, and the designers can appropriately choose the optimal solution according to the various robustness levels.

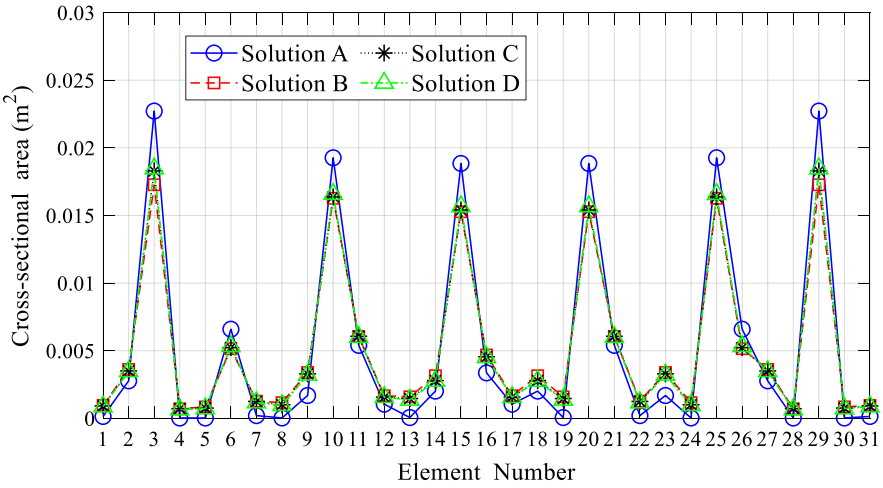

Fig. 4-23 Distribution of cross-sectional areas of solutions A, B, C and D of problem (4.20) in Example 3

Moreover, in order to further investigate the effect of relaxing worst value of the structural response on the optimal solution, the worst value is approximated by order statistic with a larger confidence level $\alpha_k = 0.99$ and $\beta = 0.99$. In this case, the minimum sample size that the worst sample (i.e., *k*=1) satisfies $\alpha_k = 0.99$ and $\beta = 0.99$ is 459 according to the theory of distribution-free tolerance interval in Sections 2.3 and 4.2. The following optimization problem is formulated and solved by GA with the same parameter values as in problem (4.19):

$$\begin{aligned} &\text{Minimize} \quad \sigma_{1:459}^{\max}\left(\boldsymbol{A};\boldsymbol{\theta}\right) \\ &\text{subject to} \quad V\left(\boldsymbol{A}\right) \le \bar{V}; \\ &\qquad\qquad \underline{A} \le A_l \le \bar{A}, \quad l = 1,2,\ldots,16 \end{aligned} \tag{4.22}$$

The optimal solution of problem (4.22) is shown in Fig. 4-24, where the maximum stress for each element is calculated without considering uncertainty. The optimal value of $\sigma_{1:459}^{\max}$ is 7.9923 $\times 10^8$ Pa, which is a little larger than the objective value of $\sigma_{1:200}^{\max}$ of Solution B due to the trade-off relationship between robustness level and minimizing the maximum stress. Note that the value of β for $\sigma_{1:200}^{\max}$ at confidence level $\alpha_k = 0.99$ is 0.977. Compared to solution B in Fig. 4-22(b), it can be seen that the cross-sectional areas of elements 1, 4, 5, 28, 30 and 31, which do not exist in solution B, have moderately large values in Fig. 4-24 to reduce the extreme worst value, resulting in different performance on minimizing the maximum stress in the structure. Since the extreme worst case is a rare event and it may cost more to build a structure which satisfies the requirement of large worst value of maximum stress, we relax the worst value to some extent and assign the sample size m_s=200 so that the computational effort will also be saved.

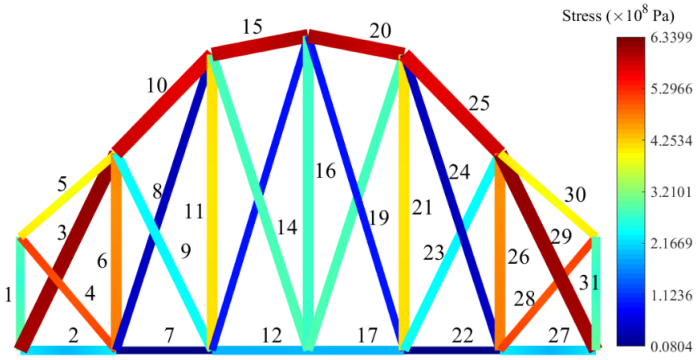

Fig. 4-24 Optimal solution of problem (4.22)

4.5.5 Example 4: multi-objective problem formulation in 4.3.2

Example 4 involves a 4×1 grid with 10 nodes and 21 elements, and the initial structure is shown in Fig. 4-25(a). The structure is pin-supported at nodes 1 and 9, and a downward vertical load F with magnitude of 100 N is applied at node 5. The design variables are the cross-sectional areas of elements 1 to 11 $\boldsymbol{A}=\left(A_1, A_2, \ldots A_{11}\right)$ incorporating symmetry of the structure, and the uncertain parameters are Young's modulus of each element and x- and y-coordinates of nodes 2, 3, 4, 6, 7, 8 and 10.

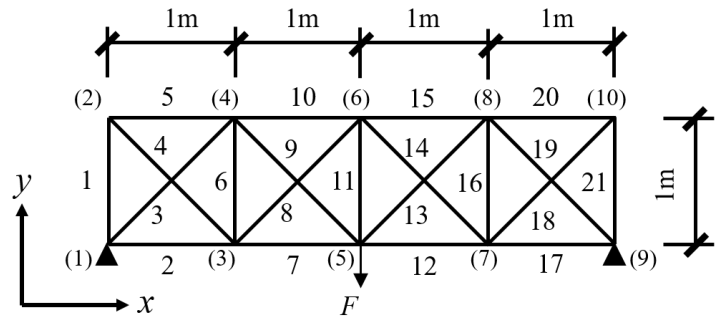

(a)

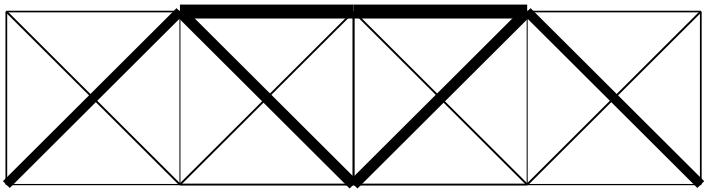

(b)

Fig. 4-25 (a) Initial ground structure of Example 4; (b) Optimal solution of problem (4.23)

First, based on Eq. (4.9), the following single objective optimization problem to minimize the maximum stress is solved

$$\begin{aligned} &\text{Minimize } \sigma^{\max} = \max_{i=1,2,\ldots,11} \sigma_i^{\max}(\boldsymbol{A}) \\ &\text{subject to } V(\boldsymbol{A}) \le \bar{V}; \\ &\qquad \underline{A} \le A_l \le \bar{A},\ l = 1,2,\ldots,11 \end{aligned} \tag{4.23}$$

In a similar manner as Example 3, based on the optimal solution of problem (4.23), we formulate the following multi-objective optimization problem:

$$\begin{aligned} &\text{Minimize } \sigma^{\max}(\boldsymbol{A}),\ \sigma_{1:200}^{\max}(\boldsymbol{A};\boldsymbol{\theta}),\ \sigma_{50:200}^{\max}(\boldsymbol{A};\boldsymbol{\theta}),\ \sigma_{100:200}^{\max}(\boldsymbol{A};\boldsymbol{\theta}) \\ &\text{subject to } V(\boldsymbol{A}) \le \bar{V}; \\ &\qquad \underline{A} \le A_l \le \bar{A},\ l = 1,2,\ldots,11 \end{aligned} \tag{4.24}$$

The optimal solution of problem (4.23) using the parameter values in Table 4-5 is shown in Fig. 4-25(b), and the four solutions A, B, C and D from the 70 Pareto optimal solutions of problem (4.24), which have the minimum objective values of $\sigma^{\max}$, $\sigma_{1:200}^{\max}$, $\sigma_{50:200}^{\max}$ and $\sigma_{100:200}^{\max}$, respectively, are presented in Fig. 4-26, together with the corresponding maximum edge stress obtained without considering uncertainty. The computational efforts for solving problems (4.23) and (4.24) are also listed in Table 4-13. The elements with cross-sectional areas less than 0.0001 m^2 have been removed from Fig. 4-26, and the distribution of cross-sectional areas are plotted in Fig. 4-27. As

seen from Figs. 4-26 and 4-27, although solutions B, C and D have the same structural topology, their distributions of cross-sectional areas are not exactly the same.

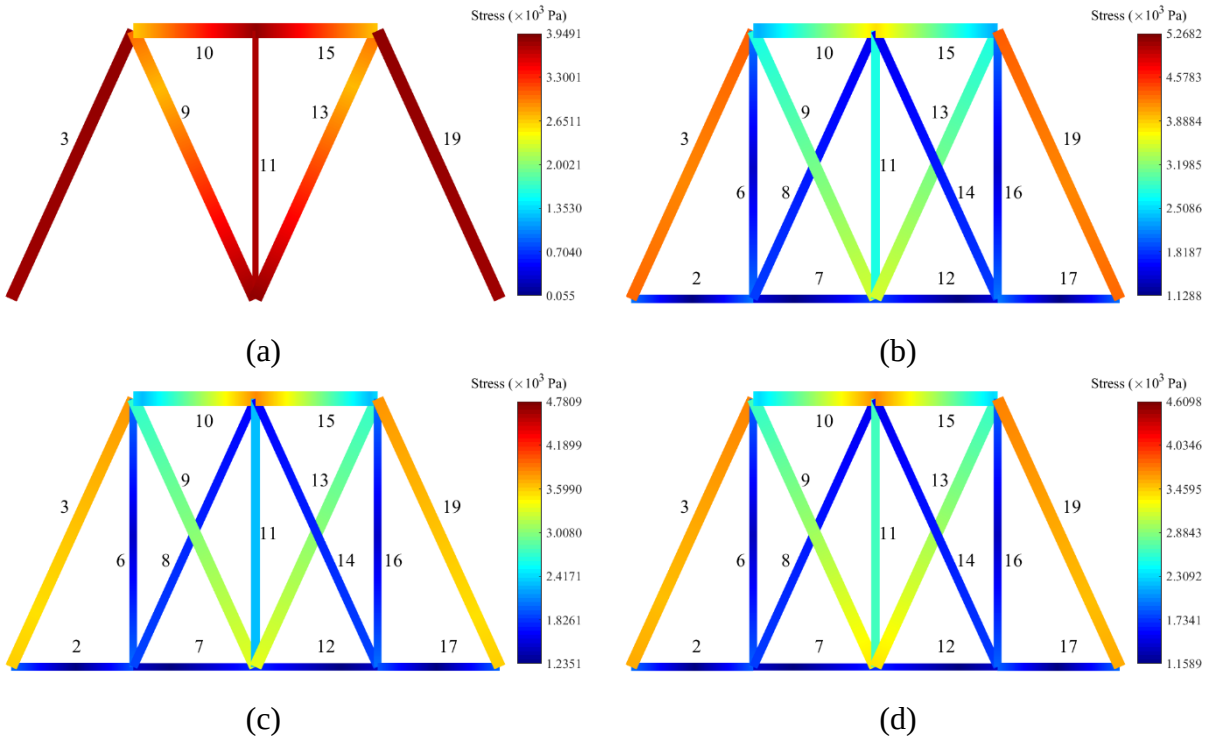

Fig. 4-26 Pareto optimal solutions of problem (4.24): (a) Solution A; (b) Solution B; (c) Solution C; (d) Solution D

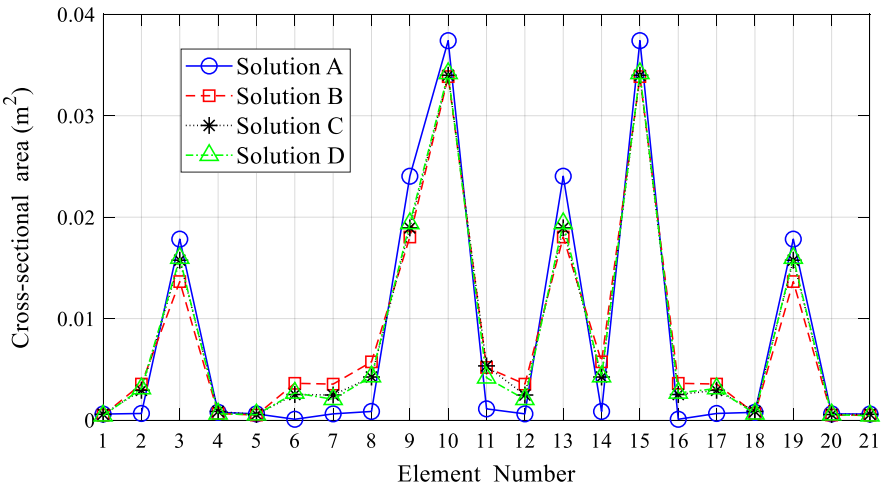

Fig. 4-27 Distribution of cross-sectional areas of solutions A, B, C and D of problem (4.24) in Example 4

Table 4-16 Objective value and structural volume of solutions A, B, C and D of problem (4.24) in Example 4 before removing thin elements

Solution	$\sigma^{\max}$ (Pa)	$\sigma^{\max}_{1:200}$ (Pa)	$\sigma^{\max}_{50:200}$ (Pa)	$\sigma^{\max}_{100:200}$ (Pa)	V (m^3)
A	3949.13	15475.38	9526.87	7193.64	0.2
B	5268.16	6618.92	5984.07	5615.98	0.2
C	4780.90	6998.41	5742.66	5268.61	0.2
D	4609.75	7091.41	5842.31	5178.45	0.2

Based on Eq. (4.15), we further formulate the following optimization problem by using trimmed means as objective functions:

$$\begin{aligned} &\text{Minimize } \sigma^{\max}(\boldsymbol{A}),\ \hat{\sigma}^{\max}_{2:200}(\boldsymbol{A};\boldsymbol{\theta}),\ \hat{\sigma}^{\max}_{50:200}(\boldsymbol{A};\boldsymbol{\theta}),\ \hat{\sigma}^{\max}_{100:200}(\boldsymbol{A};\boldsymbol{\theta}) \\ &\text{subject to } V(\boldsymbol{A}) \le \bar{V}; \\ &\qquad \underline{A} \le A_l \le \bar{A},\ \ l = 1,2,\ldots,11 \end{aligned} \tag{4.25}$$

where

$$\hat{\sigma}^{\max}_{k:200}(\boldsymbol{A};\boldsymbol{\theta}) = \frac{1}{3}\left(\sigma^{\max}_{k-1:200} + \sigma^{\max}_{k:200} + \sigma^{\max}_{k+1:200}\right),\ \ k = 2,50,100 \tag{4.26}$$

Note that the arguments $\boldsymbol{A}$ and $\boldsymbol{\theta}$ of order statistics in the right-hand side of Eq. (4.26) have been omitted for brevity. After solving problem (4.25), we select four solutions A*, B*, C* and D* among the Pareto optimal solutions which have the smallest objective values of $\sigma^{\max}$, $\hat{\sigma}^{\max}_{2:200}$, $\hat{\sigma}^{\max}_{50:200}$ and $\hat{\sigma}^{\max}_{100:200}$, respectively. These solutions and the corresponding distributions of cross-sectional areas are plotted in Figs. 4-28 and 4-29, respectively. Compared to the results obtained by solving problem (4.24), we can see that although solutions A*, B*, C* and D* are not exactly the same as solutions A, B, C and D, respectively, they have similar shapes and topologies after removing thin elements with cross-sectional areas less than 0.0001 m^2. Their distributions of cross-sectional areas are also close, demonstrating that multi-objective optimization problems (4.24) and (4.25) would lead to similar structures. We list the objective values and structural volumes of solutions A*, B*, C* and D* before removing thin elements in Table 4-17, and the conclusions drawn from Table 4-16 can also apply for Table 4-17.

Table 4-17 Objective values and structural volume of solutions A*, B*, C* and D* of problem (4.25) in Example 4 before thin elements

Solution	$\sigma^{\max}$ (Pa)	$\hat{\sigma}^{\max}_{2:200}$ (Pa)	$\hat{\sigma}^{\max}_{50:200}$ (Pa)	$\hat{\sigma}^{\max}_{100:200}$ (Pa)	V (m^3)
A*	3962.36	14762.3	9432.21	7155.88	0.2
B*	5150.72	6572.23	5925.88	5504.99	0.2
C*	4790.73	6820.37	5700.54	5255.23	0.2
D*	4580.95	6981.48	5842.58	5180.97	0.2

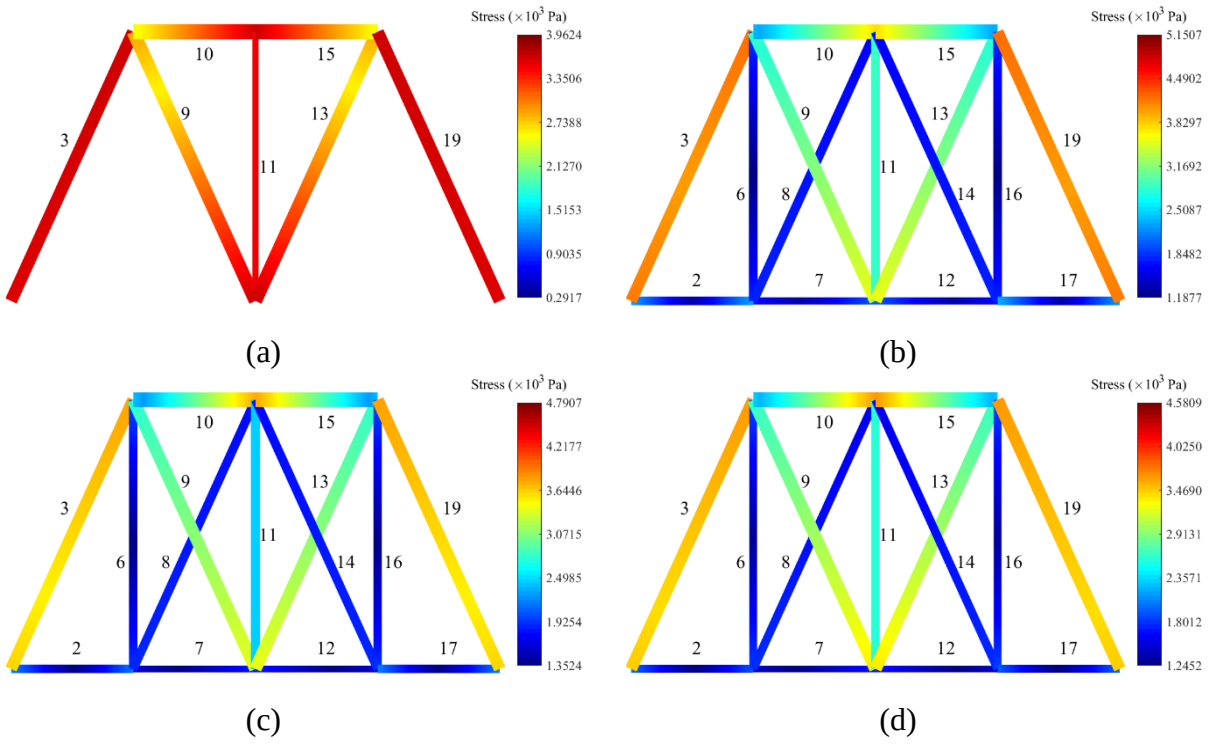

Fig. 4-28 Pareto optimal solutions of problem (4.25): (a) Solution A*; (b) Solution B*; (c) Solution C*; (d) Solution D*

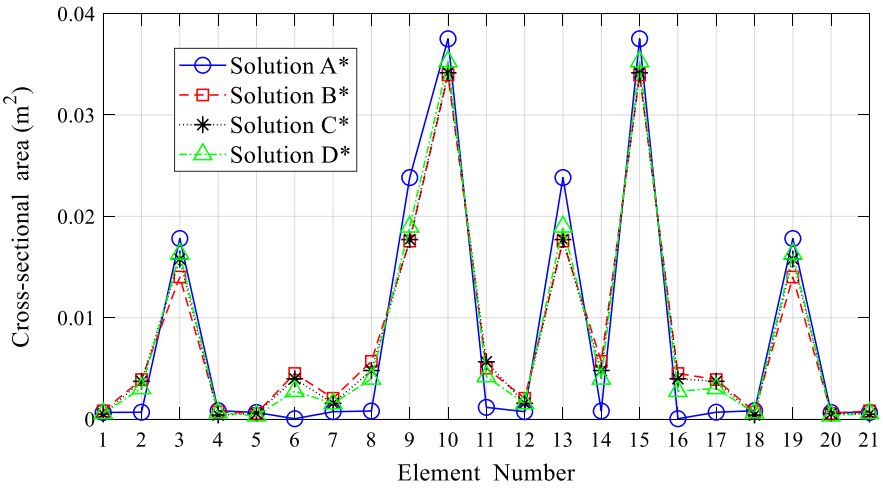

Fig. 4-29 Distribution of cross-sectional areas of solution A*, B*, C* and D* of problem (4.25) in Example 4

Based on the solutions of problems (4.24) and (4.25), we further investigate the variations of solutions A, B, C, D and A*, B*, C*, D*, respectively. 2000 random seeds are used to generate 2000 groups of 200 samples for $\boldsymbol{\theta} = (\Delta \boldsymbol{x}, \Delta \boldsymbol{y}, \Delta \boldsymbol{E})$, and the mean values and standard deviations of the objective functions $\sigma^{\max}$, $\sigma^{\max}_{1:200}$, $\sigma^{\max}_{50:200}$, $\sigma^{\max}_{100:200}$ and $\sigma^{\max}$, $\hat{\sigma}^{\max}_{2:200}$, $\hat{\sigma}^{\max}_{50:200}$, $\hat{\sigma}^{\max}_{100:200}$ are listed in

Tables 4-18 and 4-19, respectively. It can be observed from Table 4-18 that the standard deviation of $\sigma^{\max}$ for each deterministic solution is 0, and the corresponding mean values are the same as those listed in Table 4-16. Besides, solutions A, B, C and D have the smallest mean value of objective functions $\sigma^{\max}$, $\sigma^{\max}_{1:200}$, $\sigma^{\max}_{50:200}$ and $\sigma^{\max}_{100:200}$, respectively, which confirms the accuracy of optimization process. It is worth noting that solution B has the largest standard deviation of $\sigma^{\max}_{1:200}$ among all the objective functions and at the same time has the smallest standard deviation of $\sigma^{\max}_{1:200}$ among all the four solutions, and the standard deviation of $\sigma^{\max}_{1:200}$ for solution B is larger than the standard deviations of $\sigma^{\max}_{50:200}$ and $\sigma^{\max}_{100:200}$ for solutions C and D, respectively. This verifies that the extreme value corresponding to $k = 1$ has more variation than the order statistics with larger values of k.

The same conclusion can be drawn from Table 4-19 for solutions A*, B*, C* and D* and objective functions $\sigma^{\max}$, $\hat{\sigma}^{\max}_{2:200}$, $\hat{\sigma}^{\max}_{50:200}$ and $\hat{\sigma}^{\max}_{100:200}$. Comparison between Tables 4-18 and 4-19 shows that the standard deviations of $\hat{\sigma}^{\max}_{2:200}$ for solution B*, $\hat{\sigma}^{\max}_{50:200}$ for solution C* and $\hat{\sigma}^{\max}_{100:200}$ for solution D* are smaller than those of $\sigma^{\max}_{1:200}$ for solution B, $\sigma^{\max}_{50:200}$ for solution C and $\sigma^{\max}_{100:200}$ for solution D, respectively, indicating that the robust optimization using trimmed means as objective functions will lead to solutions which are less sensitive to the uncertain parameters.

Table 4-18 Mean value (Pa) and standard deviation (Pa) of objective values of solutions A, B, C and D of problem (4.24) in Example 4

Solution	A		B		C		D	
Variation	Mean	Std. Dev.	Mean	Std. Dev.	Mean	Std. Dev.	Mean	Std. Dev.
$\sigma^{\max}$	3949.13	0	5268.16	0	4780.91	0	4609.75	0
$\sigma^{\max}_{1:200}$	15585.87	878.94	7018.64	206.94	7447.45	248.3	7495.61	251.74
$\sigma^{\max}_{50:200}$	9344.63	288.23	5923.11	44.57	5757.67	86.42	5817.05	87.49
$\sigma^{\max}_{100:200}$	7457.03	226.38	5646.81	32.03	5251.68	63.66	5218.24	58.97

Table 4-19 Mean value (Pa) and standard deviation (Pa) of objective values of solutions A*, B*, C* and D* of problem (4.25) in Example 4

Solution	A*		B*		C*		D*	
Variation	Mean	Std. Dev.	Mean	Std. Dev.	Mean	Std. Dev.	Mean	Std. Dev.
$\sigma^{\max}$	3962.36	0	5150.72	0	4790.73	0	4580.94	0
$\hat{\sigma}^{\max}_{2:200}$	14842.48	674.77	6877.83	150.88	7094.47	168.92	7320.2	184.88
$\hat{\sigma}^{\max}_{50:200}$	9274.31	291.96	5841.14	50.08	5701.11	79.4	5812.24	88.97
$\hat{\sigma}^{\max}_{100:200}$	7368.72	226.08	5532.99	34.3	5229.55	65.68	5206.35	53.4

In order to compare the convergence properties of the optimization process, we solve problems (4.24) and (4.25), respectively, 10 times with different random seeds. From each trial we can obtain the sets of solutions A, B, C, D and A*, B*, C* and D* which have the smallest values of the corresponding four objective functions, respectively, among the Pareto optimal solutions. Then we calculate the mean value, standard deviation, and maximum and minimum values of these solution sets as listed in Table 4-20. It can be observed that for $\sigma^{\max}$ the difference of the statistical information between the two solution sets is very small. This is because the optimal solution of problem (4.23) is added into the initial population of both problems (4.24) and (4.25). By contrast, the standard deviations of $\sigma_{1:200}^{\max}$, $\sigma_{50:200}^{\max}$ and $\sigma_{100:200}^{\max}$ are larger than those of $\hat{\sigma}_{2:200}^{\max}$, $\hat{\sigma}_{50:200}^{\max}$ and $\hat{\sigma}_{100:200}^{\max}$, respectively. This is mainly because the trimmed means are less sensitive to the outliers in the samples and can be referred as a robust estimator of quantile structural response. Therefore, the multi-objective optimization problem (4.25) is more stable than those of problem (4.24) due to the smoothness of the objective functions during the optimization process.

Table 4-20 Statistical information of problems (4.24) and (4.25) in Example 4

Solution set	Problem (4.24)				Problem (4.25)			
Objective	$\sigma^{\max}$	$\sigma_{1:200}^{\max}$	$\sigma_{50:200}^{\max}$	$\sigma_{100:200}^{\max}$	$\sigma^{\max}$	$\hat{\sigma}_{2:200}^{\max}$	$\hat{\sigma}_{50:200}^{\max}$	$\hat{\sigma}_{100:200}^{\max}$
Max. (Pa)	3971.81	7255.42	5813.48	5219.33	3969.66	7056.81	5815.25	5203.84
Min. (Pa)	3949.13	6618.92	5555.50	5039.94	3948.07	6565.64	5611.88	5067.77
Mean (Pa)	3965.95	6904.60	5696.22	5144.06	3965.49	6742.10	5699.17	5138.22
Std. Dev. (Pa)	5.86	227.70	70.56	50.37	5.67	162.50	60.67	46.38

4.6 Conclusions

In this chapter a worst case approach is proposed for RSO of plane frame structures. To avoid large computational cost, the worst structural response is represented by the quantile response, and uncertainties are modeled by random variations without any assumption on their distribution information. Based on the theory of distribution-free one-side tolerance interval, order statistic is used for approximation of the quantile response and defining the robustness level. Robustness is indicated by the order *k* with specified sample size and confidence level. With this definition of structural robustness, two kinds of RSO problem formulations are presented, one is a robust simultaneous shape and topology optimization of plane frames under volume and global stability constraints, and the other is a multi-objective robust shape and topology optimization of plane frames under volume constraint, in which the order statistics or trimmed means with various orders serve as objectives to obtain solutions with different robustness levels. For each problem formulations two kinds of numerical examples are investigated to illustrate the effectiveness of the proposed method, and the conclusions are drawn as follows:

(1) For the optimization with global stability constraint, the problem is converted into an RSO problem with semi-infinite constraints, and a numerical penalization method is used to alleviate

the singularity phenomenon, whose effectiveness is confirmed by a simple example to minimize the maximum stress without considering uncertainty.

(2) It is shown that solutions of deterministic and robust optimization problems have different shapes and topologies. While the solution of robust optimization contains some elements which are not effective to minimize the stress without considering uncertainty, those elements are helpful to reduce the worst value of stress and increase the global linear buckling load factor, resulting in a structure less sensitive to the uncertainty.

(3) Unexpectedly large stress in the short member should be neglected during the optimization procedure to provide an accurate stress to be minimized. The numerical results confirm that the differences of the solutions before and after further modification are sufficiently small.

(4) For multi-objective optimization the values of order k of order statistics and trimmed means are selected in accordance with the maximum, quartile, and median structural responses, and they are served as multiple objectives, together with the one without considering uncertainty. It is shown that some elements have increased their cross-sectional areas after robust optimization, while they have little contribution to the reduction of stresses of optimal solution without considering uncertainty.

(5) The solutions obtained by using trimmed means have smaller standard deviations than those obtained by using simple order statics. In addition, comparison of results obtained from 10 different random seeds shows that multi-objective optimization procedure with trimmed means is more stable than the one with order statistics, indicating that trimmed means is less sensitive to the outliers in the samples and referred to a better indicator of the structure robustness.

(6) However, the computational effort is relatively intensive since m_s analyses are needed to calculate the objective and constraint values every time, and the computational time could be long when eigenvalue analysis is included as shown in Table 4-13. With regard to the application to real engineering problem, surrogate model and other truncated approximation could be used to replace the FEA to improve the efficiency when it is time consuming.

Chapter 5

Reliability-based optimization

5.1 Brief introduction

Chapter 5 is to present a quantile-based SORA method for RBSO of plane frames, in which the reliability of constraints are estimated using L-moments, and a brief introduction is given as follows.

In Section 5.2, the framework of quantile-based SORA is presented, which is formulated based on the equivalence between reliability constraint and the quantile of structural response. The optimal solution of original RBSO problem is asymptotically obtained by solving a series of deterministic optimization problems by shifting the limits of constraints, and a reduction coefficient is introduced to avoid drastic shifting between two consecutive iterations. Moreover, a stopping criteria is also proposed to prevent obtaining an excessively conservative result.

In Section 5.3, the details of quantile estimation using L-moments are given. The quantile function is obtained by integrating the corresponding density-quantile function, which is estimated using MEM subject to sample L-moment constraints. The original constrained MEM problem is first transformed to Lagrangian functional, and then the values of unknown Lagrangian multipliers are found by solving another unconstrained convex optimization problem.

In Section 5.4, two kinds of quantile-based SORA problem formulations are presented. One is to minimize the structural volume under nodal displacement constraints, and the other is to minimize the structural volume under both displacement and global stability constraints. A penalization method using approximated Heaviside function is used to alleviate singularity phenomenon in global stability, and the corresponding formulations of sensitivity analysis are also derived.

In Section 5.5, four numerical examples are explored to demonstrate the effectiveness of the two methods proposed in Section 5.4, and the influence of global stability constraint on the optimal result is also investigated. Finally, some conclusions are drawn in Section 5.6.

5.2 Quantile-based SORA

Let $\boldsymbol{d}$ and $\boldsymbol{\theta}$ denote the vectors of design variables and random variables representing the uncertainties, respectively. The RBSO problem can be generally given as [18]

$$\begin{aligned} &\text{Miminize } W(\boldsymbol{d}) \\ &\text{subject to } \Pr\left\{g_j(\boldsymbol{d};\boldsymbol{\theta}) \le \bar{g}_j\right\} \ge R_j,\ j=1,2,\cdots,n_g; \\ &\qquad \underline{\boldsymbol{d}} \le \boldsymbol{d} \le \bar{\boldsymbol{d}} \end{aligned} \tag{5.1}$$

Where $W(\boldsymbol{d})$ is the objective function to be minimized; $g_j(\boldsymbol{d};\boldsymbol{\theta})$ is the *j*th performance function under uncertainty and n_g is the number of performance functions; $\bar{g}_j$ is the prescribed upper bound of $g_j(\boldsymbol{d};\boldsymbol{\theta})$; R_j is the target probability of R_j not to exceed $\bar{g}_j$; $\underline{\boldsymbol{d}}$ and $\bar{\boldsymbol{d}}$ are the vectors of lower and upper bounds for $\boldsymbol{d}$, respectively. Note that the vector of design variables $\boldsymbol{d}$ in problem (5.1) includes deterministic design variables and the mean values of random design variables.

Based on Eq. (5.1) and the equivalent description between the reliability constraint and the quantile of structural response [145], we define the n_g quantiles

$$Q_{R_j}(\boldsymbol{d};\boldsymbol{\theta}) = \inf\left\{Q : \Pr\left\{g_j(\boldsymbol{d};\boldsymbol{\theta}) \le Q\right\} \ge R_j\right\},\ j=1,2,\cdots,n_g \tag{5.2}$$

as alternatives for the n_g reliability constraints in problem (5.1), where $Q_{R_j}(\boldsymbol{d};\boldsymbol{\theta})$ is the *j*th quantile corresponding to the *j*th performance function $g_j(\boldsymbol{d};\boldsymbol{\theta})$ and target probability R_j. Then, we can rewrite the problem (5.1) in terms of quantiles as follows:

$$\begin{aligned} &\text{Miminize } W(\boldsymbol{d}) \\ &\text{subject to } Q_{R_j}(\boldsymbol{d};\boldsymbol{\theta}) \le \bar{g}_j,\ j=1,2,\cdots,n_g; \\ &\qquad \underline{\boldsymbol{d}} \le \boldsymbol{d} \le \bar{\boldsymbol{d}} \end{aligned} \tag{5.3}$$

It can be observed that the target values of n_g probabilities $R_j\left(j=1,2,\ldots,n_g\right)$ are now implicitly incorporated in problem (5.3) by the corresponding quantiles defined in Eq. (5.2), bridging the equivalence between problems (5.1) and (5.3) [145]. The random variables in problem (5.3) are assumed to be mutually independent. For general cases where some or all the random variables are correlated, they can be transformed into independent random variables by various methods like the well-known Rosenblatt or Nataf transformations [146][147] or other transformation methods without requiring the marginal PDF of each random variable [148]. Therefore, for simplicity the discussion of RBSO problem is limited to independent random variables.

According to the quantile-based SORA [93][94], the optimal solution of problem (5.3) can be obtained by solving a series of deterministic optimization problems where the upper bounds for

performance functions are shifted at each iteration to ensure that the quantile $Q_{R_j}\left(\boldsymbol{d};\boldsymbol{\theta}\right)$ is on the boundary. Denote the shifting value of $\overline{g}_j$ at the (k+1)th iteration as $\overline{c}_j^{k+1}$ which is calculated as

$$\overline{c}_j^{k+1} = Q_{R_j}\left(\boldsymbol{d}^k;\boldsymbol{\theta}\right) - g_j\left(\boldsymbol{d}^k\right),\ j=1,2,\cdots,n_g \tag{5.4}$$

Then the (k+1)th deterministic optimization problem of quantile-based SORA is formulated as

$$\begin{aligned} &\text{Miminize } W\left(\boldsymbol{d}\right) \\ &\text{subject to } g_j\left(\boldsymbol{d}\right) \le \overline{g}_j - \varepsilon_j \overline{c}_j^{k+1},\ j=1,2,\cdots,n_g; \\ &\qquad \underline{\boldsymbol{d}} \le \boldsymbol{d} \le \overline{\boldsymbol{d}} \end{aligned} \tag{5.5}$$

where in Eq. (5.4) $\boldsymbol{d}^k$ is the solution of problem (5.5) at the kth iteration, and $g_j\left(\boldsymbol{d}^k\right)$ is the value of jth performance function without uncertainty; $Q_{R_j}\left(\boldsymbol{d}^k;\boldsymbol{\theta}\right)$ represents the jth quantile corresponding to the solution $\boldsymbol{d}^k$ and random variables $\boldsymbol{\theta}$; the reduction coefficient ε_j is employed to avoid drastically shifting the boundaries determined as follows

$$\varepsilon_j \begin{cases} 0.1 & 2\overline{g}_j \le \overline{c}_j^{k+1} \\ 0.5 & \text{if } \overline{g}_j \le \overline{c}_j^{k+1} < 2\overline{g}_j,\ j=1,2,\ldots,n_g \\ 1 & \text{otherwise} \end{cases} \tag{5.6}$$

Because the solution of problem (5.5) has not been found yet at the initial iteration (i.e., k = 0) and there is no information about the corresponding quantile, the value of $\overline{c}_j^1$ is set to 0 for the initial iteration [89].

Eqs. (5.4) and (5.5) constitute one iteration of quantile-based SORA, and in order to prevent obtaining an excessively conservative result, the optimization procedure is considered convergent at the kth iteration if: (1) All the reliability constraints are satisfied; (2) At least one of the reliability constraints retains equality. The mathematical expressions of the two criteria are given as

$$Q_{R_j}\left(\boldsymbol{d}^k;\boldsymbol{\theta}\right) \le \overline{g}_j,\ j=1,2,\cdots,n_g \text{ and } Q_{R_{j_e}}\left(\boldsymbol{d}^k;\boldsymbol{\theta}\right) = \overline{g}_{j_e},\ \exists j_e \in \left\{1,2,\cdots,n_g\right\} \tag{5.7}$$

5.3 Estimation of quantile using L-moments

As discussed in Section 5.2, one of the main steps in quantile-based SORA is to calculate the quantile $Q_{R_j}\left(\boldsymbol{d}^k;\boldsymbol{\theta}\right)$ in Eq. (5.4) after solving problem (5.5) at each iteration. In this section, a quantile estimation method is proposed for obtaining the desired quantile $Q_{R_j}\left(\boldsymbol{d}^k;\boldsymbol{\theta}\right)$, which utilizes the MEM subject to constraints specified in terms of sample L-moments [101][103].

Suppose after the kth iteration the jth (j=1,2,⋯,n_g) performance function under uncertainty is a continuous random variable $Z_j^k = g_j\left(\boldsymbol{d}^k;\boldsymbol{\theta}\right)$ with CDF $F_j^k\left(z_j^k\right)$ and PDF $f_j^k\left(z_j^k\right)$. Let $Q_j^k(q)$ and $Q_j'^k(q)$ denote the quantile function and density-quantile function of Z_j^k for $0<q<1$, respectively. It can be observed from Eqs. (5.2) and (5.4) that the value of $Q_{R_j}\left(\boldsymbol{d}^k;\boldsymbol{\theta}\right)$ in Eq. (5.4) can be calculated using quantile function as $Q_j^k\left(R_j\right)$.

Since $Q_j^k(q)$ is the inverse function of $F_j^k\left(z_j^k\right)$, $f_j^k\left(z_j^k\right)$ and $Q_j'^k(q)$ are reciprocals with each other, and the entropy of Z_j^k, denote by H_j^k, can be written in terms of $Q_j'^k(q)$ as follows [106]:

$$H_j^k = \int_{-\infty}^{+\infty}\left\{-\ln f_j^k\left(z_j^k\right)\right\} f_j^k\left(z_j^k\right) dz_j^k = \int_0^1 \ln Q_j'^k(q)\, dq \tag{5.8}$$

According to MEM, the most unbiased estimation of $Q_j'^k(q)$ maximizes the entropy in Eq. (5.8) subject to available statistical information such as central moments. Assuming the exact distribution of Z_j^k is unknown beforehand and the central moments can only be inferred from limited data of samples, it is recognized that the estimation of higher order central moment from a set of random samples tends to be biased when the sample size is small [99][102]. Therefore, instead of using central moments, L-moments are used as alternatives of the available statistical information in MEM. Let $LM_{j,r}^k$ denote the rth (r≥1) order L-moment of Z_j^k, and according to Eq. (2.14) it can be rewritten with respect to $Q_j^k(q)$ as follows

$$LM_{j,r}^k = r^{-1}\sum_{k=0}^{r-1}(-1)^k\binom{r-1}{k}\mathrm{E}\left(Z_{k+1:r}\right) = \int_0^1 P_{r-1}^*(q)\,Q_j^k(q)\,dq \tag{5.9}$$

where $P_{r-1}^*(q)$ is the (r-1)th order shifted Legendre polynomial. Define the indefinite integral as

$$K_r(q) = \int_q^1 P_{r-1}^*(v)\,dv \tag{5.10}$$

Then the integration in Eq. (5.9) can be further rewritten in terms of $Q_j'^k(q)$ using Eq. (5.10) and the technique of integration by parts as follows [106]:

$$LM_{j,r}^k = \int_0^1 K_r(q)\,Q_j'^k(q)\,dq - \left[K_r(q)\,Q_j^k(q)\right]_0^1 \tag{5.11}$$

where $\left[K_r(q)\,Q_j^k(q)\right]_0^1$ represents the difference of $K_r(q)\,Q_j^k(q)$ at q equal to 0 and 1. As discussed in Section 2.3, when only a set of random samples are available, $LM_{j,r}^k$ can be estimated by sample L-moments which are calculated using order statistics [118]. Let $\boldsymbol{\theta}_1,\boldsymbol{\theta}_2,\cdots,\boldsymbol{\theta}_{m_s}$ denote the m_s i.i.d. vectors of uncertainties, and the corresponding m_s values of $Z_j^k = g_j\left(\boldsymbol{d}^k;\boldsymbol{\theta}\right)$ are

denoted by $Z_{j,1}^k = g_j\left(\boldsymbol{d}^k;\boldsymbol{\theta}_1\right)$, $Z_{j,2}^k = g_j\left(\boldsymbol{d}^k;\boldsymbol{\theta}_2\right)$, …, $Z_{j,m_s}^k = g_j\left(\boldsymbol{d}^k;\boldsymbol{\theta}_{m_s}\right)$. We further define $Z_{j,1:m_s}^k, Z_{j,2:m_s}^k, \cdots, Z_{j,m_s:m_s}^k$ as the permutation of $Z_{j,1}^k, Z_{j,2}^k, \cdots, Z_{j,m_s}^k$ in an descending order, i.e., $Z_{j,1:m_s}^k \geq \cdots \geq Z_{j,i:m_s}^k \geq \cdots \geq Z_{j,m_s:m_s}^k$, and $Z_{j,i:m_s}^k$ is called the *i*th order statistic. Then based on Eqs. (2.15) and (2.16), the *r*th order sample L-moment of Z_j^k, denoted by $lm_{j,r}^k$, are calculated by

$$lm_{j,r}^k = \sum_{s=0}^{r-1}(-1)^{r-1-s}\binom{r-1}{s}\binom{r-1+s}{s}b_s \tag{5.12}$$

$$b_s = m_s^{-1}\sum_{i=1}^{m_s}\frac{(m_s-i)(m_s-i-1)\cdots(m_s-i-s+1)}{(n-1)(n-2)\cdots(n-s)}Z_{j,i:m_s}^k \tag{5.13}$$

where b_s in Eq. (5.13) is the sample PWMs of Z_j^k. According to Ref. [106], the MEM estimates $Q_j'^k(q)$ by maximizing the entropy defined as Eq. (5.8) subject to the first n_L L-moments, and the problem reads

$$\begin{aligned}&\text{Maximize } \int_0^1 \ln Q_j'^k(q)\,dq\\ &\text{subject to } lm_{j,r}^k = \int_0^1 K_r(q)Q_j'^k(q)\,dq - \left[K_r(q)Q_j^k(q)\right]_0^1,\ r=1,2,\cdots,n_L\end{aligned} \tag{5.14}$$

Note that in Eq. (5.14) the value of $lm_{j,r}^k$ is calculated by Eqs. (5.12) and (5.13) from a set of available data. Let $h_{j,r}^k = lm_{j,r}^k + \left[K_r(q)Q_j^k(q)\right]_0^1$ and rewrite problem (5.14) as

$$\begin{aligned}&\text{Maximize } \int_0^1 \ln Q_j'^k(q)\,dq\\ &\text{subject to } h_{j,r}^k = \int_0^1 K_r(q)Q_j'^k(q)\,dq,\ r=1,2,\cdots,n_L\end{aligned} \tag{5.15}$$

From the definition of $K_r(q)$ in Eq. (5.10), it can be observed that the value of $K_r(q)$ at q=1 is 0 with any arbitrary order r due to the integration range, and at q=0 the value of $K_r(q)$ is also 0 for order $r \geq 2$ and $K_r(0)=1$ for $r=1$ due to the form of shifted Legendre polynomial. Therefore, $h_{j,r}^k$ can be reduced to $lm_{j,r}^k$ for $r \geq 2$ and $lm_{j,r}^k - Q_j^k(0)$ for $r=1$.

Instead of directly solving problem (5.15), we seek to maximize the following Lagrangian functional of the entropy:

$$\bar{H}_j^k(q) = \int_0^1 \ln Q_j'^k(q)\,dq - \sum_{r=1}^{n_L}\lambda_{j,r}\left(\int_0^1 K_r(q)Q_j'^k(q)\,dq - h_{j,r}^k\right) \tag{5.16}$$

where $\lambda_{j,r}\left(r=1,2,\cdots,n_L\right)$ represent the unknown Lagrangian multipliers. The optimality condition (Euler-Lagrangian equation) for maximizing $\bar{H}_j^k(q)$ with respect to $Q_j'^k(q)$ yields the estimated $Q_j'^k(q)$ as

$$Q_j'^k(q) = 1 \Big/ \sum_{r=1}^{n_L} \lambda_{j,r} K_r(q) \tag{5.17}$$

and the Lagrangian multipliers in Eq. (5.17) are determined by finding the stationary point of the following functional:

$$\Gamma(\boldsymbol{\lambda}_j) = -\int_0^1 \ln\left(\sum_{r=1}^{n_L} \lambda_{j,r} K_r(q) \right) dq + \sum_{r=1}^{n_L} \lambda_{j,r} h_{j,r}^k \tag{5.18}$$

where $\boldsymbol{\lambda}_j = \left(\lambda_{j,1}, \lambda_{j,2}, \cdots, \lambda_{j,n_L}\right)$. It can be observed that the stationary point of Eq. (5.18) satisfies the equality constraints given in problem (5.14), and it can be efficiently found using numerical algorithms since $\Gamma(\boldsymbol{\lambda}_j)$ in Eq. (5.18) is a convex function. A brief proof for the convexity of $\Gamma(\boldsymbol{\lambda}_j)$ is given in Appendix A3. Once the values of $\boldsymbol{\lambda}_j$ and $Q_j'^k(q)$ are determined, the quantile function $Q_j'^k(q)$ can be obtained by integral

$$Q_j^k(q) = Q_j^k(0) + \int_0^q Q_j'^k(v)\, dv \tag{5.19}$$

Because the exact value of $Q_j^k(0)$ is usually unknown beforehand, one can estimate $Q_j^k(0)$ by the corresponding smallest order statistic $Z_{j,m_s:m_s}^k$, and $Q_j^k(q)$ in Eq. (5.19) is approximated by

$$Q_j^k(q) \approx Z_{j,m_s:m_s}^k + \int_0^q Q_j'^k(v)\, dv \tag{5.20}$$

and then the quantile $Q_{R_j}(\boldsymbol{d}^k; \boldsymbol{\theta})$ in Eq. (5.4) can be estimated as $Q_j^k(R_j) \approx Z_{j,m_s:m_s}^k + \int_0^{R_j} Q_j'^k(v)\, dv$.

It is worth noting that in the proposed method the quantile function is obtained by integrating the density-quantile function Eq. (5.17). The original constrained MEM problem is first transformed to Lagrangian functional, and then the values of unknown Lagrangian multipliers are found by solving another unconstrained convex optimization problem which is similar to the traditional MEM in PDF estimation [149]. Therefore, unlike the method in Ref. [94], the proposed method does not depend on the initial guesses of the Lagrangian multipliers. Moreover, since the value of $K_r(q)$ at $q = 1$ is 0 for any arbitrary order r, it can be expected that the estimated density-quantile function $Q_j'^k(q) = 1 \Big/ \sum_{r=1}^{n_L} \lambda_{j,r} K_r(q)$ will tend to be infinite as q approaches 1. Therefore, in the following numerical examples Eq. (5.20) is integrated to q = 0.9999 to avoid numerical difficulty for obtaining the quantile function.

5.4 Problem formulation

In the following two formulations of quantile-based SORA are presented for shape and topology optimization of plane frames. One is to minimize the structural volume under displacement constraints, and the other includes both displacement and global stability constraints, where a

continuous strategy is used to penalize the geometrical stiffness matrices of thin elements using approximated Heaviside function.

5.4.1 Problem with displacement constraints

Let $\boldsymbol{d}$ be the design variables for shape and topology optimization including x- and y-coordinates $\boldsymbol{x}$ and $\boldsymbol{y}$ of nodes and cross-sectional areas $\boldsymbol{A}$ of Euler-Bernoulli beam elements. Based on Eq. (5.5), the (k+1)th deterministic shape and topology optimization problem of plane frames of quantile-based SORA to minimize structural volume with displacement constraints can be written as

$$\begin{aligned} &\text{Miminize } V\left(\boldsymbol{x},\boldsymbol{y},\boldsymbol{A}\right) \\ &\text{subject to } g_j\left(\boldsymbol{x},\boldsymbol{y},\boldsymbol{A}\right) \le \bar{g}_j - \varepsilon_j \bar{c}_j^{k+1},\ j=1,2,\cdots,n_g; \\ &\qquad \underline{\boldsymbol{x}} \le \boldsymbol{x} \le \bar{\boldsymbol{x}};\ \underline{\boldsymbol{y}} \le \boldsymbol{y} \le \bar{\boldsymbol{y}};\ \underline{\boldsymbol{A}} \le \boldsymbol{A} \le \bar{\boldsymbol{A}} \end{aligned} \tag{5.21}$$

where g_j represents the jth displacement constraint, $\bar{c}_j^{k+1}$ is calculated by Eq. (5.4) as $\bar{c}_j^{k+1} = Q_{R_j}\left(\boldsymbol{x}^k,\boldsymbol{y}^k,\boldsymbol{A}^k;\boldsymbol{\theta}\right) - g_j\left(\boldsymbol{x}^k,\boldsymbol{y}^k,\boldsymbol{A}^k\right),\ j=1,2,\cdots,n_{\mathrm{g}}$, and $V\left(\boldsymbol{x},\boldsymbol{y},\boldsymbol{A}\right)$ is the total structural volume.

In order to prevent the existence of extremely short members during shape optimization, the method in Chapter 3 is introduced in which the FDM is applied on an auxiliary truss structure to optimize the shape of plane frame. Let $\boldsymbol{x}_{\mathrm{free}}$, $\boldsymbol{y}_{\mathrm{free}}$ and $\boldsymbol{x}_{\mathrm{fix}}$, $\boldsymbol{y}_{\mathrm{fix}}$ denote the x- and y-coordinates of free nodes and fixed nodes, respectively, and $\boldsymbol{t}$ be the force densities of the members of auxiliary truss. Problem (5.21) is rewritten as

$$\begin{aligned} &\text{Miminize } V\left(\boldsymbol{x}_{\mathrm{free}}\left(\boldsymbol{t}\right),\boldsymbol{y}_{\mathrm{free}}\left(\boldsymbol{t}\right),\boldsymbol{A}\right) \\ &\text{subject to } g_j\left(\boldsymbol{x}_{\mathrm{free}}\left(\boldsymbol{t}\right),\boldsymbol{y}_{\mathrm{free}}\left(\boldsymbol{t}\right),\boldsymbol{A}\right) \le \bar{g}_j - \varepsilon_j \bar{c}_j^{k+1},\ j=1,2,\cdots,n_g; \\ &\qquad \underline{\boldsymbol{t}} \le \boldsymbol{t} \le \bar{\boldsymbol{t}};\ \underline{\boldsymbol{A}} \le \boldsymbol{A} \le \bar{\boldsymbol{A}} \end{aligned} \tag{5.22}$$

with $\bar{c}_j^{k+1} = Q_{R_j}\left(\boldsymbol{x}_{\mathrm{free}}\left(\boldsymbol{t}^k\right),\boldsymbol{y}_{\mathrm{free}}\left(\boldsymbol{t}^k\right),\boldsymbol{A}^k;\boldsymbol{\theta}\right) - g_j\left(\boldsymbol{x}_{\mathrm{free}}\left(\boldsymbol{t}^k\right),\boldsymbol{y}_{\mathrm{free}}\left(\boldsymbol{t}^k\right),\boldsymbol{A}^k\right),\ j=1,2,\cdots,n_g$. Note that in problem (5.22) the design variables are the force densities $\boldsymbol{t}$ and the cross-sectional areas $\boldsymbol{A}$, and $\boldsymbol{x}_{\mathrm{free}}$ and $\boldsymbol{y}_{\mathrm{free}}$ can be obtained by solving Eq. (2.4) in Section 2.2.

In the numerical examples, problem (5.22) is solved using an SQP library, and the sensitivity coefficients are calculated based on Eqs. (3.14)-(3.17) as given in Section 3.4. Flowchart of the corresponding quantile-based SORA is given in Fig. 5-1.

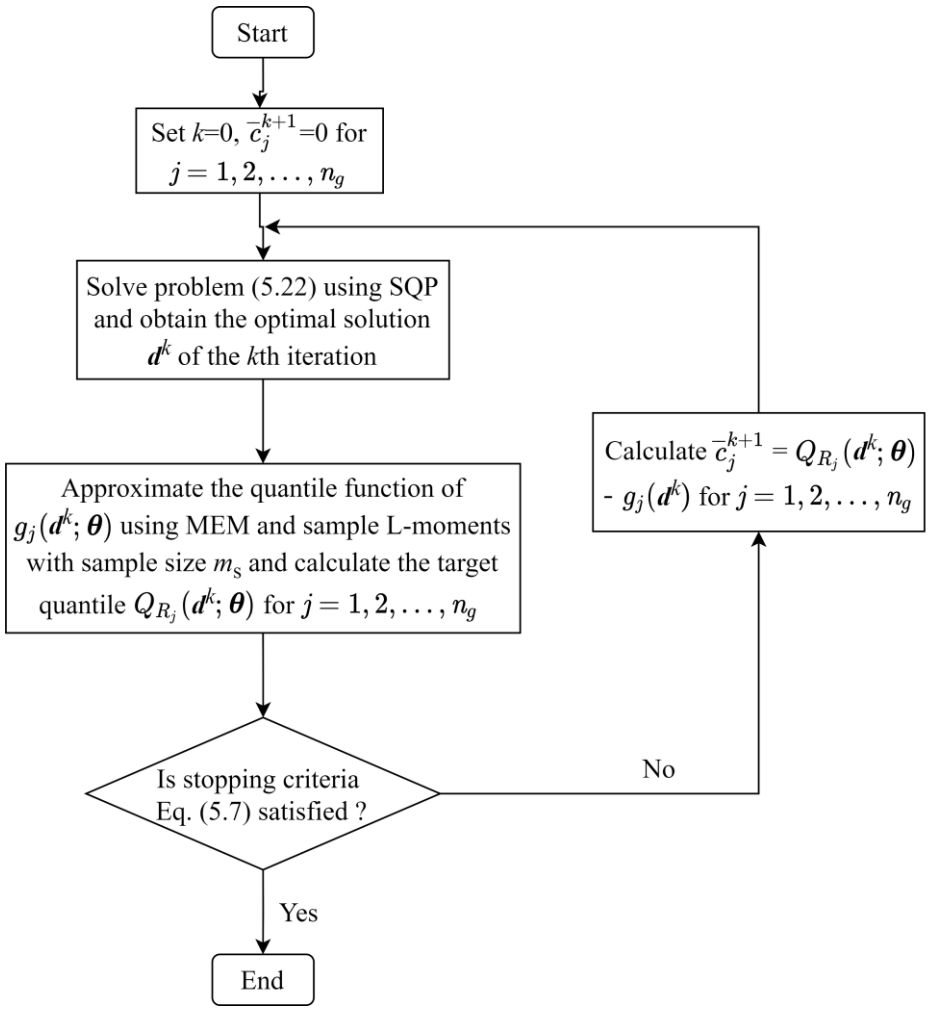

Fig. 5-1 Flowchart of quantile-based SORA in Section 5.4.1

5.4.2 Problem with both displacement and global stability constraints

In order not to confuse the global stability constraint with displacement constraints in a general problem formulation as given in Section 5.2, let λ^{cr} be the linear buckling load factor and $\underline{\lambda}$ be the corresponding lower bound, and denote their reciprocals as $\gamma^{\mathrm{cr}} = 1/\lambda^{\mathrm{cr}}$ and $\bar{\gamma} = 1/\underline{\lambda}$ as in Section 4.3.1, respectively. Then by adding a global stability constraint to problem (5.22), the (k+1)th deterministic optimization of quantile-based SORA with both displacement and global stability constraints is formulated as

$$\begin{aligned}
&\text{Minimize } V\left(\boldsymbol{x}_{\text{free}}(\boldsymbol{t}), \boldsymbol{y}_{\text{free}}(\boldsymbol{t}), \boldsymbol{A}\right) \\
&\text{subject to } g_j\left(\boldsymbol{x}_{\text{free}}(\boldsymbol{t}), \boldsymbol{y}_{\text{free}}(\boldsymbol{t}), \boldsymbol{A}\right) \le \bar{g}_j - \varepsilon_j \bar{c}_j^{k+1}, j = 1, 2, \ldots, n_g; \\
&\qquad \gamma^{\mathrm{cr}}\left(\boldsymbol{x}_{\text{free}}(\boldsymbol{t}), \boldsymbol{y}_{\text{free}}(\boldsymbol{t}), \boldsymbol{A}\right) \le \bar{\gamma} - \varepsilon_\gamma \bar{c}_\gamma^{k+1}; \\
&\qquad \underline{\boldsymbol{t}} \le \boldsymbol{t} \le \bar{\boldsymbol{t}};\ \underline{\boldsymbol{A}} \le \boldsymbol{A} \le \bar{\boldsymbol{A}};
\end{aligned} \tag{5.23}$$

with $\bar{c}_{\gamma}^{k+1} = Q_{R_\gamma}\left(\boldsymbol{x}_{\text{free}}\left(\boldsymbol{t}^k\right), \boldsymbol{y}_{\text{free}}\left(\boldsymbol{t}^k\right), \boldsymbol{A}^k; \boldsymbol{\theta}\right) - \gamma^{\text{cr}}\left(\boldsymbol{x}_{\text{free}}\left(\boldsymbol{t}^k\right), \boldsymbol{y}_{\text{free}}\left(\boldsymbol{t}^k\right), \boldsymbol{A}^k\right)$, where Q_{R_γ} and ε_γ are the quantile and coefficient with respect to γ^{cr} which are defined by Eqs. (5.3) and (5.6), respectively.

Similar to Section 4.3.1, the penalization method is used to exclude the contributions of geometrical stiffness matrices of thin elements to the global geometrical stiffness matrix. In order to solve problem (5.23) using SQP in the similar manner as Section 5.2.1, the geometrical stiffness matrix of a thin element should be penalized by a continuous numerical scheme for conveniently deriving the sensitivity coefficient. Therefore, the element geometrical stiffness matrix is penalized using an approximate Heaviside function

$$\bar{\boldsymbol{K}}_{Gk_e} = H\left(A_{k_e}\right)\boldsymbol{K}_{Gk_e},\ k_e = 1, 2, \ldots, m_e \tag{5.24}$$

where A_{k_e}, $\boldsymbol{K}_{Gk_e}$ and $\bar{\boldsymbol{K}}_{Gk_e}$ are the cross-sectional area, and the 6-by-6 original and penalized element geometrical stiffness matrices of element k_e, respectively, and m_e is the number of beam elements in the structure; $H\left(A_{k_e}\right)$ is the approximated Heaviside function defined as

$$H\left(A_{k_e}\right) = \frac{1}{2}\left[1 + \text{erf}\left(\frac{A_{k_e} - \mu}{\delta\sqrt{2}}\right)\right] \tag{5.25}$$

where erf(·) is the error function with two parameters μ and δ. It can be seen from Eq. (5.25) that the approximate Heaviside function is continuous and differentiable, and the parameter μ controls the threshold value of cross-sectional area below which the element geometrical stiffness matrix is penalized, whereas the parameter δ controls the band of transition around μ. Figure 5-2 shows the shape of $H\left(A_{k_e}\right)$ in Eq. (5.25) with a positive value of μ and different values of δ. It is confirmed that that when the value of δ decreases, the band of transition becomes narrower and sharper. Therefore, the values of μ and δ should be small enough to exclude the geometrical stiffness matrices of thin elements from the global geometrical stiffness matrix.

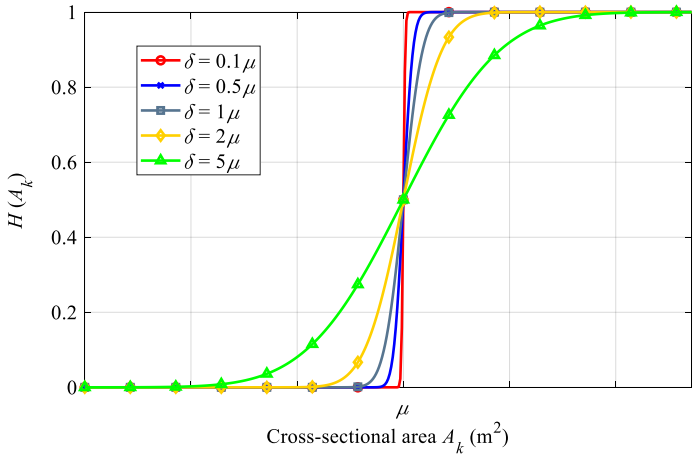

Fig. 5-2 Approximate Heaviside function with different values of δ

Moreover, the sensitivity coefficients of λ^{cr} with respect to design variables $\boldsymbol{t}$ and $\boldsymbol{A}$ are given as follows. Let $\boldsymbol{\varphi}^{\mathrm{cr}}$ be the buckling mode corresponding to the linear buckling load factor λ^{cr} which satisfies the following normalization condition [8]:

$$\boldsymbol{\varphi}^{\mathrm{cr}T}\boldsymbol{K}_G\boldsymbol{\varphi}^{\mathrm{cr}}=1 \tag{5.26}$$

where $\boldsymbol{K}_G$ is the n_{dof}-by-n_{dof} global geometrical stiffness matrix. Then, based on Eqs. (2.4) and (5.26), the sensitivity coefficients of linear buckling load factor λ^{cr} with respect to the design variables t_i and $A_{i_{\mathrm{e}}}$ can be computed as follows [8]:

$$\begin{aligned}
&\frac{\partial\lambda^{\mathrm{cr}}}{\partial t_i}=\sum_{j=1}^{n_{\mathrm{free}}}\left(\frac{\partial\lambda^{\mathrm{cr}}}{\partial x_{\mathrm{free},j}}\frac{\partial x_{\mathrm{free},j}}{\partial t_i}+\frac{\partial\lambda^{\mathrm{cr}}}{\partial y_{\mathrm{free},j}}\frac{\partial y_{\mathrm{free},j}}{\partial t_i}\right),\ i=1,2,\ldots,m;\\
&\frac{\partial\lambda^{\mathrm{cr}}}{\partial A_{i_{\mathrm{e}}}}=\boldsymbol{\varphi}^{\mathrm{cr}T}\frac{\partial\boldsymbol{K}}{\partial A_{i_{\mathrm{e}}}}\boldsymbol{\varphi}^{\mathrm{cr}}+\lambda^{\mathrm{cr}}\sum_{k_{\mathrm{e}}=1}^{m_{\mathrm{e}}}\boldsymbol{\varphi}^{\mathrm{cr}T}\left(\frac{\partial H\left(A_{k_{\mathrm{e}}}\right)}{\partial A_{i_{\mathrm{e}}}}\boldsymbol{K}_{Gk_{\mathrm{e}}}+\frac{\partial\bar{\boldsymbol{K}}_{Gk_{\mathrm{e}}}}{\partial N_{k_{\mathrm{e}}}}\frac{\partial N_{k_{\mathrm{e}}}}{\partial A_{i_{\mathrm{e}}}}\right)\boldsymbol{\varphi}^{\mathrm{cr}T},\ i_{\mathrm{e}}=1,2,\ldots,m_{\mathrm{e}}
\end{aligned} \tag{5.27}$$

where m is the number of members and m_{e} is the number of beam elements; $\boldsymbol{K}$ is the n_{dof}-by-n_{dof} global elastic stiffness matrix and $N_{k_{\mathrm{e}}}$ is the axial force of element k_{e}. Note that in Eq. (5.27) the sizes of $\boldsymbol{K}_{Gk_{\mathrm{e}}}$ and $\bar{\boldsymbol{K}}_{Gk_{\mathrm{e}}}$ are n_{dof}-by-n_{dof} which are different from those in Eq. (5.24), and the entries of $\boldsymbol{K}_{Gk_{\mathrm{e}}}$ and $\bar{\boldsymbol{K}}_{Gk_{\mathrm{e}}}$ in Eq. (5.27) corresponding to the DOFs of element k_{e} are given by those in Eq. (5.24), where the other entries are all zero. Besides, m_{e} is no less than m since some of the members will be modeled by four beam elements for linear buckling analysis as stated in Section 2.4.

By denoting the length of element k_{e} as $l_{k_{\mathrm{e}}}$, the derivatives of $\partial\lambda^{\mathrm{cr}}/\partial x_{\mathrm{free},j}$ and $\partial\lambda^{\mathrm{cr}}/\partial y_{\mathrm{free},j}$ are calculated by

$$\begin{aligned}
&\frac{\partial\lambda^{\mathrm{cr}}}{\partial x_{\mathrm{free},j}}=\boldsymbol{\varphi}^{\mathrm{cr}T}\frac{\partial\boldsymbol{K}}{\partial x_{\mathrm{free},j}}\boldsymbol{\varphi}^{\mathrm{cr}}+\lambda^{\mathrm{cr}}\sum_{k_{\mathrm{e}}=1}^{m_{\mathrm{e}}}\boldsymbol{\varphi}^{\mathrm{cr}T}\left(\frac{\partial\bar{\boldsymbol{K}}_{Gk_{\mathrm{e}}}}{\partial l_{k_{\mathrm{e}}}}\frac{\partial l_{k_{\mathrm{e}}}}{\partial x_{\mathrm{free},j}}+\frac{\partial\bar{\boldsymbol{K}}_{Gk_{\mathrm{e}}}}{\partial N_{k_{\mathrm{e}}}}\frac{\partial N_{k_{\mathrm{e}}}}{\partial x_{\mathrm{free},j}}\right)\boldsymbol{\varphi}^{\mathrm{cr}T}\\
&\frac{\partial\lambda^{\mathrm{cr}}}{\partial y_{\mathrm{free},j}}=\boldsymbol{\varphi}^{\mathrm{cr}T}\frac{\partial\boldsymbol{K}}{\partial y_{\mathrm{free},j}}\boldsymbol{\varphi}^{\mathrm{cr}}+\lambda^{\mathrm{cr}}\sum_{k_{\mathrm{e}}=1}^{m_{\mathrm{e}}}\boldsymbol{\varphi}^{\mathrm{cr}T}\left(\frac{\partial\bar{\boldsymbol{K}}_{Gk_{\mathrm{e}}}}{\partial l_{k_{\mathrm{e}}}}\frac{\partial l_{k_{\mathrm{e}}}}{\partial y_{\mathrm{free},j}}+\frac{\partial\bar{\boldsymbol{K}}_{Gk_{\mathrm{e}}}}{\partial N_{k_{\mathrm{e}}}}\frac{\partial N_{k_{\mathrm{e}}}}{\partial y_{\mathrm{free},j}}\right)\boldsymbol{\varphi}^{\mathrm{cr}T}
\end{aligned} \tag{5.28}$$

It can be seen from Eqs. (5.27) and (5.28) that the derivatives of approximate Heaviside function $\partial H\left(A_{k_{\mathrm{e}}}\right)/\partial A_{i_{\mathrm{e}}}$ is nonzero only when elements k_{e} and i_{e} belong to the same member, and the derivatives of axial force with respect to the cross-sectional area and the coordinates of free nodes in Eqs. (5.27) and (5.28), namely, $\partial N_{k_{\mathrm{e}}}/\partial A_{i_{\mathrm{e}}}$, $\partial N_{k_{\mathrm{e}}}/\partial x_{\mathrm{free},j}$ and $\partial N_{k_{\mathrm{e}}}/\partial y_{\mathrm{free},j}$, can be obtained by directly differentiating the equilibrium equation Eq.(3.1) at element level, that is [125]

$$\bar{\boldsymbol{f}}_{k_{\mathrm{e}}}=\bar{\boldsymbol{k}}_{k_{\mathrm{e}}}\bar{\boldsymbol{u}}_{k_{\mathrm{e}}} \tag{5.29}$$

where $\bar{\boldsymbol{f}}_{k_e} = \left[-N_{k_e}, M_{k_e 1}, -S_{k_e}, N_{k_e}, M_{k_e 2}, S_{k_e}\right]^T$ is nodal force vector, in which $M_{k_e 1}$ and $M_{k_e 2}$ are the bending moments at the two ends of element k_e, and S_{k_e} is the shear force. For simplicity the details of differentiations of Eq. (5.29) with respect to A_{k_e}, $x_{\text{free},j}$ and $y_{\text{free},j}$ are referred to Ref. [125].

5.5 Numerical examples

In this section, four numerical examples are presented to investigate effectiveness of the methods proposed in Section 5.4, where examples 1 and 2 include displacement constraints only, and examples 3 and 4 include both displacement and global stability constraints. The deterministic optimization problems (5.22) and (5.23) are solved using an SQP algorithm in *fmincon* of Optimization Toolbox of MATLAB 2018a [124]. For each example the members of the frame structure are assumed to have solid circular cross-section, and the crossing members are not connected at their intersection. Besides, the node number and the member number shown in the initial structures of the examples are indicated by those with and without parentheses, respectively.

5.5.1 Parameter settings

Assuming that the fixed nodes are precisely located for simplicity, the uncertainties in x- and y-coordinates are considered only in the free nodes and denoted as $\Delta\boldsymbol{x}_{\text{free}}$ and $\Delta\boldsymbol{y}_{\text{free}}$, respectively. Therefore, the vector of random variables is given as $\boldsymbol{\theta} = (\Delta\boldsymbol{x}_{\text{free}}, \Delta\boldsymbol{y}_{\text{free}}, \Delta\boldsymbol{A}, \Delta\boldsymbol{E})$. The eccentricity e in Section 2.4 is set to 0.01 in accordance with Ref. [143], and the random variables are characterized by uniform distribution, i.e., $\Delta\boldsymbol{x}_{\text{free}} \in \left[\Delta\boldsymbol{x}_{\text{free,lower}}, \Delta\boldsymbol{x}_{\text{free,upper}}\right]$, $\Delta\boldsymbol{y}_{\text{free}} \in \left[\Delta\boldsymbol{y}_{\text{free,lower}}, \Delta\boldsymbol{y}_{\text{free,upper}}\right]$, $\Delta\boldsymbol{A} \in \left[\Delta\boldsymbol{A}_{\text{lower}}, \Delta\boldsymbol{A}_{\text{upper}}\right]$ and $\Delta\boldsymbol{E} \in \left[\Delta\boldsymbol{E}_{\text{lower}}, \Delta\boldsymbol{E}_{\text{upper}}\right]$, and the subscripts of lower and upper represent the lower and upper bounds, respectively, for the corresponding uncertain parameters. The first four sample L-moments (i.e., n_{L}=4) in Eqs. (5.14)-(5.18) are used to estimate the quantile function with sample size m_{s}=50, and the MCS with sample size 1×10^5 is implemented to investigate accuracy of the quantile estimation by MEM using sample L-moments. To compare with the result at the final iteration, the result at the initial iteration is also displayed in the numerical examples. Moreover, as discussed in Section 2.4, for examples 3 and 4 the number of beam elements to simulate one frame member is dependent on the member length during optimization process. It will be simulated by four beam elements if the member length is longer than 0.1m, otherwise it will be simulated by only one beam element, and the correlation length L_{exp} in Eq. (2.20) in Section 2.4 is 0.1m. The parameter values listed in Table 5-1 are used for the four numerical examples of shape and topology optimization of plane frames if not specified explicitly, where $\boldsymbol{I}$ is the vector with all entries equal to 1.

Table 5-1 Parameter settings of examples 1-4

Parameters	Examples 1 and 2	Examples 3 and 4
Lower bound $\Delta \boldsymbol{x}_{\text{free,lower}}$ (m)	$-0.02\boldsymbol{I}$	$-0.02\boldsymbol{I}$
Upper bound $\Delta \boldsymbol{x}_{\text{free,upper}}$ (m)	$0.02\boldsymbol{I}$	$0.02\boldsymbol{I}$
Lower bound $\Delta \boldsymbol{y}_{\text{free,lower}}$ (m)	$-0.02\boldsymbol{I}$	$-0.02\boldsymbol{I}$
Upper bound $\Delta \boldsymbol{y}_{\text{free,upper}}$ (m)	$0.02\boldsymbol{I}$	$0.02\boldsymbol{I}$
Lower bound $\Delta \boldsymbol{A}_{\text{lower}}$ (m^2)	$-0.02\boldsymbol{A}$	$-0.02\boldsymbol{A}$
Upper bound $\Delta \boldsymbol{A}_{\text{upper}}$ (m^2)	$0.02\boldsymbol{A}$	$0.02\boldsymbol{A}$
Lower bound $\Delta \boldsymbol{E}_{\text{lower}}$ (m^2)	$-0.05\boldsymbol{E}$	$-0.05\boldsymbol{E}$
Upper bound $\Delta \boldsymbol{E}_{\text{upper}}$ (m^2)	$0.05\boldsymbol{E}$	$0.05\boldsymbol{E}$
Nominal value of $\boldsymbol{E}$ (Pa)	$3\times10^{11}\boldsymbol{I}$	$3\times10^{11}\boldsymbol{I}$
Sample size m_s of sample L-moments	50	50
Sample size m_{MCS} of MCS	1×10^{5}	1×10^{5}
Upper bound $\overline{\boldsymbol{A}}$ (m^2)	$0.02\boldsymbol{I}$	$0.02\boldsymbol{I}$
Lower bound $\underline{\boldsymbol{A}}$ (m^2)	$1\times10^{-7}\boldsymbol{I}$	$1\times10^{-7}\boldsymbol{I}$
Upper bound $\overline{\boldsymbol{t}}$ (N/m)	$1000\boldsymbol{I}$	$1000\boldsymbol{I}$
Lower bound $\underline{\boldsymbol{t}}$ (N/m)	$-1000\boldsymbol{I}$	$-1000\boldsymbol{I}$
Target probability R_j	0.99	0.99
Target probability R_γ	--	0.99
Upper bound for displacement $\overline{g}_j$ (m)	3×10^{-3}	3×10^{-3}
Lower bound $\underline{\lambda}$	--	20
Upper bound $\overline{\gamma}$	--	0.05
Correlation length L_{exp} (m)	--	0.1
Eccentricity e	--	0.01
Parameter μ in Eq. (5.25) (m^2)	--	6×10^{-5}
Parameter δ in Eq. (5.25) (m^2)	--	1×10^{-5}

5.5.2 Example 1: Problem with displacement constraints in 5.4.1

The first example considers a 3×2 grid cantilever frame with 12 nodes and 27 members, and the initial structure is shown in Fig. 5-3. The structure is pin-supported at nodes 1, 2 and 3 and a downward vertical load F = 1000 kN is applied at node 11; therefore the fixed nodes for FDM are selected as nodes 1, 2, 3 and 11. Based on Eq. (5.22) and Table 5-1, the optimization problem is formulated to minimize the structural volume subject to reliability constraint on the downward vertical displacement of node 11 as follows

$$\begin{aligned} &\text{Minimize } V\left(\boldsymbol{x}_{\text{free}}(\boldsymbol{t}), \boldsymbol{y}_{\text{free}}(\boldsymbol{t}), \boldsymbol{A}\right) \\ &\text{subject to } g_{11}\left(\boldsymbol{x}_{\text{free}}(\boldsymbol{t}), \boldsymbol{y}_{\text{free}}(\boldsymbol{t}), \boldsymbol{A}\right) \le 3\times10^{-3} - \varepsilon_{11}\overline{c}_{11}^{k+1};\ \underline{\boldsymbol{t}} \le \boldsymbol{t} \le \overline{\boldsymbol{t}};\ \underline{\boldsymbol{A}} \le \boldsymbol{A} \le \overline{\boldsymbol{A}}; \end{aligned} \tag{5.30}$$

where g_{11} is the vertical displacement of node 11 without considering uncertainty, and $\bar{c}_{11}^{k+1}$ is the shifting value on the upper bound of g_{11} at the (k+1)th iteration. The optimization procedure converged at k=3, and the results at the initial and final iteration are presented in Fig. 5-4. The structural volume and quantile $Q_{R_{11}}$ at initial and final iteration are listed in Table 5-2, where the quantiles obtained by MCS with sample size m_{MCS} are listed in the parentheses. The nodal locations, force densities, cross-sectional areas and member lengths are also given in Tables 5-3 and 5-4. As can be seen from Fig. 5-4 and Tables 5-2 to 5-4, the results at the initial and final iteration have similar shapes, however, the cross-sectional area of each member has increased before reaching the final iteration to satisfy the displacement constraint at node 11, leading to a larger structural volume and a smaller $Q_{R_{11}}$ compared to the result at the initial iteration.

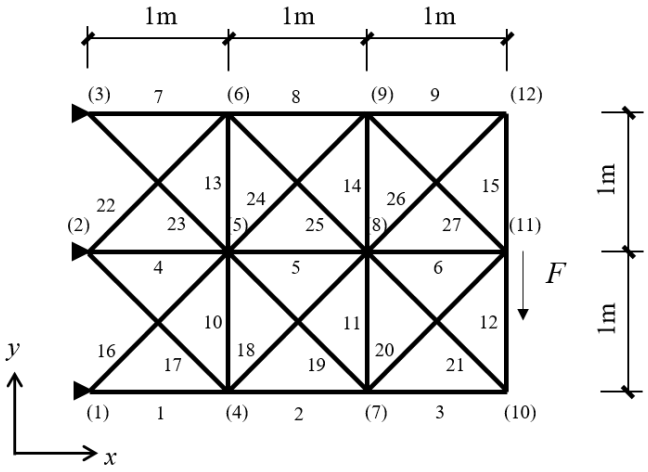

Fig. 5-3 Initial structure of Example 1

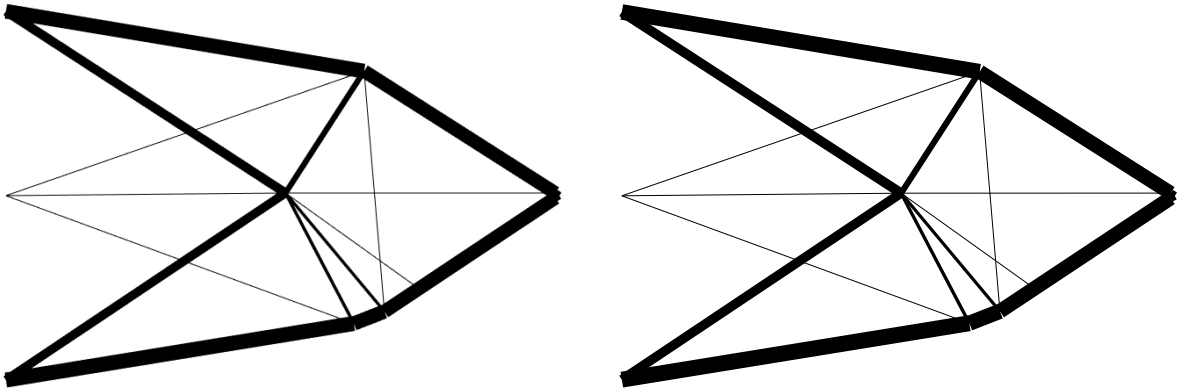

(a) (b)

Fig. 5-4 Results of Example 1 at: (a) initial iteration; (b) final iteration

Table 5-2 Structural volumes and quantiles $Q_{R_{11}}$ of the results of Example 1 at the initial and final iterations

Result	Initial iteration	Final iteration
Structural volume (m^3)	9.2167×10^{-2}	9.8017×10^{-2}
Quantile $Q_{R_{11}}$ (m)	3.199×10^{-3} (3.175×10^{-3})	3.0×10^{-3} (2.973×10^{-3})

Table 5-3 Location of nodes of the results of Example 1 at the initial and final iteration

Node	Initial iteration		Final iteration	
	x-coordinate (m)	*y*-coordinate (m)	*x*-coordinate (m)	*y*-coordinate (m)
1	0	0	0	0
2	0	1	0	1
3	0	2	0	2
4	1.8857	0.3067	1.8852	0.3068
5	1.5154	1.0144	1.5149	1.0144
6	1.9414	1.6754	1.9409	1.6753
7	2.2633	0.4784	2.2625	0.4787
8	2.0518	0.3718	2.0511	0.3718
9	2.9785	1.0144	2.9776	1.0148
10	2.4708	0.6290	2.4701	0.6291
11	3	1	3	1
12	2.9785	0.9886	2.9777	0.9882

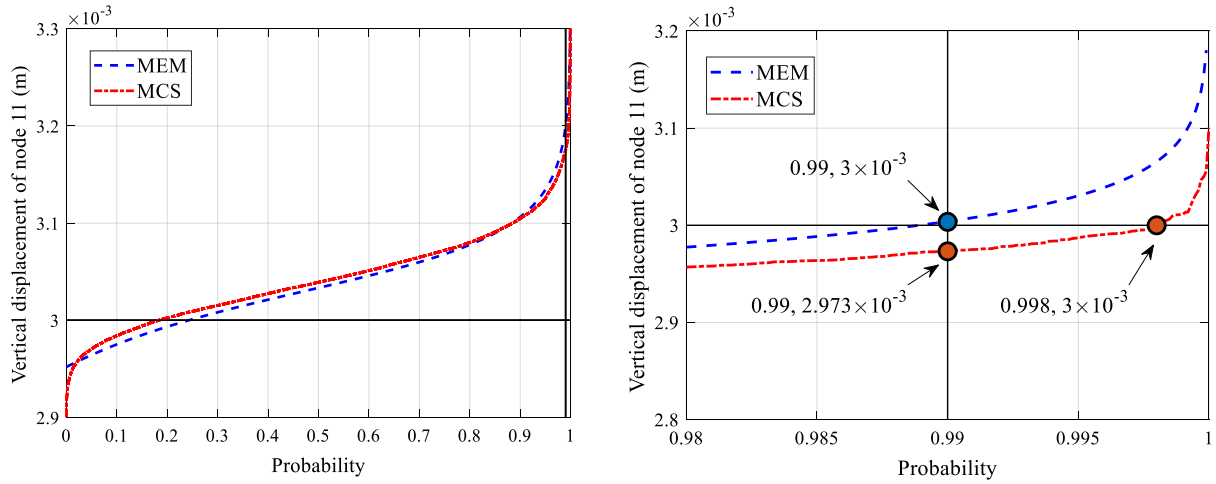

(a) (b)

Fig. 5-5 Quantile functions of vertical displacement of node 11 of Example 1 at the results of: (a) initial iteration; (b) final iteration

Moreover, the quantile functions of vertical displacement of node 11 obtained by MCS and MEM with sample L-moments are given in Fig. 5-5 for both results at initial and final iteration. It can be observed from Fig. 5-5(a) and Table 5-2 that when uncertainty is taken into consideration for the result at the initial iteration, the probability of the vertical displacement of node 11 exceeding the upper bound 3×10^{-3} m is about 0.8, which means the structure has low reliability. On the other hand, although the structural volume at the final iteration increased about 7% from the initial iteration, the reliability constraint on the vertical displacement of node 11 is satisfied, and the estimated quantile $Q_{R_{11}}$ using the proposed MEM is close to the one obtained by MCS where the relative error is around 2% as shown in Fig. 5-5 (b), indicating that the proposed method is able to estimate the quantile function with satisfactory accuracy.

Table 5-4 Force densities, cross-sectional areas and member lengths of the results of Example 1 at the initial and final iterations

Member	Initial iteration			Final iteration		
	Force density (N/m)	Cross-sectional area (m^2)	Member length (m)	Force density (N/m)	Cross-sectional area (m^2)	Member length (m)
1	0.7491	0.0102	1.9104	0.7489	0.0109	1.9101
2	1.3772	1.00×10^{-7}	0.4148	1.3774	1.00×10^{-7}	0.4146
3	0.7021	3.59×10^{-7}	0.2563	0.7021	1.00×10^{-7}	0.2563
4	0.3807	1.00×10^{-7}	1.5155	0.3809	1.00×10^{-7}	1.5150
5	0.1951	0.00207	0.8370	0.1951	0.00218	0.8368
6	0.7478	1.00×10^{-7}	1.1373	0.7484	1.00×10^{-7}	1.1379
7	-0.7517	0.0100	1.9683	-0.7516	0.0107	1.9678
8	-0.6716	0.00921	1.2298	-0.6720	0.00982	1.2293
9	-0.2787	0.00452	0.0257	-0.2788	0.00484	0.0266
10	0.2944	0.00218	0.7987	0.2942	0.00230	0.7986
11	1.0208	3.93×10^{-7}	0.2368	1.0210	3.95×10^{-7}	0.2368
12	0.3521	4.54×10^{-7}	0.6462	0.3521	1.00×10^{-7}	0.6467
13	0.2404	0.00392	0.7864	0.2402	0.00417	0.7863
14	-0.6716	1.00×10^{-7}	1.1276	-0.6710	1.00×10^{-7}	1.1277
15	-2.4518	0.00517	0.0243	-2.4517	0.00555	0.0252
16	0.2554	0.00609	1.8236	0.2553	0.00645	1.8232
17	-0.4243	1.00×10^{-7}	2.0091	-0.4243	1.00×10^{-7}	2.0086
18	1.2129	0.00977	0.1784	1.21291	0.0105	0.1782
19	-0.1673	1.00×10^{-7}	0.9201	-0.1657	1.00×10^{-7}	0.9196
20	0.6315	1.00×10^{-7}	0.9026	0.6315	1.00×10^{-7}	0.9031
21	0.0970	1.00×10^{-7}	0.4916	0.0973	1.00×10^{-7}	0.4917
22	0.3322	1.00×10^{-7}	2.0555	0.3319	1.00×10^{-7}	2.0550
23	0.3549	0.00629	1.8077	0.3553	0.00667	1.8073
24	0.8960	1.00×10^{-7}	1.4630	0.8957	1.00×10^{-7}	1.4627
25	-0.1406	1.00×10^{-7}	1.3083	-0.1404	1.00×10^{-7}	1.3082
26	-0.0568	0.00933	1.1132	-0.0589	0.00996	1.1128
27	-0.3659	0.00506	0.02588	-0.3659	0.00542	0.0268

To further investigate effectiveness of introducing FDM into quantile-based SORA for shape and topology optimization of plane frames, the result at the final iteration is modified by combining the three closely spaced nodes 9, 11 and 12 to the single node 11, and removing the members 2, 3, 4, 6, 11, 12, 14, 17, 19, 20, 21, 22, 24 and 25, which have very small cross-sectional areas, from the structure to obtain a distinct structural shape and topology as shown in Fig. 5-6(a), and the corresponding locations of nodes, cross-sectional areas and member lengths are listed in Tables 5-5 and 5-6. The quantile functions of vertical displacement of node 11 obtained by MCS and MEM with sample L-moments are given in Fig. 5-6 (b), and the structural volumes, nominal values and quantiles of the displacement constraint functions before and after modification are also given in Table 5-7 for comparison, in which the quantiles obtained by MCS are listed in the parentheses.

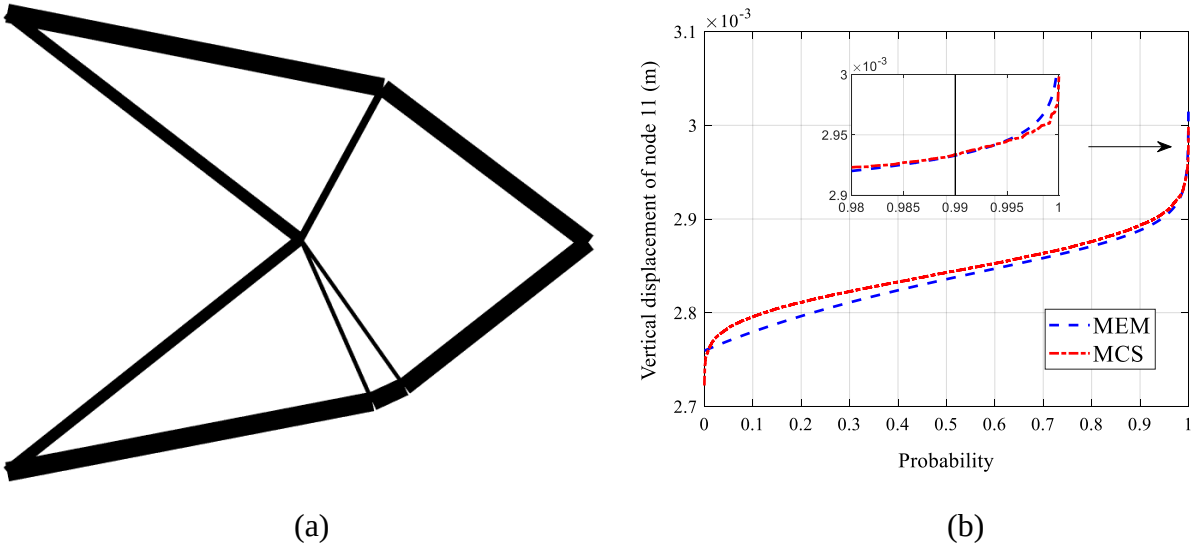

(a) (b)

Fig. 5-6 Results of Example 1 after modification: (a) Optimal shape; (b) Quantile functions of vertical displacement of node 11

Table 5-5 Location of nodes of optimal result of Example 1 after modification

Node	1	2	3	4	5	6	11
x-coordinate (m)	0	0	1.8852	1.5149	1.9409	2.0511	3
y-coordinate (m)	0	2	0.3068	1.0144	1.6753	0.3718	1

It can be observed from Table 5-7 that due to regularity of the stiffness matrix, the nominal value of the displacement constraint after modification is only slightly smaller than that before modification. This is mainly because the removal of thin members from the structure results in a small decrease in structural volume and stiffness. However, the quantile after modification is smaller than that before modification, resulting in a structure with a little higher reliability than the requirement. The main reason for this result is that since the closely spaced nodes are merged to a single node and thin members are removed, only 7 nodes and 10 members are left in the distinct

result as displayed in Fig. 5-6(a) and Tables 5-5 and 5-6. Accordingly, the quantile of the stochastic displacement decreases a little after modification because less uncertainties are involved in the structure, indicating that by introducing the FDM into quantile-based SORA a feasible result can be obtained without melting nodes, and the feasibility still remains in the final distinct structure with no extremely thin members or closely space nodes. This way, an optimal shape with small numbers of nodes and members satisfying reliability constraint can easily be obtained by combining FDM and SORA methods.

Table 5-6 Cross-sectional areas and member lengths of optimal result of Example 1 after modification

Element		Cross-sectional area (m^2)	Member length (m)
Node 1	Node 2		
1	3	0.0109	1.9100
4	6	0.00218	0.8368
2	5	0.0107	1.9678
5	11	0.00982	1.2293
3	4	0.00230	0.7986
4	5	0.00417	0.7863
1	4	0.00645	1.8232
3	6	0.0105	0.1782
2	4	0.00667	1.8073
6	11	0.00996	1.1128

Table 5-7 Structural volumes, quantiles and nominal values of constraints of Example 1 before and after modification

Result	Before modification	After modification
Structural volume (m3)	9.8017×10^{-2}	9.8016×10^{-2}
Nominal value of constraint (m)	2.820×10^{-3}	2.828×10^{-3}
Quantile of constraint (m)	3.0×10^{-3} (2.973×10^{-3})	2.932×10^{-3} (2.933×10^{-3})

5.5.3 Example 2: Problem with displacement constraints in 5.4.1

In the second numerical example, we investigate the optimal shape and topology of a 6×1 grid bridge-frame where the 14 nodes are connected by 31 members, and the initial structure is shown in Fig. 5-7. The structure is pin-supported at node 1 and roller-supported at node 13. At each of the nodes 3, 5, 7, 9 and 11, a downward vertical load with magnitude 1000 kN is applied. Accordingly, these 7 nodes are considered as fixed nodes for shape optimization using FDM.

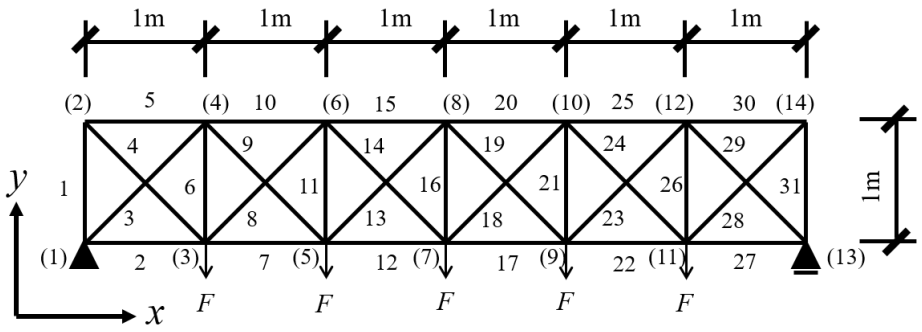

Fig. 5-7 Initial structure of Example 2

The optimization problem is to minimize the structural volume subject to reliability constraints on the downward vertical displacements of nodes 3, 5, 7, 9 and 11. Based on Eq. (5.22) and Table 5-1, the (k+1)th deterministic optimization in quantile-based SORA is formulated as

$$\begin{aligned} &\text{Minimize } V\left(\boldsymbol{x}_{\text{free}}(\boldsymbol{t}), \boldsymbol{y}_{\text{free}}(\boldsymbol{t}), \boldsymbol{A}\right) \\ &\text{subject to } g_j\left(\boldsymbol{x}_{\text{free}}(\boldsymbol{t}), \boldsymbol{y}_{\text{free}}(\boldsymbol{t}), \boldsymbol{A}\right) \le 3\times10^{-3} - \varepsilon_j \bar{c}_j^{k+1},\ j = 3,5,7,9,11 \\ &\quad \underline{\boldsymbol{t}} \le \boldsymbol{t} \le \bar{\boldsymbol{t}};\ \underline{\boldsymbol{A}} \le \boldsymbol{A} \le \bar{\boldsymbol{A}}; \end{aligned} \tag{5.31}$$

where g_j is the vertical displacement of node j without uncertainty, and $\bar{c}_j^{k+1}$ is the shifting value on the upper bound of g_j at the (k+1)th iteration.

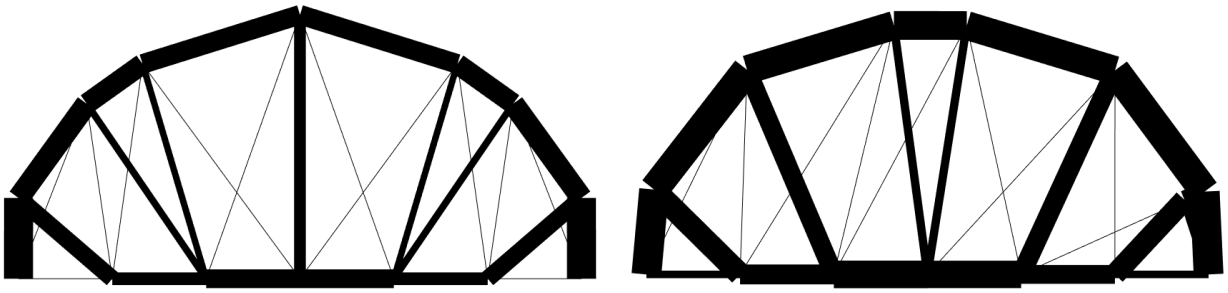

(a) (b)

Fig. 5-8 Results of Example 2 at: (a) initial iteration; (b) final iteration

The optimization procedure converged at k=34, and the results at the initial and final iteration are shown in Fig. 5-8. Table 5-8 shows the structural volumes and quantiles of the results at the initial and final iteration where the quantiles obtained by MCS are listed in the parentheses. The locations of nodes, force densities, cross-sectional areas and member lengths at the initial and final iteration are listed in Tables 5-9 and 5-10. We can see from Fig. 5-8(a) and Tables 5-9 and 5-10

that the structure obtained at the initial iteration is unstable in horizontal direction if the bending stiffness is small, and therefore the quantiles of vertical displacements of nodes 3, 5, 7, 9 and 11 are significantly larger than 3×10^{-3} m as shown in Table 5-8. The quantile functions of the displacements of these five nodes obtained by the proposed MEM and MCS are presented in Fig. 5-9(a) for the result at the initial iteration. It can be observed that the upper bound of the displacements 3×10^{-3} m corresponds to the probability of only about 0.4 for these five quantile functions, while the quantile functions obtained by the proposed MEM approximately fit those obtained by MCS. Moreover, the quantile Q_{R_7} of node 7 is smaller than quantiles Q_{R_j} of the other four nodes 3, 5, 9 and 11, which are indicated by the solid vertical line in Fig. 5-9(a). The main reason for this would be that node 7 is symmetrically connected by two thick horizontal members 12 and 17 and one vertical member 16, making the nodal stiffness less sensitive to the asymmetric uncertainties.

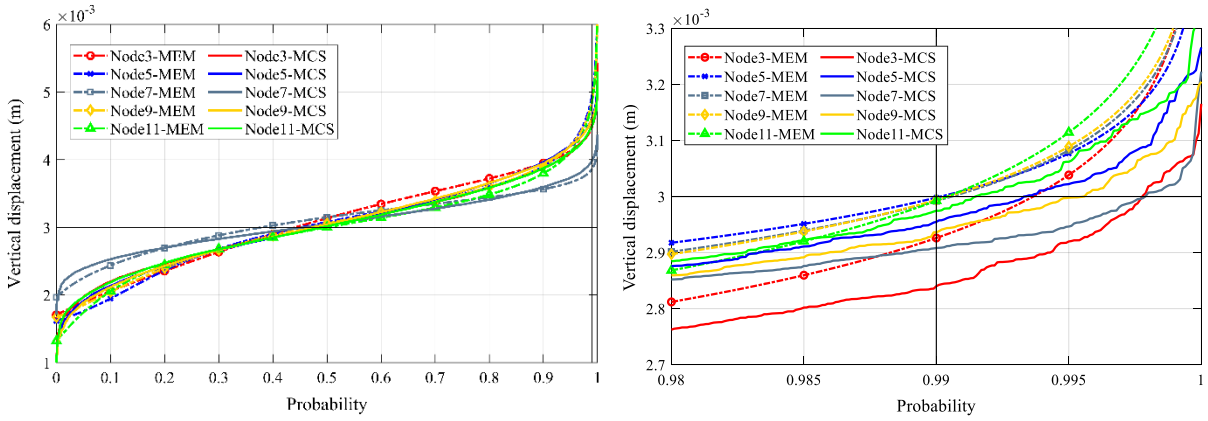

Fig. 5-9 Quantile functions of vertical displacements of nodes 3, 5, 7, 9 and 11 of Example 2 at the results of: (a) initial iteration; (b) final iteration

On the contrary, the result at the final iteration is stable in both vertical and horizontal directions due to the increase of cross-sectional areas of members 2 and 27 as shown in Fig. 5-8(b), Tables 5-9 and 5-10. Figure 5-9(b) displays the quantile functions of vertical displacements of nodes 3, 5, 7, 9 and 11 of the result at the final iteration. We can see from Table 5-8 and Fig. 5-9(b) that the relative error between quantile functions obtained by the proposed MEM with sample L-moments and MCS is around 3%. The equality holds for the displacement constraint of node 5, while the constraints of other four nodes are also satisfied with slightly higher reliability than the requirement.

Table 5-8 Structural volumes and quantiles Q_{R_j} of the results of Example 2 at the initial and final iterations

Result	Initial iteration	Final iteration
Structural volume (m^3)	0.2728	0.3861
Quantile Q_{R_3} (m)	4.490×10^{-3} (4.516×10^{-3})	2.926×10^{-3} (2.840×10^{-3})
Quantile Q_{R_5} (m)	4.962×10^{-3} (4.625×10^{-3})	3.0×10^{-3} (2.954×10^{-3})
Quantile Q_{R_7} (m)	3.866×10^{-3} (3.988×10^{-3})	2.992×10^{-3} (2.908×10^{-3})
Quantile Q_{R_9} (m)	4.883×10^{-3} (4.606×10^{-3})	2.994×10^{-3} (2.936×10^{-3})
Quantile $Q_{R_{11}}$ (m)	4.866×10^{-3} (4.502×10^{-3})	2.993×10^{-3} (2.974×10^{-3})

Table 5-9 Location of nodes of the results of Example 2 at initial and final iterations

Node	Initial iteration		Final iteration	
	x-coordinate (m)	*y*-coordinate (m)	*x*-coordinate (m)	*y*-coordinate (m)
1	0	0	0	0
2	0.00161	0.8611	0.0817	0.9028
3	1	0	1	0
4	0.7276	1.8660	1.0733	2.1766
5	2	0	2	0
6	1.3225	2.2903	2.6415	2.6477
7	3	0	3	0
8	3.0000	2.8149	3.4190	2.6472
9	4	0	4	0
10	4.6772	2.2904	5.0011	2.1695
11	5	0	5	0
12	5.2722	1.8662	5.9590	0.8813
13	6	0	6	0
14	5.9984	0.8611	5.7428	0.7927

Table 5-10 Force densities, cross-sectional areas and member lengths of the results of Example 2 at initial and final iterations

Member	Initial iteration			Final iteration		
	Force density (N/m)	Cross-sectional area (m^2)	Member length (m)	Force density (N/m)	Cross-sectional area (m^2)	Member length (m)
1	-4.2451	0.01950	0.8611	-8.0102	0.0200	0.9065
2	-0.4437	1.00×10^{-7}	1	-1.6791	0.005013	1
3	0.6192	1.00×10^{-7}	2.0029	2.1740	1.00×10^{-7}	2.4269
4	0.4073	0.01138	1.3184	-2.1750	0.01529	1.2878
5	0.30179	0.01476	1.2397	0.3018	0.02	1.6143
6	1.4748	1.00×10^{-7}	1.8858	6.1282	1.00×10^{-7}	2.1779
7	0.6607	0.00854	1	2.3062	0.01335	1
8	-0.9181	1.00×10^{-7}	2.3129	-3.9185	1.00×10^{-7}	3.1153
9	1.5906	0.004665	2.2585	0.78232	0.01277	2.3657
10	-0.1634	0.01388	0.7306	-0.1635	0.01931	1.6374
11	-0.4086	0.00433	2.3884	4.0304	1.00×10^{-7}	2.7243
12	2.7744	0.01255	1	6.5428	0.01847	1
13	-0.3667	1.00×10^{-7}	2.9873	-4.2966	1.00×10^{-7}	3.0036
14	-0.0961	1.00×10^{-7}	2.8389	2.1693	0.005614	2.6719
15	-0.0376	0.01315	1.7576	-0.0375	0.01925	0.7775
16	-0.06201	0.007858	2.8149	-4.9602	0.005586	2.6802
17	1.5919	0.01255	1	1.6626	0.01834	1
18	0.6089	1.00×10^{-7}	2.8388	3.8661	1.00×10^{-7}	2.9515
19	-0.2899	1.00×10^{-7}	2.9873	0.8785	1.00×10^{-7}	2.7103
20	0.2262	0.01314	1.7573	0.2263	0.01919	1.6526
21	-0.7517	0.004327	2.3884	-2.6384	0.01302	2.3894
22	-0.6006	0.008546	1	-4.9624	0.01254	1
23	1.8957	0.004668	2.2586	4.9905	1.00×10^{-7}	2.1482
24	0.6664	1.00×10^{-7}	2.3131	3.3449	1.00×10^{-7}	2.1695
25	-0.02156	0.01388	0.7307	-0.0215	0.0200	1.6053
26	0.01296	1.00×10^{-7}	1.8859	-1.2331	1.00×10^{-7}	1.3025
27	0.2494	1.00×10^{-7}	1	1.0612	0.005001	1
28	-0.6394	0.01138	1.3184	-6.5217	0.01441	1.0864
29	-0.3378	1.00×10^{-7}	2.0031	1.0221	0.0200	0.8823
30	0.1868	0.01476	1.23999	0.1868	0.01251	0.2336
31	-2.1711	0.01950	0.86109	-4.2898	0.006430	0.8334

Furthermore, in order to illustrate how Eq. (5.7) prevents obtaining a conservative result, Fig. 5-10 displays the iteration histories of the total structural volume, which is the objective function, and the maximum value of the five quantiles Q_{R_j} of the vertical displacements of nodes 3, 5, 7, 9 and 11, where the horizontal line represents the limit of displacement constraint (i.e., 3×10^{-3} m). As shown in Figs. 5-8 and 5-10, since the result at initial iteration is unstable in *x*-direction when the bending stiffness is small, the maximum value of the five quantiles Q_{R_j} at $k = 0$ is about 0.49

and large shifting values would be applied to the upper bounds of constraints for the next iteration where an extremely narrow feasible domain is constructed. Therefore, it can be expected that the result at k = 1 would have large structural volume to satisfy the displacement constraints, and as displayed in Fig. 5-10 the maximum value of the five quantiles Q_{R_j} for k=1 is far less than 3×10^{-3}m, which indicates the result is highly reliable. In order to prevent obtaining such excessively conservative result, the upper bounds of the constraints for the next iteration are relaxed by Eqs. (5.4) and (5.5), and we can see from Fig. 5-10 that the structural volume of the result at k = 2 is reduced compared to that at k = 1; however, the maximum value of the five quantiles Q_{R_j} also increases and exceeds 3×10^{-3}m. Hence, the quantile-based SORA procedure keeps going until stopping criteria Eq. (5.7) is reached, where the structural volume and the maximum value of the five quantiles Q_{R_j} increases and decreases alternatively. In this example the SORA procedure converged to the final result at k = 34 with all the constraints are satisfied and at least one of them holds equality. However, the structural volume is significantly reduced compared to the result at k = 1, showing that instead of obtaining a conservative result, a result with smaller objective value which satisfies all the reliability constraints can be found by using Eq. (5.7) as stopping criteria. Note that because none of the shifting values is smaller than $\overline{g}_j$, the five coefficients ε_j are always 1 according to Eq. (5.6).

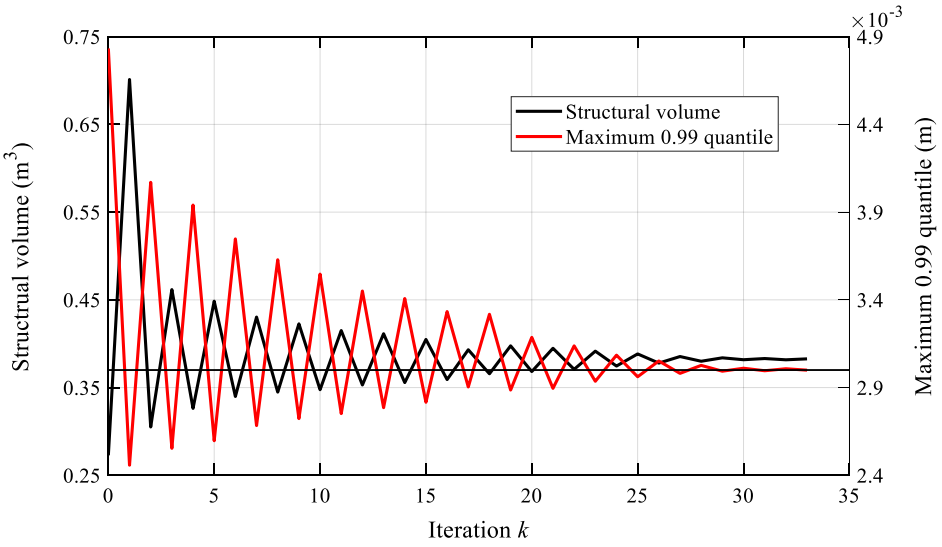

Fig. 5-10 Iteration histories of objective and maximum 0.99 quantile of constraints of Example 2

5.5.4 Example 3: Problem with displacement and buckling constraints in 5.4.2

The third example is to optimize a cantilever frame with same initial structure, supporting and loading conditions as in Example 1. Based on Table 5-1 and Eq. (5.23), the deterministic optimization problem at the (k+1)th iteration of quantile-based SORA is to minimize the structural

volume subject to constraints on global stability and downward vertical displacement of node 11, and the problem is formulated as

$$\begin{aligned} &\text{Minimize } V\left(\boldsymbol{x}_{\text{free}}(\boldsymbol{t}), \boldsymbol{y}_{\text{free}}(\boldsymbol{t}), \boldsymbol{A}\right) \\ &\text{subject to } g_{11}\left(\boldsymbol{x}_{\text{free}}(\boldsymbol{t}), \boldsymbol{y}_{\text{free}}(\boldsymbol{t}), \boldsymbol{A}\right) \le 3\times10^{-3} - \varepsilon_{11}\bar{c}_{11}^{k+1} \\ &\qquad \gamma^{\text{cr}}\left(\boldsymbol{x}_{\text{free}}(\boldsymbol{t}), \boldsymbol{y}_{\text{free}}(\boldsymbol{t}), \boldsymbol{A}\right) \le 0.05 - \varepsilon_{\gamma}\bar{c}_{\gamma}^{k+1};\ \underline{\boldsymbol{t}} \le \boldsymbol{t} \le \bar{\boldsymbol{t}};\ \underline{\boldsymbol{A}} \le \boldsymbol{A} \le \bar{\boldsymbol{A}}; \end{aligned} \tag{5.32}$$

The optimization procedure converged at k = 4, and the results at the initial and final iteration are presented in Fig. 5-11. The structural volumes and quantiles $Q_{R_{11}}$ and $Q_{R_{\gamma}}$ of the results at the initial and final iteration are listed in Table 5-11 in which the quantiles obtained by MCS are listed in the parentheses. The nodal locations, force densities, cross-sectional areas and member lengths are also given in Tables 5-12 and 5-13.

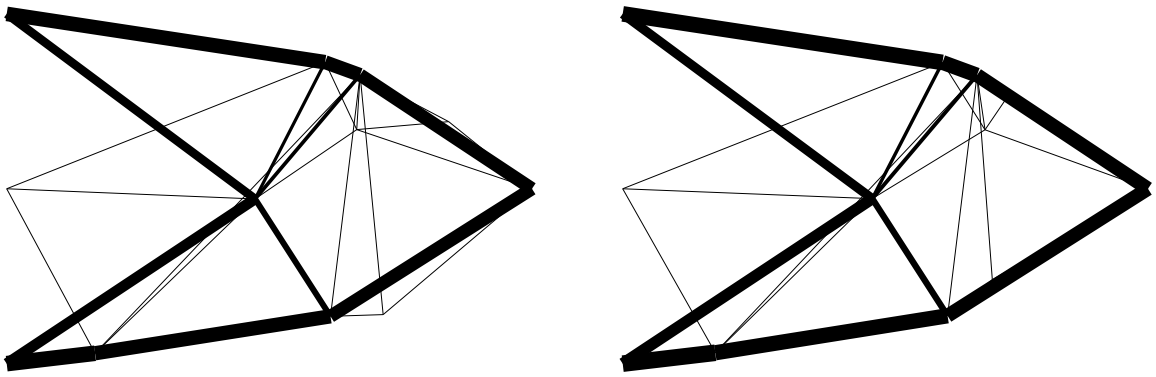

(a) (b)

Fig. 5-11 Results of Example 3 at: (a) initial iteration; (b) final iteration

Table 5-11 Structural volumes and quantiles $Q_{R_{11}}$ of the results of Example 3 at the initial and final iterations

Result	Initial iteration	Final iteration
Structural volume (m^3)	9.3190×10^{-2}	9.9652×10^{-2}
Quantile $Q_{R_{11}}$ (m)	3.2548×10^{-3} (3.2378×10^{-3})	2.9926×10^{-3} (2.9789×10^{-3})
Quantile $Q_{R_{\gamma}}$	6.6555×10^{-2} (6.0751×10^{-2})	5×10^{-2} (4.9815×10^{-2})

As we can see from Fig. 5-11 and Tables 5-11 to 5-13, although the results at the initial and final iteration have similar shapes, the cross-sectional areas of elements have increased at the final iteration to satisfy the constraints, leading to a larger structural volume and different structural

performance. Compared to the results obtained in Example 1, it is observed that when the global stability constraint is included, the structural volumes at the initial and final iteration are larger than those obtained without global stability constraint, respectively, while their shapes are similar to each other.

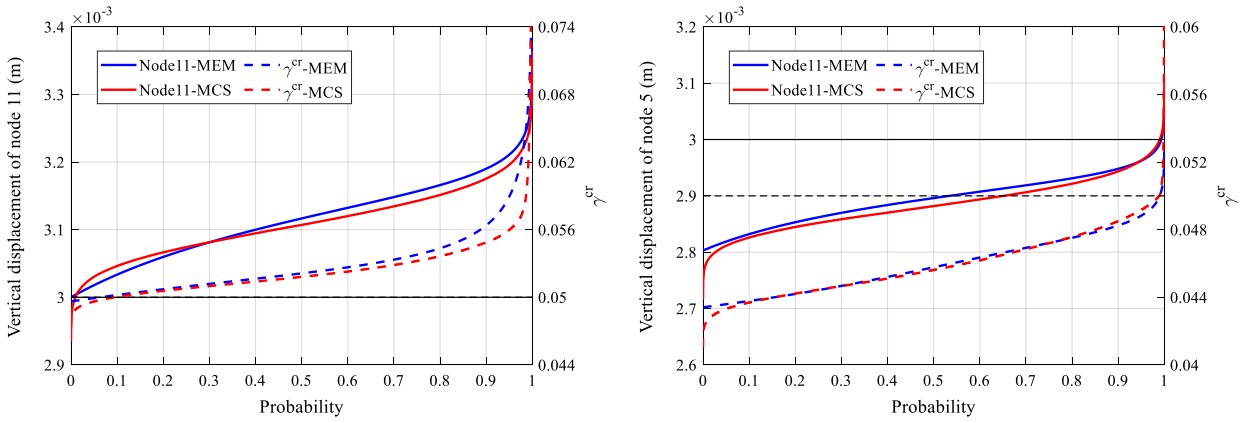

(a) (b)

Fig. 5-12 Quantile functions of vertical displacement of node 11 and global stability of Example 3 at the results of: (a) initial iteration; (b) final iteration

Table 5-12 Location of nodes of the results Example 3 at the initial and final iteration

Node	Initial iteration		Final iteration	
	x-coordinate (m)	*y*-coordinate (m)	*x*-coordinate (m)	*y*-coordinate (m)
1	0	0	0	0
2	0	1	0	1
3	0	2	0	2
4	0.5046	0.0594	0.5287	0.0622
5	1.4183	0.9417	1.4251	0.9435
6	1.8185	1.7237	1.8263	1.7224
7	1.8492	0.2706	1.8553	0.2738
8	2.0183	1.6508	2.0235	1.6499
9	1.9991	1.3383	2.0693	1.3373
10	2.1500	0.2804	2.1110	0.4799
11	3	1	3	1
12	2.5243	1.3838	2.2019	1.5325

Furthermore, the quantile functions of vertical displacement of node 11 and global stability are presented in Fig. 5-12 for the results at the initial and final iteration, where the quantile functions obtained by MCS are also included. It can be seen from Fig. 5-12 and Table 5-11 that at the initial iteration, both the probabilities of exceeding the limits $\bar{g}_{11} = 3\times10^{-3}\text{m}$ and $\bar{\gamma} = 0.5$ are over 0.9;

however, at the final iteration the quantiles of $Q_{R_{11}}$ and Q_{R_y} for both reliability constraints are satisfied with target probabilities listed in Table 5-1. Besides, compared to Fig. 5-5(a) in Example 1, the probability of vertical displacement of node 11 exceeding the upper bound in Fig. 5-12(a) is larger than that in Fig. 5-5(a). This is because in this example the uncertainties in nodal locations are not only considered in the two end nodes of the member, but also in the intermediate nodes along the member as discussed in Section 5.4.2, making the structural response more sensitive to the uncertainty.

Table 5-13 Force densities, cross-sectional areas and member lengths of the results of Example 3 at the initial and final iterations

Member	Initial iteration			Final iteration		
	Force density (N/m)	Cross-sectional area (m^2)	Member length (m)	Force density (N/m)	Cross-sectional area (m^2)	Member length (m)
1	-2.5317	0.01067	0.5081	-2.5095	0.01135	0.5324
2	0.5260	0.0098	1.3610	0.4951	0.01046	1.3433
3	0.5616	1.00×10^{-7}	0.3009	0.6733	1.00×10^{-7}	0.3284
4	0.2360	1.00×10^{-7}	1.4195	0.2448	1.00×10^{-7}	1.4262
5	0.4526	0.002526	0.9288	0.5024	0.002665	0.9257
6	0.3017	0.009038	1.1778	-0.0333	0.009664	1.1729
7	-0.3780	0.010006	1.8394	-0.3955	0.01073	1.8472
8	-1.4593	1.00×10^{-7}	0.4256	-1.4349	1.00×10^{-7}	0.4553
9	0.3531	1.00×10^{-7}	0.5271	0.01065	1.28×10^{-7}	0.2360
10	-1.0288	1.00×10^{-7}	1.2701	-1.1026	1.00×10^{-7}	1.2570
11	-0.2141	1.00×10^{-7}	1.3905	-0.3370	1.00×10^{-7}	1.3863
12	0.1844	1.00×10^{-7}	1.1136	0.19672	1.00×10^{-7}	1.02990
13	0.6330	0.002183	0.8784	0.62648	0.002332	0.8761
14	2.04083	1.00×10^{-7}	0.3131	2.0854	1.00×10^{-7}	0.3159
15	-0.8579	2.44×10^{-7}	0.6112	-0.3943	1.9257×10^{-7}	0.9594
16	1.4628	0.007401	1.7025	1.4743	0.007857	1.7091
17	1.1859	1.00×10^{-7}	1.0674	1.1791	1.00×10^{-7}	1.0765
18	-0.2949	1.00×10^{-7}	2.1963	-0.2487	1.00×10^{-7}	2.1806
19	0.03922	0.004095	0.7974	0.09156	0.004352	0.7959
20	0.51392	0.008948	1.3624	0.5073	0.009566	1.3555
21	-0.0928	1.00×10^{-7}	1.3767	0.03121	7.64×10^{-7}	1.1731
22	0.01814	1.00×10^{-7}	1.9572	-0.00013	1.00×10^{-7}	1.963
23	-0.4770	0.005956	1.7696	-0.4710	0.006369	1.7740
24	0.43262	1.00×10^{-7}	0.7032	0.3088	1.00×10^{-7}	0.7549
25	-0.6887	0.009572	0.2127	-0.6216	0.01025	0.2101
26	-1.1730	3.68×10^{-7}	0.5720	-1.7719	1.9339×10^{-7}	0.2135
27	-0.2367	1.00×10^{-7}	1.0565	-0.05994	1.00×10^{-7}	0.9899

5.5.5 Example 4: Problem with displacement and buckling constraints in 5.4.2

The last example is to investigate the optimal shape and topology of a bridge frame which has the same initial structure, supporting and loading conditions as in Example 2. The optimization problem is to minimize the structural volume subject to constraints on the downward vertical displacements of nodes 3, 5, 7, 9 and 11 and global stability. According to Eq. (5.23) and Table 5-1, the (k+1)th optimization problem of quantile-based SORA is formulated as

$$\begin{aligned} &\text{Minimize } V\left(\boldsymbol{x}_{\text{free}}(\boldsymbol{t}), \boldsymbol{y}_{\text{free}}(\boldsymbol{t}), \boldsymbol{A}\right) \\ &\text{subject to } g_j\left(\boldsymbol{x}_{\text{free}}(\boldsymbol{t}), \boldsymbol{y}_{\text{free}}(\boldsymbol{t}), \boldsymbol{A}\right) \le 3\times10^{-3} - \varepsilon_j \bar{c}_j^{k+1},\ j = 3,5,7,9,11 \\ &\qquad \gamma^{\text{cr}}\left(\boldsymbol{x}_{\text{free}}(\boldsymbol{t}), \boldsymbol{y}_{\text{free}}(\boldsymbol{t}), \boldsymbol{A}\right) \le 0.05 - \varepsilon_\gamma \bar{c}_\gamma^{k+1};\ \underline{\boldsymbol{t}} \le \boldsymbol{t} \le \bar{\boldsymbol{t}};\ \underline{\boldsymbol{A}} \le \boldsymbol{A} \le \bar{\boldsymbol{A}}; \end{aligned} \tag{5.33}$$

The optimization procedure converged at k = 59, and the results at the initial and final iterations are presented in Fig. 5-13. Table 5-14 lists the structural volumes and quantiles $Q_{R_j}\left(j = 3,5,7,9,11\right)$ and Q_{R_γ} of the results at the initial and final iteration where those obtained by MCS are given within the parenthesis. The locations of nodes, force densities, cross-sectional areas and member lengths are listed in Tables 5-15 and Table 5-16.

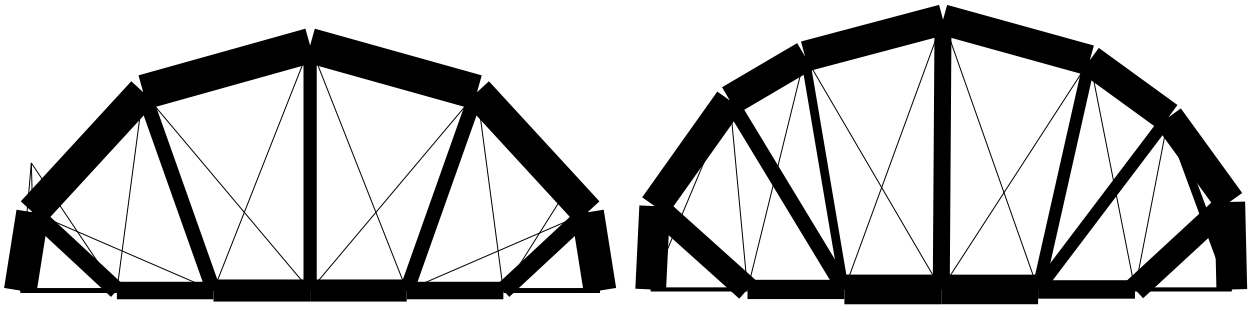

(a) (b)

Fig. 5-13 Results of Example 4 at: (a) initial iteration; (b) final iteration

Compared to the result at the initial iteration of Example 2 shown in Fig. 5-8(a), the structure in Fig. 5-13(a) is stable in both x- and y-directions due to the inclusion of global stability constraint in problem (5.33). The structural volume also increased to 0.2899 m^3 which is about 6.3% larger than that listed in Table 5-8. However, the quantiles $Q_{R_j}\left(j = 3,5,7,9,11\right)$ listed in Table 5-14 are all larger than the corresponding values in Table 5-8 of Example 2, which is similar to the comparison of quantiles of displacements of nodes 11 between Examples 1 and 3. The main reason may also be the consideration of uncertainties in the locations of intermediate nodes of members in problem (5.33). The quantile functions of the displacements of these five nodes and global stability are presented in Fig. 5-14(a) for the result at initial iteration, in which the solid and dashed horizontal lines represent the upper bounds for displacement and global stability constraints,

respectively. Similar to Fig. 5-9(a) in Example 2, since node 7 is connected by three thick members 12, 16 and 17, the frame will be less influenced by the uncertainties and has the smallest quantile Q_{R_7} of vertical displacement among these five nodes.

Table 5-14 Structural volumes and quantiles Q_{R_j} of the results of Example 4 at the initial and final iterations

Result	Initial iteration	Final iteration
Structural volume (m^3)	0.2899	0.4089
Quantile Q_{R_3} (m)	5.0161×10^{-3} (4.9594×10^{-3})	2.6982×10^{-3} (2.6932×10^{-3})
Quantile Q_{R_5} (m)	5.4799×10^{-3} (5.2825×10^{-3})	2.5572×10^{-3} (2.5558×10^{-3})
Quantile Q_{R_7} (m)	4.7125×10^{-3} (4.5265×10^{-3})	3×10^{-3} (2.9941×10^{-3})
Quantile Q_{R_9} (m)	5.6177×10^{-3} (5.2786×10^{-3})	2.8440×10^{-3} (2.8547×10^{-3})
Quantile $Q_{R_{11}}$ (m)	6.1215×10^{-3} (5.7181×10^{-3})	2.8955×10^{-3} (2.8036×10^{-3})
Quantile Q_{R_y}	5.2116×10^{-2} (5.1335×10^{-2})	3.5231×10^{-2} (3.6008×10^{-2})

Table 5-15 Locations of nodes of the results of Example 4 at initial and final iterations

Node	Initial iteration		Final iteration	
	x-coordinate (m)	*y*-coordinate (m)	*x*-coordinate (m)	*y*-coordinate (m)
1	0	0	0	0
2	0.1145	1.3210	0.04184	0.8624
3	1	0	1	0
4	0.1284	0.8102	0.8173	1.9570
5	2	0	2	0
6	1.2724	2.0538	1.5929	2.4143
7	3	0	3	0
8	3.0000	2.5370	3.0186	2.7936
9	4	0	4	0
10	4.7276	2.0538	4.5333	2.3730
11	5	0	5	0
12	5.8716	0.8102	5.3451	1.7818
13	6	0	6	0
14	5.680	1.0813	5.9785	0.9060

Table 5-16 Force densities, cross-sectional areas and member lengths of the results of Example 4 at initial and final iterations

Member	Initial iteration			Final iteration		
	Force density (N/m)	Cross-sectional area (m^2)	Member length (m)	Force density (N/m)	Cross-sectional area (m^2)	Member length (m)
1	-3.5482	1.00×10^{-7}	1.3259	-12.7318	0.02	0.8634
2	0.05967	0.002781	1	-3.0087	0.0027	1
3	2.6996	0.01838	0.8203	4.3328	1.00×10^{-7}	2.1208
4	0.8656	1.00×10^{-7}	1.5903	-4.4735	0.01614	1.2891
5	-0.1519	1.00×10^{-7}	0.5109	-0.1519	0.02	1.3415
6	0.2983	0.009777	1.1901	9.2649	1.00×10^{-7}	1.9655
7	1.1373	0.009830	1	-2.3428	0.01256	1
8	-0.1875	1.00×10^{-7}	2.0717	-5.4980	1.00×10^{-7}	2.4860
9	0.7001	1.00×10^{-7}	2.0394	-2.2410	0.00975	2.2866
10	-0.00071963	0.01815	1.6897	-0.0007190	0.02	0.9003
11	0.3248	0.008201	2.1789	5.8366	0.005683	2.4483
12	2.7764	0.01242	1	0.5568	0.01937	1
13	-0.09239	1.00×10^{-7}	2.7270	-3.1163	1.00×10^{-7}	2.9734
14	0.4847	1.00×10^{-7}	2.6838	6.1722	2.74×10^{-7}	2.7944
15	0.1919	0.01965	1.7939	0.1918	0.02	1.4752
16	-0.8754	0.007428	2.5370	-5.2474	0.01105	2.7936
17	1.7418	0.01241	1	8.8494	0.01929	1
18	1.0835	1.00×10^{-7}	2.6838	0.3192	1.00×10^{-7}	2.8253
19	0.01611	1.00×10^{-7}	2.7270	-9.1797	1.00×10^{-7}	2.9609
20	-0.1081	0.01964	1.7939	-0.1081	0.02	1.5720
21	0.4574	0.008201	2.1789	11.9002	0.007966	2.4322
22	1.3799	0.009829	1	-5.3019	0.01204	1
23	0.02414	1.00×10^{-7}	2.0395	-0.8953	0.007978	2.2325
24	0.07711	1.00×10^{-7}	2.0718	-0.3331	1.00×10^{-7}	2.4184
25	0.2903	0.01815	1.6897	0.2902	0.02	1.0042
26	-0.6404	0.009776	1.1900	3.7135	1.00×10^{-7}	1.8149
27	1.1027	0.002781	1	-1.5264	0.0027	1
28	1.2582	1.00×10^{-7}	1.2777	-5.3269	0.01564	1.3336
29	3.2862	0.01838	0.8203	2.5879	0.005636	1.8983
30	-0.07498	1.00×10^{-7}	0.3315	-0.07498	0.02	1.0808
31	-4.7744	1.00×10^{-7}	1.1274	-7.8486	0.02	0.9063

On the other hand, the result at the final iteration has different shape and topology from the result at the initial iteration, and the corresponding quantile functions of the displacements of nodes 3, 5, 7, 9 and 11 and global stability are presented in Fig. 5-14(b). It can be observed from Fig. 5-14 and Table 5-14 that for the result at final iteration, only the displacement constraint of node 7 is active and the quantile Q_{R_γ} is much smaller than the limit $\bar{\gamma}=0.05$, indicating that the global stability can be enhanced to some extent by applying displacement constraints on some nodes of

the structure. This phenomenon is also mentioned in the Ref. [61] by discussing the relation between nodal and global stabilities. Therefore, in this example the reliability of global stability is higher than those of displacements of nodes 3, 5, 7, 9 and 11, and all the constraints are satisfied with a equality on the displacement constraint of node 7.

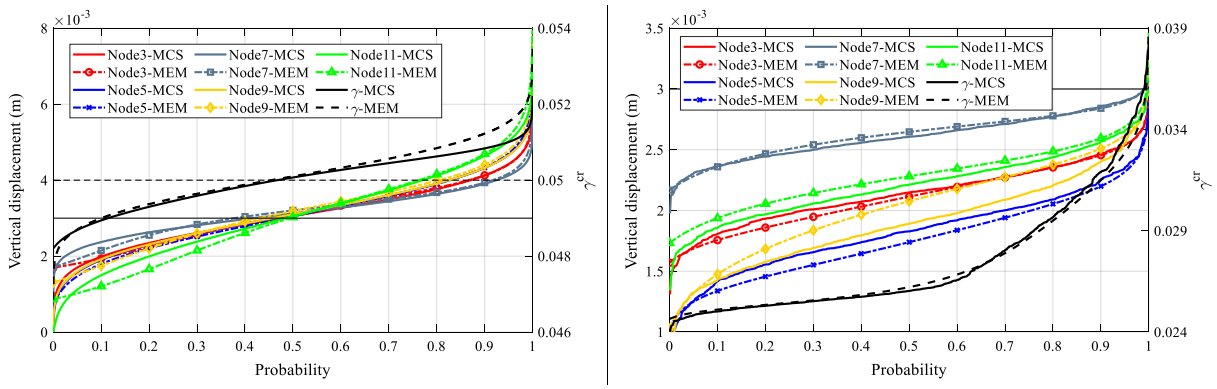

(a) (b)

Fig. 5-14 Quantile functions of vertical displacements of nodes 3, 5, 7, 9 and 11 and global stability of Example 4 at the results of: (a) initial iteration; (b) final iteration

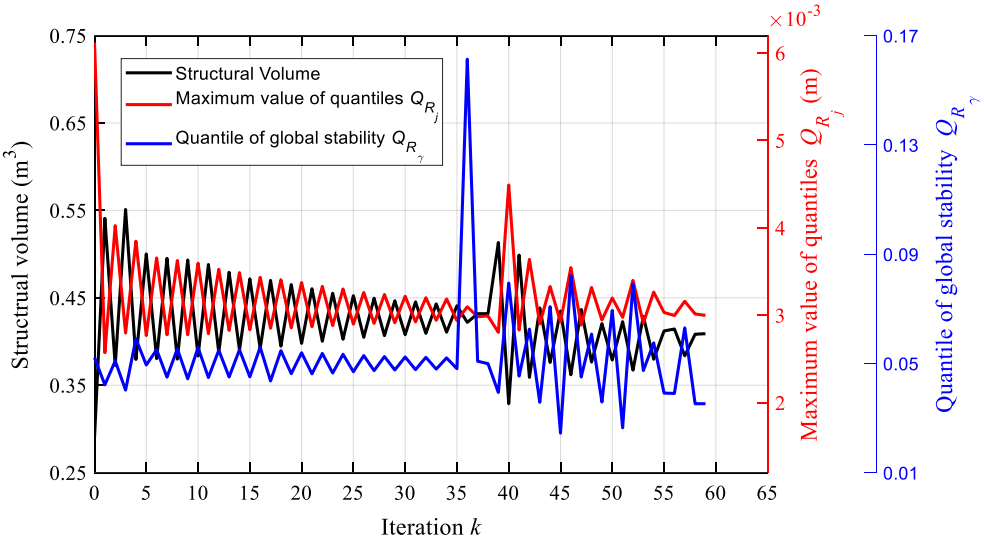

Fig. 5-15 Iteration histories of objective and maximum 0.99 quantile of constraints of Example 4

Moreover, Fig. 5-15 displays the iteration histories of the total structural volume, maximum value of quantiles $Q_{R_j}\left(j=3,5,7,9,11\right)$ of displacements and quantile Q_{R_γ} of global stability. It can be seen from Fig. 5-15 that at k = 0 the maximum value of the five quantiles Q_{R_j} is larger than

6×10^{-3} m, resulting in a shifting value greater than the limit $\bar{g}_j = 3\times10^{-3}\text{m}$. Hence, based on Eq. (5.6), the reduction coefficient ε_j in problem (5.33) is 0.5 to avoid drastically shifting the limit of the constraint. Similarly, as for quantile Q_{R_γ} of global stability, it is close to 0.17 at k = 37 which results in a shifting value greater than twice of the limit $\bar{\gamma} = 0.05$, and then the reduction coefficient ε_γ is 0.1 according to Eq. (5.6) to smoothly continue the optimization procedure. Compared to Fig. 5-10 in Example 2, although the iteration histories of objective and maximum 0.99 quantile of constraints in Fig. 5-15 are more oscillatory, it is also able to converge to the final result, where Eq. (5.6) is used to alleviate the oscillation caused by the large shifting values on the limit of constraints. Besides, the structural volume at the final iteration is smaller than that at k = 1 with all the constraints satisfied, showing the effectiveness of stopping criteria Eq. (5.7) to prevent obtaining conservative result in the same manner as Example 2.

5.6 Conclusions

In this chapter a quantile-based SORA is proposed for reliability-based shape and topology optimization of plane frames. The shifting value on the limit of constraint is calculated in terms of quantile, and a reduction coefficient is employed to avoid drastic shifting. The MEM subject to sample L-moments is integrated to estimate the density-quantile function of constraint, and the original MEM problem is solved by using Lagrangian multiplier method, while the unknown Lagrangian multipliers are determined by solving an unconstrained convex optimization problem. Then the quantile function is obtained by integrating the corresponding density-quantile function. Moreover, two stopping criteria are used to prevent obtaining excessively conservative result. Based on the above framework, two kinds of optimization problems is formulated. One is to minimize the structural volume under single or multiple displacement constraints, and the other is to minimize the structural volume under both displacement and global stability constraints, on which a penalization method is applied to exclude pseudo buckling modes by using approximate Heaviside function. For each problem formulation two numerical examples are investigated to illustrate effectiveness of the proposed method, and the conclusions are drawn as follows:

(1) The proposed method is able to obtain an optimal result satisfying single or multiple reliability constraints, and the quantile function of the constraint can be properly estimated using MEM subject to sample L-moment constraints, while the number of samples for estimating the quantiles are limited to a small size.

(2) An excessively conservative result can be avoided by the proposed stopping criteria, and the drastic shifting on the limit of constraint is also alleviated by the reduction coefficient when the structure is sensitive to the uncertainty.

(3) It can be seen from Examples 2 and 4 that compared to the iteration history of optimization procedure without global stability constraint, the one with global stability constraint is more oscillatory mainly due to the jump of quantile of global stability. However, it is also able to converge to a feasible optimal result where the structure is more stable than the requirement as

shown in Table 5-14, indicating that the global stability could be enhanced to some extent by applying displacement constraints on some nodes of the structure.

Chapter 6

Summaries and future study

6.1 Summaries

This research focuses on exploring new shape and topology optimization methods and problem formulations for frame structures considering uncertainties in variables and parameters. In order to alleviate difficulty due to melting nodes when shape optimization is considered, FDM is introduced to indirectly control the member length by limiting force density, where an auxiliary pin-jointed structure is used for applying FDM to determine the shape of frame structure to be optimized. Moreover, since uncertainties are unavoidable in the real physical world, and their distribution information are usually unknown in the early stage of design process, order statistics and the corresponding L-moments are employed into the problem formulations of RSO and RBSO, respectively, to assess the structural robustness and reliability in which no prior assumption is made on the distribution information of uncertainty. Besides, global stability constraint is also included by implementing linear buckling analysis, and the penalization method is used to handle the singularity phenomenon due to superficial member buckling. Chapter 1 gives the background and literature review of the present research, and the summaries of Chapters 2-5 are listed as follows.

Chapter 2 introduces some concepts and techniques which will be used for optimization of frame structures in this research. First, the basic idea of FDM is given with definitions of force density, connectivity matrix and fixed and free nodes. Unlike traditional FDM, the fixed nodes are defined as the supporting nodes, loading nodes and the nodes with specific requirements, and the locations of free nodes are obtained by solving equilibrium equations, which will be used for shape optimization of frame structure in Chapters 3-5. Second, in order to conveniently approximate maximum structural response, the order statistics of structural response under uncertainty is defined in a descending order, and some useful properties of order statistics are also discussed to derive the theory of distribution-free tolerance interval, which will be used to define the structural robustness in Chapter 4. Based on the order statistics, the calculations of L-moments and sample L-moments are also given, and they will be used to estimate the structural reliability in Chapter 5. Third, the detailed implementations of modeling uncertainties in nodal locations, cross-sectional areas and Young's modulus are illustrated, where no assumption is made on their distribution information, and they will be incorporated into RSO and RBSO problems in Chapters 4 and 5, respectively. Finally, a simple example is used to demonstrate the singularity phenomenon in

global stability, which is caused by the negative contributions of geometrical stiffness matrices of thin elements to the global geometrical stiffness matrix.

Chapter 3 presents a new method for simultaneous optimization of shape, topology and cross section of plane frames. Compliance against specified loads is minimized under volume constraint. Difficulty caused by the melting nodes can be alleviated to some extent by introducing force densities as design variables for defining the geometry, where the side constraints are assigned for force densities to indirectly avoid the existences of extremely short members. Sensitivity coefficients of the objective and constraint functions with respect to the design variables are also explicitly calculated. After the optimal shape and cross-section of the frame are obtained, the shape and topology are further improved by removing the thin members and combining closely spaced nodes. In the numerical examples, two kinds of optimization problems Case N and Case P with negative and positive lower bound for force density, respectively, are solved to find the optimal results. It is shown that in both problems rational shape and topology of frame structure can be achieved using the proposed method, while Case P is more stable than Case N, and the effect of bending moment on the optimal solution is also discussed.

Chapter 4 presents a worst-case approach to RSO problem of plane frames. Since the exact worst value of structural response is difficult to calculate, it is firstly relaxed to a quantile response. Then, based on the distribution-free one-side tolerance theory in order statistics, the quantile response is further approximated by the kth order statistic with given confidence level. Therefore, the structural robustness is represented by the kth order statistic and the corresponding order k. With this robustness definition, two kinds of RSO problems are formulated and for each problem formulation, two numerical examples are investigated to illustrate its effectiveness. On the one hand, a single-objective optimization is proposed to minimize the structural stress under volume and global stability constraints, and the FDM is introduced for determining the shape of frame structure. The singularity phenomenon due to superficial member buckling is alleviated by the penalization method which is confirmed by a simple example. It is shown in the numerical examples that the solution of robust optimization obtained by the proposed method is less sensitive to the uncertainty, and the stability constraint is also satisfied under uncertainty with the specified robustness and confidence level. On the other hand, a multi-objective optimization is proposed to minimize the structural stress at various robustness levels with structural volume constraint, where the order statistics or trimmed means of the response values are served as multiple objectives, together with the response value without considering uncertainty. The optimization procedure consists of two stage. In the first stage, the design variables are selected as nodal locations and cross-sectional areas, and the single-objective optimization problem is solved without uncertainty. Based on the optimal solution of the first stage, we select only cross-sectional areas as design variables and solve the multi-objective optimization problem. Examples show that optimal topology of the structure varies with the change of robustness level, and the convergence by using trimmed mean as indicator of structural robustness is better than that of the simple order statistics.

Chapter 5 presents a quantile-based SORA method for RBSO problem of plane frames. The reliability constraint is expressed in terms of quantile response with specified reliability, and the original RBSO problem is transformed into a series of deterministic optimization problems by

using the framework of SORA. Two stopping criteria are proposed to prevent obtaining an excessively conservative result with high reliability, which requires the satisfaction of all the constraints and at least one of the constraints holds in equality. The shifting value on the constraint limit is also calculated based on the quantile response, and a reduction coefficient is used to avoid oscillation caused by drastic change of the shifting value. The quantile response with specified reliability is estimated as follows: first the density-quantile function (i.e., the derivative of quantile function) is estimated using MEM subject to sample L-moments, which is less influenced by the sample size than traditional sample central moments. The MEM problem is solved by Lagrangian multiplier method, and the unknown Lagrangian multipliers are determined by further solving an unconstrained convex problem. Then, the quantile response is obtained by integrating the density-quantile function to the specified reliability. Besides, the FDM is also introduced for shape optimization to alleviate the difficulty caused by the existences of extremely short members. Based on the proposed quantile-based SORA method, two kinds of optimization problems are formulated. One is to minimize the structural volume with only displacement constraint, and the other is with both displacement and global stability constraints. In order to solve the problems using SQP, approximate Heaviside function is incorporated as penalization method to exclude the pseudo buckling mode, and the corresponding formulations of sensitivity coefficients are also derived. For each problem formulation two numerical examples are investigated to illustrate its effectiveness, and comparisons between the examples are also made to discuss the influence of global stability constraint on the optimal result and convergence property of SORA. It is shown that the result satisfying the reliability constraints can be found by both methods, and excessively conservative results can be avoided using the proposed stopping criteria. Compared to the optimization problem with only displacement constraints, the optimization procedure of the problem with displacement and global stability constraints is more oscillatory due to the drastic shifting on linear buckling load factor; however, such difficulty can be alleviated to some extent using the proposed reduction coefficient, and the optimization procedure is also able to converge to a feasible result.

6.2 Future studies

In the present research, various methods are proposed for shape and topology optimization of frame structures and their performances are investigated by a number of 2-dimensional examples. However, the uncertainties in RSO and RBSO problems are only considered in the structural and material properties. Therefore, some simple suggestions for the future study can be accordingly given as follows:

- Extending the proposed methods to 3-dimensional optimization problems.
- Considering the uncertainty in loading direction or magnitude.
- Applying the methods of RSO and RBSO to continuum structures.

In addition, in Chapter 3 the shape and topology optimization of frame structure is considered only in linear elastic case, where Young's modulus of each member is invariant during deformation. However, in practical engineering the material will exhibit inelastic or nonlinear behavior, which

is usually described by a path-dependent material model. Moreover, the external load considered in the present research is static, where dynamic excitation, such as earthquake or wind load, is also important in the structural design process, which results in a time-dependent structural response. Therefore, in order to make the results more applicable to design practice, for further study it is suggested to include the material nonlinearity and dynamic property of loads into the structural optimization problem. Existing studies have been contributed to considering optimization of nonlinear and dynamic structure systems, and a number of techniques are proposed for the design sensitivity analysis or heuristic optimization algorithms [150–154]. However, balancing the accuracy and efficiency is still a challenging work due to the fact that the path-dependent structural deformation is discontinuous and even non-differential [155]. The number of constraints rapidly increases because structural responses are evaluated at a number of time points in the time history, leading to a large computational effort [156]. One of the possible alternatives is to use a simplified and equivalent model and methodology to respectively describe the material nonlinearity and dynamical structural response, and efforts can be made in the future study to improve and provide more appropriate and easy-to-use approaches.

As for RSO problem using worst-case approach, although the optimal results obtained by the proposed methods are robust under uncertainty, it can be seen in Chapter 4 that the computational cost is expensive and the problem is limited to a small size. Its main reason is that for each objective and constraint evaluation, the number of FEA processes is equal to the sample size of order statistics, and it will increase with the increase of structural robustness and confidence level. Moreover, as discussed by Sigmund [157], when the sensitivity analysis is available for both objective and constraint functions, one should solve the optimization problem by a gradient-based method rather than a non-gradient method due to its computational efficiency. Therefore, in order to make the worst-case approach applicable to large-scale problems, in the future study it is suggested that asymptotic analysis or truncated approximation of structural response could be used to replace the real FEA for generating order statistics to save computational time [158], where the analytical or semi-analytical sensitivity analysis under uncertainty can be efficiently derived. Besides, due to the development of machine learning in the field of structural optimization, some researchers have applied the so-called stochastic gradient method to RSO and RBSO problems to reduce the computational costs, and Yamakawa and Ohsaki [97] discussed the applicability of order statistics-based method for fail-safe topology optimization by using stochastic gradient method. Further study can be implemented on this direction by enhancing its efficiency and accuracy

It is worth noting that for RBSO problem, not only the component reliability but also the system reliability has been the main concern for researchers and engineers, while in Chapter 5 only the component reliability is discussed in RBSO. Moreover, the structural reliability may vary due to time-variant operation condition and structural deterioration throughout the life-cycle of the structure, and thus including time-variant reliability constraint in RBSO problem is also important in practical engineering applications [159]. One of the main difficulties for considering system and time-variant reliability constraints is the high computational cost on handling dependent failure events among different components or time-variant limit states. Therefore, in the future study it is suggested to explore the possibility of efficiently implementing system and time-variant reliability

analysis using order statistics and L-moments, whereas some researches have proposed to accurately calculate the failure probability of extreme event using order statistics [160].

Appendix

A1 Optimization procedure of Example 1 in Chapter 3

The intermediate solutions in optimization procedure of Example 1 in Chapter 3 with $\bar{V} = 1\text{m}^3$ are shown in Figs. A1 and A2 for Cases P and N, respectively. The red and blue colors of members stand for positive and negative member forces, respectively. The figure at the top-right of Fig. A2 is trimmed to be consistent with the others, although some of the nodes and members are cut off. As seen from Figs. A1 and A2, in Case N the structure undergoes drastic variation at the beginning mainly due to the change of signs of the force densities; on the other hand, iteration in optimization procedure with Case P has "smoother" shape variation leading to a monotonic convergence to the solution.

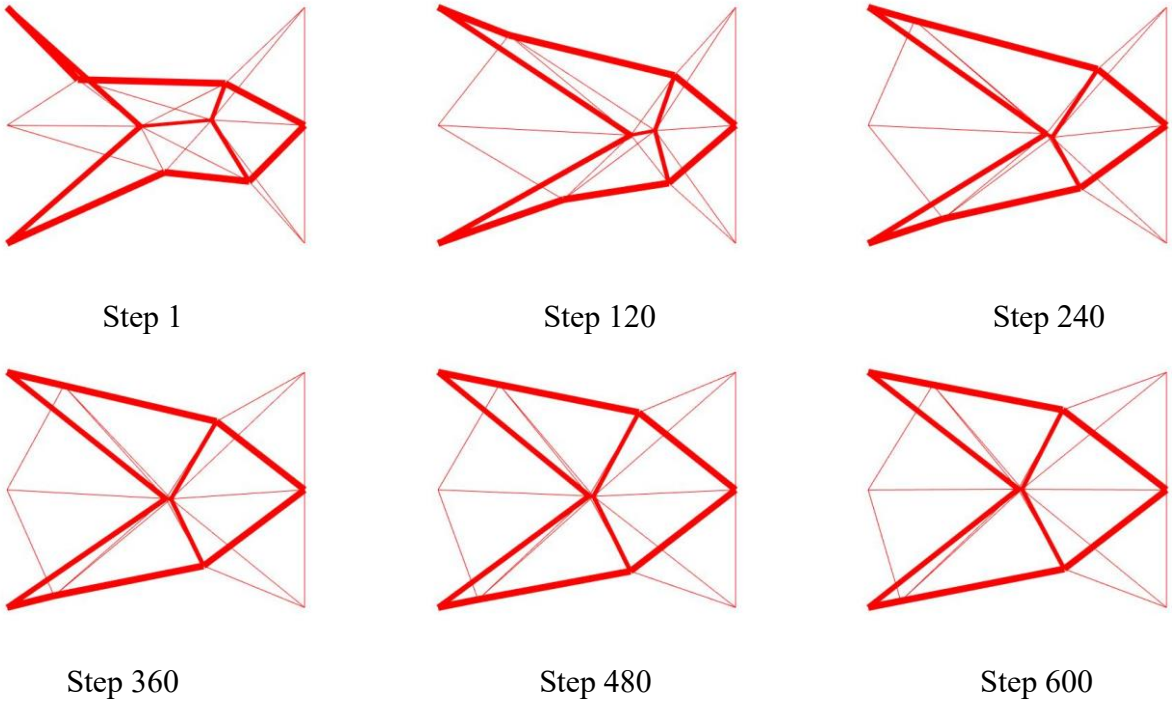

Fig. A1 Intermediate solutions of Example 1 in Chapter 3 for Case P

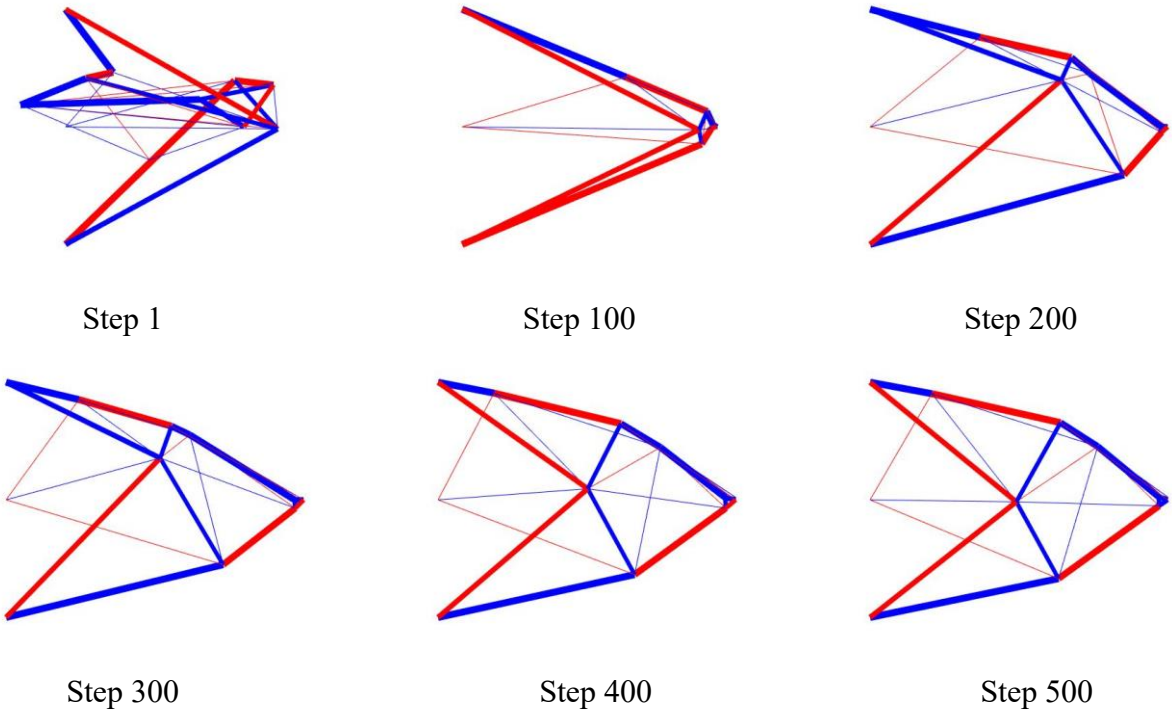

Fig. A2 Intermediate solutions of Example 1 in Chapter 3 for Case N

A2 Statistical investigation of Example 1 in Chapter 4

According to Eq. (4.1), the confidence level α_k of the first order statistic (k = 1) with sample size m_s=150 to approximate the 95% quantile should be 0.9995, which means the probabilities of $\sigma_{1:150}$ and $\gamma_{1:150}$ no less than the corresponding 95% quantiles should be no less than 0.9995. In order to verify this property, a total of 1000 random seeds are used to generate 1000 groups of 150 samples for the uncertainties to investigate the variations of solution R of Example 1 in Chapter 4 due to difference in sample sets. The mean values, standard deviations, maximum and minimum values of $\sigma_{1:150}$ and $\gamma_{1:150}$ are listed in Table A1. The values of 95% quantiles of σ and γ obtained by MCS with sample size 1×10^4 are also listed in Table A1. Based on the results of $\sigma_{1:150}$ and $\gamma_{1:150}$ from the 1000 groups of 150 samples, the number of $\sigma_{1:150}$ less than 226.315 MPa is 2 and the number of $\gamma_{1:150}$ less than 0.0904 is 0, indicating that the confidence levels of both of $\sigma_{1:150}$ and $\gamma_{1:150}$ approximating the 95% quantile are greater than 0.9995 for the solution R. Moreover, because the order statistics $\sigma_{1:150}$ and $\gamma_{1:150}$ approximate the extreme quantiles at the tails of the unknown distributions, the mean values of $\sigma_{1:150}$ and $\gamma_{1:150}$ from 1000 groups of 150 samples should be greater than the corresponding 99.3% quantiles using the connection between the order statistics of standard uniform distribution and arbitrary distribution, which is written as

$$
\begin{aligned}
&F_\sigma\left(\frac{1}{1000}\sum_{i=1}^{1000}\sigma_{1:150}^{i}\right)\geq\frac{1}{1000}\sum_{i=1}^{1000}F_\sigma\left(\sigma_{1:150}^{i}\right)\approx\mathrm{E}\left(F_\sigma\left(\sigma_{1:150}\right)\right)=\mathrm{E}\left(U_{1:150}\right)=0.993\\
&F_\gamma\left(\frac{1}{1000}\sum_{i=1}^{1000}\gamma_{1:150}^{i}\right)\geq\frac{1}{1000}\sum_{i=1}^{1000}F_\gamma\left(\gamma_{1:150}^{i}\right)\approx\mathrm{E}\left(F_\gamma\left(\gamma_{1:150}\right)\right)=\mathrm{E}\left(U_{1:150}\right)=0.993
\end{aligned}
\tag{A1}
$$

where F_σ and F_γ are the CDFs corresponding to σ and γ^{cr} in Eq. (4.7), respectively, and E in Eq. (A1) represents the expectation operator as in Section 2.3; $U_{1:150}$ represents the first order statistic of standard uniform distribution with sample size 150. Comparing the results listed in Table A1, it can be seen that the mean values of $\sigma_{1:150}$ and $\gamma_{1:150}$ are all greater than the corresponding 99.3% quantiles, indicating that solution R of Example 1 in Chapter 4 is able to preserve the robustness of the structure under different sample sets in statistical sense. Besides, it should be noted that there might be an over-fitting phenomenon if the same uncertainty set is used during optimization procedure; however, the statistical property of solution R of Example 1 in Chapter 4 indicates that the confidence level is satisfied with different sample sets of uncertainties.

Table A1 Statistical information of solution R of Example1 in Chapter 4

Structural response	Mean	Std. dev.	Max	Min	95% quantile	99.3% quantile
$\sigma_{1:150}$ (MPa)	247.2407	8.1407	275.7838	223.4451	226.3159	243.1942
$\gamma_{1:150}$	0.09268	8.424×10^{-4}	0.09572	0.09052	0.09041	0.09219

Furthermore, in order to investigate the variations of order statistics caused by difference in samples, the following two problems, in which the first and second order statistics are taken respectively, are formulated and solved 10 times for Example 1 in Chapter 4 with different random seeds for the uncertain objective and global stability constraint functions:

$$
\begin{aligned}
&\text{Minimize } s\\
&\text{subject to } \sigma_{1:150}\left(\boldsymbol{x}_{\mathrm{free}}(\boldsymbol{t}),\boldsymbol{y}_{\mathrm{free}}(\boldsymbol{t}),\boldsymbol{A};\boldsymbol{\Theta}\right)\leq s;\\
&\qquad\gamma_{1:150}^{\mathrm{cr}}\left(\boldsymbol{x}_{\mathrm{free}}(\boldsymbol{t}),\boldsymbol{y}_{\mathrm{free}}(\boldsymbol{t}),\boldsymbol{A};\boldsymbol{\Theta}\right)\leq\gamma_{\mathrm{U}};\\
&\qquad V\left(\boldsymbol{x}_{\mathrm{free}}(\boldsymbol{t}),\boldsymbol{y}_{\mathrm{free}}(\boldsymbol{t}),\boldsymbol{A}\right)\leq V_{\mathrm{U}};\underline{\boldsymbol{t}}\leq\boldsymbol{t}\leq\overline{\boldsymbol{t}};\quad\underline{\boldsymbol{A}}\leq\boldsymbol{A}\leq\overline{\boldsymbol{A}}
\end{aligned}
\tag{A2}
$$

$$
\begin{aligned}
&\text{Minimize } s\\
&\text{subject to } \sigma_{2:150}\left(\boldsymbol{x}_{\mathrm{free}}(\boldsymbol{t}),\boldsymbol{y}_{\mathrm{free}}(\boldsymbol{t}),\boldsymbol{A};\boldsymbol{\Theta}\right)\leq s;\\
&\qquad\gamma_{2:150}^{\mathrm{cr}}\left(\boldsymbol{x}_{\mathrm{free}}(\boldsymbol{t}),\boldsymbol{y}_{\mathrm{free}}(\boldsymbol{t}),\boldsymbol{A};\boldsymbol{\Theta}\right)\leq\gamma_{\mathrm{U}};\\
&\qquad V\left(\boldsymbol{x}_{\mathrm{free}}(\boldsymbol{t}),\boldsymbol{y}_{\mathrm{free}}(\boldsymbol{t}),\boldsymbol{A}\right)\leq V_{\mathrm{U}};\underline{\boldsymbol{t}}\leq\boldsymbol{t}\leq\overline{\boldsymbol{t}};\quad\underline{\boldsymbol{A}}\leq\boldsymbol{A}\leq\overline{\boldsymbol{A}}
\end{aligned}
\tag{A3}
$$

The mean values, standard deviations, maximum and minimum values of $\sigma_{1:150}$, $\sigma_{2:150}$, $\gamma_{1:150}$ and $\gamma_{2:150}$ of both problems (A2) and (A3) are listed in Tables A2 and A3, respectively. It can be observed from Table A2 that although $\sigma_{1:150}$ and $\gamma_{1:150}$ vary due to difference in sample sets, their standard deviations are not relatively large compared to the corresponding mean values. The standard deviations of $\sigma_{1:150}$ and $\gamma_{1:150}$ in Table A2 are larger than the standard deviations of $\sigma_{2:150}$ and $\gamma_{2:150}$ in Table A3. However, the ranges between the maximum and minimum values of $\sigma_{1:150}$ and $\gamma_{1:150}$ in Table A2 are smaller than those of $\sigma_{2:150}$ and $\gamma_{2:150}$ in Table A3, indicating that the results obtained by using first order statistics vary in a narrower range due to difference in sample sets, while the results obtained by using second order statistics vary mostly close to the mean values but in a wider range. Moreover, a trade-off relationship is observed such that the mean values and standard deviations of the first order statistics $\sigma_{1:150}$ and $\gamma_{1:150}$ in Table A3 are larger than those of $\sigma_{1:150}$ and $\gamma_{1:150}$ listed in Table A2, and similar relationship can be also found by comparing the results of second order statistics $\sigma_{2:150}$ and $\gamma_{2:150}$ in Tables A2 and A3. Therefore, the standard deviations of the extreme order statistics, such as $\sigma_{1:150}$ and $\gamma_{1:150}$, of the final result would be smaller if the extreme order statistics are selected as the objective and constraint functions, while the standard deviations of the non-extreme order statistics of the final result would be smaller than that of extreme order statistics. However, since the extreme order statistics can provide a higher robustness level of the structure, where the probability of the structural response exceeding the extreme order statistics is lower than that of non-extreme order statistics, the extreme order statistics can serve as objective and constraint functions to obtain a structure with prescribed higher robustness level.

Table A2 Statistical information of problem (A1) for Example 1 in Chapter 4

Structural response	Mean	Std. dev.	Max	Min
$\sigma_{1:150}$ (MPa)	237.9236	7.6261	252.3201	229.3373
$\gamma_{1:150}$	0.0932	0.001797	0.0943	0.0906
$\sigma_{2:150}$ (MPa)	237.1836	7.1678	252.0981	229.3365
$\gamma_{2:150}$	0.0927	0.001528	0.0942	0.0899

Table A3 Statistical information of problem (A2) for Example 1 in Chapter 4

Structural response	Mean	Std. dev.	Max	Min
$\sigma_{1:150}$ (MPa)	245.6271	12.7975	271.7269	234.6596
$\gamma_{1:150}$	0.0989	0.001904	0.1090	0.0948
$\sigma_{2:150}$ (MPa)	227.3847	7.1650	248.0602	220.0783
$\gamma_{2:150}$	0.0985	0.001351	0.1009	0.0943

A3 Proof for convexity of $\Gamma(\boldsymbol{\lambda})$ in Chapter 5

Consider the following function

$$\Gamma(\boldsymbol{\lambda}) = -\int_0^1 \ln\left(\sum_{r=1}^{n} \lambda_r K_r(u)\right) du + \sum_{r=1}^{n} \lambda_r h_r \tag{A4}$$

where the *n* variables are $\boldsymbol{\lambda} = (\lambda_1, \lambda_2, \ldots, \lambda_n)$; $\boldsymbol{h}_r$ and $K_r(r = 1, 2, \ldots, n)$ are *n* constant functions and polynomials with arbitrary orders, respectively, which are kept constant during the optimization process for finding the variables $\boldsymbol{\lambda}$. Obviously, the part $\sum_{r=1}^{n} \lambda_r h_r$ is convex since it is a linear combination of variables, and the other part $-\int_0^1 \ln\left(\sum_{r=1}^{n} \lambda_r K_r(u)\right) du$ is also convex which can be proven by using the following two properties [161]:

Property 1: Suppose $f(\boldsymbol{\lambda}, u)$ is convex in $\boldsymbol{\lambda}$ for each $u \in \Omega$, and $\omega(u) \geq 0$ for each $u \in \Omega$, then the function *g* defined as

$$g(\boldsymbol{\lambda}) = \int_{\Omega} \omega(u) f(\boldsymbol{\lambda}, u) du \tag{A5}$$

is convex in $\boldsymbol{\lambda}$.

Property 2: Suppose $f: R^n \to R, A \in R^{n \times m}$, and $b \in R^n$. Define $g: R^m \to R$ by

$$g(\boldsymbol{\lambda}) = f(A\boldsymbol{\lambda} + b) \tag{A6}$$

with $\text{domain } g = \{\boldsymbol{\lambda} | A\boldsymbol{\lambda} + b \in \text{domain } f\}$. Then if *f* is convex, so is *g*; if *f* is concave, so is *g*.

Because the negative logarithmic function is convex, $-\ln\left(\sum_{r=1}^{n} \lambda_r K_r(u)\right)$ is convex with respect to $\boldsymbol{\lambda}$ for a specific value of *u* according to Property 2, and the integration $-\int_0^1 \ln\left(\sum_{r=1}^{n} \lambda_r K_r(u)\right) du$ with respect to *u* is also convex according to Property 1 as $\omega(u) = 1$ for $u \in [0,1]$. Thus, Eq. (A4) is convex.

Reference

1. Wang L, Shen W, Xie H, et al (2002) Collaborative conceptual design - State of the art and future trends. CAD Comput Aided Des 34:981–996. https://doi.org/10.1016/S0010-4485(01)00157-9
2. Hayashi K (2021) Reinforcement Learning for Optimal Design of Skeletal Structures. Kyoto university
3. Bendsøe MP, Sigmund O (2003) Topology Optimization: Theory, Methods, and Applications. Springer
4. Lagaros ND, Psarras LD, Papadrakakis M, Panagiotou G (2008) Optimum design of steel structures with web openings. Eng Struct 30:2528–2537. https://doi.org/10.1016/j.engstruct.2008.02.002
5. Zegard T, Paulino GH (2016) Bridging topology optimization and additive manufacturing. Struct Multidiscip Optim 53:175–192. https://doi.org/10.1007/s00158-015-1274-4
6. Lewiński T, Sokół T, Graczykowski C (2019) Michell structures. Springer International Publishing
7. Michell AGM (1904) The Limits of Economy of lllaterial in Frame-structures . Philos Mag Ser 6 8:589–597. https://doi.org/10.1080/14786440409463229
8. Ohsaki M (2010) Optimization of Finite Dimensional Structures. CRC Press, Boca Raton
9. K. Svanberg (1987) The Method of Moving Asymptotes - A New Method for Structural Optimization. Int J Numer Methods Eng 24:359–373
10. Long K, Wang X, Du Y (2019) Robust topology optimization formulation including local failure and load uncertainty using sequential quadratic programming. Int J Mech Mater Des 15:317–332. https://doi.org/10.1007/s10999-018-9411-z
11. Ohsaki M (1995) Genetic algorithm for topology optimization of trusses. Comput Struct 57:219–225. https://doi.org/10.1016/0045-7949(94)00617-C
12. Valdez SI, Marroquín JL, Botello S, Faurrieta N (2018) A meta-heuristic for topology optimization using probabilistic learning. Appl Intell 48:4267–4287. https://doi.org/10.1007/s10489-018-1215-1
13. Kallioras NA, Kazakis G, Lagaros ND (2020) Accelerated topology optimization by means of deep learning. Struct Multidiscip Optim 62:1185–1212. https://doi.org/10.1007/s00158-020-02545-z
14. Hayashi K, Ohsaki M (2021) Reinforcement learning for optimum design of a plane frame

under static loads. Eng Comput 37:1999–2011. https://doi.org/10.1007/s00366-019-00926-7

15. Beghini LL, Beghini A, Katz N, et al (2014) Connecting architecture and engineering through structural topology optimization. Eng Struct 59:716–726. https://doi.org/10.1016/j.engstruct.2013.10.032

16. Schuëller GI, Jensen HA (2008) Computational methods in optimization considering uncertainties - An overview. Comput Methods Appl Mech Eng 198:2–13. https://doi.org/10.1016/j.cma.2008.05.004

17. Elishakoff I, Ohsaki M (2010) Optimization and Anti-optimization of Structures Under Uncertainty. World Scientific, London

18. Choi S-K, Grandhi R V., Canfield RA (2007) Reliability-based Structural Design. Springer, London

19. Ben-Tal A, El Ghaoui L, Nemirovski A (2009) Robust optimization. Princeton University Press

20. Beyer HG, Sendhoff B (2007) Robust optimization - A comprehensive survey. Comput Methods Appl Mech Eng 196:3190–3218. https://doi.org/10.1016/j.cma.2007.03.003

21. Valdebenito MA, Schuëller GI (2010) A survey on approaches for reliability-based optimization. Struct Multidiscip Optim 42:645–663. https://doi.org/10.1007/s00158-010-0518-6

22. Kanno Y (2020) On three concepts in robust design optimization: absolute robustness, relative robustness, and less variance. Struct Multidiscip Optim 62:979–1000. https://doi.org/10.1007/s00158-020-02503-9

23. Lee KH, Park GJ (2001) Robust optimization considering tolerances of design variables. Comput Struct 79:77–86. https://doi.org/10.1016/S0045-7949(00)00117-6

24. Dunning PD, Kim HA (2013) Robust Topology Optimization: Minimization of Expected and Variance of Compliance. AIAA J 51:2656–2664. https://doi.org/10.2514/1.J052183

25. Thore CJ, Holmberg E, Klarbring A (2017) A general framework for robust topology optimization under load-uncertainty including stress constraints. Comput Methods Appl Mech Eng 319:1–18. https://doi.org/10.1016/j.cma.2017.02.015

26. Takezawa A, Nii S, Kitamura M, Kogiso N (2011) Topology optimization for worst load conditions based on the eigenvalue analysis of an aggregated linear system. Comput Methods Appl Mech Eng 200:2268–2281. https://doi.org/10.1016/j.cma.2011.03.008

27. Ohsaki M, Katsura M (2012) A random sampling approach to worst-case design of structures. Struct Multidiscip Optim 46:27–39. https://doi.org/10.1007/s00158-011-0752-6

28. Mogami K, Nishiwaki S, Izui K, et al (2006) Reliability-based structural optimization of frame structures for multiple failure criteria using topology optimization techniques. Struct Multidiscip Optim 32:299–311. https://doi.org/10.1007/s00158-006-0039-5

29. Enevoldsen I, Sorensen J. (1994) Reliability-based optimization in structural engineering.

Struct Saf 15:169–196

30. Aoues Y, Chateauneuf A (2010) Benchmark study of numerical methods for reliability-based design optimization. Struct Multidiscip Optim 41:277–294. https://doi.org/10.1007/s00158-009-0412-2

31. Rozvany GIN (1996) Difficulties in truss topology optimization with stress, local buckling and system stability constraints. Struct Optim 11:213–217. https://doi.org/10.1007/BF01197036

32. Zhou M (1996) Difficulties in truss topology optimization with stress and local buckling constraints. Struct Optim 11:134–136. https://doi.org/10.1007/BF01376857

33. Ohsaki M, Ikeda K (2010) Stability and Optimization of Structures: Generalized Sensitivity Analysis. Springer, Sendai

34. Asadpoure A, Nejat SA, Tootkaboni M (2020) Consistent pseudo-mode informed topology optimization for structural stability applications. Comput Methods Appl Mech Eng 370:113276. https://doi.org/10.1016/j.cma.2020.113276

35. Ohsaki M, Kanno Y (2001) Optimum Design of Finite Dimensional Systems with Coincident Critical Points. In: Proc. Fourth World Cong. Structural Multidisciplinary Optim. (WCSMO4). Dalian, China

36. Tugilimana A, Filomeno Coelho R, Thrall AP (2018) Including global stability in truss layout optimization for the conceptual design of large-scale applications. Struct Multidiscip Optim 57:1213–1232. https://doi.org/10.1007/s00158-017-1805-2

37. Evgrafov A (2005) On globally stable singular truss topologies. Struct Multidiscip Optim 29:170–177. https://doi.org/10.1007/s00158-004-0428-6

38. Lindgaard E, Dahl J (2013) On compliance and buckling objective functions in topology optimization of snap-through problems. Struct Multidiscip Optim 47:409–421. https://doi.org/10.1007/s00158-012-0832-2

39. Gao X, Ma H (2015) Topology optimization of continuum structures under buckling constraints. Comput Struct 157:142–152. https://doi.org/10.1016/j.compstruc.2015.05.020

40. Gao X, Li Y, Ma H, Chen G (2020) Improving the overall performance of continuum structures: A topology optimization model considering stiffness, strength and stability. Comput Methods Appl Mech Eng 359:1–23. https://doi.org/10.1016/j.cma.2019.112660

41. Kirsch U, Taye S (1986) On optimal topology of grillage structures. Eng Comput 1:229–243. https://doi.org/10.1007/BF01200139

42. Adil B, Cengiz B (2019) Optimal design of truss structures using weighted superposition attraction algorithm. Eng Comput. https://doi.org/10.1007/s00366-019-00744-x

43. Dorn WS, Gomory RE, Greenberg HJ (1964) Automatic design of optimal structures. J Mech 3:25–52

44. Hemp W Optimum Structures. Oxford University Press, Oxford

45. Sokół T (2011) A 99 line code for discretized Michell truss optimization written in Mathematica. Struct Multidiscip Optim 43:181–190. https://doi.org/10.1007/s00158-010-0557-z

46. Smith ODS (1998) Generation of ground structures for 2D and 3D design domains. Eng Comput (Swansea, Wales) 15:462–500. https://doi.org/10.1108/02644409810219820

47. Lewiński T, Rozvany GIN (2008) Exact analytical solutions for some popular benchmark problems in topology optimization III: L-shaped domains. Struct Multidiscip Optim 35:165–174. https://doi.org/10.1007/s00158-007-0157-8

48. Topping BH V. (1983) Shape Optimization of Skeletal Structures: A Review. J Struct Eng 109:1933–1951. https://doi.org/10.1061/(asce)0733-9445(1983)109:8(1933)

49. Gil L, Andreu A (2001) Shape and cross-section optimization of a truss structure. Comput Struct 79:681–689. https://doi.org/10.1016/S0045-7949(00)00182-6

50. Lamberti L, Pappalettere C (2003) A numerical code for lay-out optimization of skeletal structures with sequential linear programming. Eng Comput 19:101–129. https://doi.org/10.1007/s00366-003-0258-y

51. Achtziger W (2007) On simultaneous optimization of truss geometry and topology. Struct Multidiscip Optim 33:285–304. https://doi.org/10.1007/s00158-006-0092-0

52. Ohsaki M (1998) Simultaneous optimization of topology and geometry of a regular plane truss. Comput Struct 66:69–77. https://doi.org/10.1016/S0045-7949(97)00050-3

53. Wang D, Zhang WH, Jiang JS (2002) Combined shape and sizing optimization of truss structures. Comput Mech 29:307–312. https://doi.org/10.1007/s00466-002-0343-x

54. Wang D, Zhang WH, Jiang JS (2002) Truss shape optimization with multiple displacement constraints. Comput Methods Appl Mech Eng 191:3597–3612. https://doi.org/10.1016/S0045-7825(02)00297-9

55. Ohsaki M, Hayashi K (2017) Force density method for simultaneous optimization of geometry and topology of trusses. Struct Multidiscip Optim 56:1157–1168. https://doi.org/10.1007/s00158-017-1710-8

56. Hayashi K, Ohsaki M (2019) FDMopt: Force density method for optimal geometry and topology of trusses. Adv Eng Softw 133:12–19. https://doi.org/10.1016/j.advengsoft.2019.04.002

57. Schek HJ (1974) The force density method for form finding and computation of general networks. Comput Methods Appl Mech Eng 3:115–134. https://doi.org/10.1016/0045-7825(74)90045-0

58. Zhang JY, Ohsaki M (2006) Adaptive force density method for form-finding problem of tensegrity structures. Int J Solids Struct 43:5658–5673

59. Kimura T, Ohsaki M, Yamaoka Y (2018) Shape and topology optimization of shear wall consisting of latticed blocks. In: Proc. IASS Symposium 2018, Boston, USA. Int. Assoc. Shell and Spatial Struct, Paper No. 234, 2018

60. Kimura T, Ohsaki M, Yamaoka Y (2019) Shape and topology optimization of latticed shear wall utilising contact to existing frame. J Struct Constr Eng （in Japanese） 84:385–391. https://doi.org/10.3130/aijs.84.385

61. Descamps B, Filomeno Coelho R (2014) The nominal force method for truss geometry and topology optimization incorporating stability considerations. Int J Solids Struct 51:2390–2399. https://doi.org/10.1016/j.ijsolstr.2014.03.003

62. Guest JK, Igusa T (2008) Structural optimization under uncertain loads and nodal locations. Comput Methods Appl Mech Eng 198:116–124. https://doi.org/10.1016/j.cma.2008.04.009

63. Asadpoure A, Tootkaboni M, Guest JK (2011) Robust topology optimization of structures with uncertainties in stiffness - Application to truss structures. Comput Struct 89:1131–1141. https://doi.org/10.1016/j.compstruc.2010.11.004

64. Doltsinis I, Kang Z (2004) Robust design of structures using optimization methods. Comput Methods Appl Mech Eng 193:2221–2237. https://doi.org/10.1016/j.cma.2003.12.055

65. Tootkaboni M, Asadpoure A, Guest JK (2012) Topology optimization of continuum structures under uncertainty - A Polynomial Chaos approach. Comput Methods Appl Mech Eng 201–204:263–275. https://doi.org/10.1016/j.cma.2011.09.009

66. Jalalpour M, Guest JK, Igusa T (2013) Reliability-based topology optimization of trusses with stochastic stiffness. Struct Saf 43:41–49. https://doi.org/10.1016/j.strusafe.2013.02.003

67. Du L, Choi KK (2008) An inverse analysis method for design optimization with both statistical and fuzzy uncertainties. Struct Multidiscip Optim 37:107–119. https://doi.org/10.1007/s00158-007-0225-0

68. Picheny V, Kim NH, Haftka RT (2010) Application of bootstrap method in conservative estimation of reliability with limited samples. Struct Multidiscip Optim 41:205–217. https://doi.org/10.1007/s00158-009-0419-8

69. Du X, Chen W (2000) Towards a better understanding of modeling feasibility robustness in engineering design. J Mech Des Trans ASME 122:385–394. https://doi.org/10.1115/1.1290247

70. Au FTK, Cheng YS, Tham LG, Zeng GW (2003) Robust design of structures using convex models. Comput Struct 81:2611–2619. https://doi.org/10.1016/S0045-7949(03)00322-5

71. Lombardi M, Haftka RT (1998) Anti-optimization technique for structural design under load uncertainties. Comput Methods Appl Mech Eng 157:19–31. https://doi.org/10.1016/S0045-7825(97)00148-5

72. Kanno Y, Takewaki I (2006) Confidence ellipsoids for static response of trusses with load and structural uncertainties. Comput Methods Appl Mech Eng 196:393–403. https://doi.org/10.1016/j.cma.2006.04.007

73. Kanno Y, Takewaki I (2006) Sequential semidefinite program for maximum robustness design of structures under load uncertainty. J Optim Theory Appl 130:265–287. https://doi.org/10.1007/s10957-006-9102-z

74. Guo X, Bai W, Zhang W, Gao X (2009) Confidence structural robust design and optimization under stiffness and load uncertainties. Comput Methods Appl Mech Eng 198:3378–3399. https://doi.org/10.1016/j.cma.2009.06.018

75. Kanno Y, Xu G (2010) A mixed integer programming for robust truss topology optimization with stress constraints Yoshihiro. Int J Numer Methods Eng 83:1675–1699. https://doi.org/10.1002/nme

76. Fu Z, Wang C, Zhao J (2017) Truss topology optimization under uncertain nodal locations with proportional topology optimization method. Mech Based Des Struct Mach 45:190–206. https://doi.org/10.1080/15397734.2016.1163640

77. Ohsaki M, Yamakawa M, Fan W, Li Z (2019) An order statistics approach to multiobjective structural optimization considering robustness and confidence of responses. Mech Res Commun 97:33–38. https://doi.org/10.1016/j.mechrescom.2019.04.003

78. Yamakawa M, Ohsaki M (2016) Robust design optimization considering parameter variation of seismic characteristics using order statistics. Jounal Struct Eng (In Japanese) 62B:381–388

79. Rocchetta R, Crespo LG, Kenny SP (2020) A scenario optimization approach to reliability-based design. Reliab Eng Syst Saf 196:106755. https://doi.org/10.1016/j.ress.2019.106755

80. Kharmanda G, Olhoff N, Mohamed A, Lemaire M (2004) Reliability-based topology optimization. Struct Multidiscip Optim 26:295–307. https://doi.org/10.1007/s00158-003-0322-7

81. Wu YT (1994) Computational methods for efficient structural reliability and reliability sensitivity analysis. AIAA J 32:1717–1723. https://doi.org/10.2514/3.12164

82. Tu J, Choi KK, Park YH (1999) A new study on reliability-based design optimization. J Mech Des 121:557. https://doi.org/10.1115/1.2829499

83. Lee I, Choi KK, Du L, Gorsich D (2008) Inverse analysis method using MPP-based dimension reduction for reliability-based design optimization of nonlinear and multi-dimensional systems. Comput Methods Appl Mech Eng 198:14–27. https://doi.org/10.1016/j.cma.2008.03.004

84. Rahman S, Wei D (2008) Design sensitivity and reliability-based structural optimization by univariate decomposition. Struct Multidiscip Optim 35:245–261. https://doi.org/10.1007/s00158-007-0133-3

85. Chen X, Hasselman TK, Neill DJ (1997) Rreliability based structural design optimization for practical application. In: 38th AIAA/ASME/ASCE/AHS/ASC Structures, Structural Dynamics and Materials Conference and Exhibit and AIAA/ASME/AHS Adaptive Structural Forum. Kissimmee, Florida, p 1407

86. Liang J, Mourelatos ZP, Tu J (2008) A single-loop method for reliability-based design optimisation. Int J Prod Dev 5:76–92. https://doi.org/10.1504/IJPD.2008.016371

87. Meng Z, Keshtegar B (2019) Adaptive conjugate single-loop method for efficient reliability-based design and topology optimization. Comput Methods Appl Mech Eng

344:95–119. https://doi.org/10.1016/j.cma.2018.10.009

88. Weiji L, Li Y (1994) An effective optimization procedure based on structural reliability. Comput Struct 52:1061–1067. https://doi.org/10.1016/0045-7949(94)90090-6

89. Du X, Chen W (2004) Sequential optimization and reliability assessment method for efficient probabilistic design. J Mech Des 126:225. https://doi.org/10.1115/1.1649968

90. Du X (2008) Saddlepoint approximation for sequential optimization and reliability analysis. J Mech Des 130:1–11. https://doi.org/10.1115/1.2717225

91. Chen Z, Qiu H, Gao L, Li P (2013) An optimal shifting vector approach for efficient probabilistic design. Struct Multidiscip Optim 47:905–920. https://doi.org/10.1007/s00158-012-0873-6

92. Hao P, Wang Y (2020) A new reliability-based design optimization method with multiple-design points using the active learning kriging. In: Asian Congress of Structural and Multidisciplinary Optimization 2020. Seoul, Korea (Online Conference)

93. Li G, Yang H, Zhao G (2020) A new efficient decoupled reliability-based design optimization method with quantiles. Struct Multidiscip Optim 61:635–647. https://doi.org/10.1007/s00158-019-02384-7

94. He W, Yang H, Zhao G, et al (2021) A quantile-based SORA method using maximum entropy method with fractional moments. J Mech Des 143:1–12. https://doi.org/10.1115/1.4047911

95. Li G, He W, Zeng Y (2019) An improved maximum entropy method via fractional moments with Laplace transform for reliability analysis. Struct Multidiscip Optim 59:1301–1320. https://doi.org/10.1007/s00158-018-2129-6

96. Kanno Y (2019) A data-driven approach to non-parametric reliability-based design optimization of structures with uncertain load. Struct Multidiscip Optim 60:83–97. https://doi.org/10.1007/s00158-019-02199-6

97. Yamakawa M, Ohsaki M (2020) Fail-safe topology optimization via order statistics with stochastic gradient descent. In: Asian Congress of Structural and Multidisciplinary Optimization 2020. Seoul, Korea (Online Conference)

98. Hosking JRM (1990) L-Moments: Analysis and Estimation of Distributions Using Linear Combinations of Order Statistics. J R Stat Soc Ser B 52:105–124. https://doi.org/10.1111/j.2517-6161.1990.tb01775.x

99. Zhao Y-G, Tong M-N, Lu Z-H, Xu J (2020) Monotonic expression of polynomial normal transformation based on the first four L-moments. J Eng Mech 146:06020003. https://doi.org/10.1061/(asce)em.1943-7889.0001787

100. Lee U, Lee I Sampling-based reliability analysis using deep feedforward neural network. In: Asian Congress of Structural and Multidisciplinary Optimization 2020. Seoul, Korea (Online Conference)

101. Vapnik VN (2013) The Nature of Statistical Learning Theory. Springer science & business

media

102. Pandey MD (2000) A direct approach to the estimation of quantile function using the maximum entropy principle. Struct Saf 22:4

103. Deng J, Pandey MD (2008) Estimation of the maximum entropy quantile function using fractional probability weighted moments. Struct Saf 30:307–319. https://doi.org/10.1016/j.strusafe.2007.05.005

104. Pandey MD (2001) Extreme quantile estimation using order statistics with minimum cross-entropy principle. Probabilistic Eng Mech 16:31–42. https://doi.org/10.1016/S0266-8920(00)00004-7

105. Pandey MD (2001) Minimum cross-entropy method for extreme value estimation using peaks-over-threshold data. Struct Saf 23:345–363. https://doi.org/10.1016/S0167-4730(02)00008-5

106. Hosking JRM (2007) Distributions with maximum entropy subject to constraints on their L-moments or expected order statistics. J Stat Plan Inference 137:2870–2891. https://doi.org/10.1016/j.jspi.2006.10.010

107. Ohsaki M, Fujisawa K, Katoh N, Kanno Y (1999) Semi-definite programming for topology optimization of trusses under multiple eigenvalue constraints. Comput Methods Appl Mech Eng 180:203–217. https://doi.org/10.1016/S0045-7825(99)00056-0

108. Kanno Y, Ohsaki M, Katoh N (2001) Sequential semidefinite programming for optimization of framed structures under multimodal buckling constraints. Int J Struct Stab Dyn 1:585–602

109. Ben-Tal A, Jarre F, Kočvara M, et al (2000) Optimal Design of Trusses Under a Nonconvex Global Buckling Constraint. Optim Eng 1:189–213. https://doi.org/10.1023/A:1010091831812

110. Weldeyesus AG, Gondzio J, He L, et al (2020) Truss geometry and topology optimization with global stability constraints. Struct Multidiscip Optim 62:1721–1737. https://doi.org/10.1007/s00158-020-02634-z

111. Torii AJ, Lopez RH, Miguel LFF (2015) Modeling of global and local stability in optimization of truss-like structures using frame elements. Struct Multidiscip Optim 51:1187–1198. https://doi.org/10.1007/s00158-014-1203-y

112. Madah H, Amir O (2017) Truss optimization with buckling considerations using geometrically nonlinear beam modeling. Comput Struct 192:233–247. https://doi.org/10.1016/j.compstruc.2017.07.023

113. Guo X, Cheng G, Yamazaki K (2001) A new approach for the solution of singular optima in truss topology optimization with stress and local buckling constraints. Struct Multidiscip Optim 22:364–372. https://doi.org/10.1007/s00158-001-0156-0

114. Guo X, Cheng GD, Olhoff N (2005) Optimum design of truss topology under buckling constraints. Struct Multidiscip Optim 30:169–180. https://doi.org/10.1007/s00158-004-0511-z

115. Bendsøe MP (1989) Optimal shape design as a material distribution problem. Struct Optim 1:193–202. https://doi.org/10.1007/BF01650949

116. Kanno Y, Ohsaki M (2003) Minimum principle of complementary energy of cable networks by using second-order cone programming. Int J Solids Struct 40:4437–4460. https://doi.org/10.1016/S0020-7683(03)00215-4

117. Prescott P, Arnold BC, Balakrishnan N, Nagaraja HN (1993) A First Course in Order Statistics. Society for Industrial and Applied Mathematics

118. Hosking J, JR Wallis (2005) Regional Frequency Analysis: An Approach Based on L-moments. Cambridge University Press

119. Zienkiewicz OC, Taylor RL, Zhu JZ (2005) The finite element method: its basis and fundamentals. Elsevier, Oxford

120. Czarnecki S (2003) Compliance optimization of the truss structures. Comput. Assist. Mech. Eng. Sci. 10:117–137

121. Kirsch U, Bogomolni M, Sheinman I (2007) Efficient structural optimization using reanalysis and sensitivity reanalysis. Eng Comput 23:229–239. https://doi.org/10.1007/s00366-007-0062-1

122. Arora JS, Haug EJ (1979) Methods of Design Sensitivity Analysis in Structural Optimization. AIAA J 17:970–974. https://doi.org/10.2514/3.61260

123. Achtziger W (1998) Multiple-load truss topology and sizing optimization: Some properties of minimax compliance. J Optim Theory Appl 98:255–280. https://doi.org/10.1023/A:1022637216104

124. Mathworks (2018) Optimzation Toolbox User's Guide R2018a

125. Changizi N, Kaboodanian H, Jalalpour M (2017) Stress-based topology optimization of frame structures under geometric uncertainty. Comput Methods Appl Mech Eng 315:121–140. https://doi.org/10.1016/j.cma.2016.10.039

126. McGuire W, Gallagher RH, Ziemian RD (2000) Matrix structural analysis. John Wiley

127. Ito M, Kim NH, Kogiso N (2018) Conservative reliability index for epistemic uncertainty in reliability-based design optimization. Struct Multidiscip Optim 57:1919–1935. https://doi.org/10.1007/s00158-018-1903-9

128. Moon M, Cho H, Choi KK, Lamb D (2018) Confidence-based reliability assessment considering limited numbers of both input and output test data. 2027–2043

129. Kanno Y (2019) A data-driven approach to non-parametric reliability-based design optimization of structures with uncertain load. Struct Multidiscip Optim. https://doi.org/10.1007/s00158-019-02199-6

130. Gabrel V, Murat C, Thiele A (2014) Recent advances in robust optimization: An overview. Eur J Oper Res 235:471–483. https://doi.org/10.1016/j.ejor.2013.09.036

131. Holmstr K, Anders OG, Edvall MM (2007) Tomlab Optimization. In: User ' S Guid.

Tomlab/CONOPT. https://tomopt.com/docs/TOMLAB_CONOPT.pdf

132. Park C, Kim NH, Haftka RT (2015) The effect of ignoring dependence between failure modes on evaluating system reliability. Struct Multidiscip Optim 52:251–268. https://doi.org/10.1007/s00158-015-1239-7

133. Noh Y, Choi KK, Du L (2009) Reliability-based design optimization of problems with correlated input variables using a Gaussian Copula. Struct Multidiscip Optim 38:1–16. https://doi.org/10.1007/s00158-008-0277-9

134. Mathworks (2018) Statistics and Machine Learning Toolbox User's Guide 2018a

135. Jekel CF, Haftka RT (2020) Risk allocation for design optimization with unidentified statistical distributions. AIAA Scitech 2020 Forum 1 PartF:1–9. https://doi.org/10.2514/6.2020-0415

136. Boland PJ, Hollander M, Joag-Dev K, Kochar S (1996) Bivariate dependence properties of order statistics. J Multivar Anal 56:75–89. https://doi.org/10.1006/jmva.1996.0005

137. Avérous J, Genest C, Kochar SC (2005) On the dependence structure of order statistics. J Multivar Anal 94:159–171. https://doi.org/10.1016/j.jmva.2004.03.004

138. Navarro J, Balakrishnan N (2010) Study of some measures of dependence between order statistics and systems. J Multivar Anal 101:52–67. https://doi.org/10.1016/j.jmva.2009.04.016

139. Yamada S, Kanno Y (2016) Relaxation approach to topology optimization of frame structure under frequency constraint. Struct Multidiscip Optim 53:731–744. https://doi.org/10.1007/s00158-015-1353-6

140. Le C, Norato J, Bruns T, et al (2010) Stress-based topology optimization for continua. Struct Multidiscip Optim 41:605–620. https://doi.org/10.1007/s00158-009-0440-y

141. Kirsch U (1990) On singular topologies in optimum structural design. Struct Optim 2:133–142

142. Sigmund O (2001) A 99 line topology optimization code written in matlab. Struct Multidiscip Optim 21:120–127. https://doi.org/10.1007/s001580050176

143. Pedersen CBW (2003) Topology optimization of 2D-frame structures with path-dependent response. Int J Numer Methods Eng 57:1471–1501. https://doi.org/10.1002/nme.787

144. Rajan SD (1995) Sizing, shape, and togology design optimization of trusses using genetic algorithm. J Struct Eng 121:1480–1487. https://doi.org/10.1007/978-3-319-93025-1_4

145. Moustapha M, Sudret B, Bourinet JM, Guillaume B (2016) Quantile-based optimization under uncertainties using adaptive Kriging surrogate models. Struct Multidiscip Optim 54:1403–1421. https://doi.org/10.1007/s00158-016-1504-4

146. Melchers RE, Beck AT (2018) Structural Reliability Analysis and Prediction. John wiley & sons

147. Der Kiureghian A, Liu PL (1986) Structural reliability under incomplete probability

information. J Eng Mech 112:85–104

148. Tong MN, Zhao YG, Lu ZH (2021) Normal transformation for correlated random variables based on L-moments and its application in reliability engineering. Reliab Eng Syst Saf 207:107334. https://doi.org/10.1016/j.ress.2020.107334

149. Xi Z, Hu C, Youn BD (2012) A comparative study of probability estimation methods for reliability analysis. Struct Multidiscip Optim 45:33–52. https://doi.org/10.1007/s00158-011-0656-5

150. Ohsaki M (2005) Design sensitivity analysis and optimization for nonlinear buckling of finite-dimensional elastic conservative structures. Comput Methods Appl Mech Eng 194:3331–3358. https://doi.org/10.1016/j.cma.2004.12.021

151. Ohsaki M (2001) Sensitivity of optimum designs for spatially varying ground motions. J Struct Eng 127:1324–1329

152. Martins JRRA, Hwang JT (2013) Review and unification of methods for computing derivatives of multidisciplinary computational models. AIAA J 51:2582–2599. https://doi.org/10.2514/1.J052184

153. Miguel LFF, Fadel Miguel LF (2012) Shape and size optimization of truss structures considering dynamic constraints through modern metaheuristic algorithms. Expert Syst Appl 39:9458–9467. https://doi.org/10.1016/j.eswa.2012.02.113

154. Liu K, Detwiler D, Tovar A (2017) Optimal design of nonlinear multimaterial structures for crashworthiness using cluster analysis. J Mech Des 139:. https://doi.org/10.1115/1.4037620

155. Alberdi R, Zhang G, Li L, Khandelwal K (2018) A unified framework for nonlinear path-dependent sensitivity analysis in topology optimization. Int J Numer Methods Eng 115:1–56. https://doi.org/10.1002/nme.5794

156. Verbart A (2018) A working-set approach for sizing optimization of frame-structures subjected to time-dependent constraints. Struct Multidiscip Optim 58:1367–1382. https://doi.org/10.1007/s00158-020-02617-0

157. Sigmund O (2011) On the usefulness of non-gradient approaches in topology optimization. Struct Multidiscip Optim 43:589–596. https://doi.org/10.1007/s00158-011-0638-7

158. Zhao T, Ramos Jr. AS, Paulino GH (2019) Material Nonlinear Topology Optimization Considering the von Mises Criterion through an Asymptotic Approach: Max Strain Energy and Max Load Factor Formulations. Int J Numer Methods Eng 1–25. https://doi.org/10.1002/nme.6038

159. Wang Z, Wang P (2013) A new approach for reliability analysis with time-variant performance characteristics. Reliab Eng Syst Saf 115:70–81. https://doi.org/10.1016/j.ress.2013.02.017

160. Zhao C (2018) Extremes of order statistics of stationary gaussian processes. Probab Math Stat 38:61–75. https://doi.org/10.19195/0208-4147.38.1.4

161. Boyd S, Vandenberghe L (2004) Convex Optimization. Cambridge University Press

Publications

Journal papers:

J1) Shen W, Ohsaki M. Geometry and topology optimization of plane frames for compliance minimization using force density method for geometry model. Eng Comput 2021; 37:2029:2046

J2) Shen W, Ohsaki M, Yamakawa M. Multiobjective robust shape and topology optimization of plane frames using order statistics. Struct Multidiscip Optim 2021; 63:75-94

J3) Shen W, Ohsaki M, Yamakawa M. Robust geometry and topology optimization of plane frames using order statistics and force density method with global stability constraint. Int J Numer Methods Eng 2021; 122:653-3677

J4) Shen W, Ohsaki M, Yamakawa M. Quantile-based sequential optimization and reliability assessment for shape and topology optimization of plane frames using L-moments. Struct Saf 2022

Oral presentations:

O1) Shen W, Ohsaki M. Shape and topology optimization of frame structures using force density method. In *Proc. 13th World Congress of Structural and Multidisciplinary Optimization* (WCSMO13), Beijing, China, Paper ID: A240449, 2019

O2) Shen W, Ohsaki M. Geometry and topology optimization of plane frame using force density method. In *Summaries of technical papers of annual meeting* (*Structure I*), Architectural Institute of Japan (AIJ), Hokuriku, Japan, pp.193-194, Paper No. 20097, 2019

O3) Shen W, Ohsaki M, Yamakawa M. Multiobjective Robust Optimization of Plane Frame using Order Statistics. In *Asian Congress of Structural and Multidisciplinary Optimization 2020* (ACSMO2020), Seoul, Korea (Online), Paper ID: W1D-1, 2020

O4) Shen W, Ohsaki M, Yamakawa M. Multiobjective robust topology optimization of plane frames using order statistics. In *Summaries of technical papers of annual meeting* (*Structure I*), Architectural Institute of Japan (AIJ), Kanto, Japan (On line), pp.287-288, Paper No. 20144, 2020

O5) Shen W, Ohsaki M, Yamakawa M. Worst-case design of plane frames using order statistics. In *Proc. 14th World Congress of Structural and Multidisciplinary Optimization* (WCSMO14), Boulder, CO, USA (On line), Paper ID: 194, 2021

O6) Shen W, Ohsaki M, Yamakawa M. Sequential optimization and reliability assessment for shape and topology of plane frames using L-moments. In *Summaries of technical papers of annual meeting* (*Structure I*), Architectural Institute of Japan (AIJ), Tokai, Japan, pp.211-212, Paper No. 20106, 2021